THÈSE

Pour obtenir le grade de

DOCTEUR DE L'UNIVERSITÉ GRENOBLE ALPES

École doctorale : PHYS - Physique
Spécialité : Nanophysique
Unité de recherche : Spintronique et Technologie des Composants

Manipulation électrique des textures topologiques de spin pour des applications dans le domaine de la mémoire et du calcul neuromorphique

Electrical manipulation of topological spin textures for memory and neuromorphic applications

Présentée par :

Ilaria DI MANICI

Direction de thèse :

Gilles GAUDIN DIRECTEUR DE RECHERCHE, CNRS DELEGATION ALPES	Directeur de thèse
Olivier BOULLE CHARGE DE RECHERCHE HDR, CNRS DELEGATION ALPES	Co-directeur de thèse
Philippe TALATCHIAN INGENIEUR CHERCHEUR, CEA CENTRE DE GRENOBLE	Co-encadrant de thèse

Rapporteurs :

JULIE GROLLIER
DIRECTRICE DE RECHERCHE, CNRS DELEGATION ILE-DE-FRANCE SUD
EDOARDO ALBISETTI
ASSOCIATE PROFESSOR, POLITECNICO DI MILANO

Thèse soutenue publiquement le **18 décembre 2025**, devant le jury composé de :

LILIANA BUDA-PREJBEANU, PROFESSEURE DES UNIVERSITES, GRENOBLE INP - UGA	Présidente
JULIE GROLLIER, DIRECTRICE DE RECHERCHE, CNRS DELEGATION ILE-DE-FRANCE SUD	Rapporteure
EDOARDO ALBISETTI, ASSOCIATE PROFESSOR, POLITECNICO DI MILANO	Rapporteur
ALES HRABEC, SENIOR SCIENTIST, ECOLE POLYTECHNIQUE FEDERALE DE ZÜRICH	Examinateur

Acknowledgements

PhD is a journey that you don't do alone. I would not be here, writing these lines, if it was not for the people that shared and accompanied me through these last three years.

First of all, I would like to send all my heartfelt thanks to my supervisor Olivier. Since my first interview I had a gut feeling telling me that working with you would have been a great choice and these last three years proved me right. Your dedication to work, your passion for research, your extreme curiosity are truly impressive and are really inspiring for someone walking his first steps in the research world. Seeing your eyes lighting up at 5 a.m. after 12 uninterrupted hours of beamtime because you saw (or you thought you saw) a skyrmion, like those of a child seeing the gifts on Christmas morning, reminded me why I chose this job.
As if I had not been lucky enough having Olivier as a supervisor, also Gilles was there. In between all the things that you had to do, supervising several students, running a startup and much more, you always found the time to spend some hours in the e-beam with me trying to find almost invisible membranes, and that, always with a smile.
I will never thank enough both of you for the all the support, all the advices, for always finding the time to discuss something with me, for reading and correcting my thesis over and over. I will be proud of myself if I ever become half of the researchers you two are.

I would also like to thank all the technicians and engineers who helped transforming the ideas into actual devices and experiments. Eyub, you really are one of the cornerstones of Spintec. Thank you very much for all the help you gave me. A big thanks also to Florian that with extreme patience and kindness taught me everything I know about nanofabrications. Thanks also to Anike for the help in the nanofabrication process, to Bruno Fernandez for the fabrication of the SiN membranes and to Stephane for all depositions he made for me and the discussions about materials. I learnt a lot from all of you.

A big thanks also to all the permanent stuff who did not supervised me directly but was always there to discuss something with me or to give an advice or a kind word: thanks to Liliana, Philippe, Kevin and many others.

What made this experience really unforgettable are the amazing people that I had the extreme luck to be surrounded with and really felt like a second family. Nuno, I ended up in your office and after a couple of days where I thought you were not happy with my presence you started feeding me with snacks and made me feel immediately welcome. You have been a great friend for me inside and outside the lab.
The office atmosphere became even nicer with the arrival of Libor (you were just on holidays though, I was the newcomer) and Louis. We shared a lot of coffees and pain au chocolat in the morning, we complained about all the experiments not working (Nuno being the most dramatic) and we had a lot of fun. Thank you for including me from day one and for all the nice mountain and non-mountain activities we did together.
I can also not forget about the adjoint office-mate Hasan that was just looking for excuses to escape C5 and to come visit us. Hasan, you are one of the nicest people I have met in these years and I am really grateful for all the time we spent together doing activities or eating uzbek food (that I am probably still digesting).
I cannot leave Miina out of the list of people that made my first year in Spintec memorable. You are truly a super cool person and I am sure you will be (you already are) an incredible researcher. Big thanks also to the other super cool lady that I had the chance to meet in Spintec, Aurelie.
Special mention to monsieur Joseba who was not just a friend but a mentor. I learnt a lot from you both scientifically and from your incredible dedication for the things that passionate you. I will never thank you enough for all the patience and the kindness you have put in teaching me things and for making me feel welcomed in the group from the first day.

I also had the big luck to start my PhD along with a large group of people with which I shared conferences, trips, tiredness about the work, happiness and fears about the future. I want to thank Capucine, Theo and Subham with who I shared the painful months of the thesis writing. Your company during these times alleviated the stress and created some nice moments that made it easier to go through the writing process. Capucine, thank

you for all the support through good and bad times, for the balcon-aperos and for always being up to organise some nice plans. Subham, thank you for all the laughter, for all the sociological discussions in the office, for complaining about whatever italian food I prepared for you and for being a very good friend. Theo, thank you for all the time we shared together and for making me feel that my opinion mattered to you. Special mention to Maxime, thanks for all the runs and the gianduia pain au chocolat for breakfast, for making me laugh when you could not find the way back to your place, you really are one of the sweetest.
Thanks also to the other PhD mates from day one Hanna, Giovanni and Marco, for bringing always a lot of fun.
The list of dedications continues with Natalia and Kuldeep, with the newcomers Alvaro and Selu that brought a new wave of fun and happiness in the lab and where there to make smile and support me in the most stressful moments, with Corrado, who has always been there to listen about my fears and concerns and made me feel understood, you all have been great friends to me. I also want to say thanks to Coline that is one of the most kind hearted people I have ever met and as well a super cool and strong young woman and Jonathan with who I enjoyed a lot the discussion about my scientific results and the funny discussions over a beer or over a nice british meal.
A big thanks also to Simone (you are doing a brilliant job, never forget to enjoy the process!) and to all the people who I had the pleasure and the luck to work with in the group.
Special thanks to the sweet Neha that brought happiness in my last months in the office.

The list of people to thank for accompanying me through this journey is not yet over. Thanks to Andrea for all the amazing skiing plans you organised and Andres (Sene) for always being up to do any kind of activity (and taking amazing pictures in the meanwhile). I bring with me a lot of nice memories of all the time we spent together, thank you for having been such nice friends.
I want also to dedicate my work to Lucile, that is one of the most brilliant people I have ever met. Thank you for all the advices and the support, I always look at you with great admiration.
Thanks to Sergi, that behind the initial shyness is one of the funniest people I have ever met and of the greatest friends I had the chance to encounter during my PhD. Thank you for all the nice moments we shared and for always making me laugh like crazy. To David, cattiva, I liked that we connected very naturally. Meeting you has been the cherry on top of my stay in Grenoble.
To Javi, that was there when I started and is still here when I leave, probably the only person that likes to organise activities more than I do. We went through thick and thin in these years and your friendship became for me a solid pillar to rely on. I am grateful to have been allowed to see the nice person you are, you made my (E)Spintec a better place.
To Alice, who is a ray of sunshine, I lost the count of the amount of halloumi we ate. Thank you for bringing your incredible creativity into my life and thank you for being an amazing friend.
Thanks to Rodrigo who has been my shoulder during these years of PhD, inside and outside the lab. Without you nothing would have been the same.

Big thanks to all my "oldest" friends from university Paolo, Mery, Cami, Anna, Ste. It feels like I have been knowing you for a lifetime now. I love how time seems to have never passed when we reunite. Your support in my life is fundamental. Special thanks to Ric, always at my side.
Big thanks to all my friends from Milan, that always made me feel like I was missed when going home to see them.

Big thanks to Antonio, the best pizzaiolo in town, for making me smile every time we crossed our path in the apartment, for the diavolo pesce while we were both going crazy writing our thesis and for all the late night balcony conversations. You made our small apartment feel like home to me.
Big thanks to Chiara, my favourite small box of stress and energy, who I admire a lot. I was very happy the day you told me that you got a PhD in Grenoble and I could have not been happier to always have you by my side along this journey. Thank you for all the things we did together and for being such an important friend.
To Lucia, who has been there through the good and the bad days, I am happy that we always find a way back to each other, your friendship means a lot to me.
To Paolo, the one that made me discover Spintec. Thanks for all the movies (with a lot of pop-corns), the discussions about books, the aperos and much more, you are a very nice friend.

I really cannot thank all these people enough for the amazing three years I spent in Grenoble, for all the nice plans in the mountains hiking (almost dying a couple of times), skiing, for all the trips and holidays, for making the time in conferences very enjoyable, for all the dinner plans, the parties and for being a great support for everything. I bring something from all of you in my heart.

Last but not least, thanks to my family, my mum, my dad and Lori for always being supportive with my decisions and for being always there even when I was far.

Abstract

In recent years, the energy consumption related to information technology has increased exponentially, partly due to the advent of artificial intelligence. Novel hardware approaches are needed to tackle this issue. Spintronics is emerging as one most promising alternatives to the conventional microelectronics. Within the framework of spintronics, nanoscale magnetic textures known as magnetic skyrmions have attracted a great interest due to their potential applications in information storage, logic and also unconventional computing technologies. However, several limitations have been encountered regarding their electrical manipulation and detection in ferromagnets, which need to be overcome before moving toward applications.

In this thesis, we address the electrical manipulation and detection of magnetic skyrmions in magnetic tracks and magnetic tunnel junctions for memory and neuromorphic computing applications. In the first part of this work, we study the current-induced dynamics of magnetic skyrmions in synthetic antiferromagnets, which are composed of two thin ferromagnetic layers antiferromagnetically coupled. We demonstrate that skyrmions in such materials can move about one order of magnitude faster than in ferromagnets, reaching speeds up to 900 m/s. This effect is explained by the compensation of the so-called gyrotropic force exerted on the skyrmions as a result of the antiferromagnetic coupling.

In the second part of the thesis, we study the electrical manipulation of skyrmions in magnetic tunnel junctions, which represents another major challenge for applications. In particular, we demonstrate the electrical control of the nucleation and annihilation process of magnetic skyrmions in magnetic tunnel junctions. To this end, we performed *operando* magnetic imaging by combining the electrical detection with x-ray microscopy. We also investigated the dynamics of the nucleation and annihilation process using time-resolved magnetic microscopy experiments. These results open a promising path toward a multi-state memory based on magnetic skyrmions.

In the third and final part of this thesis, we exploit spin textures in magnetic tunnel junctions to achieve complex temporal pattern recognition using the physical reservoir computing paradigm. For this purpose, we use the spin texture in a magnetic tunnel junction and its dynamical response to electrical stimuli as the computational and memory elements of a neural network. We first show that the voltage induced dynamics of the spin texture exhibit the non-linearity and short-term memory properties required from a physical system to be exploited as a physical reservoir computing. We then demonstrate that such a system can perform temporal signal classification, such as distinguishing in between sine and square waves, with high accuracy, and achieve good performances on other benchmark tasks for reservoir computing systems.

These results open a pathway toward nanoscale, low power artificial intelligence hardware based on the manipulation of the spin textures.

Résumé

Ces dernières années, la consommation d'énergie associée aux technologies de l'information a augmenté exponentiellement, en partie grâce à l'avènement de l'intelligence artificielle. De nouvelles approches matérielles sont donc nécessaires pour résoudre ce problème. La spintronique émerge comme l'une des alternatives les plus prometteuses à la microélectronique conventionnelle. Dans le cadre de la spintronique, les textures magnétiques à l'échelle nanométrique connues sous le nom de skyrmions magnétiques ont suscité un grand intérêt en raison de leurs applications potentielles dans le stockage d'informations, la logique et les technologies informatiques non conventionnelles. Cependant, plusieurs limitations ont été rencontrées dans leur manipulation électrique et leur détection dans les ferromagnets, qui doivent être surmontées avant de passer à des applications pratiques. Dans cette thèse, nous abordons la manipulation électrique et la détection de skyrmions magnétiques dans les pistes magnétiques et les jonctions tunnel magnétiques pour des applications de mémoire et d'informatique neuromorphique. Dans la première partie de ce travail, nous étudions la dynamique induite par le courant des skyrmions magnétiques dans les antiferromagnétiques synthétiques, qui sont composés de deux couches ferromagnétiques minces couplées antiferromagnétiquement. Nous démontrons que les skyrmions dans de tels matériaux peuvent se déplacer environ un ordre de grandeur plus rapidement que dans les ferromagnets, atteignant des vitesses allant jusqu'à 900 m/s. Cet effet s'explique par la compensation de la force dite gyrotropique agissant sur les skyrmions en raison du couplage antiferromagnétique.
Dans la deuxième partie de la thèse, nous étudions la manipulation électrique des skyrmions dans les jonctions tunnel magnétiques, ce qui représente un autre défi majeur pour les applications. En particulier, nous démontrons le contrôle électrique des processus de nucléation et d'annihilation des skyrmions magnétiques dans les jonctions tunnel magnétiques. Pour cela, nous avons réalisé une imagerie magnétique operando en combinant la détection électrique avec la microscopie à rayons X. Nous avons également étudié la dynamique des processus de nucléation et d'annihilation en utilisant des expériences de microscopie magnétique à résolution temporelle. Ces résultats ouvrent une voie prometteuse vers des dispositifs de mémoire multi-états basés sur des skyrmions magnétiques.
Dans la troisième et dernière partie de cette thèse, nous exploitons les textures de spin dans des jonctions tunnel magnétiques pour réaliser une reconnaissance temporelle complexe en utilisant le paradigme du réservoir physique. À cette fin, nous utilisons la texture de spin dans une jonction tunnel magnétique et sa réponse dynamique aux stimuli électriques comme les éléments computationnels et de mémoire d'un réseau neuronal. Nous montrons d'abord que la dynamique induite par la tension de la texture de spin présente la non-linéarité et les propriétés de mémoire à court terme nécessaires pour qu'un système physique soit utilisé comme un ordinateur réservoir physique. Nous démontrons ensuite qu'un tel système peut effectuer une classification temporelle des signaux, comme distinguer entre les ondes sinusoïdales et carrées, avec une grande précision, et obtenir de bonnes performances sur d'autres tâches de référence pour les systèmes de calcul de réservoir.
Ces résultats ouvrent une voie vers un matériel d'intelligence artificielle à l'échelle nanométrique et de faible puissance basé sur la manipulation des textures de spin.

Contents

Acknowledgements **ii**

Abstract **v**

Résumé **vii**

Contents **x**

List of Figures **xv**

List of Tables **xix**

List of Abbreviations **xxii**

List of Symbols **xxiv**

Introduction **2**

1 Notions on micromagnetism and skyrmions **7**
1.1 Micromagnetic model: energy and interactions . . . 8
1.1.1 Zeeman energy . . . 8
1.1.2 Symmetric exchange interaction . . . 8
1.1.3 Demagnetizing energy . . . 8
1.1.4 Magnetic anisotropy . . . 10
1.1.4.1 Magneto-crystalline anisotropy . . . 10
1.1.4.2 Interface anisotropy . . . 10
1.1.5 Dzyaloshinskii-Moriya interaction . . . 11
1.1.6 Interlayer exchange coupling . . . 12
1.2 Domain walls . . . 12
1.3 DW dynamics . . . 14
1.3.1 Field-driven domain wall dynamics . . . 15
1.3.2 Current-driven domain wall dynamics . . . 17
1.3.2.1 Spin transfer torque . . . 17
1.3.2.2 Spin orbit torque . . . 18
1.4 Magnetic tunnel junctions . . . 20
1.4.1 Tunneling magnetoresistance . . . 20
1.4.2 STT-switching . . . 23
1.4.3 Voltage controlled magnetic anisotropy . . . 24
1.5 Magnetic skyrmions . . . 25
1.5.1 Topology and properties . . . 25
1.5.2 Energy terms and stabilization . . . 28
1.5.3 Observation of skyrmions . . . 29
1.5.4 Current-driven skyrmion dynamics . . . 32
1.5.4.1 Current-induced skyrmion dynamics and skyrmion Hall effect . . . 33
1.5.5 Electrical detection of magnetic skyrmions . . . 36
1.6 Conclusions . . . 38

2 Experimental techniques **40**
2.1 Deposition and nanofabrication of MTJs . . . 41
2.1.1 SiN membranes . . . 41
2.1.2 Deposition of magnetic stack . . . 42
2.1.3 MTJs patterning . . . 42
2.2 Electrical characterization of MTJs . . . 45
2.2.1 Manual prober . . . 45
2.2.2 Implementation of manual prober for RC measurement . . . 46
2.3 Magnetic force microscopy . . . 47
2.4 Magneto-optical Kerr effect . . . 47
2.5 X-ray microscopy techniques . . . 48
2.5.1 X-ray magnetic circular dichroism . . . 48
2.5.2 Scanning transmission x-ray microscopy . . . 49
2.5.3 Time-resolved STXM . . . 49
2.5.4 X-ray photoemission electron microscopy . . . 51

3 Fast current-induced motion in synthetic antiferromagnets **54**
3.1 Antiferromagnetic skyrmions . . . 55
3.2 SAF systems . . . 57
3.3 Current-induced motion experiments . . . 59
3.3.1 SAF skyrmions diameter . . . 60
3.3.2 Magnetic contrast in the MFM experiments . . . 61
3.3.3 Observation of SAF skyrmions with X-PEEM . . . 61
3.4 Analytical model and micromagnetic simulations . . . 61
3.4.1 Analytical model . . . 61
3.4.2 Micromagnetic simulations of the current-induced motion . . . 63
3.4.3 Micromagnetic simulations on the inertial skyrmion dynamics . . . 65
3.4.4 Experimental magnetic properties . . . 65
3.5 Current-induced motion in Pt/Co/Ru FM stacks . . . 66
3.6 Discussion and conclusions . . . 66

4 Bipolar control of skyrmions in magnetic tunnel junctions for memory applications **69**
4.1 Introduction . . . 70
4.2 Optimized low RA stack . . . 70
4.3 Device characterization . . . 71
4.4 Operando-STXM experiments in MTJs . . . 72
4.5 Control of a skyrmion using external magnetic field . . . 73
4.6 Bipolar nucleation and annihilation of a skyrmion in an MTJ using a DC current . . . 75
4.7 Bipolar control of a skyrmion in an MTJ using current pulses . . . 76
4.8 Time-resolved bipolar control of skyrmion in a MTJ . . . 77
4.8.1 System excitation . . . 78
4.8.2 Results . . . 78
4.8.2.1 First time-resolved STXM movie . . . 79
4.8.2.2 Second time-resolved STXM movie . . . 81
4.9 Conclusions . . . 81

5 Introduction on neural networks and reservoir computing **83**
5.1 Introduction . . . 84
5.1.1 Human brain . . . 84
5.1.2 Artificial neural networks . . . 85
5.1.2.1 Feed forward neural networks . . . 87
5.1.3 Recurrent neural networks . . . 88
5.2 Reservoir computing . . . 89
5.2.1 Echo state networks . . . 89
5.2.2 Liquid state machines . . . 90
5.3 Physical reservoir computing . . . 91
5.4 Multiplexing . . . 92
5.4.1 Time multiplexing . . . 92
5.5 Implementation of spintronics PRC . . . 92
5.6 Conclusions . . . 97

6 Physical reservoir computing exploiting spin textures in magnetic tunnel junctions 99
6.1 Introduction . . . 100
6.2 Electrical characterization of the device . . . 101
6.3 Temporal characterization of the device . . . 102
6.4 Sine and square classification task . . . 104
6.4.1 Protocol . . . 105
6.4.2 Results . . . 106
6.4.3 Reservoir metrics . . . 111
6.4.4 Saturated states . . . 112
6.5 NARMA task . . . 112
6.5.1 Results . . . 113
6.6 Mackey-Glass task . . . 115
6.6.1 Results . . . 115
6.7 Conclusions . . . 115

7 Summary and perspectives 118
7.1 Summary . . . 118
7.2 Perspectives . . . 119

A Derivation of Thiele equation 123
A.1 From LLG equation to Thiele equation . . . 124
A.2 Thiele equation with DL-SOT . . . 126

B XMCD contrast 131
B.1 Contrast generated by x-ray absorption in one magnetic and two layers . . . 132
B.2 Normalization in time-resolved STXM movies . . . 132
B.3 Time-resolved image . . . 132

References 138

List of Figures

1 Moore's law . . . 2
2 Number of publications and citations in the last years using "magnetic skyrmions" as keywords . 4

1.1 Demagnetizing field . . . 9
1.2 Effective magnetic anisotropy . . . 10
1.3 Interfacial DMI . . . 11
1.4 RKKY interaction . . . 12
1.5 Domain walls . . . 13
1.6 Néel DWs . . . 14
1.7 Magnetization dynamics . . . 14
1.8 Field-induced DW motion . . . 15
1.9 Domain wall velocity . . . 16
1.10 Field-driven DW dynamics . . . 17
1.11 Spin Hall effect . . . 18
1.12 Rashba-Edelstein effect . . . 19
1.13 SOT-driven DW motion . . . 20
1.14 Tunneling barrier . . . 21
1.15 Coherent tunneling . . . 22
1.16 STT-driven magnetic switching . . . 23
1.17 Voltage controlled magnetic anisotropy . . . 25
1.18 Topological functions . . . 25
1.19 Skyrmion topology . . . 26
1.20 Néel and Bloch skyrmions and antiskyrmions . . . 27
1.21 Energy vs radius of magnetic skyrmions . . . 29
1.22 Magnetic skyrmions energy and radius dependence . . . 30
1.23 Observation of magnetic skyrmions . . . 31
1.24 Observation of current-driven skyrmion motion . . . 32
1.25 Experimental observation of the skyrmion Hall effect . . . 34
1.26 SOT-driven skyrmion motion for different configurations . . . 36
1.27 Electrical detection of magnetic skyrmions . . . 37

2.1 SiN substrate . . . 41
2.2 Definition of the MTJ pillars . . . 42
2.3 MTJ stack etching . . . 43
2.4 Bottom electrode definition . . . 43
2.5 MTJ pillar encapsulation . . . 44
2.6 Top electrode definition . . . 45
2.7 Microscopy and SEM images of the MTJ nanofabrication . . . 45
2.8 Electronic circuit connected to the manual prober for electrical measurements on MTJs . . . 46
2.9 Magnetic force microscopy . . . 47
2.10 Magneto-optical Kerr effect . . . 48
2.11 X-rays magnetic circular dichroism (XMCD) . . . 49
2.12 Scanning transmission x-ray microscopy (STXM) . . . 50
2.13 Time-resolved STXM . . . 51
2.14 X-ray photoemission electron microscopy (X-PEEM) . . . 51
2.15 XMCD-PEEM image of a Néel DW . . . 52

3.1 Antiferromagnetic skyrmions . . . 55
3.2 Experimental observation of SAF skyrmions . . . 56
3.3 SAF stack optimization . . . 57

3.4 Current-induced motion of skyrmions in a SAF measured via MFM . . . 58
3.5 Fast current–induced dynamics of SAF skyrmions with vanishing skyrmion Hall effect . . . 59
3.6 Distribution of diameter of the skyrmions diameter in the SAF . . . 60
3.7 XMCD-PEEM observation of DWs chirality in SAF sample . . . 61
3.8 Schematic of skyrmions coupling in a synthetic antiferromagnet stack . . . 62
3.9 Simulation of the current-induced skyrmion deformation and inertial dynamics . . . 64
3.10 MFM current-induced skyrmion motion images in the Pt/Co/Ru trilayer and in the SF . . . 67

4.1 Low RA MTJ stack and OOP hysteresis loops of the FeCoB wedged free layer . . . 71
4.2 Hysteresis loops of resistance versus external magnetic field applied perpendicular to the sample plane measured on the MTJ pillar used for the STXM experiments for different DC currents . . . 72
4.3 XMCD-STXM contrast for an MTJ in the AP and P states . . . 73
4.4 Magnetic field induced skyrmion nucleation in a MTJ pillar . . . 74
4.5 Expansion of a skyrmion in a MTJ pillar under external magnetic field . . . 74
4.6 Bipolar electrical control of the skyrmion nucleation and annihilation in a MTJ using DC current 75
4.7 Bipolar electric control of the skyrmion nucleation and annihilation with current pulses . . . 76
4.8 Nucleation of a skyrmion with current pulses from the P state . . . 77
4.9 Schematic of the excitation for time-resolved STXM . . . 77
4.10 Captures from time-resolved STXM for an external magnetic field of -3.8 mT and an applied DC current of 0.8 mA, normalized with a reference frame taken after the negative pulse . . . 78
4.11 Schematic of the possible dynamic frame and reference frame giving rise to the time-resolved movie in Figure 4.10 . . . 79
4.12 Time-resolved sequence at -5.5 mT and schematic of the free and reference layer magnetizations 80

5.1 Schematic of a biological neuron . . . 84
5.2 Evolution of the membrane potential and its relation to the LIF neuron approach . . . 86
5.3 Schematic functioning of a LIF neuron . . . 87
5.4 Schematic of an artifical neuron and different types of neural networks . . . 88
5.5 Linear separability . . . 91
5.6 Implementation of time-delayed virtual nodes . . . 93
5.7 Examples of PRC implemented using spintronics systems. . . . 95

6.1 High-RA MTJ stack and OOP hysteresis loop of the FeCoB wedge . . . 100
6.2 Hysteresis loops of the device for different applied DC voltage . . . 101
6.3 Resistance versus applied DC voltage at different external magnetic fields . . . 102
6.4 Stochastic jumps among intermediate resistance states as a function of the DC voltage . . . 103
6.5 Resistance relaxation in response to step function input pulses averaged 500 times . . . 104
6.6 Sine and square classification task performing time-multiplexing . . . 105
6.7 Resistance time trace for the sine and square task . . . 106
6.8 Time-multiplexed voltage input (square/sine) and corresponding sampled resistance output . . . 107
6.9 Expected and reconstructed outputs from the testing of the sines and squares classification task . 108
6.10 Principal component analysis of the reconstructed outputs . . . 109
6.11 Response of the two virtual neurons to the input signal . . . 110
6.12 R vs V for the saturated states . . . 112
6.13 NARMA imitation task . . . 113
6.14 Expected and reconstructed outputs for three different NARMA tasks . . . 114
6.15 Mackey-Glass prediction task . . . 116

A.1 Spherical coordinates and skyrmion helicity . . . 129

B.1 Schematic of the contrast resulting from x-ray absorption process . . . 132
B.2 Schematic of the normalization process with a reference frame for time-resolved STXM for positive helicity photons . . . 133
B.3 Schematic of the normalization process with a reference frame for time-resolved STXM for negative helicity photons . . . 134
B.4 Captures from time-resolved STXM for an external magnetic field of -3.8 mT and an applied DC current of 0.8 mA, normalization with a reference frame taken after the positive pulse . . . 135

List of Tables

3.1 Experimental magnetic and transport parameters. 66

6.1 Average difference in the response for points having the same input in the sines and squares classification task. 110
6.2 Calculation of the NL and MC metrics for the three cases presented in Figure 6.9. 111
6.3 Parameters for different NARMA-N tasks. 112

List of Abbreviations

Al	Aluminium
Au	Gold
Co	Cobalt
Cr	Chromium
Fe	Iron
Gd	Gadolinium
Gd	Germanium
Hf	Hafnium
Ir	Iridium
K	Potassium
MgO	Magnesium oxide
Mn	Manganese
Na	Sodium
Ni	Nickel
Pd	Palladium
Pt	Platinum
Ru	Ruthenium
Si	Silicon
SiN	Silicon nitride
Ta	Tantalum
Ti	Titanium
W	Tungsten
AF	Antiferromagnetic
AFM	Atomic force microscopy
AMR	Anisotropic magneto-resistance
ANN	Artificial neural network
AP	Anti-parallel
AWG	Arbitrary waveform generator
BE	Bottom electrode
CL	Circular left
CR	Circular right
DOS	Density of states
DL	Damping-like
DMI	Dzyaloshinskii-Moriya interaction
DW	Domain wall
e-beam	Electron beam lithography
ESN	Echo state network
FL	Field-like
FM	Ferromagnetic
FNN	Feedforward neural network
FWHM	Full width half maximum
FZP	Fresnel zone plate
GRU	Gate recurrent unit
GSG	Ground Source Ground
HM	Heavy metal
IBE	Ion beam etching
IP	In plane
LCP	Left-circularly polarized
LIF	Leaky-Integrate and Fire

LLG	Landau-Lifshits-Gilbert
LSM	Liquid state machine
LSTM	Long short term memory
MCA	Magneto crystalline anisotropy
MFM	Magnetic force microscopy
MOKE	Magneto optical Kerr effect
MRAM	Magnetic random access memory
MTJ	Magnetic tunnel junction
NM	Non-magnet(ic)
OOP	Out of plane
OSA	Order separating aperture
P	Parallel
PMA	Perpendicular magnetic anisotropy
PMMA	Poly(methyl methacrylate)
PRC	Physical reservoir computing
RC	Reservoir computing
RCP	Right-circularly polarized
RIE	Reactive ion etching
RKKY	Ruderman-Kittel-Kasuya-Yosida
RNN	Recurrent neural network
RT	Room temperature
SAF	Synthetic antiferromagnet
SEM	Scanning electron microscope
SAF	Synthetic ferromagnet
SHE	Spin Hall effect
SIA	Structural inversion asymmetry
SkHA	Skyrmion Hall Angle
SkHE	Skyrmion Hall Effect
SNN	Spiking neural network
SOC	Spin-orbit coupling
SOT	Spin-orbit torque
STO	Spin torque oscillators
STT	Spin-transfer torque
STXM	Scanning transmission X-ray microscopy
TE	Top electrode
TEM	Tunneling electron microscopy
TMR	Tunneling magnetoresistance
UHV	Ultra-high vacuum
VCMA	Voltage controlled magnetic anisotropy
XMCD	X-ray circular magnetic dichroism
X-PEEM	X-ray photoemission electron microscopy
YIG	Yittrium-Iron-Garnet

List of Symbols

A	Exchange constant	J/m
$\mathbf{B}_{\mathrm{R}}$	Rashba field	
D	Dzyaloshinskii-Moriya interaction constant	$\mathrm{J/m^2}$
$\mathrm{D_C}$	Critical DMI constant	$\mathrm{J/m^2}$
e	Electron charge	C
$\mathbf{F}_{\mathrm{X}}$	X-like force	$\mathrm{Kg\ m/s^2}$
$\mathrm{G_X}$	Conductance of X state	$1/\Omega$
$\mathbf{H}$	Magnetic field	A/m
$\mathbf{J}$	Current density	$\mathrm{A/m^2}$
$\mathbf{k}$	Wave vector	1/m
$\mathrm{K_1}$	Volume magnetic anisotropy constant	$\mathrm{J/m^3}$
$\mathrm{K_d}$	Shape anisotropy constant	$\mathrm{J/m^3}$
$\mathrm{K_s}$	Effective anisotropy constant	$\mathrm{J/m^3}$
$\mathrm{K_s}$	Surface anisotropy constant	$\mathrm{J/m^2}$
$\mathbf{m}$	Reduced magnetization	
$\mathrm{m_e}$	Electron mass	kg
$\mathrm{M_s}$	Saturation magnetization	A/m
$\mathrm{N_{sk}}$	Skyrmion number	
p	Skyrmion core polarity	
$\mathrm{P_X}$	Polarization of X state	$\mathrm{Kg\ m/s^2}$
R	Skyrmion radius	
$\mathrm{R_X}$	Resistance of X state	Ω
$\mathbf{T}_{\mathrm{X}}$	X-like torque	A/m
$\mathrm{t_X}$	Thickness of X material	m
W	Skyrmion vorticity	
α	Magnetic damping	
γ	Gyromagnetic ratio	Hz/T
Δ	DW width	m
ε_{X}	Energy density of X	
μ_{B}	Bohr magneton	J/T
μ_0	Vacuum permeability	$4\pi \times 10^{-7}\mathrm{T\,A\,/m}$
χ	VCMA coefficient	J/Vm
Ψ	Skyrmion helicity	
θ_{SH}	Spin Hall angle	
$\hbar$	Planck constant	

Introduction

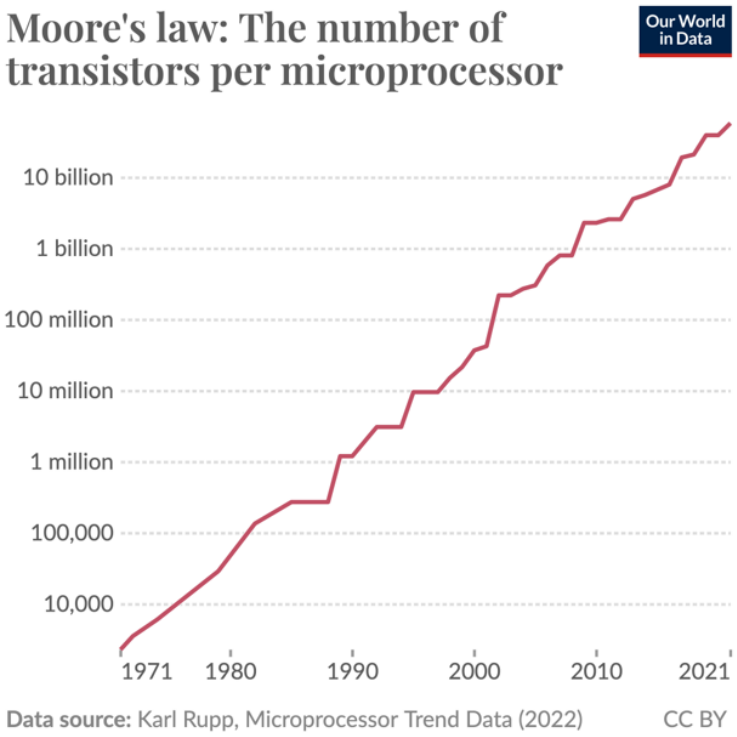

Figure 1: **Moore's law** The trend of number of CMOS transistor per microprocessor per year as predicted by the Moore's law. From OurWorldInData.

Complementary metal-oxide-semiconductor (CMOS) transistors are the elementary bricks of nearly all today electronic circuits and devices. Moore's law, i.e. the double of density of CMOS transistors every two year, has provided a metronome for semiconducting technology over the last five decades. However, as CMOS feature sizes and interconnect dimensions approach their fundamental limits, it is becoming increasingly difficult to continue along the path of scaling CMOS circuits.
The International Roadmap for Devices and Systems in 2023 [1] proposes two alternatives to approach the problem. The first consists in enhancing the functionality of CMOS by heterogeneously integrating new technologies, referred to as 'more Moore' [2]. The second approach is to develop novel devices that utilizes new information-processing methods, the so called 'beyond CMOS' technologies. This second approach is focused on the need for low-power, large-scale data processing devices, in particular to face the current rise of artificial intelligence. In the paradigm of beyond-CMOS technologies, one of the possible approaches is offered by spintronics. Spintronics, that stands for spin transport electronics, exploits the degrees of freedom given by the spin of the electrons in addition to their electrical charge for information processing.
Spintronics can be dated to the 1960s, when a group of physicists at IBM conducted a first study on the magnetoresistance due to electron tunneling [3]. Later, the improvement of thin film deposition techniques to obtain magnetic multilayers, led to a second fundamental milestone, the discovery of giant magneto-resistance (GMR) in 1988 independently by Albert Fert [4] and Peter Grunber [5]. The GMR is an effect that can be observed when two ferromagnetic layers are separated by a metallic spacer. The resistance to the applied current provided by the system depends on the relative orientation of the magnetization of the ferromagnetic layers. The GMR effect has been exploited to create magnetic field sensors, used to read data in hard disk drives for applications in various fields. A second major milestone arrived with the demonstration of the tunneling

magnetoresistance in 1991, a phenomenon discovered by Michel Julliere in 1975 [6]. This magnetoresistive effect arises when a voltage is applied to a stack consisting of two ferromagnetic layers separated by an oxide barrier. The resistance depends once again on the relative orientation of the magnetization of the two ferromagnetic layers. Devices that exploit this magnetic phenomenon are called magnetic tunnel junctions and they lie at the basis of one of the main application of spintronics, the magnetic random access memories (MRAM). The development of MRAM technology is also due to the discovery of the spin-transfer torque (STT) effect, by Berger and Slowcenszki in 1996 [7, 8]. The orientation of the magnetization of a ferromagnetic layer can be modified by a current that is passing through it. This is the STT, and it is exploited as a writing mechanisms in STT-MRAMs. The most important property of STT-MRAM is the non volatility, i.e. the fact that there is no need to use energy to maintain the state of the device since it is intrinsically encoded in the direction of the magnetization. STT-MRAM chips are produced by several companies like IBM, Samsung and Intel, as they can be embedded in CMOS based chips. Another type of MRAM that is raising a particular interest in the last years are those based on another phenomenon, the spin-orbit torque (SOT). SOT is present in systems where there is a strong spin orbit coupling (SOC) and that show inversion asymmetry, like a system made of an heavy-metal (HM) adjacent to a ferromagnetic layer. Due to SOC, when a current is injected in the HM layer, it generates a torque on the magnetization of the FM layer and can produce its switching. SOT-MRAM are based on this mechanism and they possess the potential to overcome STT-MRAMs as they propose several advantages: they can be faster, denser and the write and read mechanisms can be separated.
Another type of interaction was discovered in systems showing inversion asymmetry, the Dzyaloshinskii-Moriya interaction (DMI) [9, 10], a type of anti-symmetric exchange. It was discovered that this type of exchange can stabilize topological spin textures, like magnetic skyrmions. Magnetic skyrmions have been raising a great interest in the spintronics community due to their topological stability, small dimensions and efficient current-induced motion since their first experimental observation in 2009 [11, 12]. In Figure 2 is shown the number of articles containing the words skyrmions and magnetic skyrmions since their first experimental observation in 2009. One of the first proposals of applications based on skyrmions is the racetrack memory, where the skyrmion would represent the bit of information 1 and the absence of skyrmion would represent the bit of information 0 [13]. The systems targeted for this memory application consisted in HM/FM thin films where the skyrmions can be moved by applying current due to the SOT mechanism. Works showed the possibility of moving skyrmions with current, but also highlighted several limitations. One of the drawbacks comes from the limited velocity of FM skyrmions that hardly exceeds 100 m/s [14, 15] and a second one from the skyrmion Hall effect, an effect directly related to the skyrmion topology that bend the trajectory of skyrmions away from the current direction [16, 17]. To avoid these drawbacks it has been proposed the use of antiferromagnetic skyrmions, in specific the use of skyrmions in synthetic antiferromagnets (SAF) seems the most suitable for applications. SAF systems are composed of two ferromagnetic layers antiferromagnetically coupled through a NM layer in between them. It has been predicted that skyrmions in SAF would move faster and without skyrmion Hall effect. When my thesis started, works presenting the stabilization at room temperature of SAF skyrmions were published [18, 19], but nobody yet demonstrated the current-induced motion of antiferromagnetic skyrmions. The first objective of my thesis has been to join the work of my group in the demonstration of the current-induced motion of skyrmions in a SAF and to compare the results obtained in such a system to the velocity of skyrmions in similar ferromagnetic systems.
Another bottleneck for applications exploiting magnetic skyrmions is their electrical detection for possible applications in devices. Several works proposed to exploit the change in Hall resistivity related to the presence of magnetic skyrmions [20, 21], but the electric signal obtained was always very low. During my thesis two works were published about the electrical nucleation and detection of skyrmions in magnetic tunnel junctions [22, 23], one coming from another student in my group. An interesting application related to the possibility of nucleating and detecting skyrmions in MTJs is the creation of a multilevel memory, where, instead of having just two magnetic memory levels associated to the bits 1 and 0, as in STT-MRAM technology, an extra level could be given by an intermediate skyrmionic state. To this end, the skyrmionic state has to be accessible with current for the reading and writing operations. The second part of my PhD work focused on the demonstration of the bipolar electrical nucleation and annihilation of skyrmions in MTJ for memory applications. The electrical detection of the skyrmions has been accompanied by their imaging exploiting x-ray microscopy techniques.
Skyrmions, and more in general spintronics, have also been attracting large interest for application in the field of neuromorphic computing. Neuromorphic aims at emulating the brain approach for computation and memory. Indeed, the brain is made of neurons interconnected by synapses. Computation is performed in the neurons while memory is maintained in the synapses. Synapses are weighted connections in between the neurons whose weight depends on the usage of the connection. Since the synapses and neurons are physically interconnected, the computation and the memory occur in the same place. The architecture that is used nowadays in computers, the Von Neumann architecture, is not suitable for machine learning algorithms based on neural networks [24]. The Von Neumann architecture is indeed based on a sequential fetching of information in between the computational unit and the memory. The energy and time consumption to perform cognitive tasks for this type of hardware architecture is very high. Spintronics is a promising candidate for the creation of the building

blocks to emulate the brain behaviour, i.e. synapses and neurons. Indeed, spintronics devices can be engineered in order to provide different properties, non-volatility, stochasticity and the ability to carry information over long distances, that could be suitable for developing neuromorphic building blocks. As a third project within my thesis, I worked on the exploitation of spin textures in MTJs to achieve recognition tasks using the system as physical reservoir computing. Reservoir computing is a type of neural network with a very low training cost that consists in a single building block, the reservoir, through which the input of the system is projected in a higher dimension. The reservoir can be directly obtained using a physical system, in our case a MTJ showing intermediate resistance states due to spin textures that can be controlled with external voltage. The voltage input provides an ultra-low power excitation to the system and the detection of the reservoir states is easily performed exploiting the magneto-resistance reading in the MTJ. We proved that one of our devices was able to provide the necessary characteristic to be exploited as a reservoir and we tested its abilities using some benchmark tasks for reservoir computing systems.

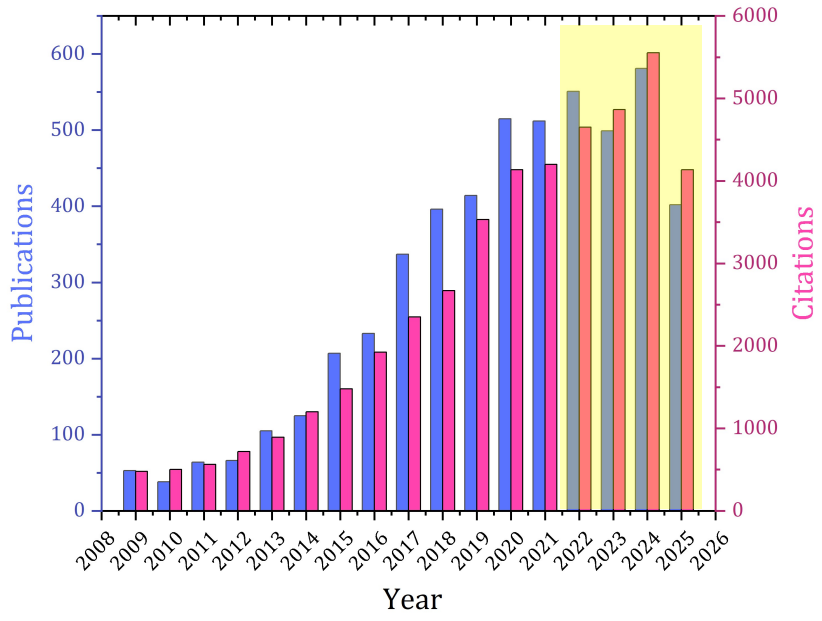

Figure 2: **Number of publications and citations in the last years using "magnetic skyrmions" as keywords** The blue bars in the plot are showing the increasing number of publications per year containing the keywords "magnetic skyrmions". In pink instead the number of citations of these articles. The initial year is chosen 2009, year of the first experimental observation of magnetic skyrmions. The yellow box highlight the years over which I carried out my PhD thesis. From Web of Science.

An outline of the manuscript is given below.

Outline This manuscript is divided in six chapters, plus a conclusive chapter that summarize the works and gives some perspectives. Two appendices are added at the end, one presenting some extended calculations and the second one describing in detail the analysis behind the observed contrast in microscopy measurement. It is also proposed a list of Figures and Tables, a list of abbreviations to facilitate the reading and a list of symbols used in the theoretical parts.

Chapter 1: Notions on micromagnetism and skyrmions Chapter 1 presents some basic theoretical concepts in magnetism and spintronics which are relevant to this thesis. I first present the energies terms that define the configuration of the magnetization in thin films. I then describe the stabilization and nature of domain walls in thin films and their motion induced by current and external magnetic field. I then discuss the physics behind magnetic tunnel junction and the possible mechanisms to achieve its switching. I finally describe what are magnetic skyrmions, and the progress made in their stabilization at room temperature in thin films, in their current-induced motion and in their electrical detection.

Chapter 2: Experimental techniques for nanofabrication and characterization I present in the second chapter the nanofabrication process used to fabricate magnetic tunnel junction, in particular on top of ultrathin membranes, for x-ray magnetic imaging. I then present the main characterization techniques used in the laboratory as well as the synchrotron technique.

Chapter 3: Fast current-induced motion in synthetic antiferromagnets I present here the work that I carried out during my first year of PhD on the current-induced motion of skyrmions in a synthetic antiferromagnet (SAF) system. I show all the experimental measurements performed in the SAF systems compared to similar ferromagnetic systems along with the micromagnetic simulations and the analytical modelling of the system.

Chapter 4: Bipolar control of skyrmions in magnetic tunnel junctions for memory applications I present in this chapter the work that I carried out during my second and third year of PhD about the bipolar electrical control of the nucleation and annihilation process of skyrmions in magnetic tunnel junctions. I present here the results obtained on the nucleation/annihilation process using electrical current. I also describe the time-resolved microscopy technique used to investigate the dynamics of the process.

Chapter 5: Introduction on neural networks and reservoir computing I introduced here some basic concepts about neural networks needed to understand the experimental work I performed, explained in chapter 6. I give first an overview on the brain architecture and how neural networks take inspiration from it. I give then a brief overview on different types of artificial neural networks, focusing my attention on the reservoir computing paradigm, a specific type of neural networks that we tried to create in our experiments. I give also an overview on applications of reservoir computing based on spintronics systems.

Chapter 6: Physical reservoir computing exploiting spin textures in magnetic tunnel junctions I show here the results obtained on performing a physical reservoir computing system by exploiting the presence of spin textures in magnetic tunnel junction. I explain in detail the dynamics of the system chosen to be exploited as a reservoir and I present the results obtained on the testing of widely used benchmark tasks for reservoir computing systems.

Chapter 7: Summary and perspectives In this chapter I present a smmary of the work described in this thesis and I propose some perspectives on the continuation of the projects shown.

Chapter 1

Notions on micromagnetism and skyrmions

Contents

1.1 Micromagnetic model: energy and interactions . . . 8
1.1.1 Zeeman energy . . . 8
1.1.2 Symmetric exchange interaction . . . 8
1.1.3 Demagnetizing energy . . . 8
1.1.4 Magnetic anisotropy . . . 10
1.1.5 Dzyaloshinskii-Moriya interaction . . . 11
1.1.6 Interlayer exchange coupling . . . 12
1.2 Domain walls . . . 12
1.3 DW dynamics . . . 14
1.3.1 Field-driven domain wall dynamics . . . 15
1.3.2 Current-driven domain wall dynamics . . . 17
1.4 Magnetic tunnel junctions . . . 20
1.4.1 Tunneling magnetoresistance . . . 20
1.4.2 STT-switching . . . 23
1.4.3 Voltage controlled magnetic anisotropy . . . 24
1.5 Magnetic skyrmions . . . 25
1.5.1 Topology and properties . . . 25
1.5.2 Energy terms and stabilization . . . 28
1.5.3 Observation of skyrmions . . . 29
1.5.4 Current-driven skyrmion dynamics . . . 32
1.5.5 Electrical detection of magnetic skyrmions . . . 36
1.6 Conclusions . . . 38

I introduce in this chapter the basic notions of micro and nanomagnetism and spintronics that will be used and referred to during the thesis work. I include all the different energy terms and basic interactions in section 1, domain walls and their dynamics (section 1.2 and 1.3), magnetic tunnel junctions and the mechanisms for their switching (section 1.4) and finally the magnetic skyrmions with a state of the art literature about their stabilization, detection and current-induced motion (section 1.5).

1.1 Micromagnetic model: energy and interactions

In a magnetic material, every atom is carrying a magnetic moment that is given by both the electron orbital motion and the intrinsic spin momentum or spin of the electrons. The magnetization $\mathbf{M}$ is defined as the magnetic moments per unit volume (in A/m). M_S is the saturation magnetization, the maximum value of magnetization achievable when all the magnetic moments in a material are aligned collinearly. Ferromagnets (FM) are magnetic materials in which the parallel alignment of the magnetic moments is favoured. The micromagnetic model was developed by Brown to facilitate the solution for the many body electrons problem in such materials. The micromagnetic model approximates the magnetization as a continuum and describes it with a vector field $\mathbf{m(r)} = \frac{\mathbf{M(r)}}{Ms}$, where $\mathbf{m(r)}$ denotes the normalized magnetization at a given position $\mathbf{r}$. The continuum approximation can be assumed as the typical length scale of variations for the atomic moments is significantly larger than the interatomic distance. The different energy terms that have to be taken into account to understand the micromagnetic behaviour of a material will be explained in the following sections.

1.1.1 Zeeman energy

The Zeeman energy is due to the interaction of the magnetization $\mathbf{m}$ of a material with an external magnetic field $\mathbf{H_{ext}}$. The Zeeman energy density (in J/m^3) is expressed as:

$$\varepsilon_Z = -\mu_0 M_S \mathbf{m} \cdot \mathbf{H_{ext}} \tag{1.1}$$

where μ_0 is the vacuum permeability. The Zeeman energy promotes the alignment of the magnetic moments along the external magnetic field.

1.1.2 Symmetric exchange interaction

The exchange interaction is the cause of long magnetic ordering. It is a quantum mechanical interaction that arises from the superposition of the wave functions of two neighbouring electrons. By the Pauli exclusion principle the total wave function must be anti-symmetric because two electrons cannot be in the same quantum state simultaneously. The Heisenberg hamiltonian extends the exchange interaction in a solid over all the couples of neighbouring atoms:

$$H_{ex} = -\sum_{i<j} J_{ij}\, \mathbf{S}_i \cdot \mathbf{S}_j \tag{1.2}$$

In the equation J_{ij} is the exchange integral between two neighbouring atoms i and j represented by their spins $\mathbf{S_i}$ and $\mathbf{S_j}$. J_{ij} assumes the value J for neighbouring atoms and 0 everywhere else in order to count only first-neighbour interactions. The sign of J defines the magnetic ordering in a material. When $J > 0$ the favoured situation is the parallel alignment of spins, leading to a ferromagnetic (FM) ordering. When $J < 0$ the favourable situations is spins anti-parallelly aligned, leading to antiferromagnetic (AF) ordering. In the continuum approximation of micromagnetism the energy density associated to exchange interaction is written as:

$$\varepsilon_{ex} = A\left((\nabla m_x)^2 + (\nabla m_y)^2 + (\nabla m_z)^2\right) \tag{1.3}$$

where A is the exchange constant or stiffness (in J/m) defined as $A \approx JS^2 n/a$, with a the lattice parameter of the solid and n the number of atoms per unit cell.

1.1.3 Demagnetizing energy

Each magnetic moment inside a solid generates a magnetic field that is called dipolar or magnetostatic field. The magnetic field generated by a dipole interacts with the magnetic fields generated by all the other dipoles. This magnetic field is called dipolar field outside the sample and demagnetizing field $\mathbf{H_d}$ inside the sample. The energy density associated to the latter is called demagnetizing energy and it represents the energy stored in a given magnetic configuration. It takes the form of a Zeeman type (see equation 1.1) energy density:

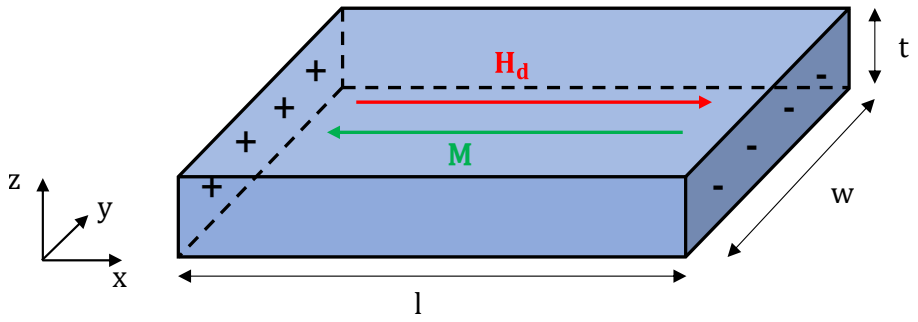

Figure 1.1: **Demagnetizing field** | Thin film geometry with $t \ll w < l$. $\mathbf{M}$ is the magnetization and $\mathbf{H_d}$ is the demagnetizing field. The magnetization tends to lie in the plane as this is the configuration that minimizes the magnetic charges, represented by the + and - on the zy faces of the film.

$$\varepsilon_d = -\frac{\mu_0 M_S}{2}\,\mathbf{m}\cdot\mathbf{H_d} \tag{1.4}$$

where the factor 1/2 is introduced not to count twice the interaction between a couple of dipoles. The energy of the interaction between two magnetic dipoles $\boldsymbol{\mu}_1$ and $\boldsymbol{\mu}_2$ is expressed by the formula:

$$E = \frac{\mu_0}{4\pi r^3}\left(\boldsymbol{\mu}_1\cdot\boldsymbol{\mu}_2 - \frac{3}{r^2}(\boldsymbol{\mu}_1\cdot\mathbf{r})(\boldsymbol{\mu}_1\cdot\mathbf{r})\right) \tag{1.5}$$

where $\mathbf{r}$ is the distance in between the two magnetic moments. The energy depends on the relative orientation of the magnetic dipoles and on their distance with a $1/r^3$ spatial dependence, making it a long range interaction. As it can be difficult to evaluate it numerically in most cases, an alternative approach proposes the use of magnetic charges. The second Maxwell equation in absence of external currents writes:

$$\nabla\cdot\mathbf{B} = 0 \tag{1.6}$$

where $\mathbf{B}$ is the induction field. $\mathbf{B}$ is given by $\mathbf{B} = \mu_0(\mathbf{H_d} + \mathbf{M})$. Inserting the last expression in equation 1.6 it is obtained $\nabla\cdot\mathbf{H_d} = -\nabla\cdot\mathbf{M}$. From this equation, in analogy with the electrostatic Maxwell equation, magnetic charges can be defined as $\rho_M = \nabla\cdot\mathbf{M}$, volume charges, and $\sigma_M = \mathbf{M}\cdot\hat{\mathbf{n}}$, surface charges, where $\hat{\mathbf{n}}$ is the unit vector normal to the surface. With these definitions, the demagnetizing energy density can be expressed in terms of magnetic charges:

$$\epsilon_d = \frac{1}{2}\mu_0\left(\int_V \rho_m\phi_d\,dV + \int_S \sigma_M\phi_d\,dS\right) \tag{1.7}$$

where ϕ_d is the scalar magnetic potential. It is important to highlight that magnetic charges do not actually exist, they are just a concept made in analogy with the electrostatic case to simplify the calculations. The energy minimum, considering only the demagnetizing field, is given by the magnetic configuration that minimizes the surface and volume charges. This means that the magnetization of a system is strongly influenced by its shape, a phenomenon called shape anisotropy. In Figure 1.1 is illustrated the example of a uniformly magnetized thin film with a length l, width w and thickness t where $t \ll w < l$. The demagnetizing field can be expressed in terms of:

$$\mathbf{H_d} = -\mathcal{N}\mathbf{M} \tag{1.8}$$

where $\mathcal{N}$ is the demagnetizing tensor. $\mathcal{N}$ is a diagonal tensor represented as:

$$\mathcal{N} = \begin{pmatrix} \mathcal{N}_x & 0 & 0 \\ 0 & \mathcal{N}_y & 0 \\ 0 & 0 & \mathcal{N}_z \end{pmatrix} \tag{1.9}$$

The trace of $\mathcal{N}$ is equal to 1, meaning $\mathcal{N}_x + \mathcal{N}_y + \mathcal{N}_z = 1$. Given the shape of the thin film, the surface magnetic charges are minimized when they lie in the yz plane so $\mathcal{N}_x < \mathcal{N}_y \ll \mathcal{N}_z$ hence $\mathcal{N}_z \approx 1$. The physical meaning is that, to minimize the energy, the magnetization is getting aligned along the z axis and any deviation from it generates a cost in term of demagnetizing energy. If l = w, an easy plane for the magnetization is defined. Calling θ the angle in between the magnetization and the normal to the film plane, the energy density can be written as:

$$\varepsilon_d = -\frac{\mu_0 {M_S}^2}{2}\sin^2\theta = -K_d\sin^2\theta \tag{1.10}$$

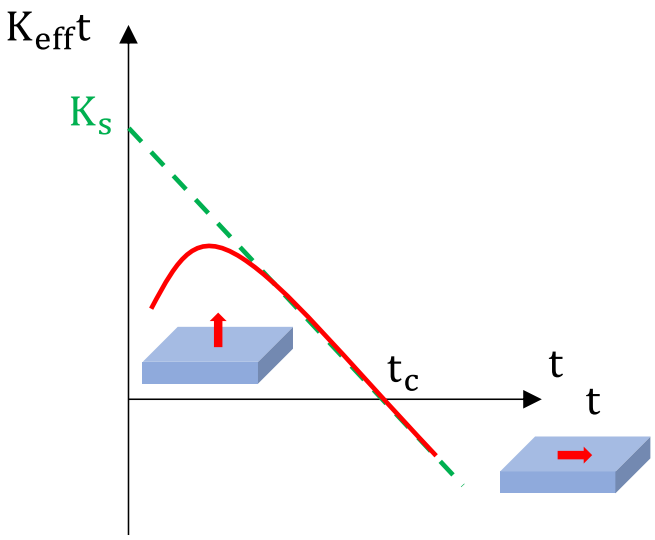

Figure 1.2: **Effective magnetic anisotropy** | Schematic of the evolution of the effective anisotropy constant with the film thickness for a Pt/Co/Ru system. The critical thickness t_c is around 1.6 nm.

where K_d is the shape anisotropy constant (in J/m^3). Therefore, the shape anisotropy favours the alignment of the magnetization in the plane of the film.

1.1.4 Magnetic anisotropy

In magnetic materials the energy depends on the direction of **M**. This dependence is not determined by the exchange energy which only tends to align spins parallel or anti parallel, no matter their direction. The dependence is due to the magnetic anisotropy, a term that refers on how the magnetic response of the material varies with the direction of the excitation that it receives. Several factors contribute to the magnetic anisotropy. One of these factors is the shape of the material, shape anisotropy, that has been presented in section 1.1.3. Other two important factors determining the magnetic anisotropy are presented in the following sections.

1.1.4.1 Magneto-crystalline anisotropy

The magneto-crystalline anisotropy (MCA) is generated by the spin-orbit interaction of the electrons inside the material. The orbitals are connected to the crystallographic structure of the solid, and this interaction makes the spins of the electrons align along some preferential crystallographic axes. Therefore, there are some easy axes along with the magnetization aligns preferentially. One case of MCA is the uniaxial anisotropy, meaning that the magnetization is favoured to align along a specific axis of the solid. The uniaxial anisotropy energy density (in second order approximation) is expressed as:

$$\varepsilon_{MC} = K_1 \sin^2 \theta \tag{1.11}$$

where K_1 is the volume magneto-crystalline anisotropy constant (in J/m^3) and θ is the angle between the magnetization direction and the high symmetry axis of the crystal. The high symmetry axis of the crystal is called easy axis, while the axes perpendicular to the easy axis are referred to as hard axes. If K_1 is positive the system presents an uniaxial anisotropy. If K_1 is negative instead, the system presents an easy plane, perpendicular to the high symmetry axis.

1.1.4.2 Interface anisotropy

The shape and magneto-crystalline anisotropy are describing the volume contribution to the direction of the magnetization. In thin films, the broken symmetry at the interfaces can generate additional terms to the total anisotropy, that can become predominant over the volume terms. The energy density associated to the interfaces is written as an uniaxial anisotropy term:

$$\varepsilon_S = \frac{K_S}{t} \sin^2 \theta \tag{1.12}$$

where K_S represents the surface anisotropy constant (in J/m^2), t the thickness of the thin film and ϑ the angle with the normal of the thin film. The interfacial anisotropy tends to align the magnetization in the out-of-plane (OOP) direction so for convention $K_S > 0$.

The total anisotropy of the system is given by the sum of the contributions coming from the shape anisotropy, the MCA and interfacial anisotropy:

$$\varepsilon_{\text{eff}} = \varepsilon_{\text{d}} + \varepsilon_{\text{MC}} + \varepsilon_{\text{S}} = \frac{\text{K}_{\text{S}}}{\text{t}} \sin^2\theta + \text{K}_1 \sin^2\theta - \frac{\mu_0 {\text{M}_{\text{S}}}^2}{2} \sin^2\theta \tag{1.13}$$

giving an effective anisotropy constant $\text{K}_{\text{eff}} = \text{K}_1 + \frac{\text{K}_{\text{s}}}{\text{t}} - \frac{\mu_0 {\text{M}_{\text{S}}}^2}{2}$. In general for a thin film the contribution of MCA is negligible with respect to the other two contributions, therefore the direction of the magnetization is decided by the sign of $\text{K}_{\text{eff}} = \frac{\text{K}_{\text{s}}}{\text{t}} - \frac{\mu_0 {\text{M}_{\text{S}}}^2}{2}$. If the interfacial anisotropy contribution overcomes the shape anisotropy contribution, the magnetization points OOP, giving rise to perpendicular magnetic anisotropy (PMA), otherwise the magnetization lies in-plane (IP). It is possible to define a critical thickness t_{c} for which $\text{K}_{\text{eff}} = 0$ above which the magnetization is favoured IP. t_{c} defines the spin reorientation transition, the thickness for which spins switch from OOP orientation to IP orientation due to the change in the anisotropy. In Figure 1.2 is presented the dependency of $\text{K}_{\text{eff}}\text{t}$ on the thickness of the thin layer for Pt/Co/Ru. The slope for large thicknesses provides the shape contribution while the intercept provides the interfacial contribution.

1.1.5 Dzyaloshinskii-Moriya interaction

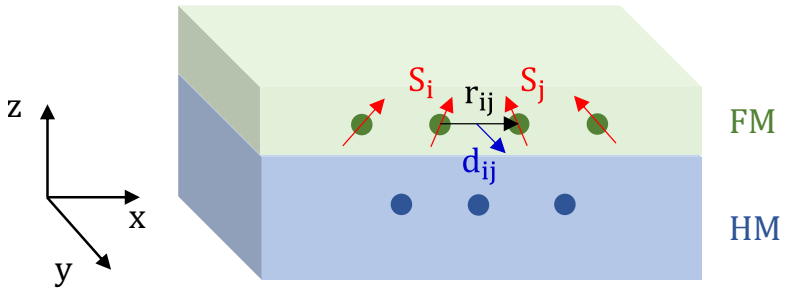

Figure 1.3: **Interfacial DMI** | Schematic of DMI arising at the interface between a FM and a HM layer.

The Dzyaloshinskii-Moriya interaction (DMI) is an antisymmetric exchange interaction that was first reported through the observation of a weak ferromagnetism in antiferromagnetic crystals. Some materials considered as antiferromagnetics, such as $\alpha\text{Fe}_2\text{O}_3$, where exhibiting a spontaneous magnetization, with very small magnetic moments compared to those brought by their ferromagnetic atoms [25]. Dzyaloshinskii in 1958 proposed a first explanation of the phenomenon studying the possible magnetic configurations based on the crystal symmetry [9]. Moryia in 1960 was able to better explain the phenomenon taking into account spin-orbit coupling (SOC) in a material lacking inversion symmetry [10, 26]. The DMI hamiltonian is:

$$\mathcal{H}_{\text{DMI}} = \mathbf{D_{ij}} \cdot (\mathbf{S_i} \times \mathbf{S_j}) \tag{1.14}$$

where $\mathbf{D_{ij}}$ is the DMI vector and $\mathbf{S_i}$ and $\mathbf{S_j}$ indicate the spins of two atomic sites i and j. The vector $\mathbf{D_{ij}}$ that depends on the crystal symmetry, is in general lying parallel or perpendicular to the line connecting the two spins. The DMI is an interaction that favours a 90° alignment in between the two spins in a plane perpendicular to that of the vector $\mathbf{D_{ij}}$, with a precise sense of rotation, the chirality. DMI competes with symmetric exchange in the short range lengths and it is fundamental for the creation of non-collinear spin textures such as chiral domain walls, spin spirals and skyrmions.
DMI was first observed in crystals of the B20 crystallographic type, were skyrmions were found. For these crystals lacking inversion symmetry the DMI is a bulk type and promotes the generation of Bloch type skyrmions [11, 12]. DMI can also arise from the interfaces of systems presenting structural inversion asymmetry (SIA) as for example a stack where a FM layer is sandwiched in between two different materials [27, 28, 29]. The origin of interfacial DMI lies in the breaking of symmetry inversion at the interface combined with a strong spin-orbit coupling coming from a heavy metal. Through first principle calculations, Yang *et al.* [30] have shown that in Pt/Co bilayer the interfacial DMI depends on the strength of the interaction between Co spins and Pt atoms due to SOC interaction. Belabbes *et al.* [31] reported that the occupation of 3d orbitals at the 3d-5d interface between the FM and HM has a critical role, determining the strength and the sign of the interfacial DMI. The results obtained with first principles calculations are consistent with experimental measurement of DMI sign and strength at the interface between different materials. Overall interfacial DMI emerges in structures presenting interfacial inversion asymmetry and its strength comes from a balance between the polarization of 3d/5d interfacial atoms and the SOC coming from the 5d electrons in the HM.
In Figure 1.3 it can be observed the DMI vector $\mathbf{D_{ij}} = \text{D}(\mathbf{r_{ij}} \times \hat{\mathbf{z}})$, where $\mathbf{r_{ij}}$ is the vector connecting the two atomic sites i and j and $\hat{\mathbf{z}}$ is the normal to the plane. The sign of D defines the sense of rotation: for a $\text{D} > 0$ the

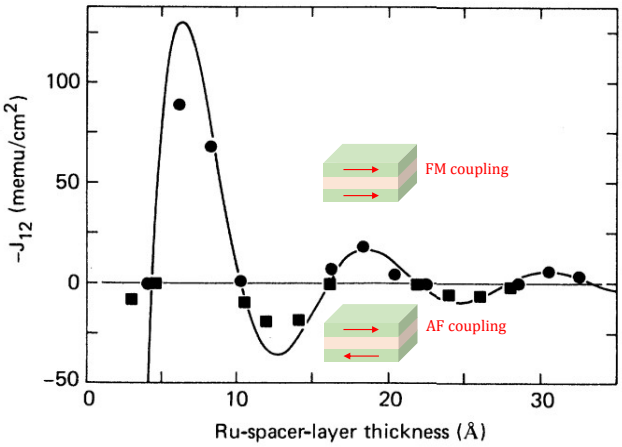

Figure 1.4: **RKKY interaction** | Interlayer exchange coupling strength J_{12} measured for a CoNi/Ru/CoNi multilayer as a function of the Ru interlayer thickness. Solid line is a fit using equation 1.17. Adapted from [37].

chirality will be left-handed (anticlockwise), while for $D < 0$ the promoted chirality is right-handed (clockwise). Co on Pt favours left handed chirality while Pt on Co favours right-handed chirality. Therefore, for a symmetric Pt/Co/Pt stack the DMI arising from the two interfaces compensates and the total DMI vanishes. In the continuum approximation the energy density associated to DMI can be written as:

$$\varepsilon_{\mathrm{DMI}} = \mathrm{D}\big((\mathbf{m}\cdot\nabla)\mathrm{m_z} - \mathrm{m_z}\nabla\cdot\mathbf{m}\big) \tag{1.15}$$

where D is the micromagnetic DMI constant (in J/m^2) [32]. The DMI constant can be expressed as $\mathrm{D} \sim \mathrm{d/at}$ where d is the amplitude of the DMI, t is the film thickness and a is the lattice parameter of the FM in the stack [30].

1.1.6 Interlayer exchange coupling

In a multilayer made of two FM layers separated by a NM layer, a coupling between the two FM layers arises, the so-called Ruderman-Kittel-Kasuya-Yosida (RKKY) interaction [33, 34, 35, 36]. The coupling between the two FM layers can be either FM or AFM depending on the thickness of the interlayer. The phenomenon is generated by the electrons in one FM layer that get spin-polarised and propagate through the NM layer. The spin-polarised electrons then interact with the magnetic moments of the second FM layer, resulting in an indirect coupling between the two. The RKKY energy density (in J/m^2) can be written as:

$$\varepsilon_{\mathrm{RKKY}} = -\mathrm{J_{12}}\mathbf{m_1}\cdot\mathbf{m_2} \tag{1.16}$$

where $\mathbf{m_1}$ and $\mathbf{m_2}$ are the magnetization of the two FM layers and J_{12} is the interlayer exchange constant that has the form:

$$\mathrm{J_{12}} \propto \frac{1}{\mathrm{t_{NM}^2}}\sin(2\mathrm{k_F t_{NM}} + \Phi). \tag{1.17}$$

where t_{NM} is the thickness of the NM layer, k_F is the Fermi wave vector of the NM layer and Φ is a constant. J_{12} has a damped oscillatory behaviour as a function of the interlayer thickness, and it promotes a FM coupling when $J_{12} > 0$ and AF coupling when $J_{12} < 0$ (see Figure 1.4).

1.2 Domain walls

A ferromagnetic material in general appears to be demagnetized or non-magnetic and reveal its magnetic properties only when placed in a magnetic field or in the presence of a permanent magnet. Weiss first proposed that a ferromagnetic body contains different regions, called domains [38], within which the magnetic moments exhibit parallel alignment, but with opposite magnetization directions among different regions, resulting in a net close to zero magnetization. At the edges of a domain, the so called domain wall (DW) appears, which separates different regions. The creation of domains and domain walls comes from a balance of energetic terms that, depending on the dimension of the sample, can favour different magnetic arrangements. The competing

energy terms are the domain wall energy, i.e. the energy cost that is necessary to create a domain wall, and the magnetostatic energy, that gets minimized when several domains are created. Considering a system that exhibits PMA, magnetic charges will appear on the top and the bottom faces of the structure. If the layer is thin, the cost of the magnetic charges in terms of the demagnetizing energy is high. Consequently, breaking the magnetic structure into domains with opposite directions, as shown in Figure 1.5a, reduces the energy. Inside the DW the spins undergo a rotation. If we take into account the exchange energy and the anisotropy energy contributions, there are possible scenarios that can be depicted. The exchange energy is minimized by spins parallelly aligned, so the best scenario for it is a large domain wall inside which neighbouring spins are rotated by a small angle one with respect to each other (see Figure 1.5b and c). This same scenario, however, is not favourable for the anisotropy energy, that would instead be minimized by an abrupt rotation of the magnetization.
The rotation inside a DW can happen in different directions, with the two limiting cases known as Bloch and Néel DW. In a Bloch DW the rotation of the spin happens in a plane parallel to the DW itself (yz plane in Figure 1.5b), while it happens in a plane perpendicular to the DW for Néel type (xz plane in Figure 1.5c). The Bloch DW type is the one that minimizes the magnetostatic energy as it prevents the creation of new magnetic charges. This is because for a Bloch DW holds the relation $\nabla \cdot \mathbf{m} = \frac{\partial m_x}{\partial x} = 0$, which is not true for a Néel DW.

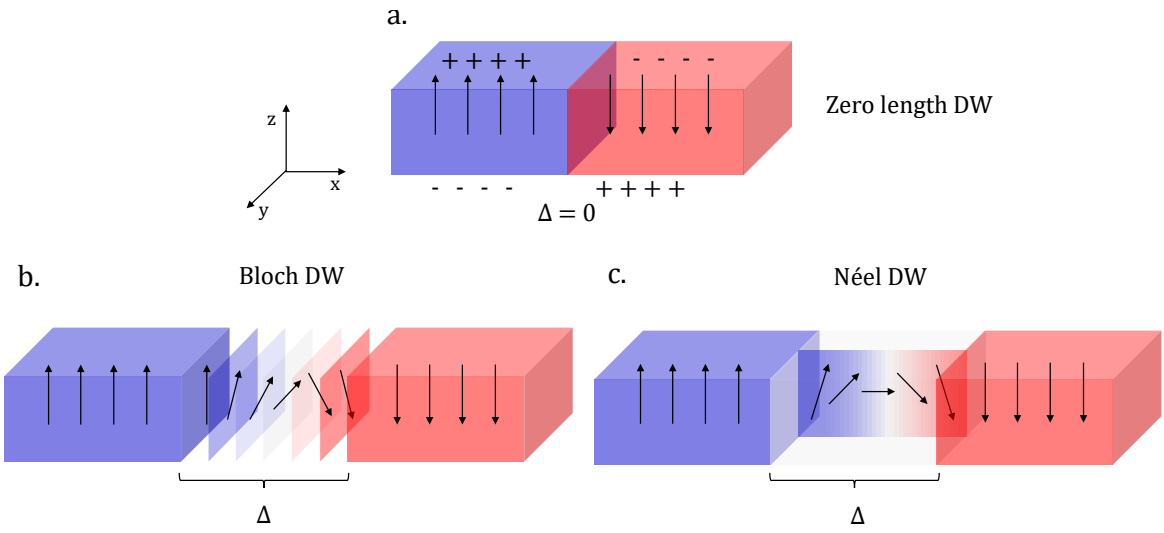

Figure 1.5: **Domain walls** | a. DW of zero width. The demagnetizing energy is minimized because magnetic charges are compensated. b. Schematic of a Bloch type DW, rotation happens in the yz plane. c. Schematic of a Néel type DW, rotation happens in xz plane.

Let us consider then the scenario of a Bloch DW separating two regions of a sample exhibiting PMA, where the magnetization is pointing respectively along the $\hat{\mathbf{z}}$ and $-\hat{\mathbf{z}}$ direction. Considering once again only the anisotropy and exchange energy density, the total energy density can be obtained summing the equations 1.3 and 1.13:

$$\varepsilon_{DW} = \varepsilon_{ex} + \varepsilon_K = A\left((\nabla m_x)^2 + (\nabla m_y)^2 + (\nabla m_z)^2\right) + K_{eff} \sin^2\theta. \tag{1.18}$$

By expressing the exchange energy density in terms of ϑ we obtain:

$$\varepsilon_{DW} = A\left(\frac{\partial\theta}{\partial y}\right)^2 + K_{eff} \sin^2\theta. \tag{1.19}$$

To calculate the stable wall profile function $\theta(y)$, ε_{DW} has to be minimized with respect to the variations of the wall profile $\delta\theta(y)$, hence:

$$\frac{\partial\varepsilon_{DW}}{\partial\theta} - \frac{\partial}{\partial y}\left(\frac{\partial\varepsilon_{DW}}{\partial\frac{\partial\theta}{\partial y}}\right) = 0 \tag{1.20}$$

$$2A\left(\frac{\partial^2\theta}{\partial y^2} - K_{eff}\sin 2\theta\right) = 0 \tag{1.21}$$

whose solution is $\theta(y) = 2\arctan\left(\exp(\frac{y}{\Delta})\right)$, where $\Delta = \sqrt{\frac{A}{K_{eff}}}$ is the width of the DW. To calculate the surface energy density we can integrate the volume energy density over the transition region of the DW using the solution just obtained for θ. This gives us:

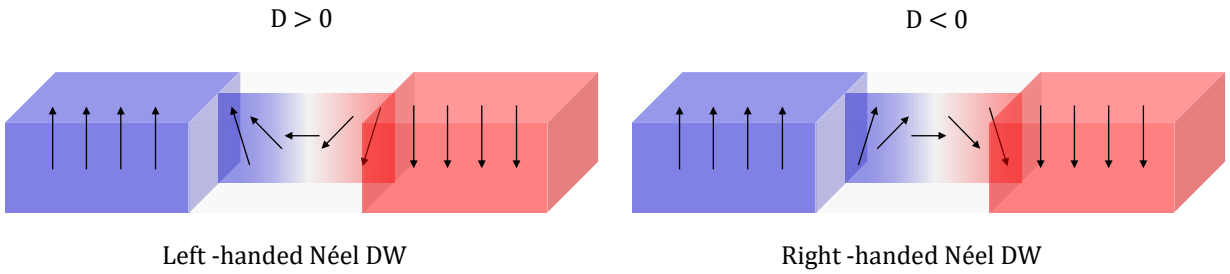

Figure 1.6: **Néel DWs** | Chiral Néel DWs in presence of DMI. On the left a left-handed Néel DW promoted by $D > 0$, on the right a right-handed Néel DW promoted by $D < 0$.

$$\sigma_{BW} = 4\sqrt{AK_{eff}} \tag{1.22}$$

So far, only the exchange energy and the anisotropy have been taken into account. For thin films, the DW type is strongly influenced by the DMI, which can promote a Néel type DW over a Bloch type DW that would be favoured by only considering the demagnetizing energy. The DMI contribution to the surface energy density is expressed as:

$$\sigma_{DW} = 4\sqrt{AK_{eff}} \pm \pi D \tag{1.23}$$

where the $\pm$ sign is put to include both the chiralities [39]. As explained in 1.1.5 when $D > 0$ the left-handed chirality is promoted while when $D < 0$ the right-handed chirality is promoted (see Figure 1.6). From the expression 1.23 we obtain a progressive transition from a Bloch DW when $D = 0$ to a Néel DW for $D > D_N$ resulting from the competition between DMI and magnetostatic energies. For $0 < D < D_N$ a mix in between a Bloch and a Néel DW is stabilized. For $\sigma_{DW} = 0$ the critical DMI value D_C is reached:

$$D_C = \frac{4\sqrt{AK_{eff}}}{\pi} \tag{1.24}$$

For $D > D_C$ the DW energy is negative and the magnetization undergoes a continuous rotation [40]. Therefore, the DMI can influence both the type of DW and establish its chirality.

1.3 DW dynamics

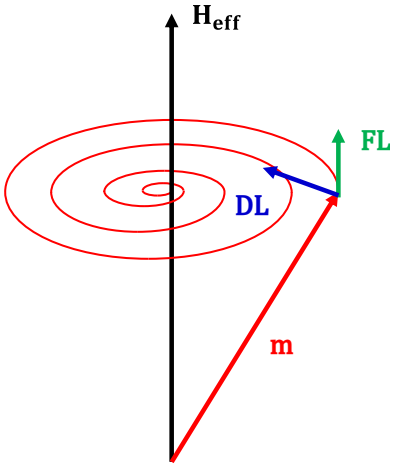

Figure 1.7: **Magnetization dynamics** | Magnetization dynamics described by the LLG equation around the effective field $\mathbf{H_{eff}}$. The FL term describes a precession around the $\mathbf{H_{eff}}$ that gets damped by the DL term.

When a magnetic moment $\boldsymbol{\mu}$ is in the presence of an external magnetic field $\mathbf{H}$, a torque $\mathbf{T} = \boldsymbol{\mu} \times \mathbf{H}$ is acting on it. For an electron $\boldsymbol{\mu} = \gamma \mathbf{S}$, where $\mathbf{S}$ is the spin and γ (GHz/T) is the electron gyromagnetic ratio, specifically $\gamma = \frac{g|e|}{2m_e}$ where g is the Landé factor ($g \approx 2$ for electrons) and e and m_e are respectively the charge and the mass of the electron. As $\mathbf{T} = \frac{d\mathbf{S}}{dt}$, we can write the variation of the magnetic moments $\frac{d\boldsymbol{\mu}}{dt} = \gamma \boldsymbol{\mu} \times \mathbf{H}$ [41]. Now we can extend the equation to the volume density of magnetic moments and take into account all the energy terms

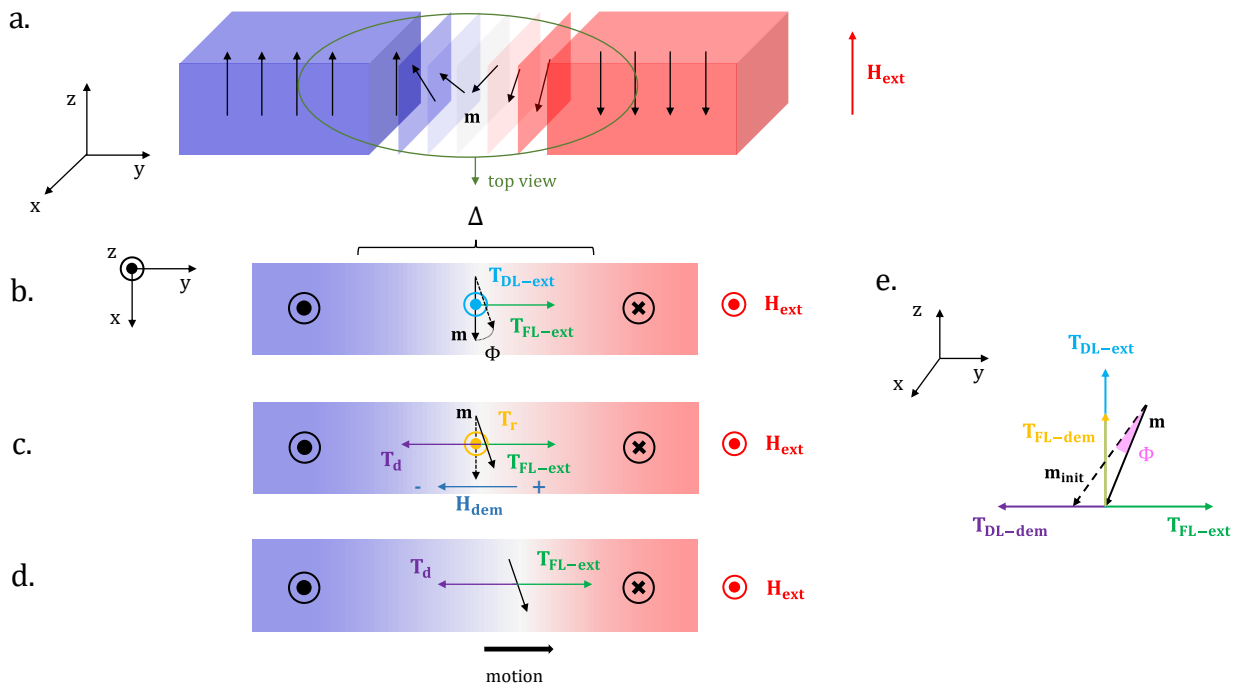

Figure 1.8: **Field-induced DW motion** | a. Schematic of a Bloch DW with a left-handed chirality along y. $\mathbf{m}$ at the center of the DW is pointing along $\hat{\mathbf{x}}$. The external field is applied along $\hat{\mathbf{z}}$. b. Top view of the scheme in a. Effect of the FL and DL torques generated by the external magnetic field on the DW. The magnetization gets tilted by an angle ϕ with respect to the x axis. c. Demagnetizing field generated by the tilting of the magnetization described in b. that provokes the appearance of magnetic charges and consequent appearance of FL and DL torques as a response to the demagnetizing field. d. Steady state motion generated by the compensation of the FL torque due to the external magnetic field and DL torque due to the demagnetizing field. e. Zoom on all the torques applied due to both external and demagnetizing field on the magnetization at the center of the DW. Here $\mathbf{m_{init}}$ represents the initial magnetization at the center of the Bloch DW aligned along $\hat{\mathbf{x}}$.

inside a material that contribute to the generation of an effective field $\mathbf{H_{eff}}$ namely, the anisotropy, exchange, dipolar, Zeeman and DMI. Doing that, we obtain the following equation:

$$\frac{\partial \mathbf{m}}{\partial t} = -\gamma_0 (\mathbf{m} \times \mathbf{H_{eff}}) \tag{1.25}$$

that describes an undamped precession of the magnetization $\mathbf{m}$ around the effective magnetic field $\mathbf{H_{eff}}$, with $\gamma_0 = \gamma \mu_0$. This equation represents a system that would continue to precess infinitely as no damping term is present in the equation. Phenomenologically, the magnetization precession inside a material gets damped by several factors. Landau and Lifshitz, followed then by Gilbert, studied ways to express the damping mechanism inside the material. The result is the so called Landau-Lifshitz-Gilbert (LLG) equation, which describes the temporal and spatial dynamics of the magnetization [41, 42]:

$$\frac{\partial \mathbf{m}}{\partial t} = -\gamma_0 (\mathbf{m} \times \mathbf{H_{eff}}) + \alpha \left(\mathbf{m} \times \frac{\partial \mathbf{m}}{\partial t} \right) \tag{1.26}$$

where α is the Gilbert damping parameter. As presented in Figure 1.7 the equation is made of two torque terms: the field-like (FL) term, coming from equation 1.25, which describes the precession around $\mathbf{H_{eff}}$ and the damping-like (DL) term that promotes the alignment of the $\mathbf{m}$ along the $\mathbf{H_{eff}}$. The combination results in a damped precession around the effective field, that will converge with a speed that depends on the α parameter, material dependent.

1.3.1 Field-driven domain wall dynamics

Magnetization reversal can happen through the propagation of DWs under the presence of an external magnetic field. The dynamics is governed by the LLG equation. We take here the case of a thin film stripe exhibiting PMA along the easy axis direction $\hat{\mathbf{z}}$ with two domains separated by a Bloch DW. The external field is applied along the z axis, so no torque is applied on the magnetization in domains parallel to the field. The described situation can be observed in Figure 1.8a. The magnetization at the center of the DW is aligned along $\hat{\mathbf{x}}$ for a

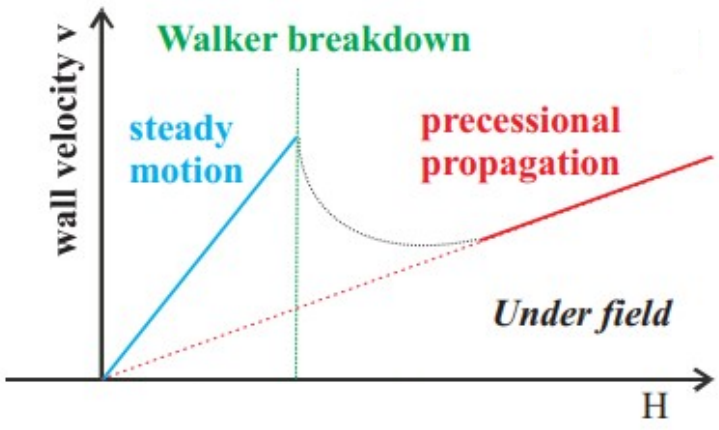

Figure 1.9: **Domain wall velocity** | Sketch of the DW velocity under the effect of an external magnetic field: first the DW is in the steady state regime where the velocity increases linearly with the external field until reaching the Walker breakdown. After the Walker breakdown there is drop in the velocity and the precessional propagation regime is reached, where the magnetization starts precessing around the external magnetic field. Adapted from [43].

Bloch DW. The torque generated by the external magnetic field on it has a FL component along y and a DL component along z (see Figure 1.8b):

$$\mathbf{T_{FL}} \propto -(\mathbf{m} \times \mathbf{H_{ext}}) = \mathrm{H_{ext}}\hat{\mathbf{y}} \tag{1.27}$$

$$\mathbf{T_{DL}} \propto -\mathbf{m} \times \left(\mathbf{m} \times \mathbf{H_{ext}}\right) = \mathrm{H_{ext}}\hat{\mathbf{z}} \tag{1.28}$$

The torque is hence rotating the magnetization away from the xy plane. The tilt in the magnetization creates magnetic charges at the edges of the domain wall and produces a demagnetising field perpendicular to the DW along $-\hat{\mathbf{y}}$. The demagnetising field generates two torque components itself acting on the $\mathbf{m}$: one, FL, a reactive torque along $\hat{\mathbf{z}}$ in the direction of the FL torque, $\mathbf{T_r}$, and a DL component $\mathbf{T_d}$ along $-\hat{\mathbf{y}}$, that opposes the FL torque component coming from the interaction with $\mathbf{H_{ext}}$ (see Figure 1.8c). While the FL torque tries to move the DW away from its Bloch configuration, the DL torque coming from the demagnetizing field compensates it. As a result, the DW propagates along the $\hat{\mathbf{y}}$ direction with a tilt away from the Bloch configuration, as can be observed in Figure 1.8d). Therefore, the DW propagation is not directly due to the external magnetic field, but due to the demagnetizing field generated by the torque of the external one on the magnetization. A zoom of all the torque components generating the propagation can be seen in Figure 1.8e. In this regime the magnetization is moving with an angle ϕ with respect to the $\hat{\mathbf{x}}$ direction, along the $\hat{\mathbf{y}}$ direction. The velocity increases linearly with $\mathbf{H_{ext}}$ and the DW mobility is high.
When $\mathbf{H_{ext}}$ reaches a critical field $\mathbf{H_w}$, called the Walker field [44], the DL torque from the demagnetizing field cannot compensate anymore for the FL torque from the external magnetic field, so the magnetization starts precessing around $\mathbf{H_{ext}}$. There is a drop in the velocity and the angle ϕ is not constant anymore. When the field is increased at even higher value the DW enters in the precessional regime, resulting in the magnetization at the center of the DW undergoing a back and forth displacement, resulting in smaller mobility (see Figure 1.9) [43].
This model is established for an ideal case, without taking into account defects or grains in the material that may lead to areas where the magnetic properties are altered with respect to the ideal case, generating some pinning sites. When a magnetic texture is stuck in a pinning site, an energy threshold has to be overcome in order to move it. The depinning field is defined as the smallest field needed to depin a texture. At finite temperature, even below the depinning field, the motion of magnetic textures can be thermally activated and will produce jumps or deformations. This regime, characterized by small velocities is called creep regime.
When the DMI is present the DW shows a Néel configuration as explained previously in 1.2. Thiaville *et al.* [40] studied the motion of DMI DWs under an external magnetic field reporting that DMI increases the Walker field extending the steady state regime, hence reaching higher velocities. This mechanism was experimentally confirmed by Pham *et al.* [45] who studied Pt/Co/AlOx, Pt/Co/GdOx and Pt/Co/Gd trilayers, all stacks exhibiting DMI. They measured the DW velocity as a function of an external applied magnetic field and compared the results with those obtained for a symmetric stack Pt/Co/Pt. They observed a large increase in the field driven DW speed (the comparison is presented in Figure 1.10). They also observed that the Walker

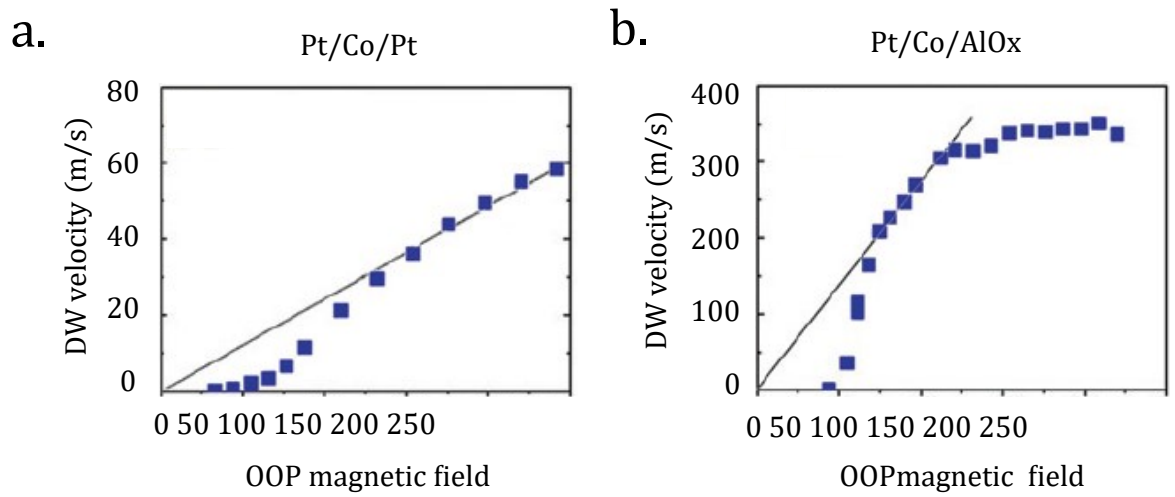

Figure 1.10: **Field-driven DW dynamics** | a. Field driven DW velocity for Pt/Co/Pt, without DMI. b. Field driven DW velocity for Pt/Co/AlOx, stack exhibiting interfacial DMI. Adapted from [45].

field is directly proportional to the DMI amplitude D. The measurement of the Walker field can therefore be used to provide an experimental measurement of the DMI.

1.3.2 Current-driven domain wall dynamics

There are two main mechanisms that can be exploited for the manipulation of the magnetization via electrical current: the spin transfer torque (STT) [46] and the spin orbit torque (SOT) [47]. Both the STT and SOT mechanisms describe the transfer of angular momentum between conduction electrons and the magnetic moment of a material. However, they differ in the source of the angular moment, as explained more in details in the following sections.

1.3.2.1 Spin transfer torque

The STT phenomenon was first proposed in 1996 by both Berger [7] and Slonczewski [8]. The phenomenon consists in a current that gets naturally polarized in a ferromagnet and crosses a DW. When crossing the DW, due to the exchange interaction, the spin polarization of the conduction electrons gets aligned to the direction of the local magnetization [48]. As the total spin must be conserved, the angular momentum gets transferred from the conduction electrons to the local magnetization, acting like a torque on the latter, the STT. The result is a displacement of the DW along the electron flow. The phenomenon was first explained introducing a torque term deriving from the exchange interaction between the conduction electrons and the local magnetization. This term, referred to as the adiabatic torque, is:

$$\mathbf{T_{ad}} = -(\mathbf{u}\cdot\nabla)\mathbf{m} \tag{1.29}$$

where $\mathbf{u} = \frac{\mathrm{Pg}\mu_\mathrm{b}}{2\mathrm{eM_s}}\mathbf{J}$ with μ_b the Bohr magneton, $\mathrm{P} > 0$ the current polarization and $\mathbf{J}$ the current density, oriented against the electron flow. The DW moves along the electron flow with a velocity given by u, the spin drift velocity. The adiabatic torque, anyway, was not able alone to explain the experimental results. Zhang *et al.* [49] and Thiaville *et al.* [50] introduced another torque term, the non-adiabatic term:

$$\mathbf{T_{non-ad}} = \beta\mathbf{m}\times\left[(\mathbf{u}\cdot\nabla)\mathbf{m}\right] \tag{1.30}$$

where β is a dimensionless parameter that contains two different contributions to the torque. The first contribution is given by the spin-flip scattering events with impurities for which the spin is not conserved due to spin-orbit coupling [50, 51, 52]. The second contribution occurs when the gradient of the magnetization is too large for the current electrons spin polarization to follow it, generating a non-local oscillatory torque [53, 54, 55].
Including both the adiabatic and the non-adiabatic torque terms, the LLG equation can be re-written as:

$$\frac{\partial\mathbf{m}}{\partial\mathrm{t}} = -\gamma_0(\mathbf{m}\times\mathbf{H_{eff}}) + \alpha\left(\mathbf{m}\times\frac{\partial\mathbf{m}}{\partial\mathrm{t}}\right) - (\mathbf{u}\cdot\nabla)\mathbf{m} + \beta\mathbf{m}\times\left[(\mathbf{u}\cdot\nabla)\mathbf{m}\right] \tag{1.31}$$

The STT effect can also be used as a mechanisms to promote the switching of ferromagnetic layers in a magnetic tunnel junction, as it will be explained more in detail in section 1.4.2 or can be exploited to probe spin-dependent phenomena with the spin pumping technique.

1.3.2.2 Spin orbit torque

The second type of mechanism that can be used to manipulate the magnetization of a ferromagnetic layer via current is the SOT. While STT originates from spin dependent scattering inside a ferromagnetic material, SOT is originated by the transfer of orbital momentum from a HM layer into spin angular moment of the local magnetic moments via spin-orbit coupling (SOC). There are two main mechanisms that give rise the SOT: the Rashba-Edelstein effect [56, 57] and the spin Hall effect (SHE) [58, 59, 60]. Both Rashba-Edelstein effect and SHE are present in a HM/FM/NM trilayer system presenting broken inversion symmetry. Only samples presenting this type of symmetry have been studied in this work.
As for the STT, also SOT introduces two terms in the LLG equation 1.26, both perpendicular to the magnetization, and orthogonal to each other, one that acts like an effective magnetic field, the FL component, and one that acts like an effective magnetic damping, the DL component. They take the shape: $\mathbf{T_{FL}} \propto \mathbf{m} \times \eta$ and $\mathbf{T_{DL}} \propto \mathbf{m} \times (\mathbf{m} \times \eta)$ where η is an effective field determined by the charge-spin conversion process via SOC [47]. The two torques can be expressed by their effective magnetic field, respectively $\mathbf{H_{FL}}$ and $\mathbf{H_{DL}}$ for the FL and DL component. The LLG equation becomes:

$$\frac{\partial \mathbf{m}}{\partial t} = -\gamma_0(\mathbf{m} \times \mathbf{H_{eff}}) + \alpha\left(\mathbf{m} \times \frac{\partial \mathbf{m}}{\partial t}\right) - \gamma_0(\mathbf{m} \times \mathbf{H_{FL}}) - \gamma_0(\mathbf{m} \times \mathbf{H_{DL}}) \tag{1.32}$$

As already said, the origin of the SOT is attributed to both SHE and Rashba-Edelstein effect. Both mechanisms give rise to both the FL and the DL components of the SOT. It is actually hard to well separate theoretically the mechanisms contributing to the SOT, but in general the SHE is used to explain the DL component of the SOT while the Rashba-Edelstein for the FL component [47]. As this applies well for HM/FM/NM trilayer systems, where the DL component of the SHE is expected to have a stronger contribution and the opposite for the FL component that is expected stronger from the Rashba-Edelstein effect, this is the approach that will be followed in the next lines.

Spin Hall effect We take as a reference a system made of an HM layer in contact with a FM layer. When a charge current $\mathbf{J}$ is passing through the HM, parallelly to the FM/HM interface, due to SOC, the spin-up and spin-down electrons are deflected in different directions, generating a spin accumulation in the boundaries, as depicted in Figure 1.11. This is known as the SHE [58, 59, 60]. This spin accumulation results in a pure spin current $\mathbf{J_S}$ transverse to the initial electrical current that gets injected into the adjacent FM layer. The spin current generates a torque on the local magnetic moment by transferring angular momentum.
Assuming $\mathbf{J}$ along $\hat{\mathbf{x}}$, the generated spin current is $\mathbf{J_S} \sim \hat{\mathbf{s}} \times \mathbf{J}$ where $\hat{\mathbf{s}}$ is the spin polarization direction, along $-\hat{\mathbf{y}}$ in Figure 1.11 on the right schematic. Therefore, the spin current propagates along $+\hat{\mathbf{z}}$, from the HM bulk towards the HM/FM interface. The effective field associated to the transfer of spin angular momentum to the local magnetic moments has the form:

$$\mathbf{H_{DL}} = \mathrm{H^0_{DL}}(\mathbf{m} \times (\hat{\mathbf{z}} \times \hat{\mathbf{j}})) \tag{1.33}$$

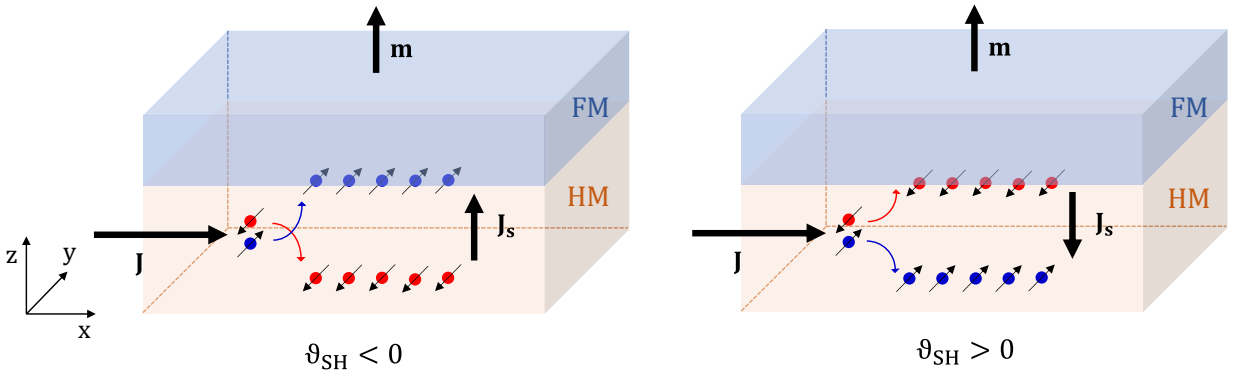

Figure 1.11: **Spin Hall effect** | Schematic of the SHE in a HM/FM bilayer. The current goes through the HM layer generating a spin accumulation on opposite interfaces whose direction depends on the sign of the spin Hall angle θ_{SH}. The spin accumulation generates a pure spin current that propagates through the HM/FM interface acting as a torque on the local magnetic moments.

where $\mathbf{j}$ is the current density unit vector and $\mathrm{H^0_{DL}} = \frac{\hbar\theta_{SH}J}{2eM_s t_F}$ takes into account the charge current J, the thickness of the FM layer and the spin Hall angle θ_{SH}. The spin Hall angle is defined as $\theta_{SH} = \frac{J_s}{J}$, and represents the maximum yield for the conversion of the charge current density into the transverse spin current density [61].

The magnitude of the spin Hall angle and its sign are material dependent. The SOC is proportional to the atomic number as Z^4 [62] so it is more effective for HM than for other materials. The SOC presents a positive θ_{SH} in materials like Pt [63, 64, 65], Pd, Ti, Au, while it has a negative sign for materials like Ta [66, 67, 64], W [68], Hf. The sign of the spin Hall angle affects the torque direction in the FM layer. Two cases are shown in Figure 1.11, respectively a $\theta_{SH} > 0$ and $\theta_{SH} < 0$.
The SOT effect generated by the spin Hall effect can be seen as a STT in which the source of spin polarized current is not the FM layer itself but the transverse current coming from the HM neighbouring layer. Due to this difference the spin polarized current is not in the longitudinal direction but transversal, but the underlying principle is the same.

Rashba-Edelstein effect The Rashba-Edelstein or inverse spin galvanic effect is induced due to an electric field gradient at an interface, so it appears in HM/FM/NM trilayer systems. The electric field $\mathbf{E}$ that appears is perpendicular to the interface. In its framework, the electrons moving along $-\hat{\mathbf{x}}$ experiences a magnetic field, the Rashba field $\mathbf{B_R} = -\frac{\mathbf{v}\times\mathbf{E}}{2c^2} \approx -\hat{\mathbf{y}}$ where c is the speed of light and $\mathbf{v}$ is the electron velocity. The interaction between the Rashba field and the electron spins is dependent on the kinetic momentum of the electron and it hence generates a momentum dependent splitting of the energy bands [69, 70]. The hamiltonian that describes this interaction is the following:

$$\mathcal{H}_{\mathcal{R}} = \alpha_R \mathbf{s} \cdot (\mathbf{k} \times \hat{\mathbf{z}}) \tag{1.34}$$

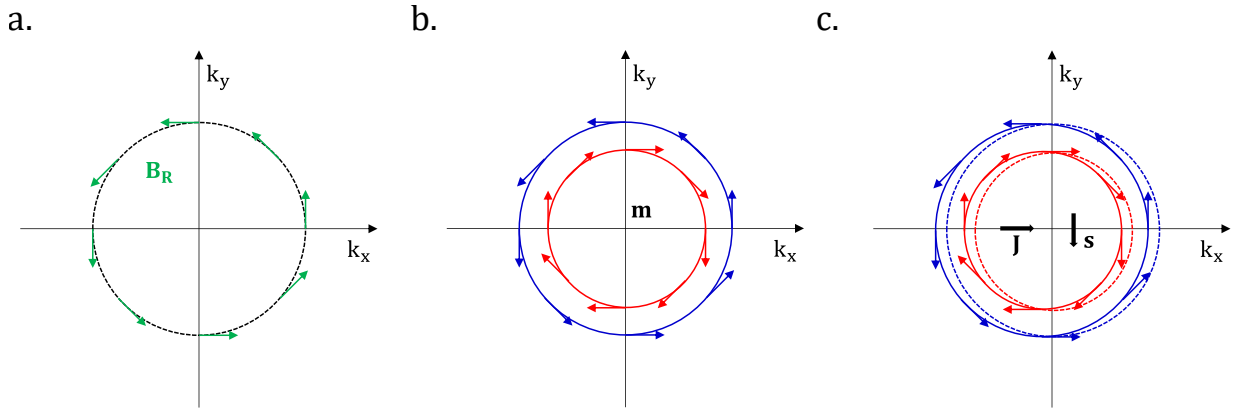

Figure 1.12: **Rashba-Edelstein effect** | a. Orientation of the Rashba magnetic field $\mathbf{B_R}$ as a function of the electron momentum $\mathbf{k}$ in the reciprocal space. b. Cut of the energy bands at the Fermi level under Rashba effect without current applied (red and blue are the cut off for the two opposite spin momentum). No net spin accumulation produced. c. Cut of the energy bands at the Fermi level under Rashba effect with applied current. The current generates a shift in the Fermi contour due to the motion of the electrons along $\mathbf{J}$. The shift produces an uneven occupation of the momentum states and hence a net spin accumulation.

where $\mathbf{s}$ is the spin, $\hbar\mathbf{k}$ is the electron's momentum and α_R is the Rashba parameter [57, 61]. The Rashba field is always orthogonal to the electron momentum, as depicted in Figure 1.12. Electrons at the interface that interact with the Rashba field get aligned parallel to it. In absence of current injection no spin accumulation arises as the Fermi surface remains centered (see Figure 1.12b). When instead a current density is applied, the Fermi surface gets shifted, generating an uneven occupation of k and -k momentum state, as observable in Figure 1.12c. In this situation the Rashba effect produces a net spin accumulation. From the spin accumulation a pure spin current is obtained that propagates through the HM/FM and produces a torque on the magnetization of the neighbouring FM layer.
One can notice that both SHE and Rashba-Edelstein effect result in a torque on the magnetization, what is different is their physical origin, because the former is a bulk effect due to SOC in the HM layer while the latter is a purely interfacial effect generated by broken inversion symmetry.

SOT-driven DW motion The stacks studied in this thesis are Pt/Co based. They present PMA and DMI with $D > 0$, meaning Néel DW with left-handed chirality. Pt/Co interface also generates a SHE with $\theta_{SH} > 0$. The case corresponding to these parameters is illustrated in Figure 1.13. For this type of stack and geometry (FM on top of HM layer, parallelly aligned) it has been shown [61] that the effect of the Rashba-Edelstein FL torque is negligible with respect to the SHE DL torque (see Figure 1.13). I will then only consider the DL torque component coming from SHE for the derivation of the current-driven motion of DWs.
From equation 1.33, for a current flowing along $\hat{\mathbf{x}}$, the DL torque associated to the spin Hall effect is $\mathbf{H_{DL}} = H^0_{DL}(\hat{\mathbf{y}} \times \mathbf{m})$. The DL torques on two consecutive DWs will be opposite, as the magnetization in the center

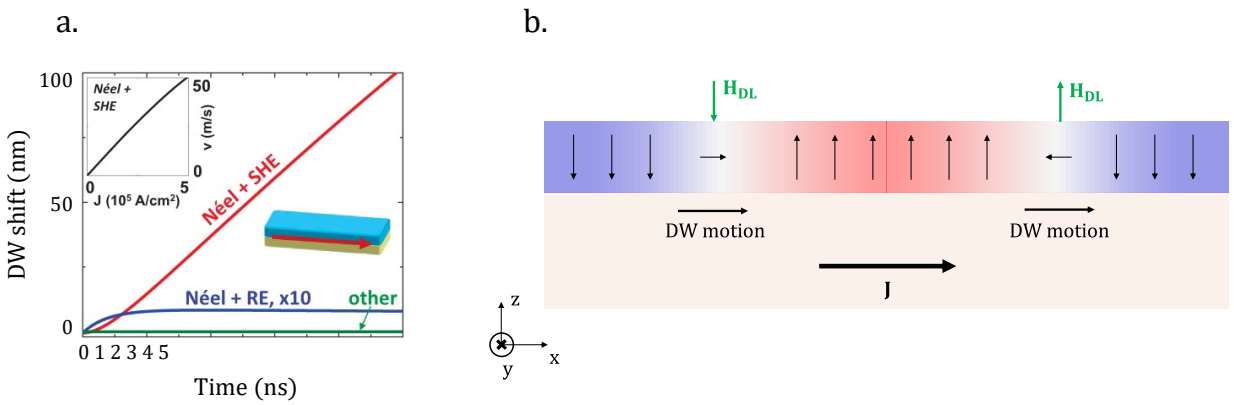

Figure 1.13: **SOT-driven DW motion** | a. Néel DW shift as a function of time under different SOT torques, in parallel geometry. For SOT generated by SHE a steady state motion is observed, while for SOT generated by Rashba-Edelstein only an initial shift is found. Adapted from [61]. b. Schematic figure of DW motion under applied current in HM/FM multilayer presenting $D > 0$ and $\theta_{SH} > 0$. Both the DWs are moved along the same direction by the DL torque generated by the SHE.

is pointing towards $\hat{\mathbf{x}}$ and $-\hat{\mathbf{x}}$ respectively, generating a motion along the current direction in both cases (see Figure 1.13). From [40], with a large DMI, the current-driven DW velocity at the steady state is:

$$v = \frac{\gamma_0 \pi D}{2\mu_0 M_s} \frac{1}{\sqrt{1 + \left(\frac{2\alpha t e D}{\hbar \theta_{SH} \Delta J}\right)^2}} \tag{1.35}$$

where t is the thickness of the FM layer.

1.4 Magnetic tunnel junctions

1.4.1 Tunneling magnetoresistance

Magnetic tunnel junctions (MTJs) are composed of two ferromagnetic layers separated by an oxide barrier. Electrons can tunnel through the oxide barrier when a bias voltage is applied to the device. The characteristic that makes these devices extremely interesting is that depending on the relative orientation of the magnetization of the two ferromagnetic layers the tunneling current is different, hence the resistance associated to the MTJ varies. This effect is called tunneling magnetoresistance (TMR). The alignment of the magnetization of the two ferromagnetic layers can be modified by mean of external magnetic field, electric current or bias voltage. These effects will be discussed more in details in the following sections. The ability of generating two different resistance states raised the interest for memory applications using MTJs, that are nowadays used as the fundamental unit of magnetoresistive random access memories (MRAM).
The TMR was first observed by Jullière in 1975 [6] in a Fe/Ge/Co tunnel junction at a very low temperature of 4.2 K in terms of variation of the conductance of 14%. The first observation of TMR at room temperature (RT) arrived in 1995 by Miyazaki *et al.* [71] in a Fe/AlOx/Fe junction and by Modera *et al.* [72] in a CoFe/AlOx/Co junction. Large magnetoresistance values, up to 100%, using monocrystalline magnesium oxide (MgO) barrier were predicted by Butler *et al.* [73] and Mathon *et al.* [74] using Fe in the FM layers. The first experimental observation of large TMR arrived in 2004 when Parkin *et al.* [75] and Yuasa *et al.* [76] found respectively $\sim 220\%$ and $\sim 180\%$ in Fe/MgO/Fe magnetic junctions at room temperature. The largest value found experimentally was observed by Ikeda *et al.* [77] in 2008 in a CoFeB/MgO/CoFeB magnetic tunnel junction at room temperature. The difference between the experimental values of TMR and those theoretically predicted are due to defects and impurities during the growth of the materials and imperfection at the interfaces that decrease the tunneling efficiency [78].
As previously said, MTJs are based on a purely quantum mechanical effect, the tunnel effect. For classical physics it is forbidden to have charge transport through an insulating layer, while for quantum mechanics there is a probability different from zero for electrons to propagate through it. Within the tunneling barrier, the electrons wave function decay exponentially as $T(E_F) \propto e^{-2qd}$ where q is the decay coefficient that can be calculated using the free electrons model and d is the thickness of the insulating barrier. The total tunneling current is given by $I = I_{1\to2} - I_{2\to1}$ where $I_{1\to2}$ ($I_{2\to1}$) is the current generated from the electrons going from the first electrode (FM1) to the second (FM2) (from the second electrode to the first). If no bias voltage is applied, the Fermi levels of the two electrodes are aligned and therefore the two tunneling currents are equivalent, resulting in a net zero current, as depicted in Figure 1.14a. When a bias voltage is applied, the Fermi level of

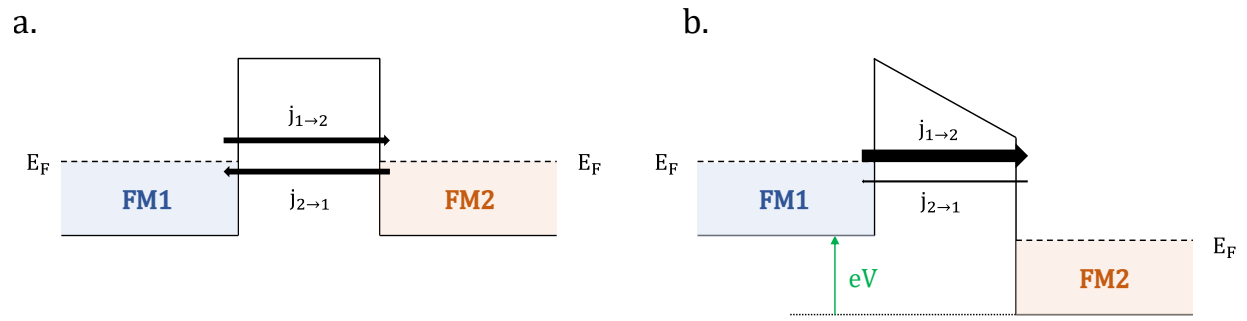

Figure 1.14: **Tunneling barrier** | a. Schematic of a tunnel barrier when no bias voltage is applied. The current going from the first ferromagnetic layer to the second is equal to the current doing the inverse path, resulting in a net zero current density. b. Schematic of a tunnel barrier when bias voltage is applied. The two currents are no longer equivalent, resulting in a net current going from FM1 to FM2.

the collectors electrode is lowered by a quantity eV with respect to that of the injector. In this way the two tunneling currents are not equivalent and there is a net current going from the injector to the collector (see Figure 1.14b). The tunneling current depends on both the barrier properties and on the probability of having occupied state at energy E in the injector and available empty states in the collector layer at the energy $E+eV$. It can be expressed by the following formula:

$$I_{1\to2}(E) = D_1(E)f_1(E)T(E)D_2(E+eV)(1-f_2(E+eV)) \tag{1.36}$$

where $D_1(E)$ and $D_2(E+eV)$ are the densities of states (DOS) respectively for electrode 1 at energy E and at energy $E+eV$ for electrode 2, and f(E) is the Fermi-Dirac distribution defining the probability of occupation of a state at energy E. Therefore, the product $D_1(E)f_1(E)$ is the probability of having available electrons at energy E in the first electrode and $D_2(E+eV)(1-f_2(E+eV))$ is the probability of having available electrons state at energy $E+eV$.
A first model to explain the TMR effect was developed by Jullière in 1975 [6]. He used the simple approach just described and made two main assumptions. The first one is that the electron spins are conserved during the tunneling, hence two different conduction channels for up spins and down spin arise, independent from each other. The second assumption is that the conductance for a specific channel is dependent on the combined effective densities of states of the two ferromagnets.
Following the first assumption, two different conduction channels DOS are introduced, $D^{\uparrow}$ for majority electrons and $D^{\downarrow}$ for minority electrons. The conductance for the parallel and antiparallel configuration of the two FM layers can be expressed by:

$$G_P \propto D_1^{\uparrow}(E_F)D_2^{\uparrow}(E_F) + D_1^{\downarrow}(E_F)D_2^{\downarrow}(E_F) \tag{1.37}$$

$$G_{AP} \propto D_1^{\uparrow}(E_F)D_2^{\downarrow}(E_F) + D_1^{\downarrow}(E_F)D_2^{\uparrow}(E_F) \tag{1.38}$$

respectively, as the majority electrons have the same spin orientation in the P configuration and opposite in the AP configuration. In the parallel configuration the conductance is higher than in the antiparallel configuration, as in the latter few states are available for majority electrons tunneling from the first FM layer, while there are a lot of available states for the few minority electrons injected. The difference in between the two conductances is expressed by the TMR ratio:

$$TMR = \frac{G_P - G_{AP}}{G_{AP}} = \frac{R_{AP} - R_P}{R_P} = \frac{2P_1P_2}{1-P_1P_2} \tag{1.39}$$

where P_1 and P_2 represent the polarization of the FM1 and FM2 respectively. The polarization P_0 of a FM is defined as:

$$P_0 = \frac{D^{\uparrow}(E_F) - D^{\downarrow}(E_F)}{D^{\uparrow}(E_F) + D^{\downarrow}(E_F)} \tag{1.40}$$

The Jullière's model [6] only works for tunnel barriers made of amorphous AlOx, for which the tunneling mechanism is incoherent, meaning that it is the same for all the electrons (see Figure 1.15a). For a crystalline barrier instead, such as an MgO barrier grown (001), the tunneling mechanism is coherent and it is based on the orbital symmetry of the occupied bands on the emitting electrode and on the available bands in the receiving electrode. The attenuation in the barrier is also depending on the symmetry of the states. Slonczeswski [79] developed a more rigorous model in 1989, taking into account the wave vector of the propagating electrons. The

main assumption is that only electrons propagating perpendicular to the layer $\mathbf{k} \approx \mathbf{k}_\perp, \mathrm{k}_{//} = 0$ are responsible for the tunneling. The polarization is written as:

$$\mathrm{P} = \frac{(\mathrm{k}_{\mathrm{F},\uparrow} - \mathrm{k}_{\mathrm{F},\downarrow})(\mathrm{q}^2 - \mathrm{k}_{\mathrm{F},\uparrow}\mathrm{k}_{\mathrm{F},\downarrow})}{(\mathrm{k}_{\mathrm{F},\uparrow} + \mathrm{k}_{\mathrm{F},\downarrow})(\mathrm{q}^2 + \mathrm{k}_{\mathrm{F},\uparrow}\mathrm{k}_{\mathrm{F},\downarrow})} = \mathrm{P}_0 \frac{\mathrm{q}^2 - \mathrm{k}_{\mathrm{F},\uparrow}\mathrm{k}_{\mathrm{F},\downarrow}}{\mathrm{q}^2 + \mathrm{k}_{\mathrm{F},\uparrow}\mathrm{k}_{\mathrm{F},\downarrow}} \tag{1.41}$$

where $\mathrm{k}_{\mathrm{F},\uparrow}$ and $\mathrm{k}_{\mathrm{F},\downarrow}$ are the wave vectors of respectively the majority and minority electrons at the Fermi level, q is the decay coefficient in the insulating layer and P_0 is the electron polarization in the Jullière's model. The new model still fails to explain the high value of TMR obtained from junctions based on a crystalline MgO barrier. To understand this effect additional band structure effects in the electrodes and the barrier must be taken into account.

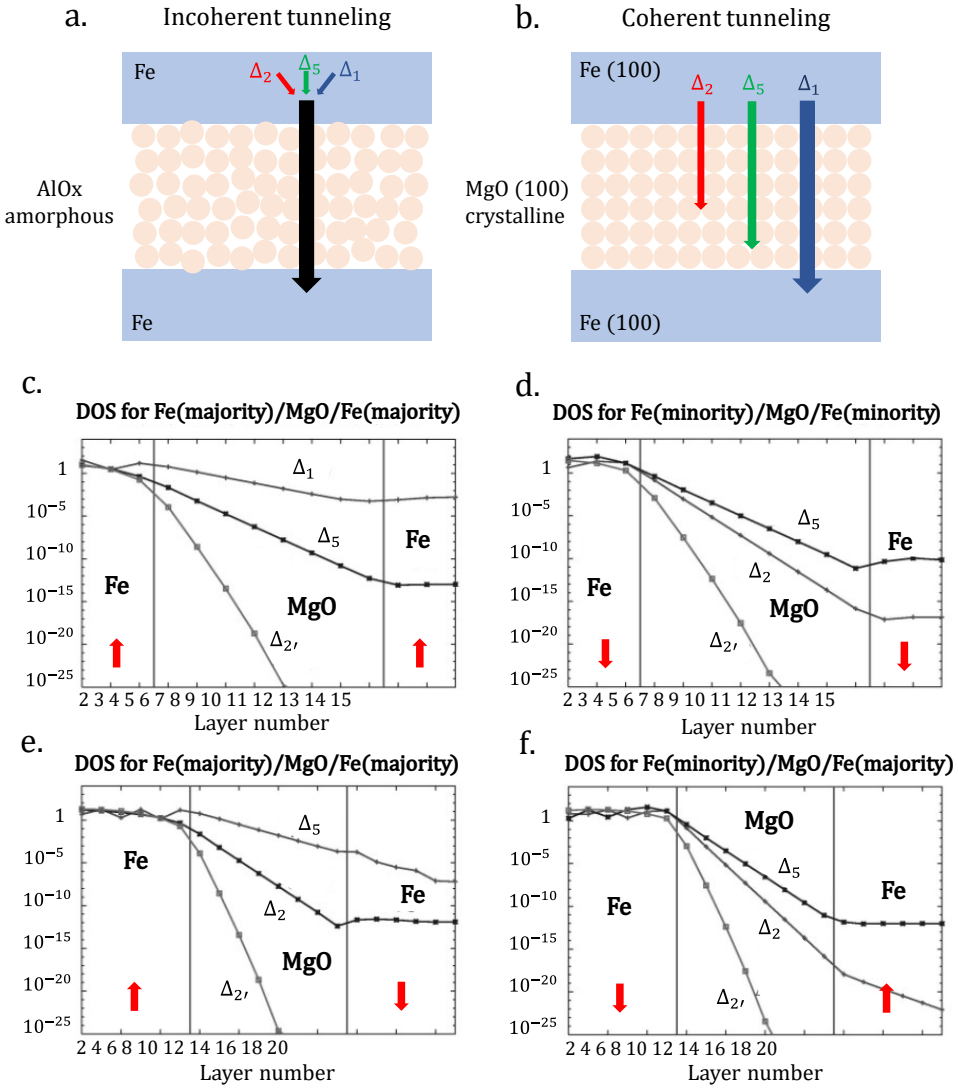

Figure 1.15: **Coherent tunneling** | a. Schematic of electrons tunneling through an amorphous barrier of AlOx. The tunneling is incoherent, no symmetry in the density of states is respected. b. Schematic of coherent tunneling in a junction with a crystalline MgO barrier. The symmetry of the DOS is respected, a higher conductance for Δ_1 states is observed. c. DOS for Fe(100)/MgO/Fe(100) system for majority electrons to majority electrons, obtained from ab initio calculation. d. DOS for Fe(100)/MgO/Fe(100) system for minority electrons to minority electrons, obtained from ab initio calculation. e. DOS for Fe(100)/MgO/Fe(100) system for majority electrons to minority electrons, obtained from ab initio calculation. f. DOS for Fe(100)/MgO/Fe(100) system for minority electrons to majority electrons, obtained from ab initio calculation. Adapted from [73].

Butler *et al.* [73] using ab initio calculation on Fe(100)/MgO/Fe(100) were able to explain the high TMR phenomenon. They reported that the tunneling conductance depends on the symmetry of the Bloch states in the electrodes and of the evanescent states in the barrier. States with different symmetry decay at different rates within the barrier. The results can be observed in Figure 1.15c, d, e and f where the tunneling DOS for

$k_{//} = 0$ in Fe(100)/MgO/Fe(100) are plotted for all the different configurations of the relative orientation of magnetization for the two Fe layers. $k_{//} = 0$ is the momentum component oriented along the (100) plane that must be conserved in the tunneling process. Along the [100] direction, referred to as Δ direction, in the Fe, there are four Bloch states for both the majority and minority channel. For the majority channel there is a Δ_1 state, a doubly degenerate Δ_5 state and a $\Delta_{2'}$ state. For the minority channel the states are the same but the Δ_1 symmetry is replaced by a Δ_2 symmetry state. As shown in Figure 1.15c, the slowest decay rate inside the barrier happens for the Δ_1 symmetry state, followed by Δ_5, while Δ_2 and $\Delta_{2'}$ have a fast decay inside the MgO due to the cubic symmetry of the MgO cell. The Δ_1 symmetry, that is present only for majority channels, explains the high conductance for the P state compared to the AP state. In the AP configurations there are no Δ_1 minority state to tunnel from or to. The contribution to the conductance of Δ_5 and Δ_2 states, that are present for both minority and majority electrons, is weaker than the Δ_1. The effect becomes even stronger for Co/MgO/Co MTJs since there are no available Δ_5 and Δ_2 states at the Fermi level.
The resulting resistance of a MTJ has two clear different states deriving from the P and AP alignement of the magnetization of the two layers. These states are used to represent bit '0' and bit '1' in the information reading process of MRAMs. In the two next sections I will dedicate some words to explain the main two writing mechanisms that are used in MRAM technology: the STT-switching and the Voltage Control of the Magnetic Anisotropy.

1.4.2 STT-switching

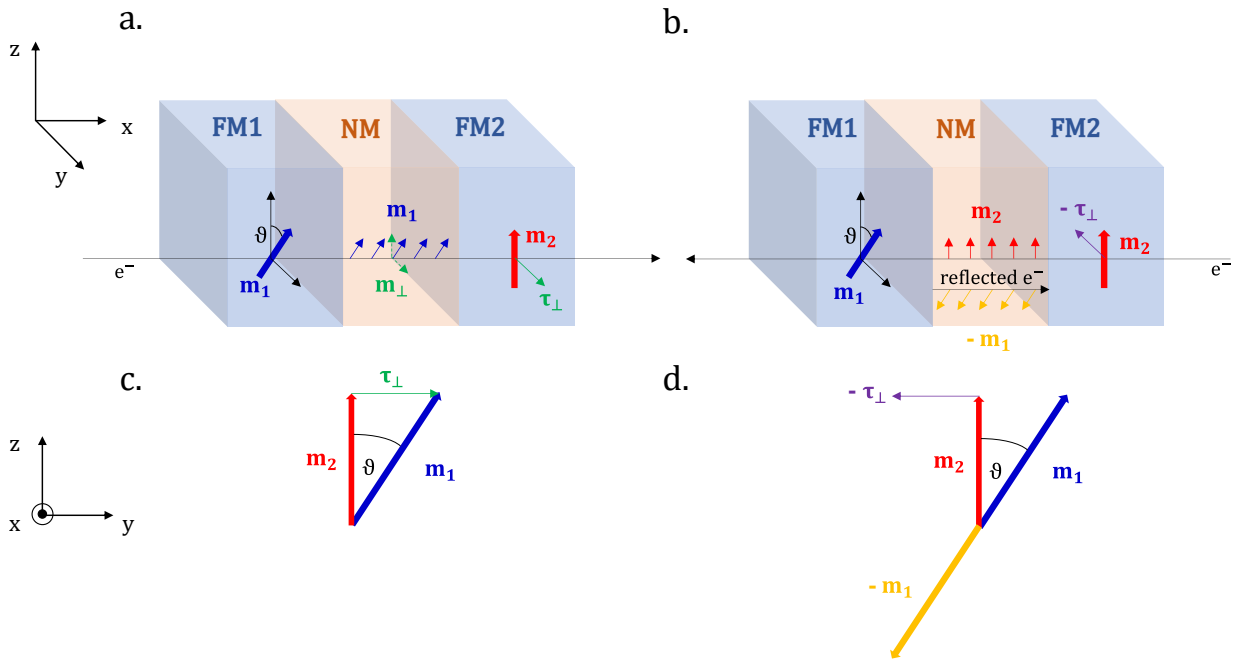

Figure 1.16: **STT-driven magnetic switching** | a. Schematic of STT in a FM/NM/FM layer for electrons going from FM1 to FM2. Resulting torque on $\mathbf{m_2}$ tends to align the magnetization along $\mathbf{m_1}$, as shown in detail in c. b. Schematic of STT in a FM/NM/FM layer for electrons going from FM2 to FM1. The torque $-\boldsymbol{\tau}_\perp$ is generated by backscattered electrons with a polarization along $-\mathbf{m_1}$.

The STT phenomenon, explained in section 1.3.2.1 for propagation of domain walls, consists in a torque generated on the local magnetic moments by the conduction electrons of the applied current. Now, instead of a single FM layer we take into account a system made of a FM1/NM/FM2, like an MTJ, where the NM is an insulator. We consider a current passing through the system, perpendicular to the interfaces. When conduction electrons flow through FM1, due to the exchange interaction, their spins tend to align along the magnetization $\mathbf{m_1}$ of the ferromagnetic layer, as shown in Figure 1.16a. The current becomes therefore spin polarized. The electrons propagate across the NM layer without changing their spin polarization and reach the NM/FM2 interface. The spins in the second ferromagnetic layer are aligned along $\mathbf{m_2}$ direction, with an angle θ with respect to $\mathbf{m_1}$. The electrons entering FM2 get quickly polarized along the direction of the local magnetization, hence losing their transverse component $\mathbf{m}_\perp$. The process implies a transfer of spin angular momentum to the local magnetic moments for conservation of angular momentum, resulting in a torque $\boldsymbol{\tau}_\perp$ on the local magnetization. If the FM2 layer is thin enough this torque can produce a switching of the local magnetization $\mathbf{m_2}$ along the $\mathbf{m_1}$ direction (see Figure 1.16a and c). This is the STT effect.
For the opposite current polarity, electrons flow from FM1 to FM2 and the process happening is the same

as the one just explained. However, some electrons, whose spin is antiparallel to the local magnetization of FM1, get backscattered as they do not find available states in FM1. They are reflected back to FM2 where they transfer once again their momentum to the local magnetization. The resulting torque is now $-\boldsymbol{\tau}_\perp$ as it drags the magnetization along $-\mathbf{m_1}$ direction, as depicted in Figure 1.16b and d. The direction of the torque is therefore dependent on the direction of the applied current and can favour either a P or an AP configuration.
In MTJs used for MRAM applications, one ferromagnetic layer has its magnetization stabilized due to proximity interaction with other magnetic layers. The magnetization of the other FM layer is free to change. The former gets referred to as the fixed layer while the latter as the free layer. The fixed layer has a defined magnetization while the magnetization of the free layer gets switched by current, so it is used to store the information. For the information writing process, when the layers are anti-parallelly oriented, a positive current passing through the fixed layer FM1 generates polarized electrons along $\mathbf{m_1}$ that transfer their momentum to the local magnetic moment of the free layer. The STT turns the magnetization of the free layer along $\mathbf{m_1}$, obtaining a parallel configuration. The backscattered electrons in this process do not affect the magnetization of the fixed layer, as it is more stable, so higher energy is required to switch it. For the transition from AP to P, a negative current is used to make electrons flow from the free layer to the reference layer. Here, as the fixed layer magnetization does not switch, the responsible for the switching of the free layer are once again the backscattered electrons.
The expression of the spin transfer torque acting on the magnetization is the following:

$$\left(\frac{\mathrm{d}\mathbf{m_2}}{\mathrm{dt}}\right)_{\mathrm{ST}} = -\mathrm{P_{spin}}\frac{\mathrm{j_{dc}}}{\mathrm{te}}\frac{\mathrm{g}\mu_\mathrm{B}}{2}\big(\mathbf{m_2}\times(\mathbf{m_2}\times\mathbf{m_1})\big) \tag{1.42}$$

where ST stand for the "Slonczewski torque" as it is often labelled [80, 81]. $\frac{\mathrm{g}\mu_\mathrm{B}}{2}\big(\mathbf{m_2}\times(\mathbf{m_2}\times\mathbf{m_1})\big)$ represents the contribution of each electron crossing the NM/FM2 interface to the torque $\boldsymbol{\tau}_\perp$, $\mathrm{j_{dc}}$ is the injected current density, t is the thickness of the free layer and $\mathrm{P_{spin}}$ is the current spin polarization at the NM/FM2 interface. An additional torque component is present, a FL torque, directed perpendicular to the $(\mathbf{m_1}, \mathbf{m_2})$ plane. For in-plane MTJs this term can have, as an undesired effect, the back-switching of the free layer. In this manuscript only perpendicular MTJs are studied, for which this second type of torque does not contribute [82].

1.4.3 Voltage controlled magnetic anisotropy

The voltage control of the magnetic anisotropy (VCMA) is another way to manipulate the magnetization, suitable for application in MTJs [83, 84, 85]. The magneto-crystalline anisotropy is one of the critical parameters that determines the orientation of the magnetization. FM films with PMA are promising for their stability but high current densities are required to switch their magnetization, a limiting factor for the applications. If instead of the current, an electric field is used to manipulate their magnetization, limitations can be overcome. The first experimental observation of MCA modification by applying an electric field was done in 2007 by Weisheit *et al.* [86] in FePt and FePd thin films, followed by other reports of VCMA in ferromagnetic films and metallic slabs [87, 88]. Community focused on VCMA at FM/MgO interfaces both experimentally [89, 90] and theoretically [91, 92]. Maruyama *et al.* [93] in 2009 were the first to test the VCMA effect in a Fe/MgO MTJ, showing that with a small electric field ($\sim 100\mathrm{mV/nm}$) they could generate around $\approx 40\%$ change in the PMA of the junction (see Figure 1.17a). An important step was the full electrical field induced switching of CoFeB/MgO/CoFeB perpendicular MTJ by Wang *et al.* [90] with a current density much smaller than that necessary to perform the switching via STT (see Figure 1.17c).
Different physical mechanisms have been pointed out to be the cause of the VCMA effect. For FM/MOx interfaces the phenomenon is predominantly explained by a modulation of the carrier density due to electric field modification of the electronic orbitals of the interfacial atoms. For transition metals like Fe and Co, the applied electric field changes the population of minority d orbitals which can generate an enhancement or a reduction of the magnetic anisotropy [94, 95]. This effect has been proven both theoretically and experimentally [91, 92].
The key element of electric field-induced switching is the change in magnetic anisotropy of the free layer. Phenomenologically, in an MTJ, when the voltage is applied, PMA gets decreased or eliminated so the magnetic moments of the free layer start precessing around the external field [96]. When the voltage is turned off, PMA is recovered, and the magnetic moments stabilize in the opposite direction. The dependence of the effective magnetic anisotropy on applied voltage can be modelled as:

$$\mathrm{K_{eff}(V)} = \frac{\mu_0 \mathrm{H_{eff}} \mathrm{M_s}}{2} \approx \frac{\mathrm{K_S(V)}}{\mathrm{t}} - 2\pi\mathrm{M_s^2} \tag{1.43}$$

where $\mathrm{K_s(V)}$ is the voltage dependent surface anisotropy and t is the thickness of the ferromagnetic layer. In general $\mathrm{K_s(V)}$ is assumed to have a linear dependence on the applied electric field E that can be expressed in terms of applied voltage V as $\mathrm{E} = \frac{\mathrm{V}}{\mathrm{d}}$, where d is the thickness of the oxide layer. The resulting function is:

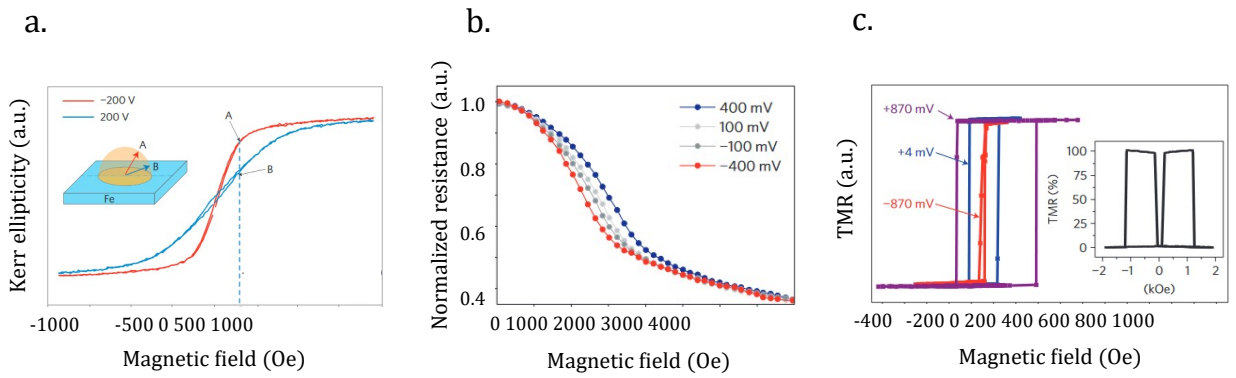

Figure 1.17: **Voltage controlled magnetic anisotropy** | a. Magneto-optical Kerr ellipticity measured as a function of the magnetic field for different applied voltages in Fe(001)/MgO(001) junction. The hysteresis curve shows a big change in the perpendicular anisotropy as a function of applied voltage. Adapted from [93]. b. Change in R dependence to the bias voltage applied as a function of an applied external perpendicular magnetic field in a FeCo/MgO/FeCo junction. Adapted from [97]. c. Minor TMR curves as a function of magnetic field for CoFeB/MgO/CoFeB MTJ for different applied bias voltages. Adapted from [90].

$$K_s(V) = K_s(0) - \chi \frac{V}{d} \tag{1.44}$$

where $K_s(0)$ is the surface anisotropy when no external voltage is applied and χ is the VCMA coefficient (in fJ/Vm). The VCMA coefficient strongly depends on the material properties and it is in general found to be in the range 10-50 fJ/Vm [83].

1.5 Magnetic skyrmions

1.5.1 Topology and properties

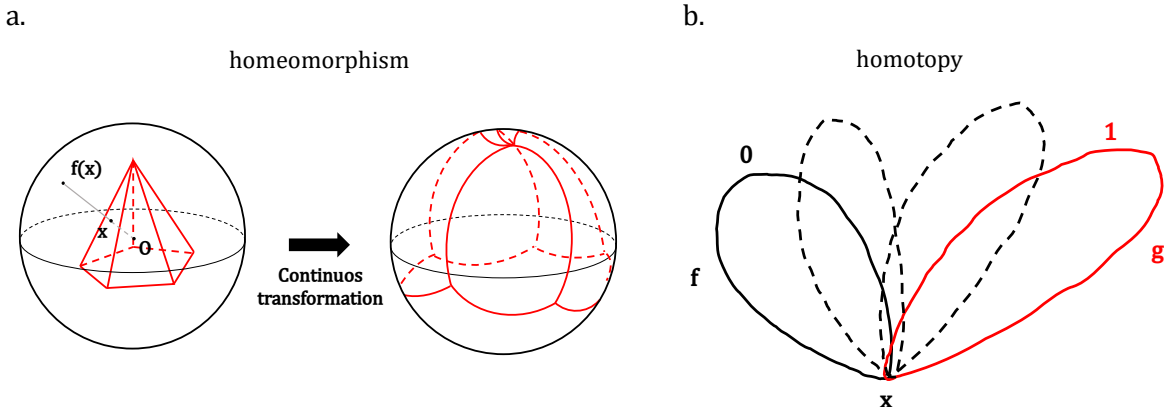

Figure 1.18: **Topological functions** | a. Schematic of an homeomorphism. The polyhedron is continuously transformed into the sphere by a point by point mapping f(x). From a topological point of view the sphere and the polyhedron are the same. b. Example of two homotopic loops f and g as it exists a map F for which F(x,0) = f and F(x,1) = g. Adapted from [98].

Topology is a branch of mathematics that investigates properties that are invariant under a continuous transformation, called topological equivalence [98]. A type of topological equivalence is the homeomorphism. If X and Y are topological spaces, a function $f : X \to Y$ is called homemorphism when it is bijection (one to one correspondance), continuous and has a continuous and inverse function $f^{-1} : Y \to X$ [99]. In Figure 1.18a it is shown an example of an homeophormism of a polyhedron and a sphere. Every point x of the surface of the polyhedron can be projected into a sphere by drawing a line passing through the point x and the center of gravity O. The same procedure can be done to transform the sphere into the polyhedron, so the function can be inverted. Another type of topological equivalence is the homotopy. With $f, g : X \to Y$ maps, if exists a map $F : X \times I \to Y$ such that $F(x, 0) = f(x)$ and $F(x, 1) = g(x)$ for all the points $x \in X$, then f is homotopic to g [99]. An example is shown in Figure 1.18, where the loop f can be continuously deformed into loop g. A peculiar

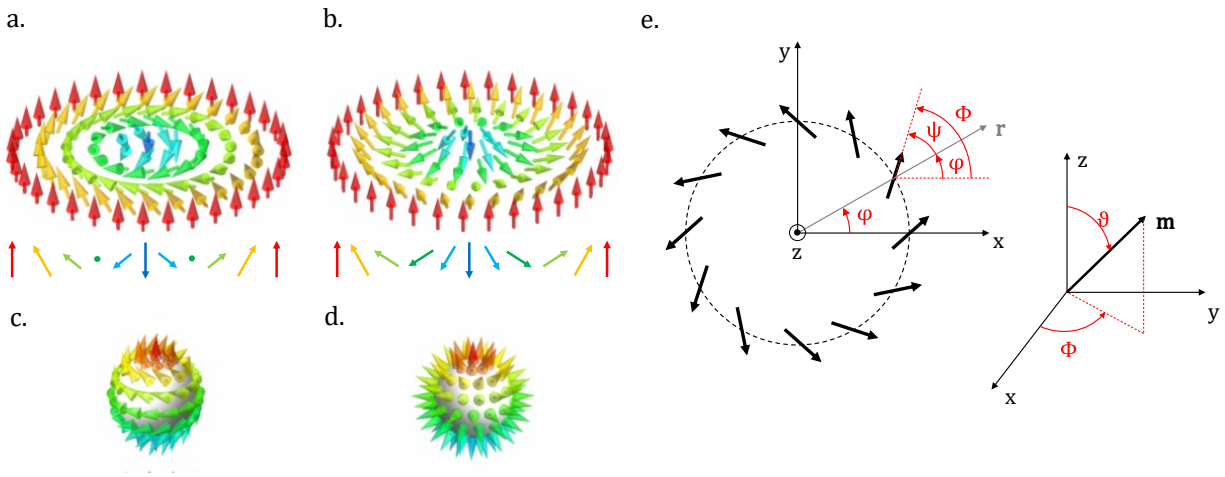

Figure 1.19: **Skyrmion topology** | a. Bloch skyrmion with the core magnetization pointing down. The rotation of the magnetization along the diameter is shown by the sequence of arrows below the picture. The rotation happens in the plane perpendicular to the radial direction. b. Néel skyrmion with the core magnetization pointing down. The rotation of the magnetization along the diameter is shown by the sequence of arrows below the picture and it can be noticed that it happens with a radial component. c. The spin configuration in a. is mapped to the unit sphere representing the order parameter. The wrapping happens once, explaining the winding number equal to 1. d. The spin configuration in c. is mapped to the unit sphere representing the order parameter. The wrapping happens once, explaining the winding number equal to 1. e. Schematic top view of a skyrmion. The angles φ and the helicity Ψ are defined, while the schematic in the right shows the spherical coordinates to define the angles ϑ and Φ.

class is the one for which the map f is the identity operation, that corresponds to the uniformly magnetized state in the magnetic context.
Homotopy theory is used to describe and classify topological defects. Topological defects are irregularities or discontinuities in the structure of a physical systems that cannot be removed by continuous deformation. Topological defects can be characterized by their winding number.
In mathematics, the winding number of a closed planar curve for a given point is the total number of times the curve travels around the point [100]. The winding number is an integer, and its sign depends on the orientation of the curve, positive for counterclockwise rotation, negative for clockwise rotation. A configuration with a winding number n can be continuously deformed into another configuration with the same winding number. Two topological defects with opposite winding numbers can be transformed into a new configuration where the winding number is given by the sum of the two. In the space of 3D spin vectors the order parameter space becomes a 3D sphere and the winding number, also called the skyrmion number is defined by [101]:

$$\mathrm{N_{sk}} = \frac{1}{4\pi} \iint \mathbf{m} \cdot \left(\frac{\partial \mathbf{m}}{\partial \mathrm{x}} \times \frac{\partial \mathbf{m}}{\partial \mathrm{y}} \right) \mathrm{d}^2\mathbf{r} \tag{1.45}$$

where $\mathbf{m}(\mathbf{r})$ is the unit vector of the local magnetization. The skyrmion number defines how many times the $\mathbf{m}(\mathbf{r})$ wraps the order parameter of the space, hence the sphere. By first expressing r in polar coordinates $\mathrm{r} = (\mathrm{r}\cos\varphi, \mathrm{r}\sin\varphi)$, $\mathbf{m}(\mathbf{r})$ can be expressed in spherical coordinates:

$$\mathbf{m}(\mathbf{r}) = \big(\cos\Phi(\varphi)\sin\vartheta(\mathrm{r}), \mathrm{r}\sin\Phi(\varphi)\sin\vartheta(\mathrm{r}), \mathrm{r}\cos\vartheta(\mathrm{r})\big) \tag{1.46}$$

where ϑ, φ and Φ are defined according to Figure 1.19e. Inserting the expression in equation 1.45 is obtained:

$$\mathrm{N_{sk}} = \frac{1}{4\pi} \int_0^{\infty} \int_0^{2\pi} \frac{\partial\vartheta}{\partial \mathrm{r}} \frac{\partial\Phi}{\partial\varphi} \sin\vartheta \, \mathrm{dr} \, \mathrm{d}\varphi \tag{1.47}$$

$$= \frac{1}{4\pi} \int_0^{2\pi} \frac{\partial\Phi}{\partial\varphi} \mathrm{d}\varphi \int_0^{\infty} \sin\vartheta \frac{\partial\vartheta}{\partial \mathrm{r}} \mathrm{dr} \tag{1.48}$$

$$= \frac{1}{4\pi} \left[-\cos\vartheta \Big|_0^{\infty} \right] \left[\Phi \Big|_0^{2\pi} \right] \tag{1.49}$$

$$\tag{1.50}$$

Skyrmions were first introduced by the physicist T. Skyrme, after whom they took the name, in 1962 to describe topological defects in a vector field for interacting particles [102]. Magnetic skyrmions were first proposed by

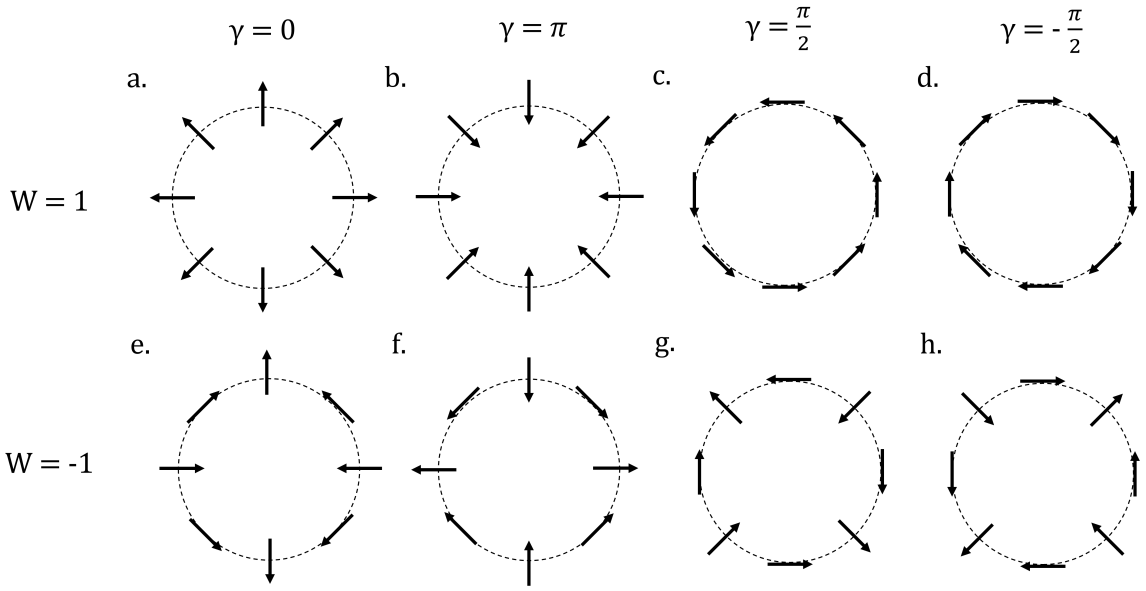

Figure 1.20: **Néel and Bloch skyrmions and antiskyrmions** | Different skyrmions and antiskyrmions configuration. Néel skyrmions are obtained for W = 1 and $\gamma = 0$ or π in a and b. Bloch skyrmions are obtained for W = 1 and $\gamma = \pi/2$ or $-\pi/2$ in c. and d. Néel antiskyrmions are obtained for W = −1 and $\gamma = 0$ or π in e. and f. Bloch anti skyrmions are obtained for W = −1 and $\gamma = \pi/2$ or $-\pi/2$ in g and h.

Bogdanov *et al.* in 1989 [103] when they were still referred to as "vortices". Skyrmions appear as a local whirling of the magnetization. In a magnetic film they are two-dimensional circular magnetic domains, enclosed by a chiral domain wall. Their magnetization is opposite in the core and in the edges, with a precise sense of rotation defined by the chirality, hence their magnetization undergoes a 360° rotation from one edge to another passing from the center. Schematics of skyrmions are depicted in Figure 1.19a and b, respectively for a Bloch and a Néel skyrmion. Following the mathematical definition given before, skyrmions are topological defects with a topological charge equal to 1, as their magnetization wraps the unit sphere, representing the order parameter, once (see Figure 1.19c and d). Their winding number can be obtained from equation 1.50:

$$\mathrm{S} = \frac{1}{4\pi}\left[-\cos\vartheta\Big|_0^{\infty}\right]\left[\Phi\Big|_0^{2\pi}\right] = \mathrm{W}\cdot\mathrm{p} \tag{1.51}$$

where p is the skyrmion core polarity and W is the skyrmion vorticity, defined as:

$$\mathrm{p} = \frac{1}{2} = \left[-\cos\vartheta\Big|_0^{\infty}\right] = [\mathrm{m_z}(0) - \mathrm{m_z}(\infty)] = \pm 1 \tag{1.52}$$

$$\mathrm{W} = \frac{1}{2\pi}\left[\Phi\Big|_0^{2\pi}\right] \tag{1.53}$$

Including the boundary conditions for a skyrmions, that are: $\mathbf{m}(\mathrm{r}\to\infty) = (0,0,1)$ and $\mathbf{m}(\mathrm{r}\to 0) = (0,0,-1)$ it is obtained $\mathrm{p} = \pm 1$. The resulting vorticity for skyrmion is equal to 1, and topological defect presenting vorticity equal to -1 are called antiskyrmions [104]. Therefore, the skyrmion number S will also be equal to ± 1. For the uniformly magnetized state S = 0, hence skyrmions cannot be continuously deformed into the uniformly magnetized state, without having to overcome a large energy barrier, because the winding number is topologically invariant. In general this property is referred to as topological protection against annihilation toward the uniformly magnetized state.
Skyrmions can be furthermore classified depending on their helicity Ψ, the phase of the angle $\Phi(\varphi) = \mathrm{W}\psi + \gamma$, where the angles are shown in Figure 1.19e. In Figure 1.20 different skyrmion and antiskyrmions structures are shown. If W = 1, with $\gamma = 0$ or $\gamma = \pi$, in Figure 1.20a and b, we are in the limiting case of Néel skyrmions, and with $\gamma = \frac{\pi}{2}$ and $\gamma = -\frac{\pi}{2}$ in that of Bloch skyrmions, (c and d in Figure 1.20). The Néel and Bloch antiskyrmions (respectively e. and f. and g. and h. in Figure 1.20) are obtained for W = −1 with the same γ values as in the skyrmions case. Skyrmions having an angle γ in between the extremes values have a configuration in between Bloch and Néel.

1.5.2 Energy terms and stabilization

The energetic stabilization of a skyrmion in a ferromagnetic film results from an interplay of all the energy terms that have been described in this chapter. Here, I followed the model developed by Bernard-Mantel *et al.* [105] that considers 1 nm thick ferromagnetic film, with an easy axis perpendicular to the plane. The energy terms that are taken into account in the model are the exchange energy E_{ex}, the anisotropy energy E_{an}, the DMI energy E_{DMI}, the demagnetizing energy E_d and the Zeeman energy E_z. Through the sum of all these energy terms, the energy functional as a function of the angle ϑ with the z axis can be expressed as:

$$E_{sk}\big[\vartheta(r)\big] = E_{ex} + E_{an} + E_{DMI} + E_d + E_z \tag{1.54}$$

$$= 2\pi t \int_0^\infty \left(A_{ex}\left[\left(\frac{d\vartheta}{dr}\right)^2 + \frac{\sin^2\vartheta}{r^2}\right] - K_u\cos^2\vartheta - D\left[\frac{d\vartheta}{dr} + \frac{\cos\vartheta\sin\vartheta}{r}\right] - \mu_0 M_s H\cos\vartheta + E_d\right) r dr \tag{1.55}$$

The demagnetising energy is composed of two contributions, one from the volume magnetic charges and one from the surface magnetic charges. Due to this term and its long range nature, analytically, it is impossible to solve the equation and numerically is quite difficult [106, 107, 108]. Restricting to the case of ultrathin films where the DW width is larger than the film thickness the volume charge contribution to the demagnetizing energy can be neglected compared to the surface one. The same assumption can be done in the case of a Néel skyrmion that has a 2π DW cross section. The analytical expression for the different energy terms can be written as:

$$E_{an} = 2\sqrt{AK_{eff}}\cdot 2\pi Rt \tag{1.56}$$

$$E_{ex} = 2\sqrt{A_{ex}K_{eff}}\cdot 2\pi Rt + \frac{E_0}{\frac{2R}{\pi\Delta}+1} \tag{1.57}$$

$$E_{DMI} = -\pi D\cdot 2\pi Rt \tag{1.58}$$

$$E_Z = 2\mu_0 M_s H_{ext}\cdot \pi R^2 t \tag{1.59}$$

$$E_d = -\mu_0 M_s^2 I\left(\frac{2R}{t}\right) 2\pi R t^2 \tag{1.60}$$

where R is the skyrmion radius, A is the exchange constant, K_{eff} is the effective anisotropy constant, D is the DMI constant and H_{ext} is the applied external magnetic field. The term in the exchange energy $\frac{E_0}{\frac{2R}{\pi\Delta}+1}$ is added as a low R correction. For R = 0 one obtains $E_{sk} = E_0 = 8\pi At$. As already said, it is impossible to have an analytical expression for the demagnetising energy, so an approximation that can work well for a large radius scenario has to be done. $I\left(\frac{2R}{t}\right)$ is a formula to take into account the surface demagnetising energy in the case of large bubbles [109]. By summing all the contributions the total energy is obtained:

$$E_{sk} = \frac{E_0}{\frac{2R}{\pi\Delta}+1} + 4\sqrt{AK_{eff}}\cdot 2\pi Rt - \pi D\cdot 2\pi Rt + 2\mu_0 M_s H_{ext}\cdot \pi R^2 t - \mu_0 M_s^2 I\left(\frac{2R}{t}\right) 2\pi R t^2 \tag{1.61}$$

To evaluate numerically the stability of the skyrmion we can use in the formula some standard parameters corresponding to Pt/Co(1nm)/MgO: A = 16 pJ/m, Ms = 1.42 MA/m, $\mu_0 H_k$ = 100mT, D = 1 mJ/m^2. In Figure 1.21 the different energy contributions are plotted as a function of the radius of the skyrmion and under different external fields of respectively 100, 50 and 25 mT.

The skyrmion is stabilized for R_{sk} such that $\frac{dE_{tot}}{dR} = 0$. It can be observed that the exchange and the anisotropy contributions are increasing with the radius of the skyrmion and they tend to converge for larger values. The DMI and demagnetizing energy contributions are decreasing with the radius of the skyrmion, meaning that these contributions tend to stabilize it against the anisotropy and the exchange contribution. The Zeeman energy has a square dependence on the skyrmion radius, so the strongest the external applied field the smallest is the radius needed to stabilize the skyrmion. To better understand the impact coming from terms whose strength can be tuned, Figure 1.22 shows the dependence of the skyrmion radius on the DMI constant D and on the anisotropy field for a range of external magnetic field for which skyrmions can be stabilized.
It is observable that by increasing the DMI value larger skyrmions are stabilized. The DMI constant can be tuned by changing the interfaces of the FM with different materials. Larger anisotropy instead leads to smaller skyrmions as it increases the skyrmion energy. The anisotropy can be decreased by increasing the thickness of the FM layer. Moving toward lower anisotropy, closer to the IP/OOP transition, will help for the stabilization of skyrmions in thin films.

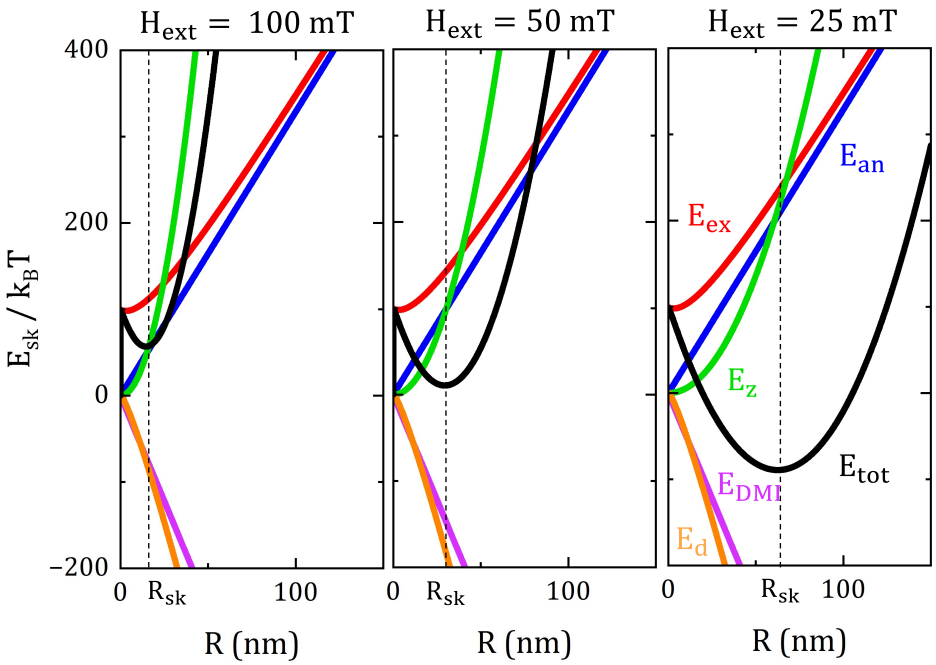

Figure 1.21: **Energy vs radius of magnetic skyrmions** | Energy contributions versus radius for a skyrmion in an infinite FM thin film for different external applied magnetic field. Parameters used for the calculations are A = 16 pJ/m, M_s = 1.42 MA/m, $\mu_0 H_k$ = 100mT, D = 1 mJ/m^2. In black is the total energy E_{tot}, in red the exchange energy contribution E_{ex}, in blue the anisotropy energy contribution E_{an}, in green the Zeeman energy contribution E_Z, in purple the DMI contribution E_{DMI} and in orange the demagnetizing energy contribution E_d.

1.5.3 Observation of skyrmions

After their theoretical prediction [103, 110], skyrmions were first observed in 2009. Muhlbauer *et al.* [12] reported the spontaneous formation of a skyrmion lattice in a chiral magnet, observed by neutron scattering at a temperature around 27 K and under a small applied OOP external magnetic field. The material in which the observation was reported is the cubic B20 compound of MnSi. This material lacks space-inversion symmetry and shows a helical magnetic order at ambient pressure without any applied magnetic field. In 2010, Yu *et al.* [111] reported the observation of a two-dimensional skyrmion lattice in $Fe_{1-x}Co_xSi$ using Lorentz TEM, after the theoretical prediction by Munzer *et al.* [112]. The observation was done with a small applied magnetic field of 50-70 mT applied for a temperature below 40 K. The size of the skyrmions arranged in an hexagonal lattice was around 90 nm (Figure 1.23a). The same group [113], still in 2010, reported the observation via Lorentz TEM of skyrmions in thin films of FeGe, an helimagnet, for a temperature close to room temperature. In all these initial observations, the skyrmions were reported to be Bloch type and their origin was attributed to bulk DMI.

Skyrmions were observed for the first time in thin films in 2011, when Heinze *et al.* [114] reported the observation of a skyrmion lattice as the magnetic ground state of an hexagonal Fe monoloayer on Ir(111) via spin-polarized scanning tunneling microscopy. In this system, the short-range four-spin interaction in the Fe and the strong DMI are generating the spontaneous alignment of the magnetization into Néel type skyrmions lattice. Nevertheless, the stabilization required a strong magnetic field and low temperature. Later, Romming *et al.* [115, 116] demonstrated the possibility to write and delete magnetic skyrmions in a PdFe bilayer grown on Ir(111) with polarized currents from a scanning tunneling microscope (Figure 1.23d and e). Still, for the observation, a high magnetic field (1.5 T) and low temperature (2.2 K) were necessary. For practical applications it was needed stabilizing skyrmions at room temperature, without or with a small external magnetic field. In 2013, in fact, a work from Sampaio *et al.* [117] showed that isolated skyrmions could be stabilized in magnetic dots presenting PMA and interfacial DMI, by performing a numerical investigation using experimental parameters. They also demonstrated the possibility to obtain the current-induced motion of skyrmions in a nanotrack by injecting a vertical spin-polarized current. This research opened up new possibilities for applications of skyrmions, such as racetracks where the information flow is carried by the skyrmions efficiently moved with current [13].

An important breakthrough arrived in 2015/2016 with the first experimental demonstrations of stabilization of isolated skyrmions in sputtered HM/FM/NM stacks. First, Jiang *et al.* [118] demonstrated the ability of nucleating skyrmions from chiral stripe domains with current in a Ta/CoFeB/TaOx trilayer (see Figure 1.23b).

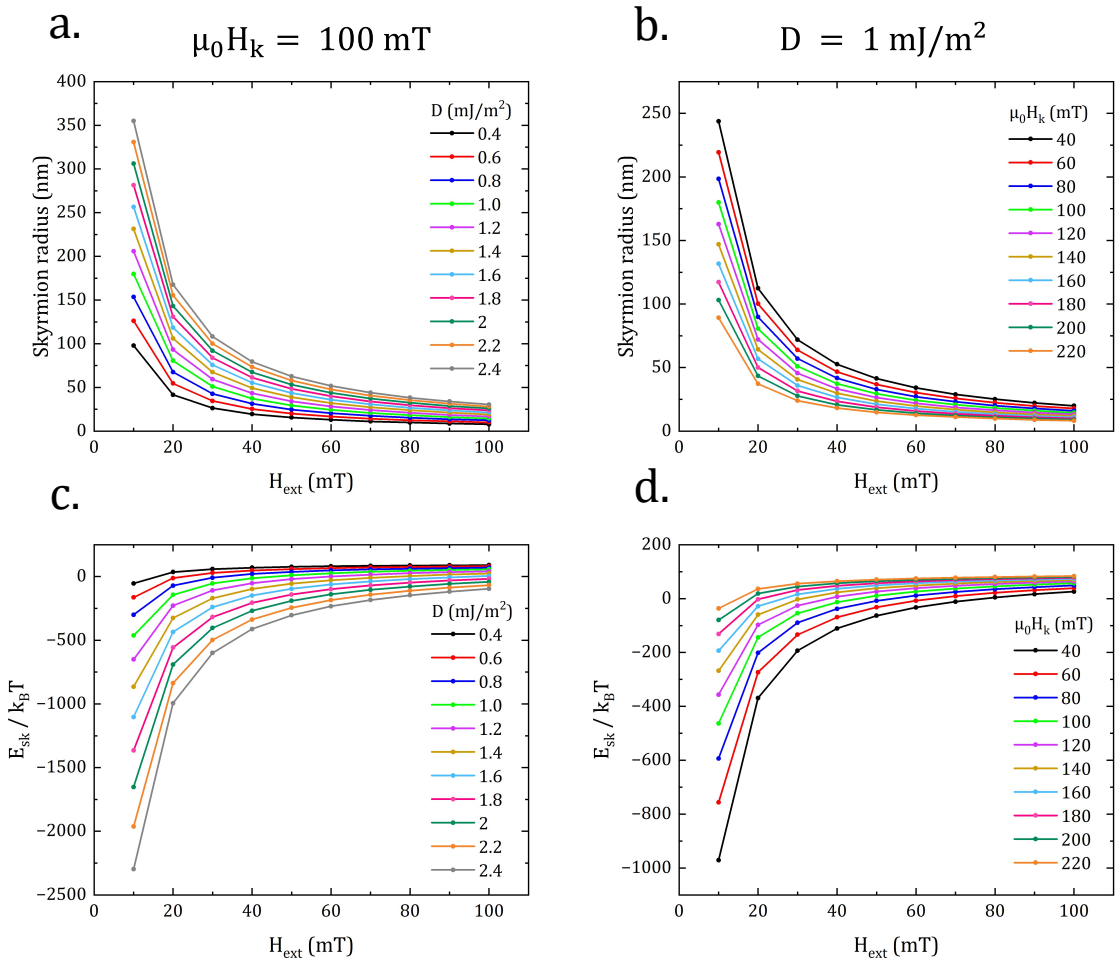

Figure 1.22: **Magnetic skyrmions energy and radius dependence** | a. Skyrmion radius as a function of the external magnetic field for different values of D ranging from 0.4 to 2.4 mJ/m$_2$, for $\mu_0 H_k$ = 100 mT. The other parameters are the same as those used in Figure 1.21. In c. the energy of the skyrmion for the same values of the DMI parameter. b. Skyrmion radius as a function of the external magnetic field for different values of the anisotropy field $\mu_0 H_k$ ranging from 40 to 240 mT and for a fixed value of D = 1 mJ/m^2. The other parameters are the same as those used in Figure 1.21. In d. the energy of the skyrmion for the same values of the DMI parameter.

The experiment was performed using a polar MOKE microscope at room temperature and at a small applied magnetic field. Boulle *et al.* [119] reported the observation of stable Néel type skyrmions at room temperature and zero applied magnetic field in sputtered Pt/Co/MgO trilayer by XMCD-PEEM (Figure 1.23f). Woo *et al.* [120] reported the observation of stable syrmions at room temperature in $[Pt/Co/Ta]_{15}$ and $[Pt/CoFeB/MgO]_{15}$ multilayers by mean of magnetic transmission soft X-ray microscopy (Figure 1.23c). Skyrmions were also observed in $[Ir/Co/Pt]_{10}$ by Moreau-Luchaire *et al.* [121] using STXM (Figure 1.23h), Ir/Fe/Co/Pt multilayer via MFM by Soumyanarayanan *et al.* [122] (Figure 1.23g) and by Jaiswal *et al.* [123] in W/CoFeB/MgO. The size of skyrmions identified in these systems goes from 30 nm in $[Ir/Co/Pt]_{10}$ [121] up to 2 µm in Ta/CoFeB/TaOx trilayer [118]. Important is to highlight that when skyrmions have large dimensions they are quite often referred to as skyrmionic bubbles. The difference in between the two topological textures has been a topic of debate [105, 124]. Skyrmionic bubbles are larger circular domain surrounded by a homochiral DW. Skyrmions and skyrmionic bubbles share the same topology as the have a winding number of 1. The main differences are their sizes and the energy necessary to stabilize them. As skyrmions are mainly stabilized by interfacial DMI, to stabilize skyrmionic bubbles the main role is played by demagnetizing energy. Skyrmionic bubbles are topologically different from the magnetic bubbles, that are circular magnetic domains stabilised by demagnetizing energy in FM films in the absence of DMI. Magnetic bubbles can present a complex topology with a winding number different from that of a skyrmion.

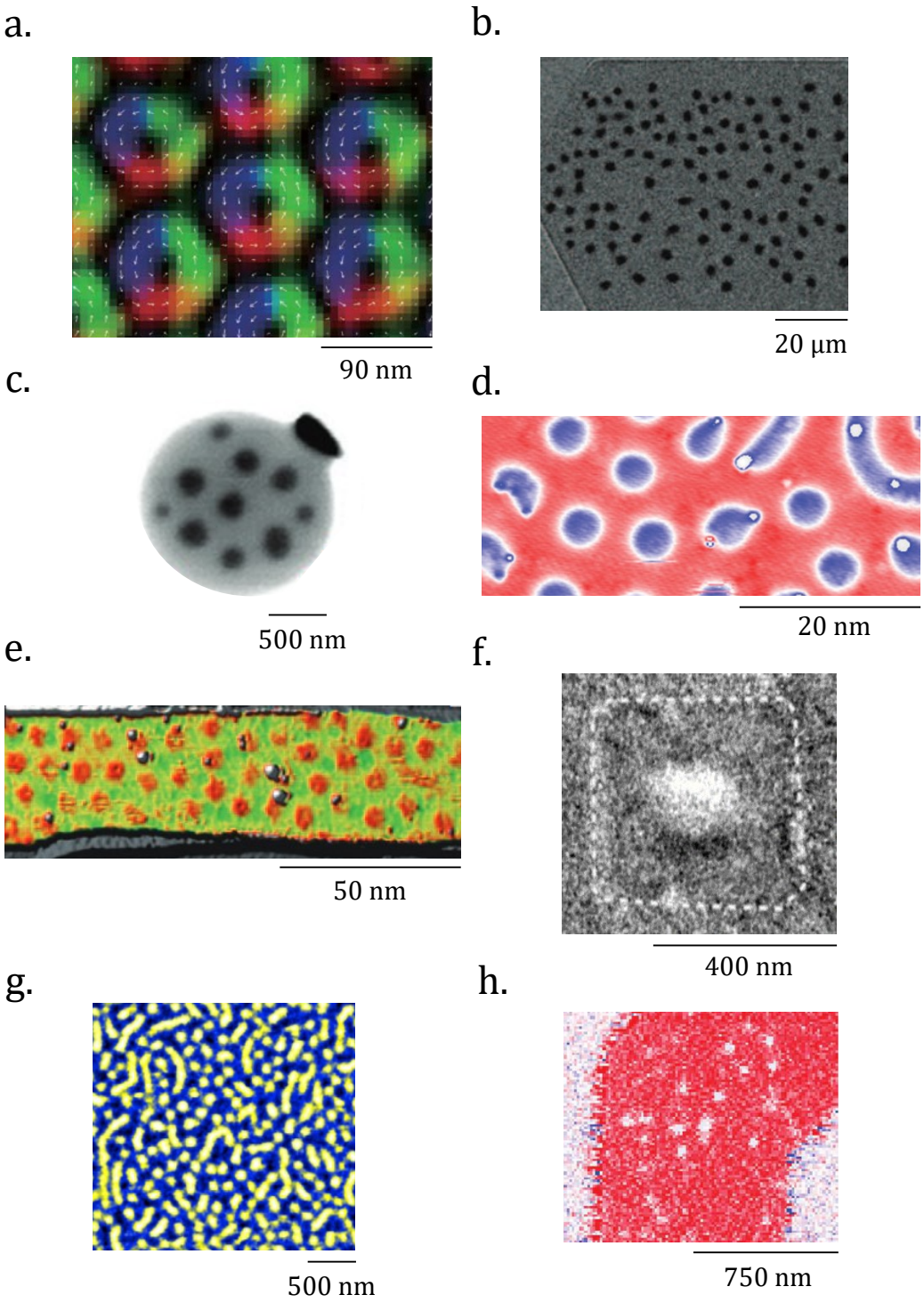

Figure 1.23: **Observation of magnetic skyrmions** | a. Skyrmion crystal in $Fe_xCo_{1-x}Si$ observed by Lorentz TEM with a magnetic field of 50 mT applied normal to the plane at a temperature of 40 K. Adapted from [111]. b. Skyrmion bubbles nucleated by current in Ta/CoFeB/TaOx under an out of plane magnetic field of 0.5 mT at RT, imaged using polar MOKE microscope. Adapted from [118]. c. STXM image of skyrmions nucleated by voltage pulses in a Pt/Co/Ta disc without external magnetic field and at RT. Adapted from [120]. d. Spin-polarized scanning transmission microscopy image of skyrmions in PdFe grown on Ir(111) at 2.2 K and under an external applied field of -1.5 T. Adapted from [116]. e. Pure hexagonal skyrmion lattice measured by scanning tunneling microscopy in PdFe bilayer grown on Ir(111), under an external field of 1.4 T at a temperature of 8 K. Adapted from [115]. f. XMCD-PEEM image of a skyrmion stabilized in a 420 nm wide square dot in Pt/Co/MgO thin film at RT and without any external applied magnetic field. From [119]. g. MFM image of Ir/Fe/Co/Pt multilayer stack under an external applied magnetic field of -100 mT at RT. Adapted from [122]. h. STXM image of the m_z component of the magnetization in $[Ir/Co/Pt]_{10}$ multilayer for an external applied magnetic field of 68 mT at RT. Adapted from [121].

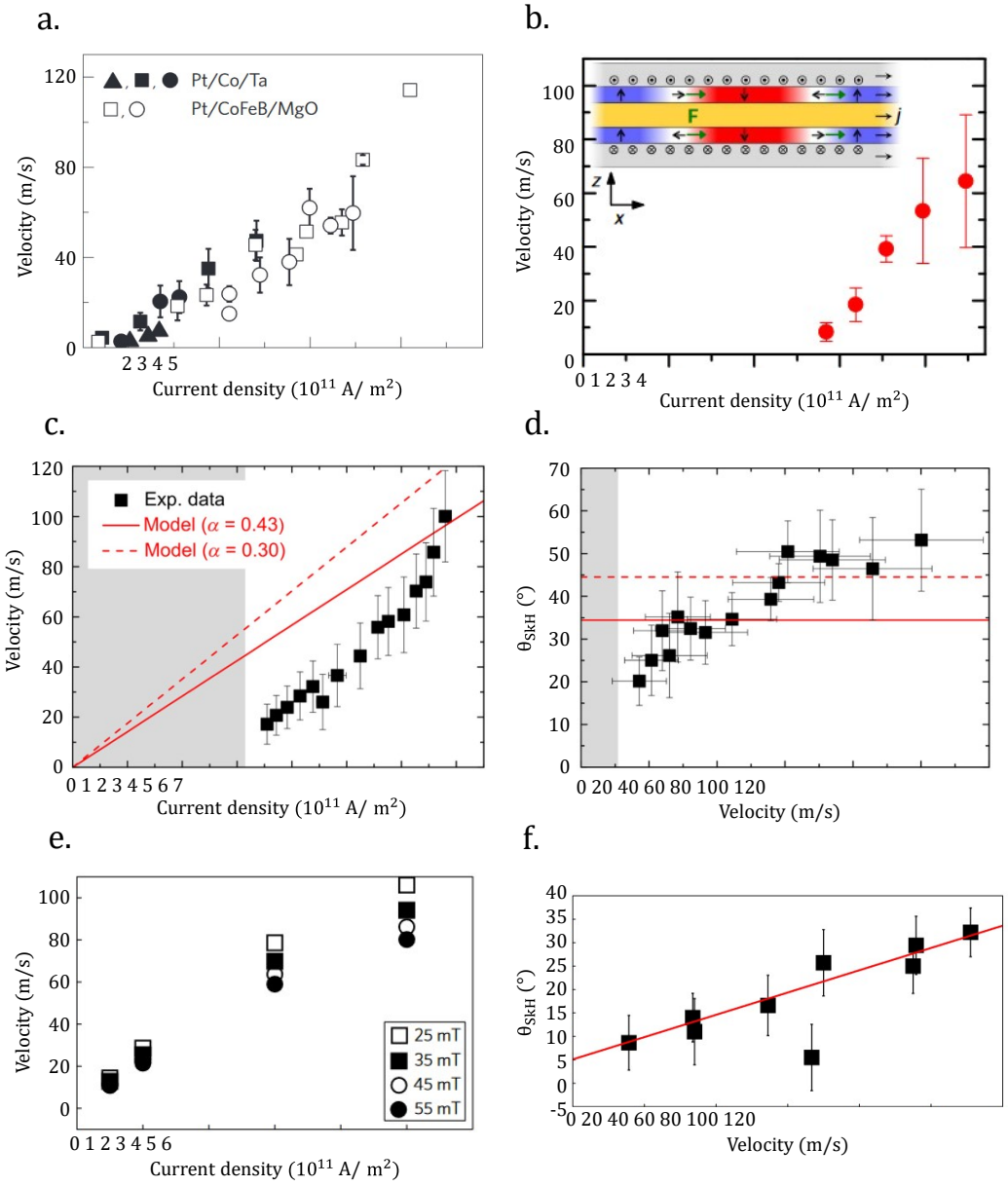

Figure 1.24: **Observation of current-driven skyrmion motion** | a. Measured skyrmions velocity as a function of the applied current density in $[Pt/Co/Ta]_{15}$ and $[Pt/CoFeB/MgO]_{15}$ multilayers. From [120]. b. Measured skyrmions velocity vs applied current density in Pt/Ni/Co/Ni/Au/Ni/Co/Ni/Pt symmetric multilayer. From [14]. c. Measured skyrmions velocity as a function of the applied current density and d. skyrmion Hall angle as a function of the measured velocity for a Pt/Co/MgO trilayer. From [15]. e. Measured skyrmions velocity as a function of the applied current density and f. skyrmion Hall angle as a function of the measured velocity for $[Pt/CoFeB/MgO]_{15}$ [17].

1.5.4 Current-driven skyrmion dynamics

Current-induced motion of skyrmions is a crucial aspect for applications. A first experimental demonstration arrived in 2010 when Jonietz *et al.* [125] showed the rotation of the skyrmion lattice in MnSi chiral magnet crystal under the effect of an applied current for a temperature around 27 K. It was highlighted that the current density used for the experiment, in the order of 10^6 A/m^2, was 5 orders of magnitude smaller than that typically used in experiments on current-driven dynamics in nanostructures. The observed current-induced motion was explained by STT. Schulz *et al.* [126] performed Hall-effect measurement on MnSi from which the skyrmion velocity as a function of the current can be extracted. Yu *et al.* [127] used a similar current density, around 10^5 A/m^2, to demonstrate the near room temperature translational motion of skyrmions driven by electrical current in the helimagnet FeGe. The motion was once again explained by STT. Iwasaki *et al.* [128] studied the current-velocity relation of skyrmion motion in chiral magnets using the Thiele equation approach showing that the easy motion is mainly due to very weak pinning by defects and impurities. Anyway these experiments showed a very slow motion of skyrmions, around 10^4 nm/s. Even if the current densities used for the motion

were very small, a linear extrapolation indicates that to reach higher velocities (10-100 m/s), similar current densities as those used for the motion of DWs should be used [13]. As the materials employed in the experiments listed above were quite thick, the actual currents used were large, so increasing the current density is unfeasible. These factors are quite limiting for applications.
As already discussed in the previous section, Sampaio *et al.* [117] showed the stabilization of isolated skyrmions in HM/FM/NM dots presenting PMA and DMI, as well as their current -nduced motion via vertical spin-polarized currents. The manipulation via SHE due to the presence of the HM layer seemed the most efficient way to induce skyrmion motion with current [129].
The first experimental observation of skyrmions current-induced motion by SOT at RT was reported in 2015 in Ta/CoFeB/TaOx [118]. Skyrmion velocities up to 25 µs were reported for a current density of $4.5 \times 10^8 \mathrm{A/m^2}$. Here, the skyrmionic bubbles were presenting sizes up to µm. This study was followed by the observation of current-induced skyrmion motion in $[\mathrm{Pt/Co/Ta}]_{15}$ and $[\mathrm{Pt/CoFeB/MgO}]_{15}$ multilayers by Woo *et al.* [120] where velocities up to 100 m/s for a current density of $\sim 5 \times 10^{11}$ A/m^2 were reached (see Figure 1.24a). The work of Legrand *et al.* [130] in 2017 reported velocities up to 25 nm/s for sub-100 nm skyrmions in Pt/Co/Ir based multilayers. Hrabec *et al.* [14] measured the current-induced skyrmion motion in a Pt/Ni/Co/Ni/Au/Ni/Co/Ni/Pt symmetric multilayer reporting values up to 80 m/s for current densities of 4.5×10^{11} A/m^2 (Figure 1.24). A high Joule dissipation for a given current density was expected for these works, as it scales with the total film thickness. Juge *et al.* [15] reported velocities up to 100 m/s for skyrmions with a diameter around 100 nm in a Pt/Co/MgO nanometric film (Figure 1.24c).
In all these works, a deviation of the skyrmion trajectory from the current direction is reported, as can be observed in Figure 1.24d and f. This effect is known as the skyrmion Hall effect (SkHE) and it is a direct consequence of the skyrmion topological charge [16, 17]. In Figure 1.25 a sketch of the phenomenon as well as its experimental observation is shown. In the following section a mathematical derivation of the skyrmion Hall effect is performed.

1.5.4.1 Current-induced skyrmion dynamics and skyrmion Hall effect

For the derivation of current-induced motion of skyrmions we consider a HM/FM/NM film exhibiting PMA and interfacial DMI. The main mechanism generating the motion is SOT, while the effect of STT can be neglected. The mechanism inducing the motion is similar to the one already explained for DWs in section 1.3.2.2. As already discussed for the DW motion, the DL term of SOT, coming mainly from the SHE, is dominant with respect to the FL term of SOT, generated predominantly by the Rashba-Edelstein effect. Therefore, also for the following derivation, only the DL-SOT term is taken into account and the FL-SOT term is omitted. The effective field associated to the DL-SOT is given by $\mathbf{H_{DL}} = \mathrm{H_{DL}^0}(\mathbf{m} \times (\hat{\mathbf{j}} \times \hat{\mathbf{z}}))$ where $\mathbf{J} = \mathrm{J}\hat{\mathbf{j}}$ is the charge current. For consistency with the SOT-driven motion derivation, we consider a Pt/Co based stack, for which the spin Hall angle θ_{SH} has a positive sign. The magnetization dynamics is then described by the LLG equation taking into account the DL-SOT term (1.32) and it has the form:

$$\frac{\partial \mathbf{m}}{\partial \mathrm{t}} = -\gamma_0 \big(\mathbf{m} \times \mathbf{H_{eff}}\big) + \alpha \left(\mathbf{m} \times \frac{\partial \mathbf{m}}{\partial \mathrm{t}}\right) - \gamma_0 \big(\mathbf{m} \times \mathbf{H_{DL}}\big) \tag{1.62}$$

The magnetization of the FM layer is defined along $\hat{\mathbf{z}}$ and with $\hat{\mathbf{j}} = \mathrm{j}\hat{\mathbf{x}}$ one obtains $\mathbf{H_{DL}} = \mathrm{H_{DL}^0}(\hat{\mathbf{y}} \times \hat{\mathbf{m}})$. The $\mathbf{H_{eff}}$ term contains all energy contributions (exchange, anisotropy, DMI, Zeeman and demagnetizing). From this point, the derivation of skyrmion motion can be done following the method proposed by Thiele [131]. In this model, skyrmions are considered as rigid bodies during their motion, so that the motion of the center of mass corresponds to that of the whole body. Under this assumption, the steady state velocity of the skyrmion is obtained by a balance of different forces:

$$\mathbf{F_{DL}} + \mathbf{G} \times \mathbf{v} - \alpha \mathcal{D} \cdot \mathbf{v} = 0 \tag{1.63}$$

where $\mathbf{F_{DL}}$ is the force generated on the skyrmion by the DL-SOT, $\mathbf{G}$ is the gyrotropic vector and $\mathcal{D}$ is the dissipation matrix. The gyrotropic vector $\mathbf{G}$ is intrinsically related to the winding number of the skyrmion $\mathrm{N_{sk}}$, and is a term that naturally comes in the derivation. In Appendix A.1 the derivation of the Thiele equation 1.63 from the LLG equation is developed. $\mathcal{D}$ is a dissipative tensor that depends on the material properties. The expressions of these terms are:

$$\mathbf{F_{DL}} = \begin{pmatrix} \mathrm{F_{DL,x}} \\ \mathrm{F_{DL,y}} \\ 0 \end{pmatrix}, \ \mathrm{F_{DL,i}} = -\mu_0 \mathrm{M_s t H_{DL}^0} \iint \left(\mathrm{m_x} \frac{\partial \mathrm{m_z}}{\partial \mathrm{x_i}} - \mathrm{m_z} \frac{\partial \mathrm{m_x}}{\partial \mathrm{x_i}}\right) \mathrm{dxdy} \tag{1.64}$$

$$\mathbf{G} = \begin{pmatrix} 0 \\ 0 \\ \mathrm{G} \end{pmatrix}, \ \mathrm{G} = -\frac{\mathrm{M_s t}}{\gamma} \iint \mathbf{m} \cdot \left(\frac{\partial \mathbf{m}}{\partial \mathrm{x}} \times \frac{\partial \mathbf{m}}{\partial \mathrm{y}}\right) \mathrm{dxdy} \tag{1.65}$$

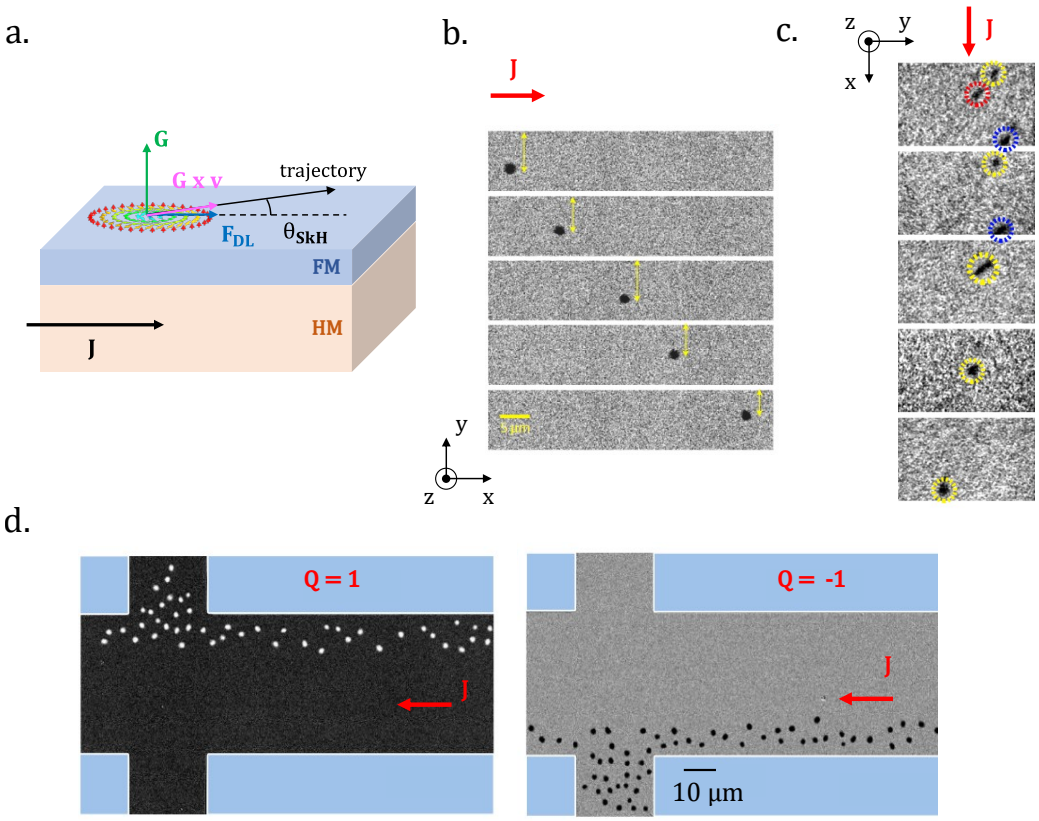

Figure 1.25: **Experimental observation of the skyrmion Hall effect** | a. Schematic of the skyrmion Hall effect. The DL torque $\mathbf{F_{DL}}$ generated by the SHE in the HM layer is the driving force of the skyrmion motion. The deviation from the current trajectory is generated by the gyrotropic vector $\mathbf{G}$ of the skyrmion. b. Sequence of MOKE microscopy images of a skyrmion moved by 50 µs current pulses in Ta/CoFeB/TaOx trilayer. The deviation from the straight trajectory of the current due to the SkHE is highlighted by the yellow arrows. From [16]. c. Sequence of XMCD-PEEM images of a skyrmion in a 3-µm wide track in Pt/Co/MgO moved by 11 ns current pulses. The trajectory of the skyrmion, circled in yellow, is visibly deviated from the current trajectory due to the SkHE. From [15]. d. MOKE microscope images showing the accumulation of skyrmions at two opposite (left and right) edges of a device made of 60 µm wide and 500 µm long tracks after repetitively applying current pulses. The accumulation side depends on the topological charge as the SkHE sign depends on the gyrotropic vector [16].

$$\mathcal{D} = \begin{pmatrix} \mathcal{D}_{xx} & \mathcal{D}_{xy} \\ \mathcal{D}_{yx} & \mathcal{D}_{yy} \end{pmatrix}, \mathcal{D}_{ij} = \frac{M_s t}{\gamma} \iint \mathbf{m} \cdot \left(\frac{\partial \mathbf{m}}{\partial x_i} \cdot \frac{\partial \mathbf{m}}{\partial x_j} \right) dxdy \tag{1.66}$$

where i = x, y and t is the thickness of the FM layer. Assuming that the skyrmion has rotational symmetry in the xy plane one has $\frac{\partial \mathbf{m}}{\partial x} \perp \frac{\partial \mathbf{m}}{\partial y}$, hence $\frac{\partial \mathbf{m}}{\partial x} \cdot \frac{\partial \mathbf{m}}{\partial y} = 0$, meaning the diagonal terms $\mathcal{D}_{xx} = \mathcal{D}_{yy} = \mathcal{D}$ and $\mathcal{D}_{xy} = \mathcal{D}_{yx} = 0$. From the expression of the skyrmion number 1.45 one can express $G = -\frac{M_s t}{\gamma} 4\pi N_{sk}$, so the above expressions become:

$$\mathbf{F_{DL}} = \begin{pmatrix} F_{DL,x} \\ F_{DL,y} \\ 0 \end{pmatrix}, F_{DL,i} = -\mu_0 M_s t H_{DL}^0 \iint \left(m_x \frac{\partial m_z}{\partial x_i} - m_z \frac{\partial m_x}{\partial x_i} \right) dxdy \tag{1.67}$$

$$\mathbf{G} = \begin{pmatrix} 0 \\ 0 \\ G \end{pmatrix}, G = -4\pi \frac{M_s t}{\gamma} N_{sk} \tag{1.68}$$

$$\mathcal{D} = \begin{pmatrix} \mathcal{D} & 0 \\ 0 & \mathcal{D} \end{pmatrix}, \mathcal{D} = \frac{M_s t}{\gamma} \iint \left(\frac{\partial \mathbf{m}}{\partial x} \right)^2 dxdy \tag{1.69}$$

Substituting these expressions in the Thiele equation 1.63, including also the velocity $\mathbf{v} = (v_x\ v_y\ 0)$ as there is no motion along $\hat{\mathbf{z}}$, one obtains:

$$\begin{pmatrix} F_{DL,x} \\ F_{DL,y} \\ 0 \end{pmatrix} + G \begin{pmatrix} -v_y \\ v_x \\ 0 \end{pmatrix} - \alpha\mathcal{D} \begin{pmatrix} v_x \\ v_y \\ 0 \end{pmatrix} = 0 \tag{1.70}$$

so solving separately for the x and y component, one obtains:

$$v_x = \frac{\alpha\mathcal{D}F_{DL,x} - GF_{DL,y}}{G^2 + \alpha^2\mathcal{D}^2} \tag{1.71}$$

$$v_y = \frac{\alpha\mathcal{D}F_{DL,y} + GF_{DL,x}}{G^2 + \alpha^2\mathcal{D}^2} \tag{1.72}$$

For Néel skyrmions $F_{DL,y} = 0$ and $F_{DL,x} = F_{DL}$ as it can be observed from Figure A.1 (opposite for Bloch skyrmions). This means that Néel skyrmions are driven parallel to the current direction by the SOT, while Bloch skyrmions are driven perpendicular to it. The expressions for the velocity components become:

$$v_x = \frac{\alpha\mathcal{D}F_{DL}}{G^2 + \alpha^2\mathcal{D}^2} \tag{1.73}$$

$$v_y = \frac{GF_{DL}}{G^2 + \alpha^2\mathcal{D}^2} \tag{1.74}$$

It can be noticed that the gyrotropic vector is generating a component of the velocity perpendicular to the current direction, hence it is the direct cause of the SkHE seen in experiments. The angle in between the two velocity components, θ_{SkH} can be derived:

$$\tan\theta_{SkH} = \frac{G}{\alpha\mathcal{D}} \tag{1.75}$$

where it can be noticed that it is independent from the current density or the skyrmion velocity, even if dependencies were observed experimentally (see Figure 1.24d and f). Probably, this dependence can be explained by the pinning from defects or impurities [15]. When the velocity is low, the flow regime is not yet reached and the SkHA does not agree with predicted values based on material parameters. Figure 1.26 shows the effect of the DL-SOT on the velocity of skyrmions of different types.
Focusing now only on Néel skyrmions, we want to extract the expression of the force $F_{DL,x}$ acting on it:

$$F_{DL,x} = F_{DL} = -\mu_0 M_s t H^0_{DL} \iint \left(m_x \frac{\partial m_z}{\partial x} - m_z \frac{\partial m_x}{\partial x} \right) dxdy \tag{1.76}$$

and by changing the reference system to spherical coordinates we obtain:

$$F_{DL,x} = F_{DL} = -\mu_0 M_s t H^0_{DL} \pi \int_0^\infty r \frac{d\vartheta}{dr} dr \tag{1.77}$$

To evaluate this integral we assume that the skyrmion has a 180° Bloch DW profile:

$$\vartheta(r) = -2\arctan\left(\exp\left(\frac{r - R}{\Delta}\right)\right) \tag{1.78}$$

and for this profile the relation $\sin\vartheta = \Delta\frac{d\vartheta}{dr}$ holds. Assuming also a large skyrmion radius (R >> D), one can set r = R in the integral. The final result of the calculation is presented here, the detailed passages can be found in appendix A.2:

$$F_{DL} \approx -\mu_0 M_s t H^0_{DL} \pi \int_0^\infty \frac{R}{\Delta} \sin\vartheta dr \approx \mu_0 M_s t H^0_{DL} \pi^2 R \tag{1.79}$$

For the dissipation tensor a similar calculation is also performed, details can be once again found in the appendix A.2 and the obtained result is:

$$D \approx \frac{M_s t}{\gamma} 2\pi \frac{R}{\Delta} \tag{1.80}$$

The gyrotropic vector can be written $G = -\frac{M_s t}{\gamma} 4\pi$ as $N_{sk} = 1$ for a Néel skyrmion. Using these derived values the final expressions for velocity and SkHA are:

$$v = \sqrt{v_x^2 + v_y^2} = \frac{R\pi\gamma}{4\sqrt{1 + \left(\frac{\alpha R}{2\Delta}\right)^2}} C_{DL} J \tag{1.81}$$

$$\tan\vartheta_{\mathrm{SkH}} = \frac{v_y}{v_x} = \frac{-2\Delta}{\alpha R} \tag{1.82}$$

where the relation $\mu_0 H_{DL}^0 = C_{DL} J$ was used, with C_{DL} the effective magnetic field per unit current density (in TA/m^2). The skyrmion velocity is linearly dependent on the current density.
The skyrmion Hall effect has detrimental drawbacks on the possible skyrmion-based application. For a magnetic racetrack device [13, 117], where skyrmions would represent the bits of information and the motion would be induced by current, the skyrmions would be driven toward the edges of the tracks by the skyrmion Hall effect, and they would either bounce back or get annihilated, resulting in a loss of information. As the SkHE is dependent on the gyrotropic vector of the skyrmion, a possible solution that has been proposed [132] is to antiferromagnetically couple two ferromagnetic systems. In this way a skyrmion generated in one ferromagnetic layer would have its counterpart in the other FM layer, with an opposite gyrotropic vector. The net gyrotropic vector would cancel out, generating a motion without skyrmion Hall effect. Another possibility would be to use antiferromagnetic skyrmions, that would present a net zero gyrotropic vector [133]. In chapter 3 I will disceuss more in detail the topic, presenting the part of my thesis work focused on antiferromagnetically coupled skyrmions.

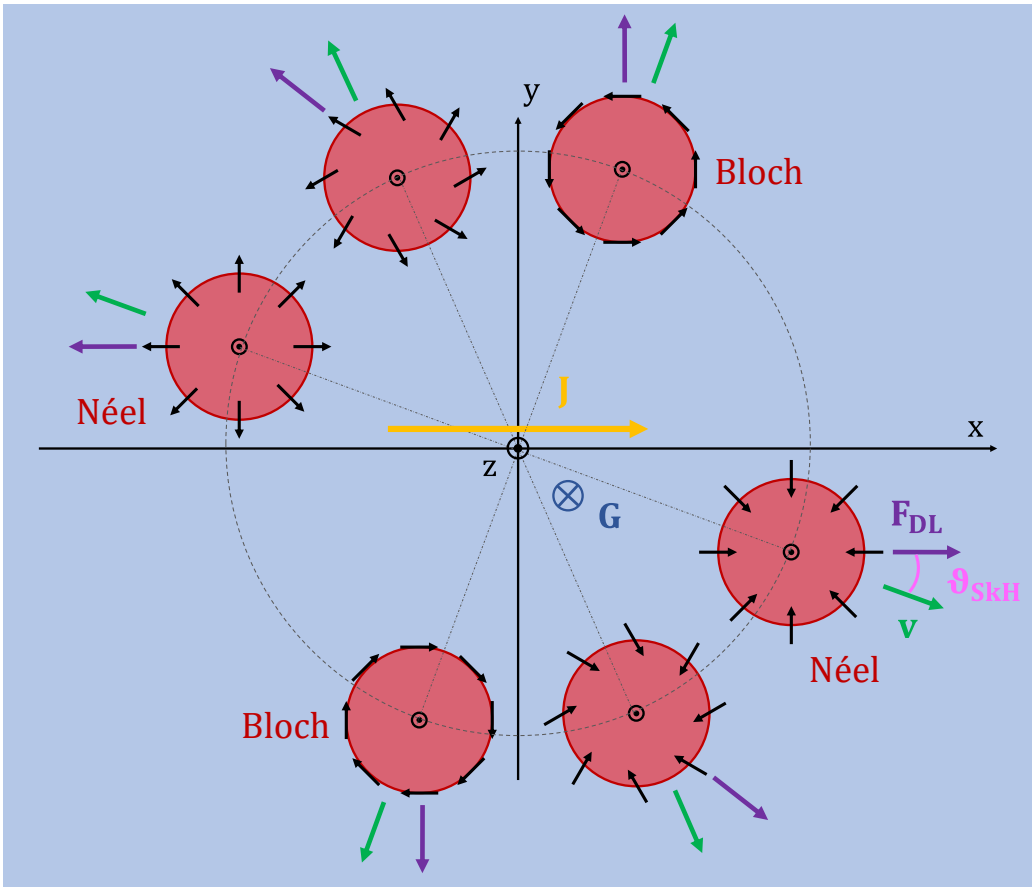

Figure 1.26: **SOT-driven skyrmion motion for different configurations** | Schematic of the effect of the DL-SOT generated by the current **J** on different skyrmions, all presenting p = 1 but with different helicities. **G** is along $-\hat{\mathbf{z}}$ for all the skyrmions. For Néel skyrmions only $F_{DL,x}$ component is present, while only $F_{DL,y}$ appears for Bloch skyrmions. The SkHA is defined as the angle between the force generated by the DL-SOT and the velocity of the skyrmion.

1.5.5 Electrical detection of magnetic skyrmions

The first electrical detection of magnetic skyrmions was done by performing Hall measurement. When a current flows through a metal subjected to an external magnetic field, the conduction electrons feel the Lorentz force generated by the external field and they are pushed on one side of the conductor. This imbalance in the carrier distribution generates a transverse potential difference, that depends directly on the external magnetic field, the Hall voltage. The transverse resistivity is $\rho_{xy}^N = \mu_0 H_{ext} R_0$, where R_0 is the ordinary Hall coefficient that depends of the material. For ferromagnetic materials, a second contribution to the Hall effect appears, called

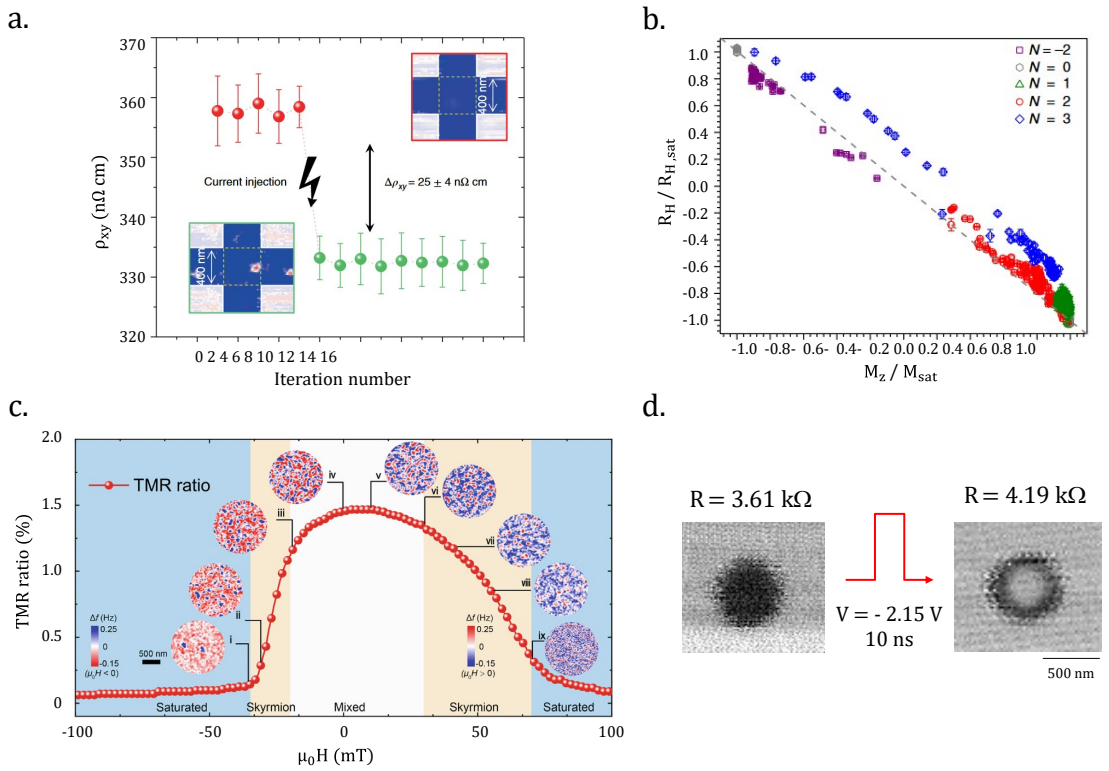

Figure 1.27: **Electrical detection of magnetic skyrmions** | a. Variation of Hall resistivity due to a single skyrmion nucleated in the Hall cross area (the yellow dashed line square). From [20]. b. Hall signal arising from spin textures for different number of skyrmions, normalized by the saturation value. From [21]. c. TMR ratio as a function of magnetic field for the detection of RT skyrmions in a MTJ device. The images taken with MFM are representing the nucleation and annihilation of spin textures, related to the change in TMR. From [134]. d. XMCD-STXM images of the nucleation of a magnetic skyrmion in a MTJ pillar with a voltage pulse, starting from the uniformly magnetized state, and corresponding jump in resistance measured in situ. Adapted from [23].

the anomalous Hall effect. This contribution generates a resistivity $\rho_{xy}^{A} = \mu_0 M_z R_s$, and, as it can be noticed, depends only on the magnetization of the material and not on the external magnetic field. The origin of this second type of Hall effect in ferromagnetic materials lies in the spin orbit coupling. The spin-orbit coupling inside the material tends to bend electrons trajectories even without an external magnetic field as long as the magnetization is present. This anomalous Hall effect can be attributed to an intrinsic Berry-curvature term in the band structure that, together with extrinsic processes, side jumps and skew scattering, arising from impurity scattering, produces a spin-dependent deflection: electrons with opposite spins are bent to opposite sides [135]. When a skyrmion is present in the material, a third contribution to the Hall effect arises, the topological Hall effect. This third contribution originates from the skyrmion itself: when conduction electrons move through the texture, the exchange interaction between their spins and the local magnetization acts as an effective magnetic field that deflects them. It is quite challenging to experimentally differentiate the topological Hall effect from the anomalous Hall effect, because the formation of magnetic skyrmions reduces the magnetization [136]. The total Hall resistivity effect can be summarize as: $\rho_{xy} = \mu_0 H_{ext} R_0 + \mu_0 M_z R_s + \mu_0 R_0 P H_{eff,z}$ where the terms are respectively the normal Hall effect contribution, the anomalous Hall effect contribution and the topological Hall effect contribution. In the formula, P is the spin polarization of conduction electrons and $H_{eff,z}$ is the effective field experienced by conduction electrons in the presence of skyrmions [137, 21].
The topological Hall effect contribution coming from magnetic skyrmions was identified in MnSi crystal [11, 138, 126, 139], thin films [140] and nanowires [141]. It was identified also in MnGe crystal [142] and in thin films of FeGe [137, 143, 144]. Other electrical detection methods rely on magnetoresistive effects, measurements of the magnetization as a function of the applied external field. Du *et al.* [145] observed jumps in the magnetoresistance associated to the formation of individual skyrmions in MnSi nanowires. Hanneken *et al.* [146, 147] used non-collinear magnetoresistance measurement to electrically detect magnetic skyrmions in PdFe grown on Ir(111). One of the main drawbacks is that all these measurements were performed at temperatures way below the room temperature.
For HM/FM/NM trilayers the stabilization and current-induced motion of magnetic skyrmions was detected only by using imaging techniques. An important breakthrough is the work of Maccariello *et al.* [20] that reports

the combination of MFM imaging and electrical transport measurement on Pt/Co/Ir based multilayers at RT. The sample was patterned with tracks and magnetic skyrmions were generated either via current pulses or injection of spin polarized current through a scanning transmission microscope tip. Their motion was measured via Hall resistivity. The authors were able to electrically detect the nucleation of a single skyrmion by change in the transverse Hall resistivity (see Figure 1.27a) and they observed that each nucleated skyrmion was bringing an equal contribution to the resistivity. The associated change in resistivity per skyrmion was around 25 nΩ cm. Zeissler *et al.* [21] performed Hall resistivity measurement combined with XMCD-STXM imaging of spin textures in Pt/Co/Ir multilayer discs of 1 µm. They measured a change in Hall resistivity of $22 \pm 2\,\mathrm{n\Omega\,cm}$ per skyrmion (in Figure 1.27b).
Anther possibility to have a larger electrical readout signal for a single skyrmion is to exploit the tunnel magnetoresistance in MTJs. Recently, Li *et al.* [134] combined MFM imaging and TMR measurement to detect skyrmions nucleated by magnetic field in MTJ devices made of Pt/Co/Ta/MgO/CoFeB/Mo at RT (see Figure 1.27c). Penthorn *et al.* [148] nucleated intermediate states in a MTJ by using repeated current pulses and measured the associated change in resistance through the TMR. He *et al.* [149] also exploited the TMR in an MTJ to detect the skyrmions nucleated at zero external magnetic field. Kasai *et al.* [150] and Chen *et al.* [22] demonstrated the nucleation of skyrmions in MTJ by using gate voltage pulses. Chen *et al.* combined the electrical detection via TMR with a MFM imaging of the magnetic skyrmion. Urrestarazu *et al.* [23] performed in operando XMCD-STXM to demonstrate the electrical nucleation of a single skyrmion in a MTJ by gate voltage. Figure 1.27d shows the nucleation of a magnetic skyrmion by mean of a voltage pulse associated with the change in R that corresponds to the nucleation event.

1.6 Conclusions

In this chapter I presented the different energy terms and basic interactions in a micromagnetic system, with a specific focus on HM/FM/NM multilayers which are the stacks used for this work. Different mechanisms to manipulate the magnetization in a FM layer were presented, in order to have an overview on the key ingredients needed to stabilize and move magnetic skyrmions. The exploitation of magnetic skyrmions for different types of applications is the main objective of my thesis work. But before presenting the work done, it was important to highlight the progress done in the last years in electrically detecting skyrmions and moving them with current. Still several challenges are to be faced in order to reach the high speed motion of skyrmions needed for applications in racetrack memories, and to achieve the controlled low power nucleation for logic applications and more exotic applications toward neuromorphic computing, a fundamental topic in the society of today. The work I performed to address these challenges is presented respectively in Chapters 3, 4 and 6, while in the next one I will present the experimental techniques that I used to perform the studies explained later.

Chapter 2

Experimental techniques

Contents

2.1 Deposition and nanofabrication of MTJs . . . 41
2.1.1 SiN membranes . . . 41
2.1.2 Deposition of magnetic stack . . . 42
2.1.3 MTJs patterning . . . 42
2.2 Electrical characterization of MTJs . . . 45
2.2.1 Manual prober . . . 45
2.2.2 Implementation of manual prober for RC measurement . . . 46
2.3 Magnetic force microscopy . . . 47
2.4 Magneto-optical Kerr effect . . . 47
2.5 X-ray microscopy techniques . . . 48
2.5.1 X-ray magnetic circular dichroism . . . 48
2.5.2 Scanning transmission x-ray microscopy . . . 49
2.5.3 Time-resolved STXM . . . 49
2.5.4 X-ray photoemission electron microscopy . . . 51

This chapter provides a detailed explanation of the nanofabrication process of MTJs, specifically on transparent membranes. To go on, the characterization techniques used during the thesis are presented. Lastly, the x-ray microscopy techniques used for imaging of the magnetic textures are explained.

2.1 Deposition and nanofabrication of MTJs

In this section I will explain in detail the process used to fabricate the MTJ nanopillars. All the devices measured during my thesis have been fabricated inside the Plateforme de Technologie Amont (PTA), the clean room facility in Spintec.
I will focus on the specific process used to fabricate MTJ nanopillars on Si_3N_4 membranes, for STXM imaging. The STXM technique, explained in detail in Section 2.5.2, requires the transmission of x-rays through the devices. Standard Si wafers, generally used as substrates for the sample fabrication in spintronics, do not satisfy the transparency requirement, since they are too thick, around 500 nm, and would absorb all the transmitted x-ray photons. The chosen substrate is composed of a Si wafer on which a SiO_2/SiN thin film was deposited on both sides using oxidation followed by liquid vapor deposition. Through an etching process the Si can be removed in some areas in order to create suspended SiN membranes, transparent to x-rays. The membranes opening process is explained in detail in Section 2.1.1.
For the nanofabrication of MTJs I followed the standard process developed by the 'MRAM' group of Spintec, that has been optimized for the tools available in the PTA, in Grenoble. This process allows us to fabricate MTJ nanopillars electrically contacted on the top and the bottom in order to perform electrical measurement, with a diameter ranging from a few µm down to 50 nm.
The fabrication on top of SiN membranes rather than on Si, requires some modification of the above mentioned process. First of all, the fragility of the substrate requires an extreme care in the handling of the wafers during the whole nanofabrication process. The extreme care includes the sticking of the wafer on top of standard unpolished Si wafers with kapton tape whenever the fabrication steps consists in the usage of a tool where the substrate is exposed to a different pressure in the front and back face. The gradient of pressure could lead to the breaking of the membranes, and the consequent fell of the pillars that were being built on top of those. Secondly, the materials used for the nanofabrication, such as the hard mask used in the first step, the top contact materials and the material used for the MTJ stack itself, as well as their thicknesses, have to be chosen in order to provide the highest possible transmission of the x-rays. The standard MRAM process involves the use of a 150 nm thick Ta hard mask to protect the pillars during the etching and a Cr/Au top electrode deposited by evaporation. The Ta hard mask has been substituted by a 150 nm Ti hard mask, as Ti has a lower absorption than Ta for the energy used for the STXM. Same for the Cr/Au that has been substituted by Ti/Al.

2.1.1 SiN membranes

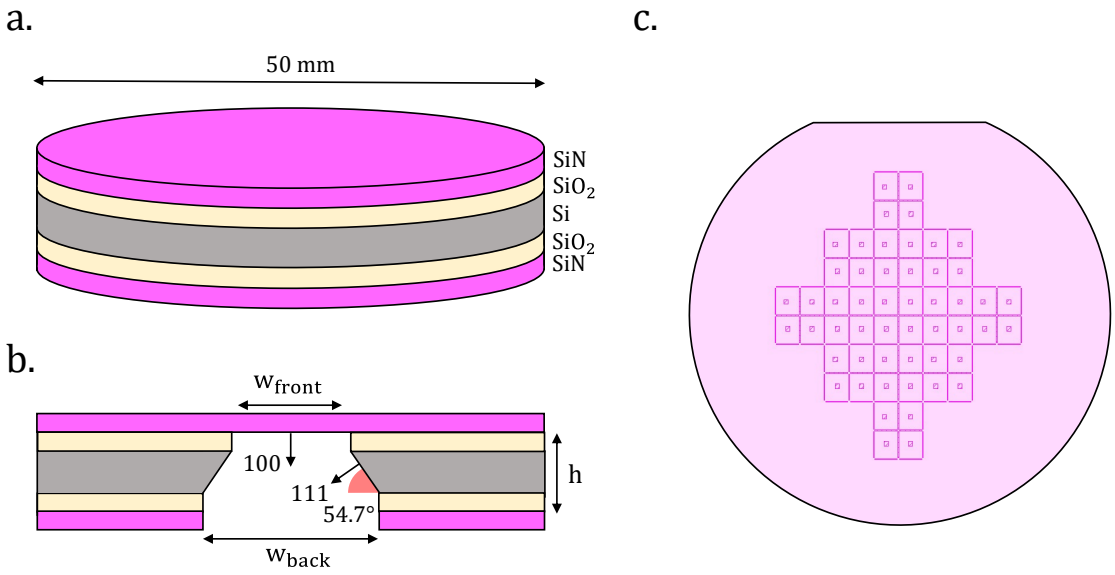

Figure 2.1: **SiN substrate** | a. Sketch of the 50 mm substrate used for the fabrication on SiN membranes. The 300 µm thick Si is covered on both sides by 150 nm of SiO_2 and 100 nm of Si_3N_4. b. Sketch of the result of the etching process to create suspended SiN membranes. c. Chessboard patterning of membranes and pre-cuts on the back of a 500 mm wafer.

The substrate used for the nanofabrication consists in a 2 inches wafer made of 300 µm of Si covered on both sides by 150 nm of SiO_2 and 100 nm of Si_3N_4 (see Figure 2.1a). The membranes are patterned on one of the two identical SiN faces, by either laser lithography or electron beam lithography, using positive resist. The membrane opening is done on the face that will be the back of the wafer for the rest of the nanofabrication process. The membrane layout is shown in Figure 2.1c. It is a chessboard pattern, that has been designed in order to maximize the number of membranes while limiting the fragility of the wafer. Together with the membranes, also some pre-cuts are patterned on the wafer in order to make the cleaving process after fabrication easier and safer. The size of the membranes and of the pre-cuts depends on the thickness of the Si substrate. The chemical etching of the membranes is performed using reactive ion etching (RIE): a first gas, SF_6, is used to remove the Si_3N_4, followed by a second gas, CHF_3, employed to etch the SiO_2. The underlying Si is not affected by the gas used and in this way it gets exposed only in the areas where the membranes will be opened, while the rest of the wafer is still protected by SiN and SiO_2 (see Figure 2.1b). The second step consists in a chemical etching using a KOH bath. KOH reacts with the Si in an anisotropic way, i.e. the etch rate is strongly dependent on the crystallographic planes. The etch rate of the Si along the (100) plane is large compared to the one along the (111) plane. The size of the membranes to pattern on the back face of the wafer w_{back} can be calculated as follows:

$$w_{back} = w_{front} + 2h\tan(\beta) \tag{2.1}$$

where $\beta = 54.7°$, is the angle between the crystallographic planes (100) and (111) of the Si, h is the thickness of Si and w_{front} is the targeted size of the membranes on the front side of the wafer, in general in between 50 and 80 µm. The KOH etching stops when it reaches the SiO_2 layer. To create suspended SiN membranes, the remaining SiO_2 is etched using a bath of HF. The schematic of the wafer after the etching process is observable in Figure 2.1b.

2.1.2 Deposition of magnetic stack

Once the substrate has been patterned with membranes, the magnetic stack can be deposited. The deposition technique used for the samples described in this thesis is magnetron sputtering, a physical vapor deposition technique. Magnetron sputtering is performed under high vacuum condition (10^{-8} mbar). In the main chamber of the sputtering machine, an Ar plasma is generated via either DC or RF excitation and it is attracted toward the target containing the material to be deposited, positioned on cathode. The atoms are physically removed from the target by the plasma and they have enough kinetic energy to move toward the surface of the substrate where they condense and deposit atomistically, forming a thin film. An oxidation process for the deposited materials as needed for the MgO barrier used for the MTJs is also possible by extracting the sample from the chamber, in an environment with controlled conditions where more oxygen is present. If the target is positioned along the axis of deposition the thickness of the thin film is homogeneous all over the substrate. A wedge of thickness is obtained by calculating the off-axis displacement of the substrate from the main deposition axis.

2.1.3 MTJs patterning

Pillar definition

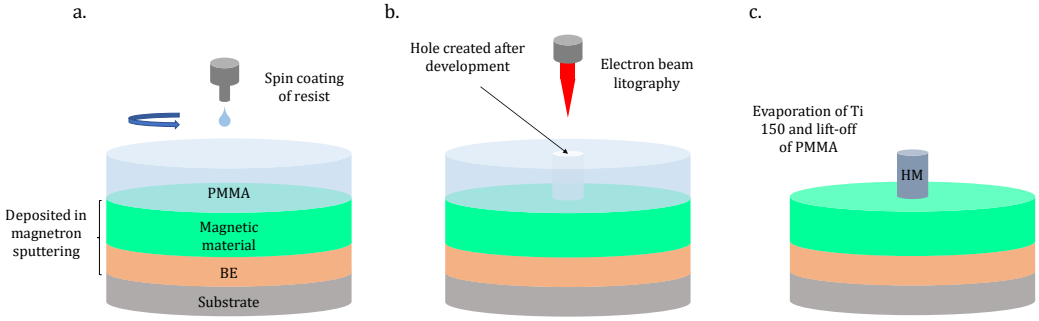

Figure 2.2: **Definition of the MTJ pillars** | a. Schematic of PMMA spin coating on the stack. b. Schematic of ebeam lithography and following development that generates a hole in the PMMA. c. Schematic of Ti 150 nm hard mask evaporation and following lift-off of PMMA resist.

Once the magnetic stack has been deposited on top of the substrate wafer, the patterning process can start. The first step consists in defining the MTJ pillars via electron beam lithography (ebeam). PMMA 4%, a positive e-beam resist, is spin coated on the wafer, baked at 180°C and exposed (Figure 2.2a). The chosen pillar size can

range from 5 µm down to 50 nm. During the lithography, an alignment is performed using the membranes as a reference, in order for the pillars to be correctly placed in the membrane centers. Some alignment marks are also patterned to be used in the following steps of the process. After the lithography, the resist is developed, meaning holes are created where the pillars will be, as shown in Figure 2.2b. These holes are filled with a metal, that is deposited via evaporation, in our case 150 nm of Ti, that is acting as a hard protective mask for the pillars during the following etching steps. The resist is then lifted-off in acetone leaving the metal to protect only the pillars and the alignment marks (see Figure 2.2c).

The magnetic stack is then etched using Ion Beam Etching (IBE), a physical etching technique that uses a plasma to physically remove atoms from the target. The etching is performed at an angle of 35° with respect to the substrate plane, in order to limit the re-deposition of etched atoms on the substrate. After the etching, a trimming is done at an angle of 80° normal to the substrate in order to remove redeposited atoms to prevent shortcuts along the walls of the pillars. During the etching, a mass spectrometer (SIMS) counts the atoms of the different species that get removed, showing on the computer screen a signal that allows to follow the etching process layer by layer as it can be observed in Figure 2.3b. The SIMS allows us to stop the etching process when desired, in our case on the Pt layer on top of the bottom electrode (BE). Not stopping the etching correctly means completely removing the bottom contact of the pillar, needed for electric characterization, hence this step is quite crucial for the fabrication.

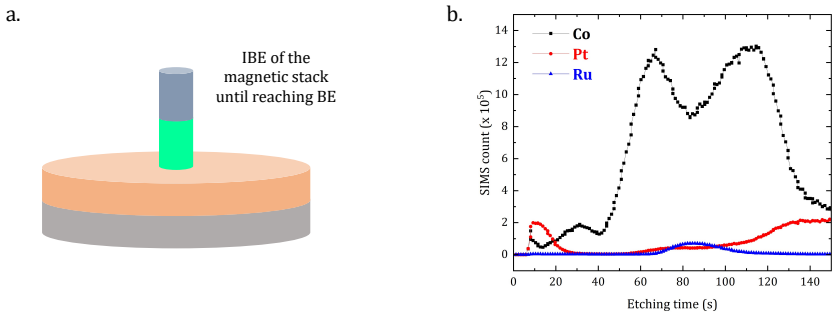

Figure 2.3: **MTJ stack etching** | a. Schematic of a pillar after the stack etching. b. SIMS signal generated by some of the different materials removed from the MTJ stack during the IBE process.

Bottom electrode definition

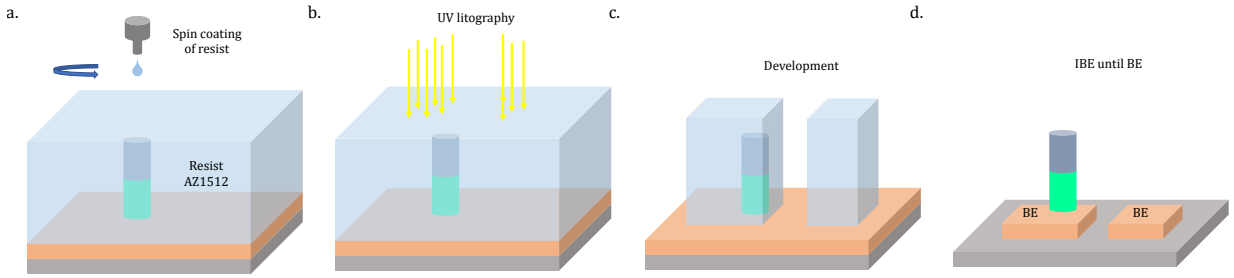

Figure 2.4: **Bottom electrode definition** | a. Schematic of positive resist spin coating. b. UV lithography. c. Development after UV lithography process, the remaining resist protects the area that will not get etched. d. Result of the etching process of BE and lift-off.

Once the pillars are defined, the definition of the bottom contact follows. To pattern the BE, the wafer is once again spin coated with a positive UV resist and exposed to UV light in the optical lithography tool (see Figure 2.4a and b). The alignment of the BE with the pillars is done thanks to the alignment marks previously patterned on the substrate. After the development, the resist remains only in the areas where the BE is defined, as it can be observed in Figure 2.4c. The rest of the material is etched once again using IBE, until the substrate is reached (Figure 2.4d). It is important to properly remove all the materials belonging to the BE, otherwise there is a risk for pillars to be short circuited. Because of this risk, the resistance of the wafer is checked with a multimeter when the etching is completed. Over-etching can cause the membranes to break, but since the thickness of SiN is 100 nm, the error margin is large enough not to make it a tricky step. What can be more problematic in this step is the risk of burning the resist protecting the BE due to heating, since the removal

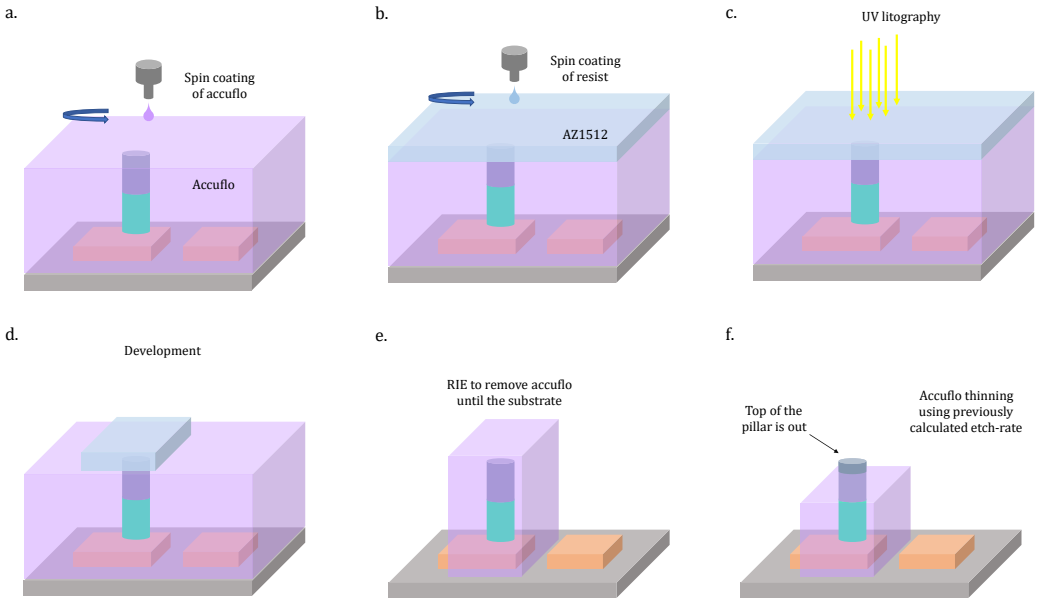

Figure 2.5: **MTJ pillar encapsulation** | a. Accuflo spin coating and baking. b. Resist spin coating. c. UV lithography of the accuflo windows. d. Development, the resist remains only on top of the windows. e. Reactive ion etching of the accuflo. f. Second RIE to expose the top of the pillar.

of all the material composing the magnetic stack can take several minutes, making it harder to lift it off after. If there is remaining burnt resist on top of the pillar, there is a risk of generating an opening in the electrical circuit because the top electrode cannot contact it. A solution that I found to reduce the risk of burning the resist is to etch in intervals of few seconds leaving the substrate to cool down in between one etching interval and the following.

Pillar encapsulation

Once the resist protecting the BE has been removed in acetone, the pillars get encapsulated in order to create an insulation in between the top and the bottom electrodes. To this end, an organic polymer called Accuflo is used. This type of material, once spin coated, gets baked at a temperature up to 250°C, in order to planarize it, dissolve the solvants and make it harden. Accuflo is chosen as insulating material for the pillars as it can get planarized, meaning it creates a uniform thickness on top of the sample. It also cannot be etched by acetone, which is still used during the rest of the process. Once the accuflo is spin coated all over the wafer, on top of it, a positive resist is spin coated once again and exposed to UV light everywhere but on some square regions around the pillars (see Figure 2.5a, b and c). The accuflo is then etched with an O_2 - Ar plasma in the RIE tool until it is removed everywhere but on the regions around the pillars where it is protected by the resist (see Figure 2.5d and e). The RIE, is a chemical etching tool, that differently from the IBE, uses specific gases to chemically react with the etched materials, removing them. In the RIE tool, an interferometer is used to measure the etching rate, by recording the oscillations while the material is getting etched. The interferometer allows us to measure the time needed to etch the accuflo from top to bottom. The accuflo thickness is measured on the accuflo windows remaining after the etching process around the pillars by mean of a profilometer, and it is in general around 500 nm. The profilometer is a tool that allows us to measure nanometric thicknesses by following the profile of a sample along a line using a tip. The etch rate is obtained by dividing the thickness measured by the etching time. The calculation of the etch rate is a crucial step for the success of the fabrication process. Indeed, the following step consists in a second etch of the accuflo in order for the pillar tip to stick out while still maintaining an insulation between the top and bottom contacts. Knowing the thickness of the pillar and of the deposited hard mask on top of it, the targeted thickness of accuflo is around 100 nm, and the etching time can be calculated thanks to the previously measured etching rate. The result of the pillar encapsulation can be seen in Figure 2.5f.

Top electrode definition

The last step consists in the patterning of the top electrode (TE). It is done using a reversible resist, meaning that the resist goes from positive to negative when exposed twice to the UV light. The first exposure is done with a mask where the top contacts are defined, that gets aligned with the present patterns on the sample by mean of the alignment marks once again (see Figure 2.6a, b and c). After the development, the TE materials,

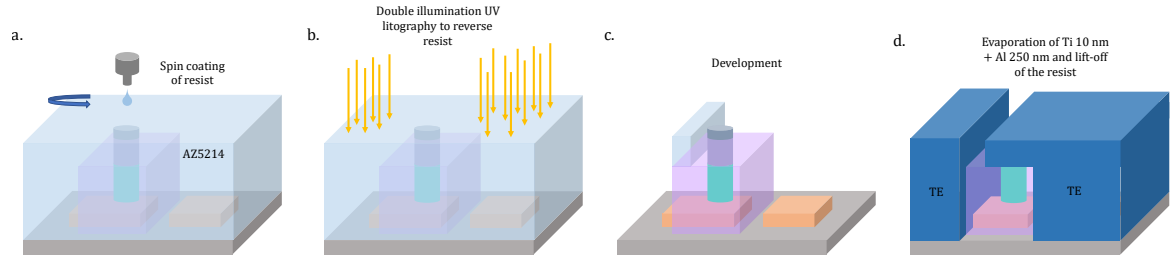

Figure 2.6: **Top electrode definition** | a. Schematic of positive resist spin coating. b. UV lithography and second exposure to reverse the resist. c. Development after UV lithography. d. Deposition of Ti 10 nm + Al 250 nm for the TE.

in our case 10 nm of Ti followed by 250 nm of Al, are deposited via physical evaporation in the holes created on the resist by the optical lithography. The resist is then lifted off in acetone and it carries away the overlying metal. The sample is ready to be tested. The final result schematic of the nanofabricated pillars is shown in Figure 2.6d.
During the nanofabrication process, the correct execution of the steps is controlled via both optical microscope and scanning electron microscope (SEM) that is used to have a more zoomed look on the pillars. Some images taken with both of this tools during the patterning can be observed in Figure 2.7.

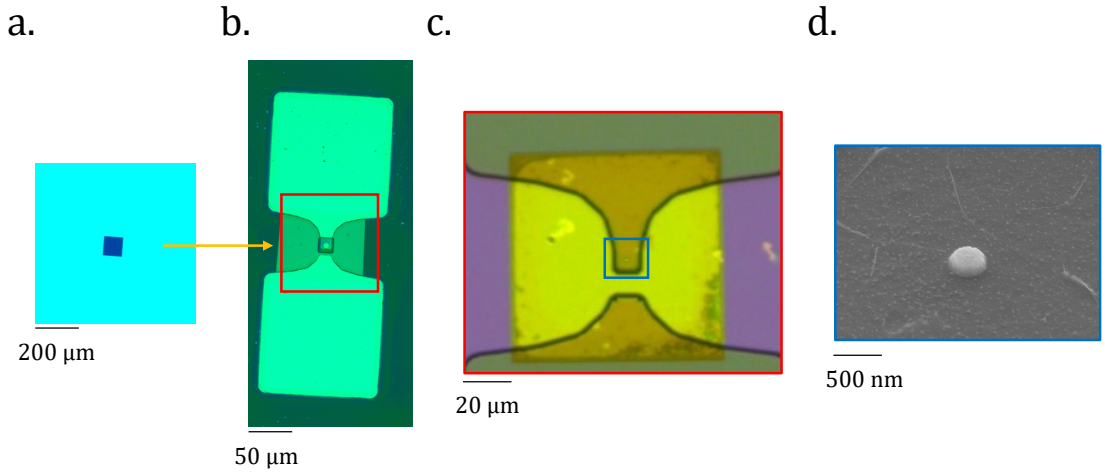

Figure 2.7: **Microscopy and SEM images of the MTJ nanofabrication** | a. Image of a SiN membrane on the substrate before the start of the nanofabrication process, taken with the optical microscope. b. Optical microscope image of a device on top of a membrane after the accuflo thinning step. c. Zoom on a pillar on top of a membrane taken with optical microscope after the bottom electrode etching step. d. SEM image of a pillar after the accuflo etching.

2.2 Electrical characterization of MTJs

2.2.1 Manual prober

After the nanofabrication of the MTJ pillars, the next step is their electrical and magnetic characterization. This is performed in a manual prober station, that allows us to electrically characterize both the pillars lying on top of the SiN membranes and those that are not. The prober station has a flat holder where the sample is placed. The holder can be moved through some screws in both x, y and z directions. A microscope placed on top of the flat holder is used to have a zoomed view of the sample in order to manually contact the pillars. The electrical contact is done through a prober that present three tips, ground/source/ground (GSG). The tips have the same pitch as the MTJ electrodes, since they were designed for measuring devices nanofabricated following the standard MRAM process. The prober is manually placed on the desired device since its motion is possible also in x, y and z direction. The source and one ground of the prober are contacted to the device that in this way gets electrically connected. The prober is connected to a sourcemeter through which it is possible to apply current or voltage and measure at the same time the resistance of the device. At the same time to perform the magnetic characterization, some coils connected to an electromagnet are placed below the holder, that allow us to generate magnetic field both IP and OOP. For our experimental measurements only the OOP

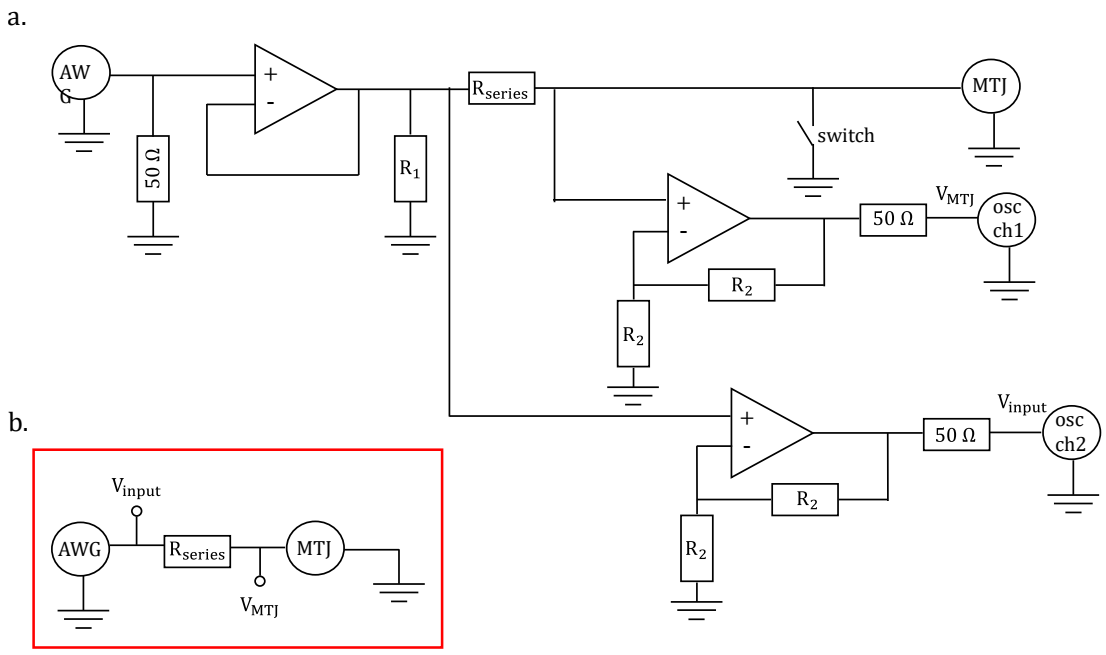

Figure 2.8: **Electronic circuit connected to the manual prober for electrical measurements on MTJs** | a. Schematic of the electric circuit implemented to measure in parallel the input voltage and the voltage drop on the MTJ. $R_1 = 1.2$ kΩ, $R_2 = 249$ Ω and $R_{series} = 820$ Ω. b. Equivalent circuit of the one in a. in terms of ideal transfer function.

magnetic field is used, therefore the sample holder is placed in a precise z position and the tip of the prober in a precise x and y position, where the OOP component of the generated magnetic field is the maximum, while at the same time the IP components are zero. After the calibration, the prober is only moved along the z direction to contact the sample, while the holder can still be moved along x and y. Some LabView programs have been written to simultaneously swipe the magnetic field and measure electrically the device. In this way it is possible to automatically perform magneto-electrical measurement on the device like its hysteresis loop, R vs H characterization, and several others. The prober is a useful tool during the preparation for a beamtime, as devices can be electrically characterized before the imaging experiments.

2.2.2 Implementation of manual prober for RC measurement

To perform the reservoir computing measurements (see chapter 6), the manual prober station was equipped with some additional tools. These measurements require the application of an arbitrary voltage input to the selected MTJ while simultaneously recording the resistance variation of the device induced by the input signal under a fixed magnetic field. To this end, the electronic circuit shown in Figure 2.8a has been implemented. The input voltage signal is generated by an Arbitrary Waveform Generator (AWG) and it passes through a buffer amplifier alimented at 5 V. The input impedance is 50 Ω, to match the output impedance of the AWG in order to avoid reflections. The entrance buffer provides a bandwidth of 500 MHz at 200 mV_{PP} and it is operational for input voltages lower than ±5V. After the entrance buffer a resistor with the value of 820 Ω is placed, chosen in order to reduce the RC component of the circuit to the minimum while maintaining a low noise on the resistance measurement on the device for low values of input voltage. The electronic circuit is then directly connected to the GSG prober to which the device can be contacted. A switch allows to disconnect the MTJ even when the GSG prober is properly landed on the device. Two buffers with a gain of 2 are connected before and after the series resistor to allow the simultaneous measurement of the input voltage signal and the voltage drop on the MTJ using an oscilloscope. The two resistors R_2, with a value of 249 Ω, are put to double the gain of the amplifier. Two channels of an oscilloscope are connected with a 50 Ω input impedance allowing the real time measurement of the resistance of the device. The circuit is equivalent to the one shown in Figure 2.8 as the attenuations are negligible:

$$R_{MTJ} = \frac{R_{series}}{\left(\frac{V_{input}}{V_{MTJ}} - 1\right)} \tag{2.2}$$

where R_{MTJ} is the resistance of the contacted device to be measured, R_{series} the series resistance, V_{input} the voltage input generated by the AWG and V_{MTJ} the measured voltage drop on the device.

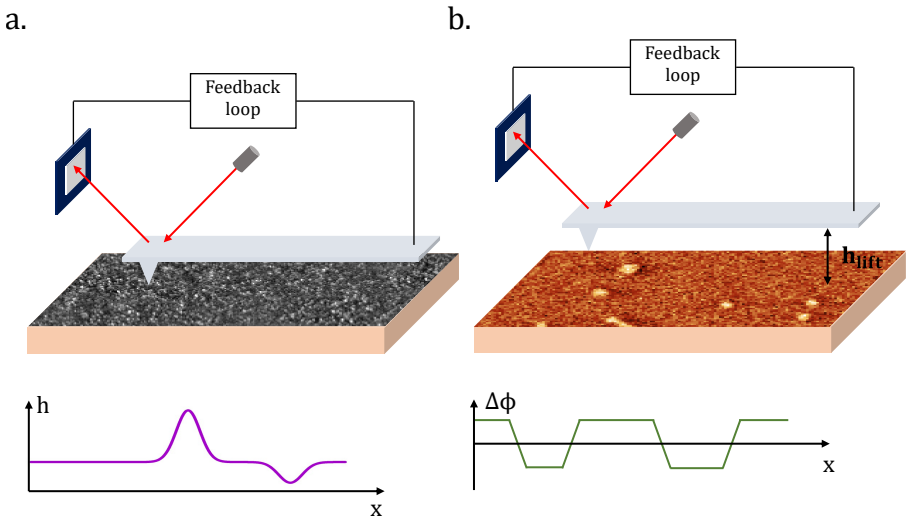

Figure 2.9: **Magnetic force microscopy** | a. Schematic of the MFM tapping mode. The height of the tip on the sample is controlled with a feedback loop by monitoring the change in oscillation and frequency of the tip in order to keep them constant. b. Schematic of the second passage of MFM tip. The height of the tip on the sample is fixed while the interaction of the magnetic stray field coming from the sample alter the phase of the tip oscillation. The feedback loop is used to bring back the tip to the initials resonance conditions.

2.3 Magnetic force microscopy

The magnetic force microscopy (MFM) is a tool that is used to probe the magnetic structure of a thin film. It is a specific mode of use of an atomic force microscopy (AFM). In an AFM, the key element is a sharp tip mounted on top of a cantilever. The cantilever is connected to a piezoelectric element that allows its motion in x, y and z direction. A laser is focused on top of the cantilever that deflects it. The reflection of the laser coming from the cantilever is recorded by a detector. The sample is mounted on a stage that can be moved in x, y and z directions. Depending on the mode of use of the AFM, the tip is interacting with the sample to probe different forces. The interaction between the tip and the sample is reflected into a bending or a motion of the cantilever, hence in a deflection of the laser that is a recorded by the detector. Through an electrical feedback loop the cantilever is brought back to its equilibrium position.
MFM uses a ferromagnetic tip to probe the stray field of the sample. In general the tip is created by coating a non-magnetic sharp tip with magnetic layers. For MFM, the measurement procedure involves two scans. The first is operated in tapping mode and allows us to measure the topographic profile of the surface. The tip is brought very close to the surface of the sample to probe Van der Waals and electrostatic forces. The tip oscillates near its resonance frequency, and the interaction with the surface generates a change in the frequency and amplitude of the oscillations. The electric feedback loop controls the tip-sample distance by keeping constant the frequency and the amplitude of the oscillations of the tip. An image of the surface can be reconstructed depending on the height of the tips in different areas. A schematic of the tapping mode measurement can be seen in Figure 2.9a. During the second scan, the tip is kept at a fixed lift-height away from the sample surface in order for the van der Waals and electrostatic interactions to be negligible. The tip is oscillating close to the resonant frequency of the cantilever. When the stray field from the sample interacts with the magnetic moment of the tip, the resonance frequency of the tip is shifted, and the changes in phase and amplitude of the oscillation are detected. The feedback loop is used to bring back the tip to its initial resonance conditions. The image of the magnetization of the sample is obtained by plotting the change in phase of the tip [151, 152, 153]. With MFM a typical resolution of 30 nm can be achieved. Schematic of the magnetic phase measurement can be observed in Figure 2.9b.
A drawback for the use of the MFM is the mutual interaction between the tip and the sample, meaning that the tip itself through its stray field can affect the magnetization of the sample, perturbing the measurements.

2.4 Magneto-optical Kerr effect

When a linearly polarised light impinges on a light-absorbing surface, its reflected component gets elliptically polarised. In the case of a ferromagnetic material, in addition to the normal reflection component, a second orthogonal reflection component arises due to the magnetization of the sample. Overall, the reflected light is elliptically polarised with the major axis rotated from the azimuthal position of the incident beam plane. This effect is known as Kerr effect and it falls within the category of magneto-optical effects, i.e. those effects for

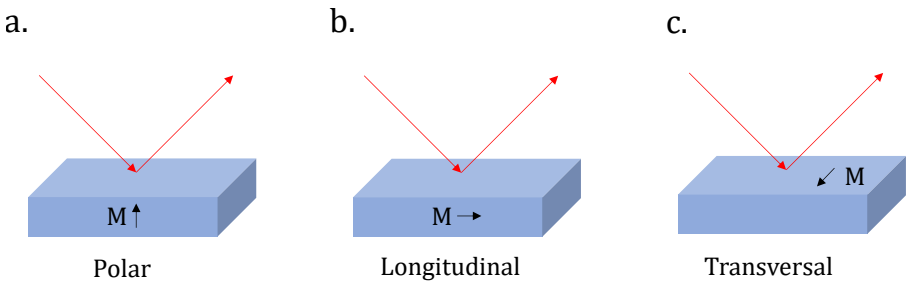

Figure 2.10: **Magneto-optical Kerr effect** | a. Schematic of polar MOKE. b. Longitudinal MOKE. c. Transversal MOKE.

which the properties of electromagnetic waves are altered due to a propagation in a material where magnetic fields are present.
The Kerr effect is divided into three different components, depending on three different geometries of the orientation of the magnetization of the sample with respect to the plane of incidence of the beam. The three geometries can be observed in Figure 2.10. The polar Kerr effect occurs when the magnetization of the sample is normal to the plane of the reflecting surface. In the longitudinal and transverse geometries the magnetization is parallel to the plane of the reflecting surface, respectively in the plane of the incident beam and perpendicular to it. In the first two cases the plane of polarisation of the reflected beam is rotated proportionally to the magnetization of the surface. In the third geometry there is no rotation but a change in the reflectance of the surface that is once again proportional to the magnetization.
The nanoMOKE [154] is an instrument that exploits the Kerr effect to characterize the magnetic properties of wafers. The nanoMOKE uses a linearly polarized red laser that is scanned and reflected on the sample surface. The reflected component collected by a detector where the Kerr component is measured, enabling the reconstruction of the magnetization of the sample. During the scan the magnetic field can also be modified by an electromagnet allowing for hysteresis loop measurements both IP and OOP.

2.5 X-ray microscopy techniques

2.5.1 X-ray magnetic circular dichroism

Dichroism is a term that refers in general to events for which photons are absorbed differently by a material depending on their polarization. The x-ray magnetic circular dichroism (XMCD), is a dichroism effect caused by anisotropies in the spins inside the material. XMCD is the difference in absorption for left and right circularly polarized light. When x-rays are absorbed by a material, they excite core electrons into empty states above the Fermi level allowing for the probing of the electronic and magnetic properties of the latters. The magnetic properties of 3d transition metals, Fe, Co and Ni, are determined by their 3d valence electrons. Due to the selection rule $\Delta L = \pm 1$, the main absorption edge for these materials is the L-edge, the one for which the electrons transit from 2p states to 3d states. Due to spin-orbit splitting, 2p levels are divided into $p_{1/2}$, singlet state for (L - S), and $p_{3/2}$, triplet state for (L + S). As a result, also the L-edge absorption gets split into the L_2 edge, transition from $p_{1/2}$ to d levels, and the L_3 edge, transition from $p_{3/2}$ to d levels [155].
The d shell of a transition metal has a spin moment that is given by the difference of the spin-up and spin-down electrons below the Fermi level. In the absorption process the spin-flip is not admitted, so spin-up electrons from the p shell can only get excited to spin-up electron in the d states and viceversa. The probability of an electron transition from p to d depends on the availability of empty states above the Fermi level, hence on the magnetization of the material. The x-rays can be either right-circularly polarized (RCP) or left-circularly polarized (LCP) carrying an opposite momentum. The momentum carried by the x-rays is transferred to the electron spin angular momentum via SOC following selection rules. It can be shown that at the L_2 edge LCP light excites with a probability of 75% spin-down electrons and of 25% spin-up electrons. On the L_3 edge instead the probability to excite spin-down electrons with LCP light is 37.5% and 62.5% that for spin-up electrons. The opposite probabilities on both edges are obtained with RCP photons as they carry the opposite momentum. In Figure 2.11a can be observed one example in which there are more spin-up empty states available than spin-down. LCP photons, which excite with higher probability spin-up electrons in the L_3 edge, get absorbed more than RCP photons, which on the opposite, favour the transition of spin-down electrons on the same edge (see Figure 2.11). On the L_2 edge the inverse situation happens, LCP photons favour the absorption of spin-down electrons while RCP photons favours the transition of spin-up electrons. By tuning the energy of the photons to the desired absorption edge, the XMCD contrast is reconstructed as the difference in absorption between LCP and RCP photons. The XMCD contrast is proportional to the projection of the magnetization along the x-ray

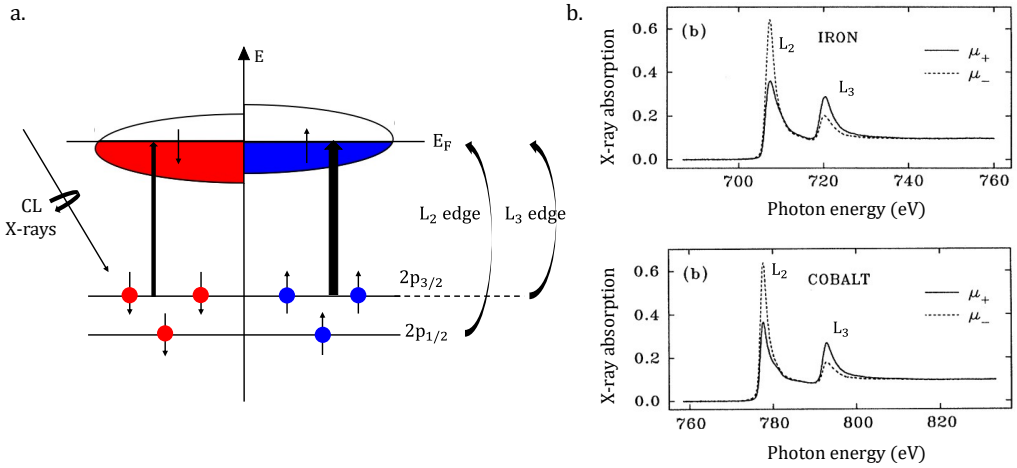

Figure 2.11: **X-rays magnetic circular dichroism (XMCD)** | a. Schematic of the electronic transition on L_3 edge generated by LCP x-rays. b. Absorption of x-rays for both Fe (top) and Co (bottom) on the L_2 and L_3 edges, for LCP and LCR polarized x-rays. The images have been adapted from [156].

beam direction. In Figure 2.11b, the absorption of LCP and RCP polarized x-rays in the L_2 and L_3 edges, for both Fe and Co can be observed. In a non-magnetic material the RCP and LCP photons would get absorbed with the same probability as the occupation of Fermi levels is identical for spin-up and spin-down electrons, resulting in zero net XMCD contrast.

2.5.2 Scanning transmission x-ray microscopy

Scanning transmission x-ray microscopy (STXM) is a scanning microscopy technique that allows for the creation of high-resolution images of the magnetization of a sample. To perform STXM, a monochromatic x-ray beam is focused and scanned across a sample. The beam first passes through a Fresnel zone plate (FZP), a system of alternating opaque and transparent concentric rings, that creates a diffraction pattern and focus the beam on the sample in a single spot. The width of the smallest diffraction ring on the FZP determines the resolution of the measurement. After the FZP, an order separating aperture (OSA) that is positioned close to the sample, filters out unwanted diffraction orders. The sample is raster scanned through the beam using piezoelectric motors in order to obtain an image. The transmitted light is collected by a photodiode point by point. A schematic of the STXM measurement setup can be seen in Figure 2.12a.
The same scan is performed twice, both with LCP and RCP light that gets absorbed with different probabilities. The XMCD contrast is obtained by subtracting the two obtained images, allowing to visualize the magnetization pattern inside the sample. To perform XMCD, the energy of the x-rays has to be set to the desired L-edge using a monochromator. The L-edge energy depends on the material contained in the sample. For the experiments present in this work, the energy was tuned either on the Fe edge, at around 709 eV, or on the Co edge, around 780 eV. The achievable resolution by STXM is smaller than 25 nm. A more detailed schematic of how the *operando* STXM measurement are performed on the MTJ pillars is shown in Figure 2.12b.

2.5.3 Time-resolved STXM

The XMCD-STXM technique described in the previous section only allows us to get static images of the magnetization before and after the application of external stimuli. It is possible to exploit the synchrotron light also to obtain sequence of images of the response of the magnetization while it gets excited with current or voltage pulses, so a time-resolved image of the magnetization dynamics.
The electrons circulate inside the synchrotron ring in bunches. When they pass through an insertion device, either a bending magnet or an undulator, their trajectory is bent and x-rays are emitted. As the passage of the electrons inside the ring happens in bunches, the x-rays emission follows the same periodicity. In Bessy synchrotron in Berlin, in the usual multibunch mode, the generation period is 2 ns (500 MHz), for an emission temporal width of 100 ps. The transmitted intensity per x-ray bunch is in the order of a single photon and it is recorded by an avalanche photodiode. Conventionally, the time-resolved synchrotron dynamics exploits the stroboscopic x-ray illumination, thereby the pump-probe experiments would be conducted with a time-scale of 2 ns. However, this limits the observation of dynamical states with excitation at frequencies multiple of 500 MHz.
To solve this problem, the method adopted in the MAXYMUS beamline in Berlin [157, 158, 159], consists in sorting the intensity result from each pulse into a different time-channel synchronized with an external electrical

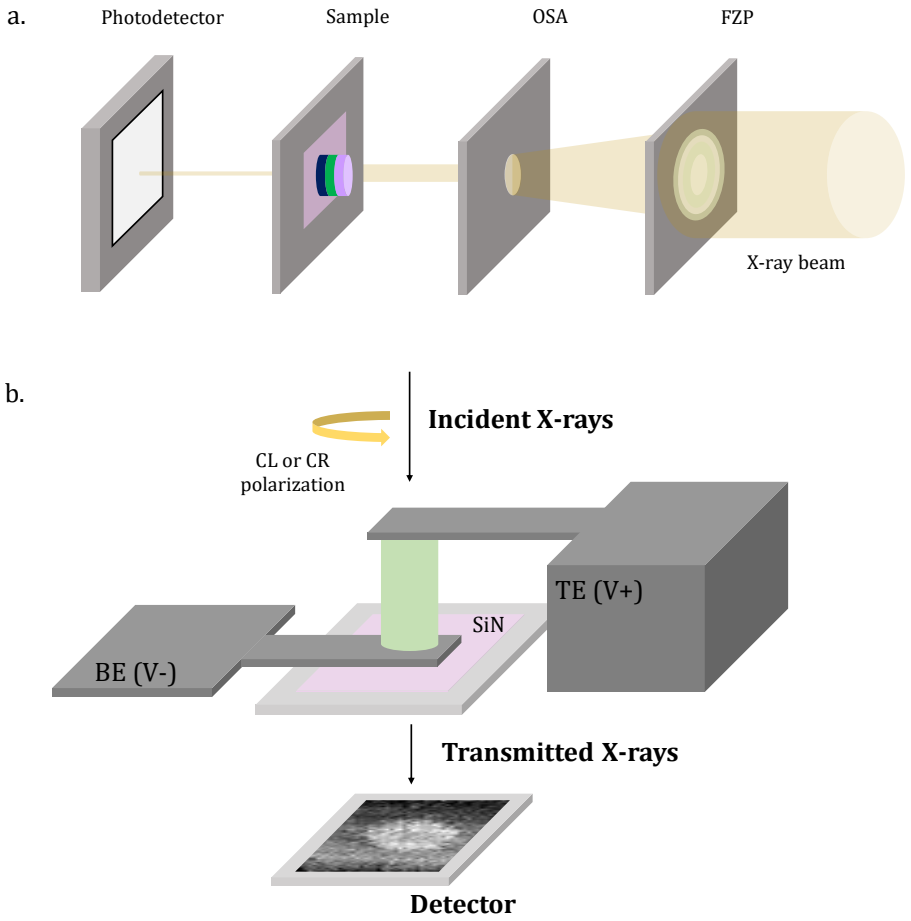

Figure 2.12: **Scanning transmission x-ray microscopy (STXM)** | a. Schematic of the components to perform STXM experiments. The FZP is illuminated by the x-ray beam and focus it on the OSA. The light transmitted by the aperture is illuminating the sample and a detector collects the transmitted radiation. b. Schematic of the absorption of LCP or RCP x-rays through the MTJ pillar. As the membrane below the pillar is transparent to x-rays, they are transmitted to the detector allowing for the reconstruction of the XMCD contrast.

pulse. This is achieved by using a fast signal discriminator for the detection of single x-ray photons and a coupled FPGA board that sorts the photon arrival events into different channels (up to 2048) according to the arrival time relative to the excitation of the sample system. By discriminating the signal obtained from different x-ray bunches, the dynamics of the system is reconstructed with higher temporal resolution than the x-ray bunch period. To further improve the temporal resolution, a time shift τ is introduced with the synchrotron clock after every pumping event. An integer number M is chosen such that $\tau = 2\,\mathrm{ns/M}$, so after M pumping cycles the original time relation is restored. For this to work the pumping period $\mathrm{T_P}$ has to be related to the synchrotron period $\mathrm{T_S} = 2\,\mathrm{ns}$ by the following formula:

$$\mathrm{T_P} = \mathrm{T_S}\frac{\mathrm{N}}{\mathrm{M}} \tag{2.3}$$

where N is the total number of channels in the acquisition. N and M are chosen to be co-prime numbers to avoid degeneration. In this way, the light sent to every channel is provided by a different x-ray bunch. Once chosen the "magic numbers" M and N, the resulting τ provides the time resolution for the measurements as long as it is equal or longer than the pulse width of the x-ray flash 100 ps. When photons come in from a bunch, the photodetector is able to store them in the correct channel by keeping track of the phase shift. The images are obtained pixel by pixel. When the STXM is focused on a single pixel, the different channels are recording the response to the excitation each one at a different time, during the whole pumping time. The final result is a sequence of images, one every τ, for the whole $\mathrm{T_P}$. An example of the pump/probe technique with $\mathrm{N} = 11$ and $\mathrm{M} = 2$ is presented in Figure 2.13b. For this approach to work it is necessary that the dynamic image is highly reproducible, otherwise the phenomenon would be canceled out by the averaging.

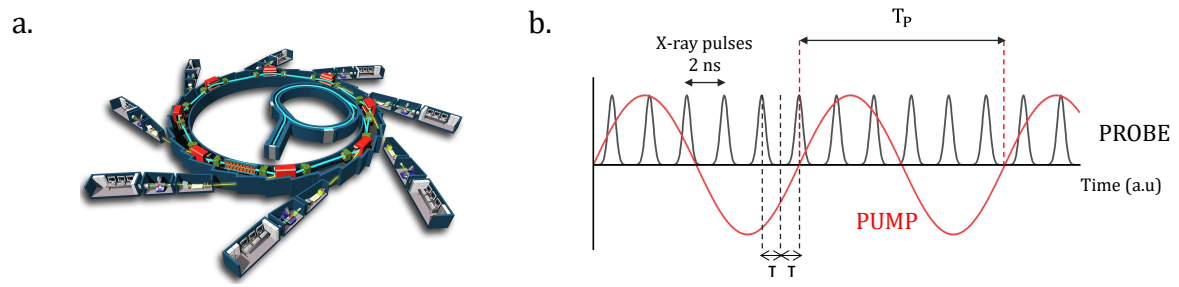

Figure 2.13: **Time-resolved STXM** | a. Schematic of a synchrotron. b. Example of the pump/probe technique. The photons arrive every 2 ns. The pump period is multiple of the probe period. In the example N = 11 and M = 2, so the $T_P = 11$ ns and τ, the shift after every bunch in between the pump and the probe, is equal to 1 ns.

2.5.4 X-ray photoemission electron microscopy

X-ray photo-emission electron microscopy (X-PEEM) is a technique to image photo-emitted secondary electrons excited by x-rays. When x-rays impinge on a sample, a primary absorption process occurs, with a transition of an electron from a core level to the valence band. This is the same mechanism explained for STXM in section 2.5.1 for the L-edge transition, in transition metals like Fe or Co. After the primary process, a secondary process called Auger decay happens. It consists in the filling of the core hole generated by the x-ray absorption by an electron coming from an intermediate state, in between the core and the Fermi level (see Figure 2.14a). For energy conservation, while the first electron goes to fill the core hole, a second electron, coming from an intermediate state in between the core and the valence band, is emitted from the material. The kinetic energy of this second emitted electron is given by the difference in between the core level and the intermediate state level. During X-PEEM experiments, the secondary emitted electrons are accelerated and collected using an electron microscope. As these electrons are originated from shallow intermediate states, PEEM is a surface sensitive technique. The mean free path of emitted secondary electrons is around 2 nm, so it is important to take into account the thickness of the capping layer on top of the magnetic layer when preparing the sample for X-PEEM, in order to avoid the absorption of all the secondary electrons before their collections.

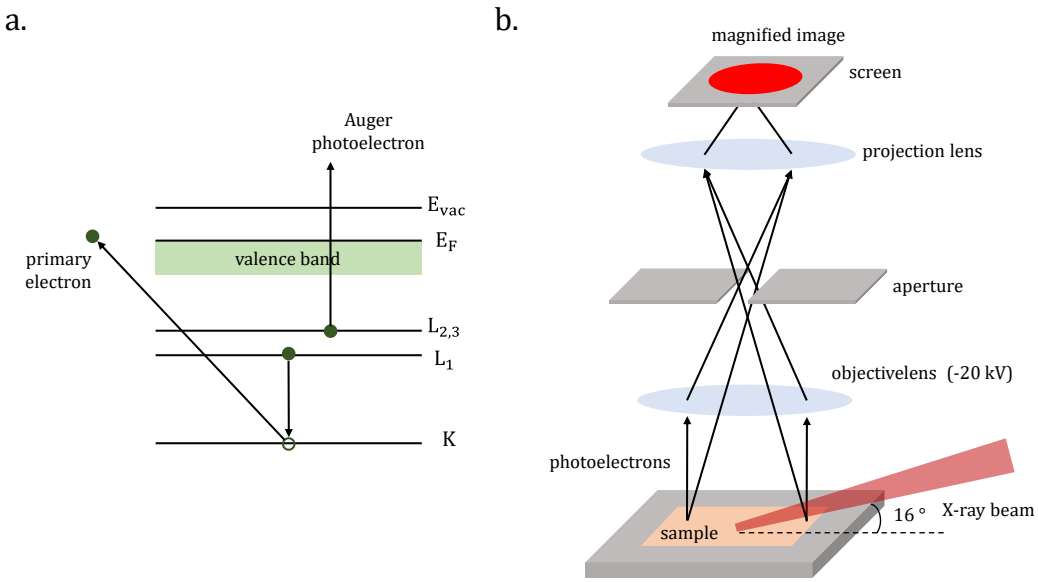

Figure 2.14: **X-ray photoemission electron microscopy (X-PEEM)** | a. Scheme of Auger photoelectrons emission. b. Schematic of X-PEEM setup. The emitted photoelectrons from the sample are collected by the objective lens, they pass through several optical elements and finally they imprint on a screen where the image is formed.

In Figure 2.14 is presented the microscope setup used to perform X-PEEM. The sample is placed in a ultra-high vacuum environment. A monochromatic beam of electrons, tuned at the energy required to induce the primary absorption of x-rays, is illuminating the sample, at an incidence angle of 16° degrees. A grazing incident angle is chosen to improve the resolution and contrast of the image as photoelectrons are emitted in a more directional way. The emitted electrons are accelerated by a strong field, in the range of 10-20 kV, toward the objective lens, that is called the cathode. The objective produces a magnified image of the sample that is further magnified

by a system of lenses and an aperture that prevents image aberrations onto an electrons-sensitive screen. The image on the screen is then recorded with a CCD camera [160, 161].
X-PEEM is a full field technique because the photoelectrons coming from different areas are collected simultaneously. As the x-rays absorption is dependent on the polarization (LCP or RCP) of the incident x-ray beam, once again it is possible to reconstruct the XMCD contrast by subtracting images obtained with the two different circular light polarizations. XMCD-PEEM has a high lateral spatial resolution, down to 25 nm, and the magnetic contrast obtained is proportional to the projection of the probed magnetization along the x-ray beam. As the incidence of the beam is at a grazing angle of 16° with respect to the sample surface, the contrast is larger for the IP component than for the OOP component.
In Figure 2.15 it can be observed how the properties of XMCD-PEEM were exploited to reconstruct the chirality of a DW structure [119]. A multidomain state in a Pt/Co/MgO film is imaged, where white and black lines emerge in the DWs, indicating respectively the magnetization being antiparallelly and parallelly aligned to the beam direction. This is a signature of a chiral Néel DW, as the magnetization rotates perpendicular to the plane of the DW. The change in contrast can be observed better in Figure2.15b, where the linescan represents the magnetic contrast along the direction of the beam. The peak and the valley correspond respectively to the white and dark lines seen in the XMCD image. From this scan we can deduce that the chirality generated by the DMI is left-handed.

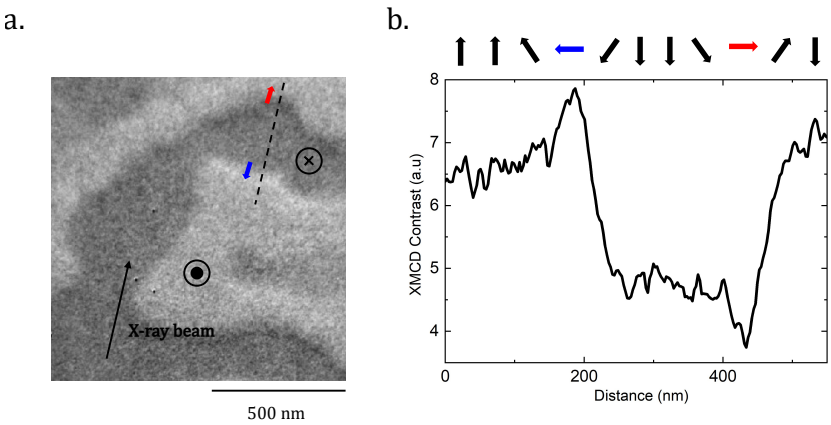

Figure 2.15: **XMCD-PEEM image of a Néel DW** | a. XMCD-PEEM image of a multidomain state in a Pt/Co/MgO film. When the DWs are perpendicular to the x-ray beam direction thin black and white lines appear, that correspond to the magnetization being aligned antiparallelly or parallelly to the x-ray beam. b. Linescan of the magnetic contrast along the dotted line in a.

Chapter 3

Fast current-induced motion in synthetic antiferromagnets

Contents

3.1 Antiferromagnetic skyrmions . . . 55
3.2 SAF systems . . . 57
3.3 Current-induced motion experiments . . . 59
3.3.1 SAF skyrmions diameter . . . 60
3.3.2 Magnetic contrast in the MFM experiments . . . 61
3.3.3 Observation of SAF skyrmions with X-PEEM . . . 61
3.4 Analytical model and micromagnetic simulations . . . 61
3.4.1 Analytical model . . . 61
3.4.2 Micromagnetic simulations of the current-induced motion . . . 63
3.4.3 Micromagnetic simulations on the inertial skyrmion dynamics . . . 65
3.4.4 Experimental magnetic properties . . . 65
3.5 Current-induced motion in Pt/Co/Ru FM stacks . . . 66
3.6 Discussion and conclusions . . . 66

3.1 Antiferromagnetic skyrmions

Skyrmions in FM layers suffer from several limitations that make applications unfeasible. First, as already pointed out in section 1.5.4.1, they are subjected to the skyrmion Hall effect, which is directly related to the skyrmion topology and deviates the trajectory of the skyrmion from that of the current direction. Skyrmions, when deviated from the current direction, get either bounced back or annihilated once reaching the edges of a track, which results in a loss of information. The amplitude of the effect, $\tan\theta_{\mathrm{SkH}} = \frac{\mathrm{G}}{\alpha\mathcal{D}}$, derived from the Thiele model, depends on the gyrotropic vector $\mathbf{G}$, on the dissipation matrix $\mathcal{D}$ and on the magnetic damping parameter α. We can rewrite the equation for the SkHA as $\theta_{\mathrm{SkHE}} = \frac{\alpha_{\mathrm{T}}}{\alpha}$ where $\alpha_{\mathrm{T}} = \frac{\mathrm{G}}{\mathcal{D}}$, and that for the skyrmion velocity as $\mathrm{v_{sk}} \sim \frac{1}{\sqrt{\alpha^2+\alpha_{\mathrm{T}}^2}}$. We can observe that the SkHE generates an additional damping parameter α_{T} that has a direct effect on the skyrmion velocity. This is a second limitation to the application of FM skyrmions, namely a limit in their velocity due to the current-induced motion coming from their topology, that can hardly exceeds 100 m/s [120, 130, 14, 15, 16, 17, 162, 163].
A possible way to address these limitations is the use of antiferromagnetic skyrmions, i.e. magnetic skyrmions in antiferromagnets [164, 133, 165, 166, 167, 168, 169]. Antiferromagnetic skyrmions are coupled skyrmions from different sublattices in the same material, each with opposite core polarity, thus opposite topological charge. The result is a net topological vector equal to zero, therefore a cancellation of the skyrmion Hall effect. The predicted current-induced motion for AF skyrmions is over 1000 m/s. A stable fractional antiferromagnetic skyrmion lattice was observed via neutron scattering in bulk $MnSc_2S_4$ [170]. Antiferromagnetic half skyrmions were also stabilized and observed in bulk Fe_2O_3 [171] and were imprinted in a thin film of IrMn from a FM layer using exchange bias [172]. A schematic of an antiferromagnetic skyrmion can be observed in Figure 3.1a.

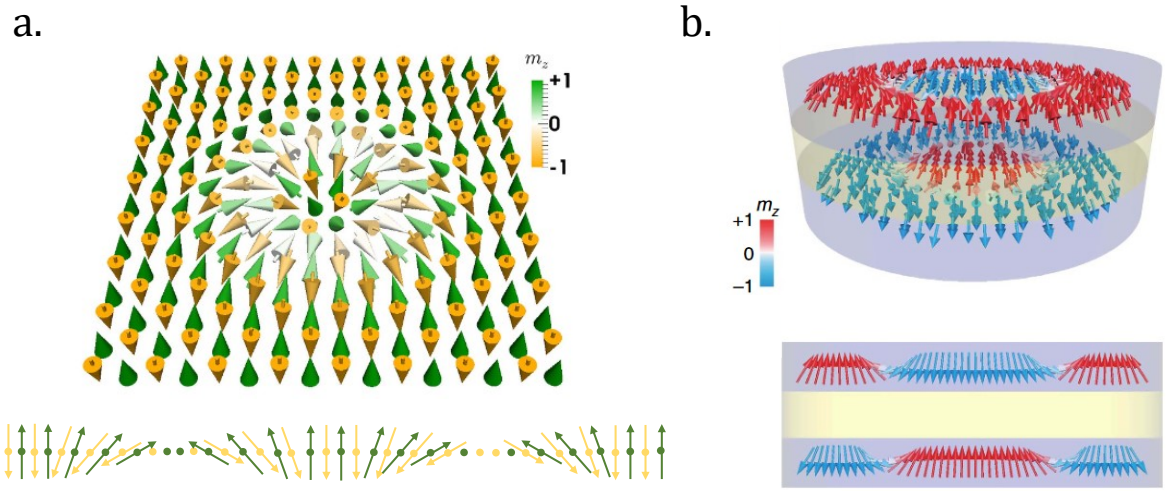

Figure 3.1: **Antiferromagnetic skyrmions** | a. Schematic of an AFM skyrmion in a material where the two sublattices (in green and in yellow) are AF coupled. Adapted from [164] b. Schematic drawing of a SAF skyrmion. The skyrmions in the two ferromagnetic layers are AF coupled, hence they show opposite magnetization. The skyrmions in the two FM layers present opposite core polarity but same chirality. From [132].

A group of materials that raised interest for antiferromagnetic skyrmions are synthetic antiferromagnets (SAF) [132, 173, 174, 175]. SAFs are composed of two FM layers that are AF coupled through a NM layer exploiting the RKKY interaction. Figure 3.1b shows a schematic of two AF coupled skyrmions in a SAF. Each skyrmion is stabilized in a FM layer and, since the layers are AF coupled, their magnetizations are opposite as well as their core polarities, while their chirality remains the same. The result is a net gyrotropic vector equal to zero, hence a cancellation of the skyrmion Hall effect.
Legrand *et al.* [18] demonstrated the RT stabilization of antiferromagnetic skyrmions in Pt/Co/Ru based multilayers. The Ru layer provides the RKKY coupling in between the two Co layers hosting the skyrmions. The materials were chosen as the Pt/Co interface has one of the highest DMI for sputtered systems, and the thickness of Co was tuned in order to be close to the reorientation transition from OOP to IP, where the anisotropy is lower. As the SAF presents a compensated magnetization, it is hard to nucleate skyrmions by applying an external magnetic field. The strategy adopted to nucleate the skyrmions in the SAF, is the use of a bias layer, i.e. another magnetic layer coupled ferromagnetically with the bottom layer of the SAF via exchange bias. MFM was used for the imaging of the magnetic texture. They observed that without the bias layer, stripe domains were stabilized while, once the bias layer was added, skyrmions were nucleated (see Figure 3.2a).

Juge *et al.* [19] used XMCD-STXM to image skyrmions in a fully compensated SAF (see Figure 3.2b). The stack was a sputtered multilayer $[Pt/FM1/Ru/Pt/FM2/Ru]_2$ where FM1 is Co/NiFe/Co and FM2 is Co. The thicknesses of the two layers were adjusted to fully compensate the net magnetization while placing the system close to the IP/OOP spin reorientation transition, to have a low anisotropy. The different elements composing the two FM layers allow to distinguish the skyrmions in the two materials, by tuning the x-ray energy either to the Fe or to the Co absorption edges. Deterministic zero-field skyrmion nucleation was achieved by localized current injection through triangular gold injectors patterned on the sample. Different current polarities could deterministically generate a nucleation and a subsequent annihilation of the skyrmion. Ultrafast laser pulses applied from the uniformly magnetized state at zero applied magnetic field were also used for nucleation.

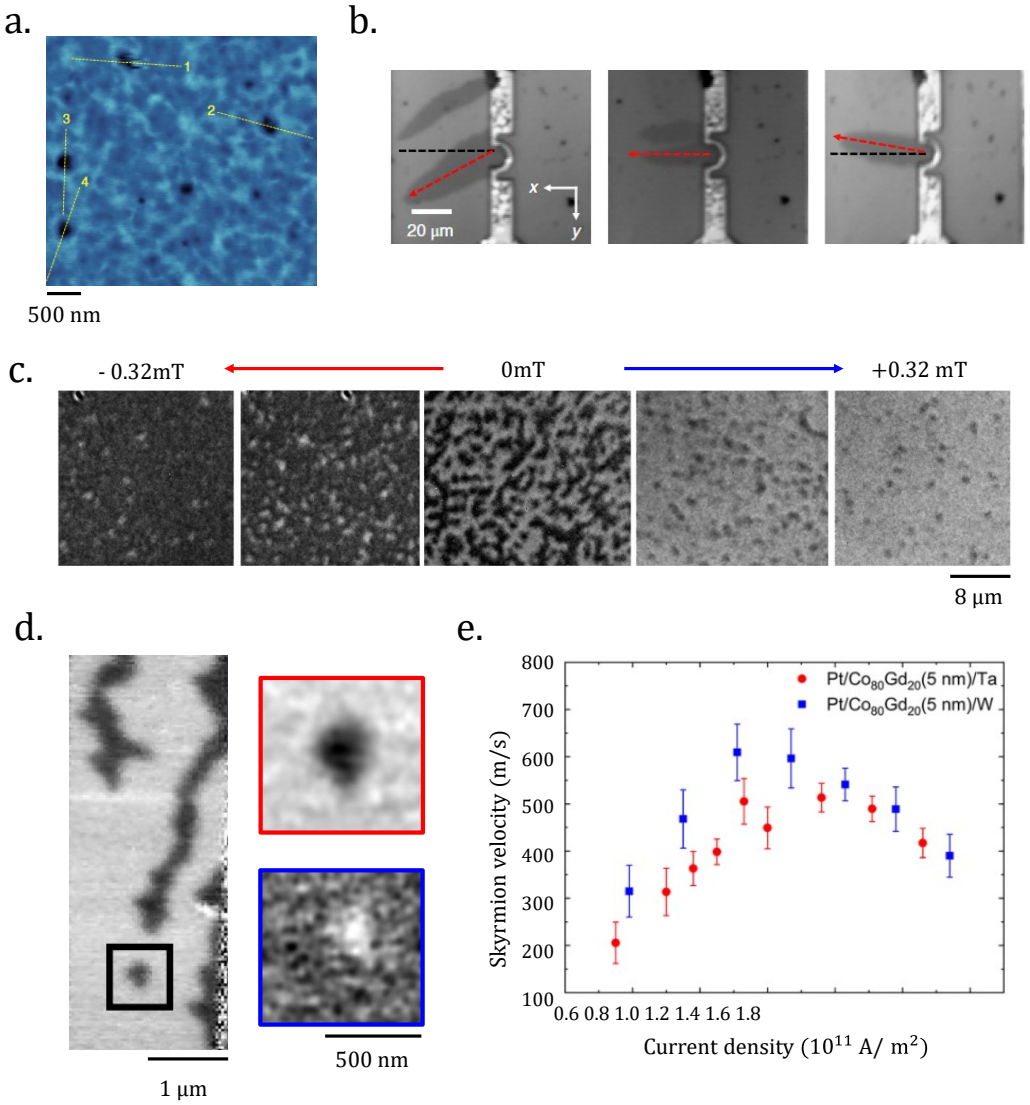

Figure 3.2: **Experimental observation of SAF skyrmions** | a. Room temperature MFM observation of skyrmions in Pt/Co/Ru SAF + bias layer system under applied magnetic field of 100 mT. Adapted from [18]. b. Elongation of a skyrmionic bubble due to current applied at different temperature in a GdCoFe ferrimagnetic stack. The magnetization of the stack varies with the temperature: in the central image the stack is fully antiferromagnetic and the SkHE vanishes compared to the left and right images where it remains visible. From [176]. c. MOKE observation of domains pattern and skyrmions at different magnetic fields of -0.32, -0.2, 0, 0.2, 0.32 mT from left to right in a non compensated SAF stack $Ta/Pt/Co(0.2)/Co_{0.19}Fe_{0.56}B_{0.25}(0.925)/Ir/Co(0.375)/Co_{0.19}Fe_{0.56}B_{0.25}(0.6)/W/Ru$ with thicknesses in nm. From [177]. d. XMCD-STXM image on the Co edge showing an isolated skyrmion (left) at zero field in $[Pt/Co/NiFe/Co/Ru/Pt/Co/Ru]_2$ compensated SAF. The images in the red and blue box are ptychography reconstruction of the skyrmion in the black boxes on the left image, acquired respectively on the Co and Fe edge. From [19]. e. Measured skyrmion velocity for ferrimagnetic films of Pt/CoGd/Ta and Pt/CoGd/W as a function of the current density. From [178].

The demonstration of current-induced dynamics in SAF systems remains a challenge. Some progress were done

by investigating ferrimagnetic materials. Hirata *et al.* [176] showed that the angle between the current direction and ferrimagnetic bubbles in GdFeCo/Pt vanishes at the compensation temperature where the net magnetic moment cancels out and the film becomes antiferromagnetic (see Figure 3.2b). Woo *et al.* [179] observed a reduced skyrmion Hall effect in GdFeCo ferrimagnetic film with respect to ferromagnetic systems in response to current pulses. The images of the skyrmions were taken via STXM. Enhanced velocities and reduced SkHA were reported by Dohi *et al.* [177] for skyrmionic bubbles in a SAF system compared to a similar ferromagnetic system (Figure 3.2c). Quessab *et al.* [178] observed vanishing SkHE and velocities up to 600 m/s in ferrimagnetic Pt/CoGd thin films (Figure 3.2d).
SAF systems combine several ingredients that make them interesting candidates for application as racetrack memories [13]: skyrmions can be stabilized and be moved efficiently with current, as they can have large PMA, strong interfacial DMI and SOT coming from the HM. The films are deposited via sputtering, which is an industrial compatible technique, and it could also be thought of integrating films with magnetic tunnel junctions for an electrical readout of the skyrmions.
In this chapter I will present our work demonstrating that skyrmions in compensated SAFs can be driven by spin orbit torque at velocities up to 900 m/s along the current direction, therefore without skyrmion Hall effect. We proved that the increase of the velocity is coming from the cancellation of the topological charge by comparison with two other samples built with the same materials as the SAF. We completed the results by comparison with an analytical model and with micromagnetic simulations of the system.

3.2 SAF systems

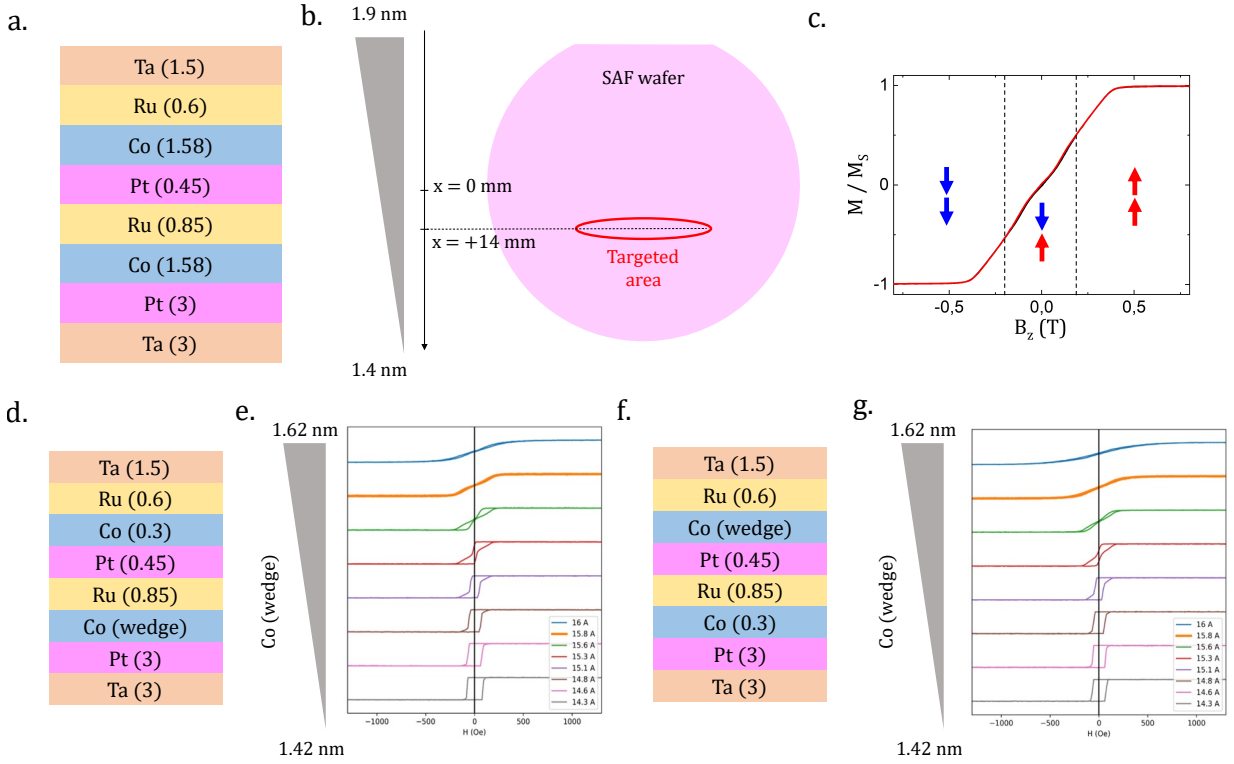

Figure 3.3: **SAF stack optimization** | a. Composition of the SAF stack. b. Sketch of the SAF wafer with the Co layer deposited as a wedge from 1.9 to 1.4 nm. The red circle marks the region where the targeted Co thickness for skyrmion stabilization is located. c. Normalized magnetic moment as a function of the OOP external magnetic field measured by vibrating sample magnetometry for the SAF sample. The black and red lines correspond respectively to decreasing and increasing magnetic field. The dashed line indicates the RKKY field. d. Schematic of the stack used to characterize the magnetic properties of the bottom Co layer. e. NanoMOKE hysteresis loops with external OOP field for the stack in d. f. Schematic of the stack used to characterize the magnetic properties of the top Co layer. g. NanoMOKE hysteresis loops with external OOP field for the stack in f.

The SAF multilayer used for the experimental measurements was optimized carefully and has the following composition: Ta(3)/Pt(3)/Co(1.58)/Ru(0.85)/Pt(0.5)/Co(1.58)/Ru(0.85)/Ta(1.5), nominal thicknesses in nm (see Figure 3.3a). The stack was deposited on a highly resistive Si substrate with its native SiO_2 via magnetron sputtering. The two Pt/Co layers are AF coupled through the Ru interlayer, via RKKY exchange coupling.

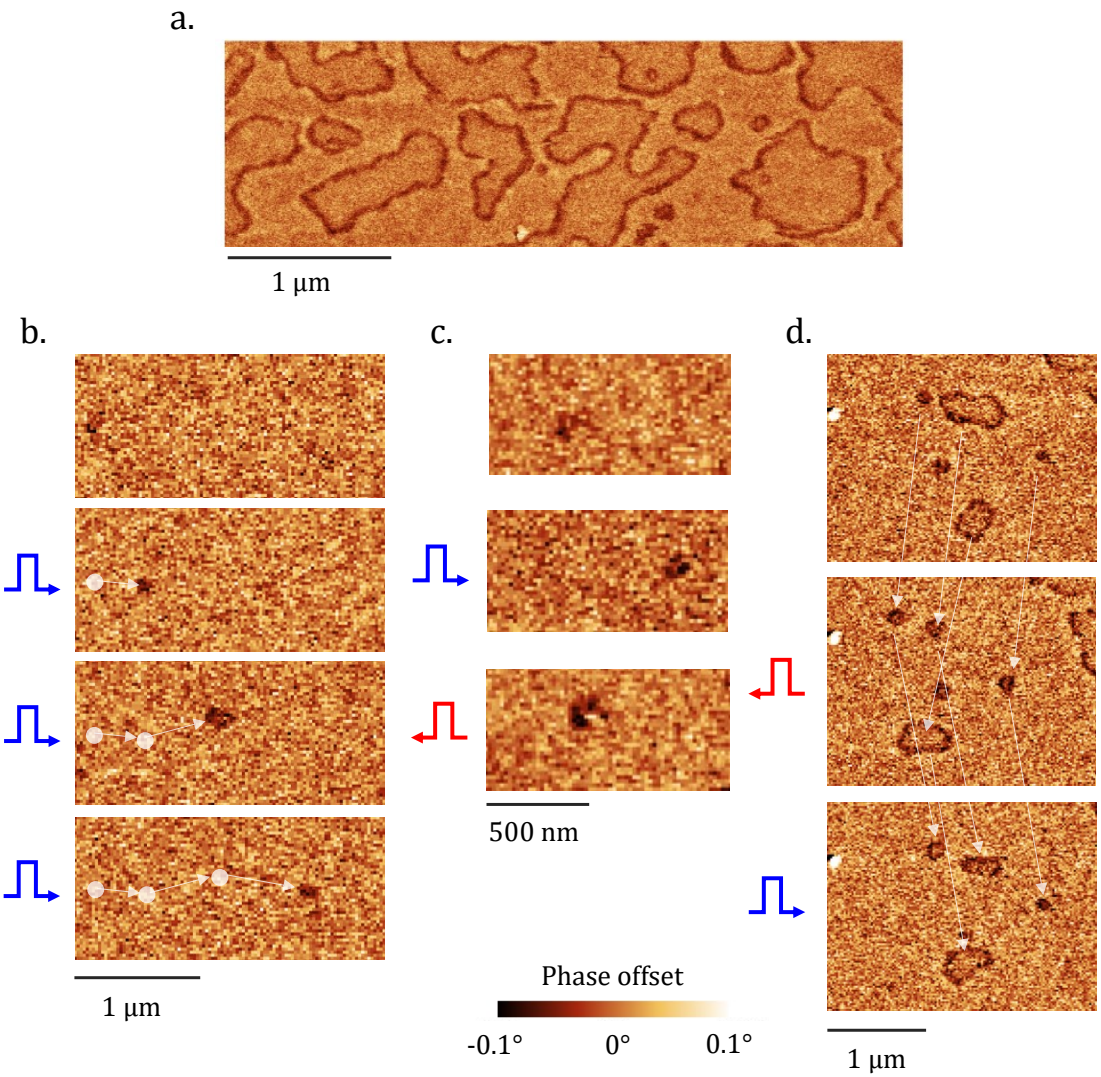

Figure 3.4: **Current-induced motion of skyrmions in a SAF measured via MFM** | a. MFM image at zero external magnetic field after a field sequence to nucleate skyrmions. b. Sequence of MFM images measured before (top) and after the consecutive injection of 1.16 ns, 1.18 ns and 0.9 ns current pulses, with a current density of respectively 8.0×10^{11}, 8.0×10^{11} and 7.6×10^{11}A/m^2. The velocities of the skyrmions are 280, 400 and 640 m/s respectively. c. Sequence of MFM images measured after the consecutive injection of two 0.6 ns long pulses with opposite polarities, with a current density of respectively 8.5×10^{11}A/m^2 and -7.9×10^{11}A/m^2. The velocities of the skyrmions are 900 and 720 m/s respectively. d. Sequence of MFM images(phase) measured before (top), after the injection of a 0.55 ns pulse with a current density of -8.2×10^{11}A/m^2 (middle) and after the injection of a 0.55 ns pulse with a current density of 7.9×10^{11}A/m^2 (bottom). All images in b, c and d are taken at zero field and the plot is the phase offset in color scale measured in lift mode.

The thickness of the Ru spacer is chosen $t_{Ru} = 0.85$ nm in order to reach the second highest possible AF coupling [180]. The thickness of the Pt layer in contact with the Ru was optimized in order to achieve similar anisotropies in both Co layers while maintaining a large RKKY interaction [181]. The Pt/Co interface provides the PMA and the DMI that are needed to stabilize the skyrmions. The Pt layers also allow for the generation of SOT that is necessary to generate the current-induced motion in the Co.
The Co thickness was targeted in order for its magnetization to be OOP but still close to IP/OOP reorientation transition, where the lower anisotropy allows for an easier skyrmion nucleation. The stack was deposited on a 100 mm wafer with the two Co layers grown as a wedge by using off-axis deposition. The thicknesses of the two Co layers vary from 1.4 nm to 1.9 nm. In order to characterize the magnetic properties of the two Co layers in the SAF and to target the desired thickness, two stacks similar to the SAF sample were deposited. In each of them one of the two Co layers was substituted by 0.3 nm of Co, so that it is magnetically dead (see Figure 3.3d and f). The other Co layer in the stack was deposited as a wedge with a thickness varying from 1.42 to 1.62 nm. The OOP hysteresis loops of the two stacks, measured with the nanoMOKE, show a gradual reorientation from OOP at lower thickness to IP when the thickness increases (see Figure 3.3e and g). The chosen Co thickness close to the OOP/IP reorientation transition is around 1.58 nm, which corresponds to a position +14 mm on

the wafer (see Figure 3.3c). From measurements on the Co bottom and top layer the perpendicular effective anisotropy fields were obtained $\mu_0 H_k = 12.4 \pm 16\,\text{mT}$ and $35.4 \pm 14\,\text{mT}$ respectively.

3.3 Current-induced motion experiments

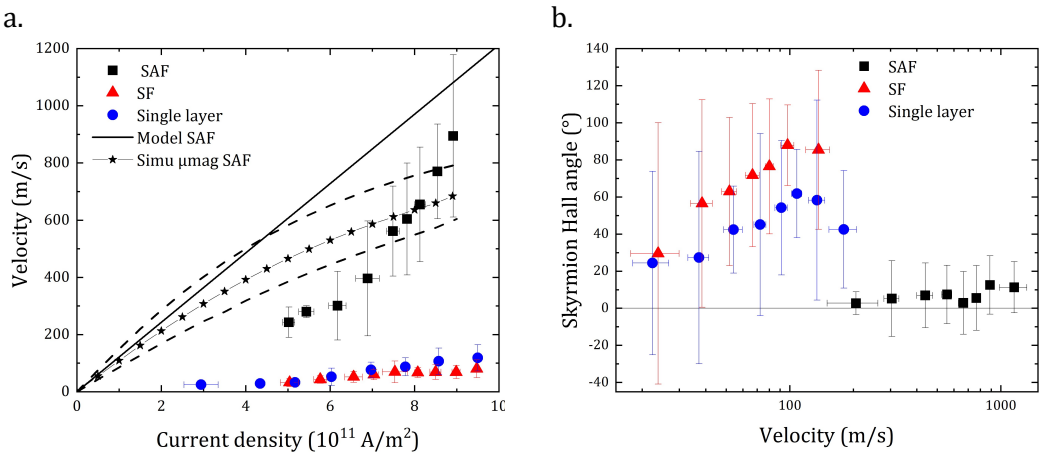

Figure 3.5: **Fast current–induced dynamics of SAF skyrmions with vanishing skyrmion Hall effect** | a. Average skyrmion velocity plotted as a function of the applied current density. The black squares show the experimental results on the SAF stack, the red triangle those for the SF and the blue circles for the Pt/Co/Ru trilayer. The black line corresponds to the analytical Thiele model using experimental parameters (equation 3.14). The black stars correspond to the velocity obtained from micromagnetic simulations for $\alpha = 0.14$. The dashed lines correspond to the velocity obtained in the micromagnetic simulations considering the error in the estimation of the damping parameter, respectively $\alpha = 0.1$ for the upper curve and $\alpha = 0.18$ for the lower curve. Average skyrmion Hall angle as a function of the skyrmion velocity for SAF skyrmions (black squares), SF skyrmions (red triangles) and single-layer skyrmions (blue circles). Each point, both in a and b, represents an average over several measurements, ranging from 3 to 47, and the error bars take into account the standard deviation of the measurement and the experimental error.

In the optimized stack, the lower effective PMA combined with the DMI reduces the DW energy and thus favours the nucleation of isolated skyrmions. Isolated skyrmions were nucleated using a magnetic field sequence consisting in a saturation OOP above the RKKY field of 205 mT and consequent return to zero field. The skyrmions were imaged by MFM. The tip used for the experiments is a low moment commercial tip from Nanosensor. It is made with a hard magnetic coating on top of an AFM tip and it is characterized by a coercivity of 250 Oe, according to the specification provided by the manufacturer.
For the current-induced motion experiment, the sample was patterned into 3 µm width and 12 µm long tracks. The tracks were contacted with gold electrodes in order to manipulate the magnetization with external current. The fabrication process consisted in a first lithography performed with e-beam to define the tracks. The tracks were then protected by an Al mask deposited by evaporation. The material outside the protected tracks was removed by IBE. The Al hard mask is then removed by mean of the solvent MIFAZ 326, which contains a molecule (TMAH) that chemically reacts with it. The electric contacts are first defined by UV lithography using a reversible resist, and after filled by evaporation of 10 nm of Ti and 100 nm of Au by evaporation. After a final lift-off the sample is ready. It presents 10 tracks in parallel contacted to the same gold electrodes. The sample was placed on a sample holder and connected to a bipolar voltage pulse generator from Kentech, that can provide a maximum voltage of 80 V with a rise time of approximately 300 ps.
The experiments were conducted by first taking an image with the MFM of the magnetic textures, second, sending a current pulse and, third, acquiring a second image after the current pulse. The displacement of the skyrmions in between the two images was measured and divided by the applied pulse length in order to obtain the motion velocity. The pulse length used for the calculation is the full-width-half-maximum (FWHM) of the transmitted pulse, sampled by an oscilloscope with 50 Ω output impedance. The possible drift in between two subsequent MFM images has been corrected by using defects in the topolographical image of the sample acquired simultaneously with the one representing the magnetic phase. In Figure 3.4, sequences of MFM images show current-induced motion experiments. In Figure 3.4b, 1 ns current pulses are injected in a sequence leading to a motion of the SAF skyrmion along the current direction. The distance and the trajectory of the skyrmion induced by the current pulse can vary due to pinning in the material [182]. On average the skyrmions move along the current direction with a minimal deviation from it ($\sim 1^\circ$). The motion along the current is consistent

with the sign of the spin Hall effect in Pt and with the sign of the DMI arising from the Pt/Co interface, left-handed [119]. Figure 3.4c shows that skyrmions can be moved back and forth by changing the polarity of the current pulses. A skyrmion is moved by a current pulse of 0.6 ns along the current direction first at 900 m/s and then at 720 m/s when the polarity is inverted. In Figure 3.4d skyrmions with different shapes are moved by first a negative current pulse and after by a positive current pulse along the current direction. It can be observed that the shape and size of some skyrmions have changed, an effect that can be explained by pinning of the magnetic skyrmions due to material inhomogeneities.
The average velocity v_{av} of the skyrmions and the average Hall angle θ_{SkH} are calculated by systematic current-induced motion experiments. Figure 3.5a shows the dependence of the skyrmion velocity v_{av} on the current density (black squares). The average velocity increases with the current density. At low current densities, from 5×10^{11} A/m^2 to 6.5×10^{11} A/m^2, we are in a low mobility regime with velocities ranging from 250 to 300 m/s, while at higher current densities higher velocities are reached. The maximum v_{av} of 895 $\pm$ 285 m/s is reached for a current density of 8.9×10^{11} A/m^2. The SkHE is vanishing with average value $\theta_{SkH} = 6.4 \pm 16.4^{\circ}$. In Figure 3.5a the black squares show the skyrmion Hall angle as a function of the skyrmion velocity. No clear dependence of the angle on the velocity is observed.

3.3.1 SAF skyrmions diameter

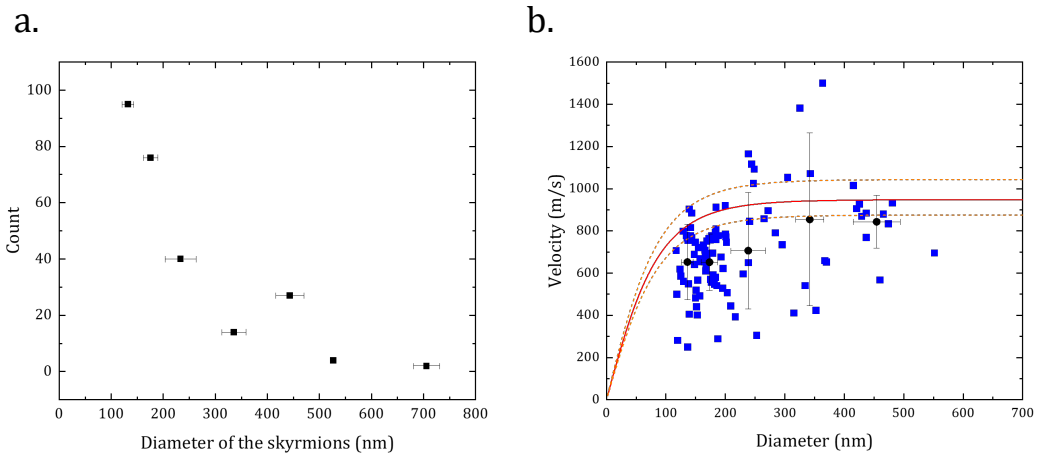

Figure 3.6: **Distribution of diameter of the skyrmions diameter in the SAF** | a. Distribution of SAF skyrmion diameters. b. Velocity of the skyrmions versus their diameter for current densities between 7.5×10^{11} and 8.9×10^{11} A/m^2. The blue dots represent single events while the black circles represent averaged values for different diameters. The red line is the prediction of the model for a current density of 8.12×10^{11} A/m^2 and the two red dotted lines the predictions for J = 7.5×10^{11} and 8.9×10^{11} A/m^2 respectively.

As previously reported, skyrmions with different shapes and sizes were observed, ranging from 100 to 700 nm in diameter, with an average of 215 $\pm$ 102 nm. The distribution of the SAF skyrmion diameters is shown in Figure 3.6a. For AF skyrmions the diameter results from a balance between the DMI, the exchange and the anisotropy energies as the dipolar field plays little role, being the net magnetization equal to zero. From the model described in ref. [183], the AF skyrmion diameter can be approximated as:

$$d \approx 2.7\Delta \frac{\left(\frac{D}{D_c}\right)^2}{\sqrt{1-\left(\frac{D}{D_c}\right)^2}} \tag{3.1}$$

where D is the DMI constant and $D_C = \frac{4\sqrt{AK_{eff}}}{\pi}$ is the critical DMI constant. The ratio in between D and D_C governs the skyrmions size. By using experimental parameters (in section 3.4.4 it is explained how they were measured), a diameter d = 197 nm was predicted, consistent with the experimental results.
We also evaluated the impact of the current on the skyrmion deformation and the impact of the skyrmion diameter on the current-induced motion. On average the deformation of the skyrmion due to the pulse is small, around 5%, excluding few events where a large deformation of more than 100% is observed. Figure 3.6b shows the skyrmion velocity as a function of the diameter (for diameters below 400 nm) for different current densities. No dependence of the average velocity on the skyrmion diameter is observed for diameters above 300 nm, while

a small decrease can be seen for diameters below 300 nm. The experimental results are also compared with the model prediction in equation 3.1 for different current densities (red lines in Figure 3.6b) which captures the reduction in skyrmion velocity for smaller skyrmions.

3.3.2 Magnetic contrast in the MFM experiments

The domain contrast observed in the MFM experiments as visible in Figure 3.4a, can be explained by the perturbation of the domain magnetization by the stray field of the MFM magnetic tip [184, 185]. This effect scales as $1/K_{eff}^2$. Therefore, the small anisotropy in our sample can explain the high contrast observed despite the low moment of the magnetic tip.
Additionally, a dip in the MFM contrast is obtained at the DW position and two successive dips in the contrast are observed when crossing a magnetic skyrmion. Micromagnetic simulations were performed to explain the phenomenon. They predicted a tiny displacement of the DW that cannot explain the systematic dips observed experimentally. An explanation for what was observed can be the formation of small ferromagnetic domains at the DW position, favored by the stray field of the tip.

3.3.3 Observation of SAF skyrmions with X-PEEM

XMCD-PEEM (see section 2.5.4) was performed on the SAF sample to image the magnetic skyrmions and DWs in order to determine their chirality. Figure 3.7a shows an XMCD-PEEM image acquired on the Co L_3 absorption edge at zero external magnetic field. The magnetic contrast is observable, even for a fully compensated SAF, as PEEM is a surface sensitive technique and thus only the photo-emitted electrons coming from the top Co layer are collected. The XMCD contrast for PEEM is around 3 times more sensitive to the IP component than to the OOP component of the magnetization. Thanks to this, it is possible to understand the internal IP structure of the DW as the rest of the sample is magnetized OOP. In Figure 3.7a the white and black contrasts that correspond to the OOP component of the magnetization, respectively down and up, are observable. Figure 3.7b displays the linescan along the dashed red line for a DW almost parallel to the x-ray beam in Figure 3.7a. It is possible to observe a peak for a white/black DW and a dip for the black/white DW. The peak means that the DW magnetization is oriented opposite to the IP component of the x-ray beam while the dip means an IP component oriented along the x-ray beam. This means that the rotation of the magnetization is happening with a left-handed chirality, in agreement with what is expected for Pt/Co/Ru interfaces [19]. Figure 3.7c shows the XMCD contrast along the linescan that corresponds to the dashed blue line in Figure 3.7a, perpendicular to the x-ray beam. As expected, we observe no peaks or dips, confirming that the magnetization is perpendicular to the beam direction, hence consistent with a Néel configuration. The chirality of the bottom layer Co is expected to be the same.

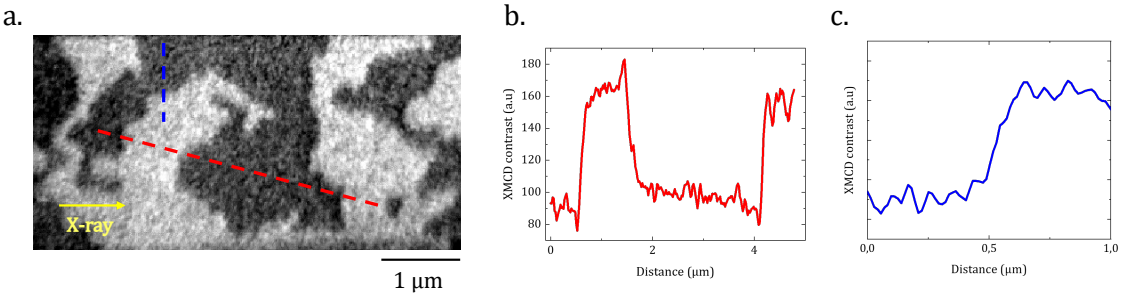

Figure 3.7: **XMCD-PEEM observation of DWs chirality in SAF sample** | a. XMCD-PEEM image of a multidomain state in the SAF sample. b. XMCD contrast profile obtained along the dashed line in red in a. c. XMCD contrast profile obtained along the dashed line in blue in a.

3.4 Analytical model and micromagnetic simulations

To understand the experimental results we performed analytical modelling and micromagnetic simulations using experimental magnetic and transport parameters.

3.4.1 Analytical model

For the SAF skyrmions we use once again the Thiele model. In this model skyrmions are considered as rigid spin textures. In section 1.5.4.1 we developed the Thiele model for FM skyrmions, starting from the Thiele

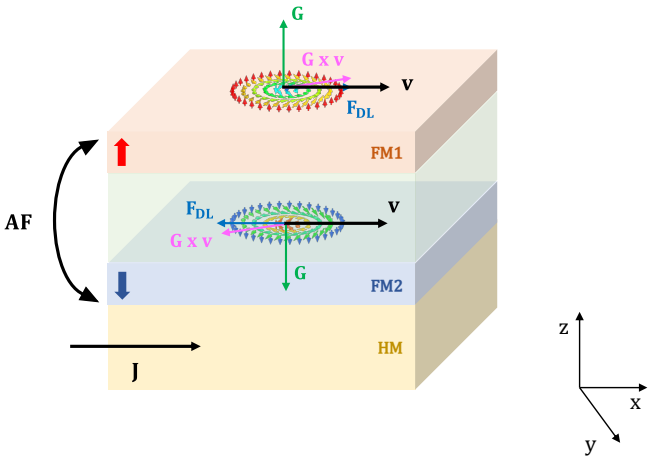

Figure 3.8: **Schematic of skyrmions coupling in a synthetic antiferromagnet stack** | Schematic representation of the dynamics in a SAF system. FM1 and FM2 are AF coupled via RKKY interaction provided by the NM layer in between them. The gyromagnetic vectors of the two skyrmions that present opposite core polarity are opposite, hence the total gyromagnetic vector is equal to zero. In this way the velocity of the skyrmions follows the same direction of the current injected through the HM layer.

equation 1.63. The dynamics of SAF skyrmions can be still described by the Thiele equation for each FM layer, adding a term to represent the RKKY coupling in between the two:

$$\mathrm{F}^1_{\mathrm{DL}} + \mathbf{G_1} \times \mathbf{v_1} - \mathrm{k}(\mathbf{R_1} - \mathbf{R_2}) - \alpha\mathcal{D}_1 \cdot \mathbf{v_1} = 0 \tag{3.2}$$

$$\mathrm{F}^2_{\mathrm{DL}} + \mathbf{G_2} \times \mathbf{v_2} - \mathrm{k}(\mathbf{R_2} - \mathbf{R_1}) - \alpha\mathcal{D}_2 \cdot \mathbf{v_2} = 0 \tag{3.3}$$

As for the equation of FM skyrmions, $\mathrm{F}^{\mathrm{i}}_{\mathrm{DL}}$ represents the DL torque acting on the skyrmion, respectively in the first FM layer for i = 1 and in the second FM layer for i=2. $\mathrm{R_i}$ is the position of the skyrmion i, $\mathbf{G_i}$ the gyrotropic vector for the skyrmion i and $\mathcal{D}_{\mathrm{i}}$ is the dissipative tensor. k is a spring constant that describes the force between the two skyrmions due to the RKKY exchange interaction. It can be written $\mathrm{d} = (\mathrm{R}_1 - \mathrm{R}_2)$, $\mathrm{F_{DL}} = \mathrm{F}^1_{\mathrm{DL}} + \mathrm{F}^2_{\mathrm{DL}}$, $\Delta\mathrm{F_{DL}} = \mathrm{F}^1_{\mathrm{DL}} - \mathrm{F}^2_{\mathrm{DL}}$, $\mathrm{v_m} = \frac{\mathbf{v_1}+\mathbf{v_2}}{2}$, $\Delta\mathbf{v} = \mathbf{v_1} - \mathbf{v_2}$. It can also be assumed that the dissipation tensor is the same for both skyrmions so $\mathcal{D}_1 = \mathcal{D}_2 = \mathcal{D}$. Since the two skyrmions are the same but with opposite core polarities, we can write $\mathbf{G_1} = -\mathbf{G_2} = \mathrm{G}\hat{\mathbf{z}}$, where the axes are defined as in Figure 3.8. The two equations 3.2 and 3.5 can be re-written as:

$$\mathrm{F_{DL}} + \mathbf{G} \times \Delta\mathrm{v} - 2\alpha\mathcal{D}\mathbf{v_m} = 0 \tag{3.4}$$

$$\Delta\mathrm{F_{DL}} + 2\mathbf{G} \times \mathbf{v_m} - 2\mathrm{k}\mathbf{d} - \alpha\mathcal{D}\Delta\mathbf{v} = 0 \tag{3.5}$$

We consider now two Néel skyrmions, as in our system, and the current flowing along the x direction. The DL torque has only an x component so $\mathbf{F_{DL}} = \mathrm{F_{DL}}\hat{\mathbf{x}}$. We can assume $\mathcal{D}$ to be diagonal so $\mathcal{D}_{\mathrm{xx}} = \mathcal{D}_{\mathrm{yy}} = \mathcal{D}$ and $\mathcal{D}_{\mathrm{xy}} = \mathcal{D}_{\mathrm{yx}} = 0$. This leads to the following expressions expressed as vectors:

$$\begin{pmatrix} \mathrm{F_{DL}} \\ 0 \\ 0 \end{pmatrix} + \mathrm{G}\begin{pmatrix} -\Delta\mathrm{v_y} \\ \Delta\mathrm{v_x} \\ 0 \end{pmatrix} - 2\alpha\mathcal{D}\begin{pmatrix} \mathrm{v_x} \\ \mathrm{v_y} \\ 0 \end{pmatrix} = 0 \tag{3.6}$$

$$\begin{pmatrix} \Delta\mathrm{F_{DL}} \\ 0 \\ 0 \end{pmatrix} + 2\mathrm{G}\begin{pmatrix} -\mathrm{v_y} \\ \mathrm{v_x} \\ 0 \end{pmatrix} - 2\mathrm{k}\begin{pmatrix} \mathrm{d_x} \\ \mathrm{d_y} \\ 0 \end{pmatrix} - \alpha\mathcal{D}\begin{pmatrix} \Delta\mathrm{v_x} \\ \Delta\mathrm{v_y} \\ 0 \end{pmatrix} = 0 \tag{3.7}$$

and hence for the x and y components:

$$\mathrm{F_{DL}} - \mathrm{G}\Delta\mathrm{v_y} - 2\alpha\mathcal{D}\mathrm{v_x} = 0 \tag{3.8}$$

$$\mathrm{G}\Delta\mathrm{v_x} - 2\alpha\mathcal{D}\mathrm{v_y} = 0 \tag{3.9}$$

$$\Delta\mathrm{F_{DL}} - 2\mathrm{G}\mathrm{v_y} - 2\mathrm{k}\mathrm{d_x} - \alpha\mathcal{D}\Delta\mathrm{v_x} = 0 \tag{3.10}$$

$$2Gv_x - 2kd_y = 0 \tag{3.11}$$

In the steady state, skyrmions have the same speed, so $\Delta v = 0$. From equation 3.8 we obtained:

$$v_x = \frac{F_{DL}}{2\alpha\mathcal{D}} \tag{3.12}$$

while from equation 3.9 we obtained $v_y = 0$. Hence, the total velocity $v = \sqrt{v_x^2 + v_y^2} = v_x$ and the SkHE gets cancelled.

As shown from the calculations in A.2 we can write $\mathbf{F_{DL}} \approx \mu_0 M_s t \pi^2 H_{DL} R \hat{\mathbf{x}}$ and $\mathcal{D} \approx \frac{2\pi M_s t'}{\gamma}\left(\frac{R}{\Delta} + \frac{\Delta}{R}\right)$ where R is the skyrmions radius and $t' = t/2$ half the film thickness. Therefore, one obtains:

$$v = v_x \approx \frac{\mu_0 H_{DL} \pi R \gamma}{2\alpha\left(\frac{R}{\Delta} + \frac{\Delta}{R}\right)} \tag{3.13}$$

Using the relation $\mu_0 H_{DL} = C_{DL} J$, where C_{DL} is the effective DL field generated by the SOT and by assuming $R >> \Delta$ it is obtained:

$$v = v_x \approx \frac{C_{DL} J \pi \Delta \gamma}{2\alpha} \tag{3.14}$$

Figure 3.5a shows the dependence of the velocity on the current density predicted by the model (black line). The model captures with accuracy the large velocities at large current densities while it does not reproduce well the observed behaviour for the low-mobility regime. The pinning can be accounted for as the reason for the mismatch, as it is known to play a major role in skyrmion dynamics and it is not taken into account by the model.

An expression valid for smaller skyrmions, without the assumption $R >> \Delta$ can also be obtained using the expression $\mathcal{D} \approx \frac{M_s t'}{\gamma}\left(\frac{2\pi R}{\Delta} + 4\pi \exp\left(-\frac{R}{2\Delta}\right)\right)$ [186], that leads to the expression for the skyrmion velocity:

$$v \approx \frac{\pi \mu_0 H_{DL} \gamma R}{2\alpha\left(\frac{R}{\Delta} + 2\exp\left(-\frac{R}{2\Delta}\right)\right)} \tag{3.15}$$

3.4.2 Micromagnetic simulations of the current-induced motion

To better understand the skyrmion dynamics observed experimentally, we performed micromagnetic simulations using experimental parameters. Simulations were performed using mumax3 [187]. The simulated system is a ferromagnet/spacer/ferromagnet trilayer structure. The magnetic parameters used can be found in table 3.1.

A Néel skyrmion was initialized in both FM layers and the total energy was minimized using the steepest conjugate gradient method. To simulate the current-induced dynamics, SOT is applied on both Co layers. The velocity was obtained, as in experiments, by dividing the net displacements of the skyrmions by the FWHM of the current pulse.

The simulations showed that the AF-coupled skyrmions moved along the current direction without skyrmion Hall effect. In Figure 3.5a it can be observed (black stars) that at low current density the micromagnetic simulations show an agreement with the theoretical predictions from the Thiele model as the velocity scales linearly with J. Above 2×10^{11} A/m^2, a sublinear drop for the simulated velocity is observed, that increases in amplitude with the current density. The dashed lines in Figure 3.5a show the error range resulting from the uncertainty on the determination of the damping parameter α. For large current densities the simulations show a good agreement with the experimental velocities.

It was also observed that the sublinear velocity drop is caused by a dynamical skyrmions deformation that gets larger as the current density increases, not taken into account in the Thiele model. When the current is switched off, the skyrmion recovers its non-deformed shape. In Figure 3.9a, it can be observed that during the pulse injection, the skyrmion expands and gets deformed in an elliptical shape. The major axis of the deformation is not perpendicular to the current direction, as already reported in previous works for FM skyrmions [15, 162, 188, 189], but it is slightly tilted. The effect has been explained as a kinetic effective field [190, 191] or as an inhomogeneous magnetization canting [192]. Along with the increasing deformation of the skyrmion, the sublinear drop in velocity is observed.

With the increasing current density, the deformation is accompanied by a rotation of the DW magnetization away from its Néel chirality (see Figure 3.1b). Similar effect has been observed for FM DW motion driven by SOT, where, due to the torque, the spins inside the DW rotate and, because of this rotation, the resultant driving force on the DW decreases, leading to a saturation of the velocity [40]. Simulations of the DW dynamics

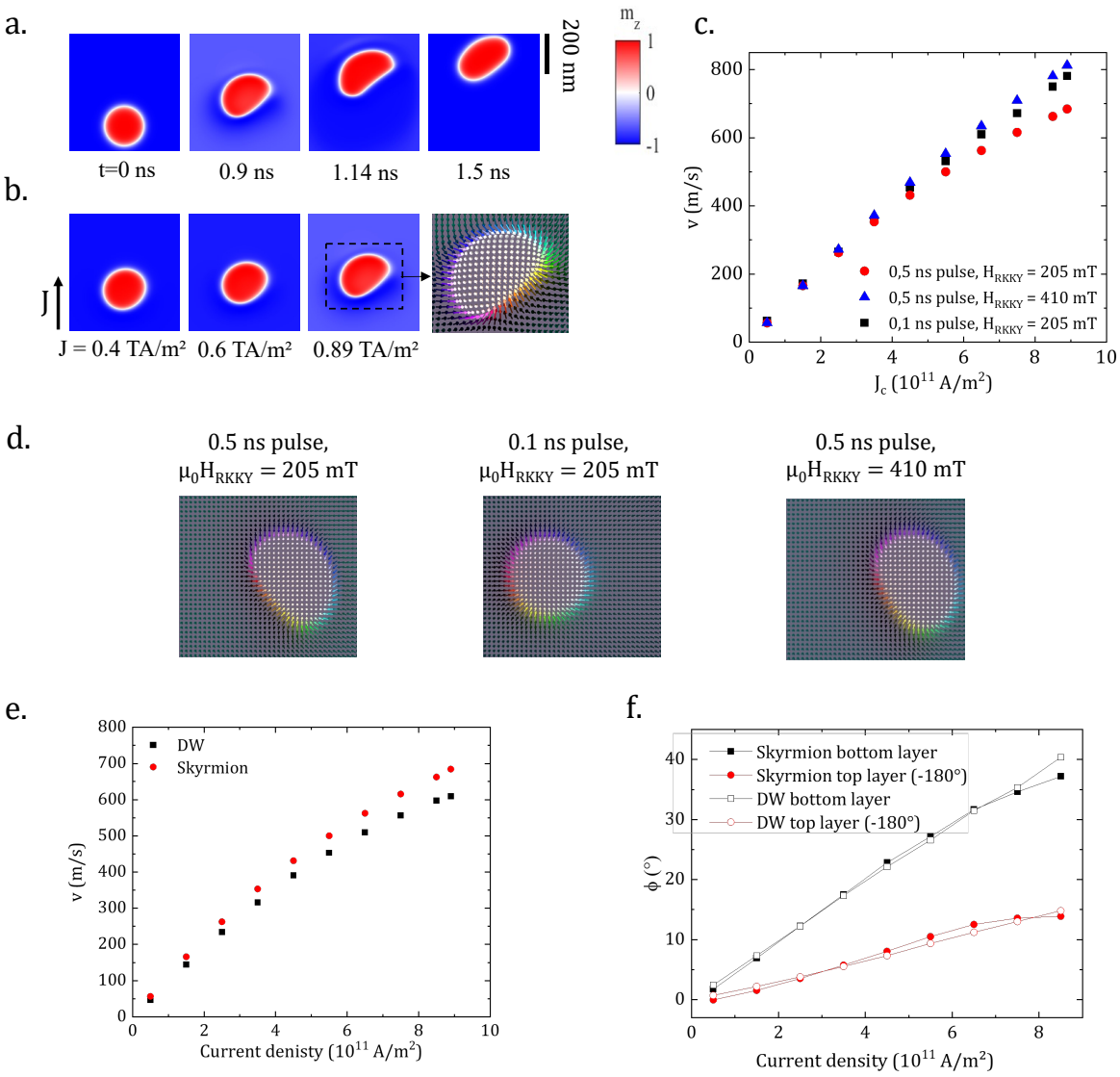

Figure 3.9: **Simulation of the current-induced skyrmion deformation and inertial dynamics** | a. Deformation of a skyrmion with time during and after a 0.5 ns gaussian current pulse with a current density of 8.9×10^{11}A/m^2. b. Deformation of a skyrmion for different current densities at the peak of a 0.5 ns pulse. The last image on the right shows the magnetization of the skyrmion at the peak of the deformation for J $= 8.9 \times 10^{11}$A/m^2 drifting away from the Néel chirality. The color wheel illustrates the orientation of the IP magnetization. c. Plot of the impact of the RKKY coupling and of the pulse length on the skyrmion velocity as a function of the current density. Red circles correspond to 0.5 ns long pulses and an RKKY field of 205 mT, blue triangles correspond to 0.5 ns and 410 mT of RKKY field and the black squares correspond to 0.1 ns pulses and 205 mT of RKKY field. d. Magnetization patterns at the peak of the current pulse for different pulse lengths and RKKY fields. e. Comparison of the velocity versus current density for DWs (red circles) and skyrmions (black squares) in a SAF. f. ϕ versus current density in the top layer (red circles) and in the bottom layer (black squares) for both DW magnetization (empty symbols) and skyrmion magnetization (full symbols) in a SAF.

in the SAF stack confirmed the hypothesis: as the current increases, the DW velocity approaches the skyrmion velocity (see Figure 3.9e) and the rotation angle ϕ of the DW and skyrmion magnetization coincide for both the top and bottom layer of the SAF (see Figure 3.9f). The observed velocity saturation can be therefore explained by a DW-like dynamics induced by the large skyrmion deformation [189]. This kind of behaviour was unexpected for AF skyrmions, as the RKKY coupling between the sublattices is expected to prevent the spins in the DW from rotating due to the current. We simulated our system with increased RKKY coupling in between the two sublattices and we observed an increase in the velocity (Figure 3.9c) for higher RKKY coupling due to a lower deformation. Another possible way to decrease the deformation is by reducing the pulse width. We simulated the response of skyrmions to shorter pulses of 100 ps and we observed once again an increase in the velocity (see Figure 3.9c and d) as the elliptical deformation and the rotation of the spins inside the

DWs were significantly reduced. Therefore, we concluded that higher velocities in SAF stacks can be obtained by either increasing the RKKY coupling in between the two FM layers, by tuning materials parameters, or by using shorter current pulses, as both approaches reduce the deformation of the skyrmion and the tilting of the spins in the DWs.

3.4.3 Micromagnetic simulations on the inertial skyrmion dynamics

We performed micromagnetic simulations to understand the inertial dynamics of the skyrmions and the impact of the RKKY on it. To this end, we computed the velocity of the skyrmions in response to a square pulse for a varying strength of the RKKY coupling. Using an RKKY value corresponding to the experimental one we observed that the skyrmion takes around 100 ps to reach a velocity plateau. Upon the rising of the current pulse, the AF-coupled skyrmions tend to move perpendicularly to the current direction in opposite directions, due to the opposite forces. Due to the RKKY coupling, a compensating force arises so that the skyrmions start moving along x with a small displacement dy. The higher the RKKY coupling the smaller is the rise/fall time of the velocity, meaning that the splitting effect is recovered quickly. A model of this inertial behaviour can be obtained starting from the Thiele model. Combining equations 3.8 and 3.10 and writing $\Delta v_y = \frac{dd_y}{dt}$ we obtain:

$$\left(F_{DL} + \frac{\alpha\mathcal{D}}{2k}\frac{dF_{DL}}{dt}\right) - 2\alpha\mathcal{D}v_x = m\frac{dv_x}{dt} \tag{3.16}$$

where $m = \frac{G^2}{2k\alpha\mathcal{D}}\left(1 + \left(\frac{\alpha D}{G}\right)^2\right)$ is an inertial mass. The characteristic time constant is $\tau = \frac{m}{2\alpha\mathcal{D}}$. For circular skyrmion one can show that $k \approx 2\pi J_{RKKY}\left(\frac{R}{\Delta} + \frac{\Delta}{R}\right)$, hence the relaxation time scales as $\frac{1}{\tau} \sim J_{RKKY}$, in agreement with what observed in micromagnetic simulations. Still, the total skyrmion displacement Δx, remains proportional to $v_0 T$, where T is the pulse length and v_0 is the steady state velocity. Therefore, the inertial effect does no affect the measured averaged velocity and hence the possible applications based on the position of the skyrmions.

3.4.4 Experimental magnetic properties

I will quickly explain how the measurements of the magnetic properties of the SAF stack were performed, but I will not go into details as I did not performed them myself. All the measured magnetic properties can be found in table 3.1.
The magnetic damping is measured by inducing the DW motion with OOP magnetic pulses and monitoring the dynamics with a polar MOKE [193]. The velocity is estimated by the average value of the DW displacement measured in all the in-plane directions. In the compensated SAF this measurement cannot be obtained due to the vanishing magnetization, therefore the SF sample (see section 3.5) was used instead. The exchange can be done as we can assume that the SOT and magnetic damping are only little affected by the thickness of the Ru interlayer. At remanence only multidomain states were observed, so in order to obtain larger domains, the thickness of the Co was decrease to 1.3 nm for the DW experiments. The magnetic damping was then estimated assuming a dependency $1/t_{Co}$. A higher damping was found for the single Pt/Co/Ru stack.
For the DMI coefficient still the SF sample was used. The experiment consists in expanding circular magnetic domains with OOP field pulses in the presence of an IP magnetic field. The velocity of the DW is minimal when the IP field compensates the DMI field, hence the DW gets a Bloch configuration [194], as the DMI field can be seen as a longitudinal field localized on the Néel DW.
For the SOT measurements both the SF stack and a stack to mimic only the bottom layer of the SAF stack were used. The SOT was measured using the second harmonic measurements, i.e. the measurement of the first and second harmonic response of the anomalous Hall voltage and planar Hall voltage when a small alternating current is applied [195]. The measurements were performed with both IP and OOP angle scans. From the OOP angle scans it is possible to extract the anisotropy field. From the second harmonic Hall with IP angles measurements both the FL and DL components of the SOT can be measured as their contributions have different angular symmetries.
The saturation magnetization was measured from the dependence of the magnetic moment on the Co magnetic film thickness in Pt/Co/Ru layer [181].
The gyromagnetic ratio is measured by ferromagnetic resonance in Pt/Co/Pt and Pt/Co/Ru ultrathin films.
The table 3.1 summarizes all the magnetic parameters used in the analytical model and in the micromagnetic simulations.

Parameter	Symbol	Value	Unit
Saturation magnetization	M_s	1.43 ± 0.05	MA/m
Exchange constant	A_{ex}	16 ± 6	pJ/m
DMI constant	D	0.62 ± 0.24	mJ/m^2
Anisotropy field (top)	$H_{k,top}$	12.4 ± 16	mT
Anisotropy field (bottom)	$H_{k,bottom}$	35.4 ± 13	mT
Anisotropy constant (top)	K_{top}	1.29 ± 0.09	MJ/m^3
Anisotropy constant (bottom)	K_{bottom}	1.31 ± 0.09	MJ/m^3
Damping-like SOT field	$H_{DL\text{-}SOT}$	2.21 ± 0.14	10^{-14} T m^2/A
Field-like SOT field	$H_{FL\text{-}SOT}$	0.53 ± 0.06	10^{-14} T m^2/A
Gilbert damping constant	α	0.14 ± 0.04	—
Effective magnetic thickness (Co)	t_{Co}	1.3 ± 0.15	nm
RKKY field	H_{RKKY}	205 ± 5	mT
Domain wall width	Δ	27 ± 7.6	nm
Gyromagnetic ratio	γ	194.8 ± 6.3	GHz/T

Table 3.1: Experimental magnetic and transport parameters.

3.5 Current-induced motion in Pt/Co/Ru FM stacks

In order to better understand the impact of the magnetic compensation on the increase in velocity, we performed the same current-induced motion measurements on two stacks that share most of their properties with the SAF stack used in experiments. The stacks used are the Pt/Co/Ru trilayer and the Pt/Co/Ru synthetic ferromagnet (SF), that is like a SAF but for which the thickness of Ru (1.4 nm instead of 0.85 nm) provides a FM coupling in between the two Co layers via RKKY. The stacks are shown in Figure 3.10a and d. It can be noticed that all the thicknesses are kept as in the SAF sample, with the exception of the Ru interlayer for the SF stack. The samples were deposited once again on a wedge, and the Co thickness targeted for the experiments was the same as in the SAF experiments, in order to be close to the IP/OOP reorientation transition. To nucleate the skyrmions a small OOP field was necessary since, at remanence, both samples were presenting stripe domains. For the SF an OOP field of around 15 mT was applied to nucleate the skyrmions. The average diameter of the skyrmions in this sample was found to be 215 nm. For the trilayer, still a field of around 15 mT was used to nucleate the skyrmions that were found to have an average diameter of 107 nm.
To perform the experiments, the samples were patterned following the same procedure used as for the SAF. Once again the skyrmion velocity was obtained by measuring the skyrmion displacement from MFM images before and after the pulse application and dividing it by the FWHM of the applied pulse measured on an oscilloscope. Figure 3.10b and c show MFM images of skyrmions in the SF before and after current pulses. The motion of the skyrmions is highlighted by white arrows. The respective MFM images for the single layer are shown in Figure 3.10e and f for both positive and negative current pulses. By taking several images at different current densities for both the stacks, a statistic on the average velocity has been obtained. In Figure 3.5a the velocity versus current density for the SF and the Pt/Co/Ru trilayer are plotted, respectively with red triangles and blue circles. In contrast to the SAF stack, a maximum velocity of ~ 120 m/s is measured in the Pt/Co/Ru trilayer and only 80 m/s for the SF stack. These values are consistent with previous current-induced motion experiments in FM thin films [120, 15]. The error bars once again take into account both the standard deviation of the measurement and the measurement error. The average skyrmion Hall angle θ_{SkHE} shows an increasing dependence on the velocity for both stacks. It saturates eventually at $\sim 60^\circ$ for the Pt/Co/Ru trilayer and at $\sim 85^\circ$ for the Pt/Co/Ru SF. A dependence on the velocity, even if not predicted by the Thiele model, has been observed and reported previously for FM stacks [15, 162, 196]. It is generally attributed to the interaction of the skyrmions with the material disorder, which decreases the displacement at low current densities and consequently the velocity and the skyrmion Hall angle.
The experiments on the Pt/Co/Ru trilayer and on the SF demonstrated that the high velocity reached by the skyrmions and the cancellation of the skyrmion Hall effect are directly related to the magnetic compensation in the SAF as predicted, because they cannot be explained by other magnetic properties of the chosen materials.

3.6 Discussion and conclusions

In this chapter we have demonstrated an enhancement of current-induced skyrmion velocity in a SAF, up to 9 times more than what was observed previously for FM stacks, along with the cancellation of the skyrmion Hall effect. The experiments have been conducted by measuring the displacement of the skyrmions in between

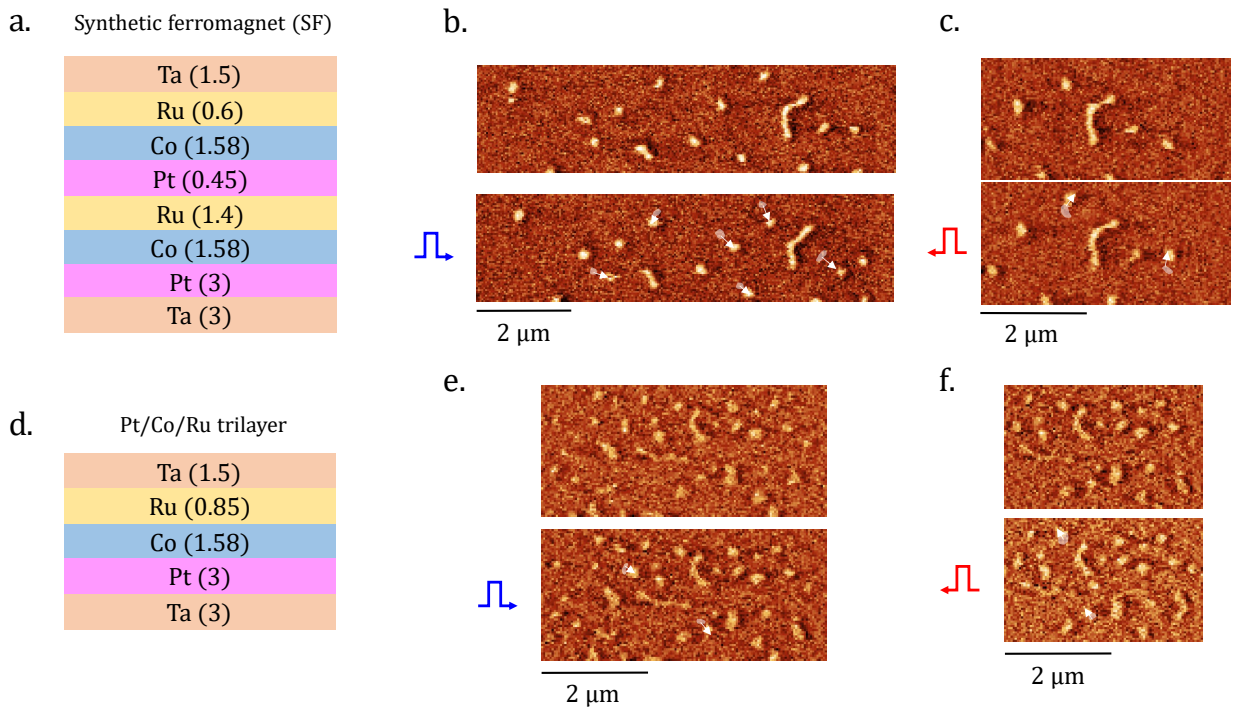

Figure 3.10: **MFM current-induced skyrmion motion images in the Pt/Co/Ru trilayer and in the SF** | a. Synthetic ferromagnetic stack. The Ru thickness provides a FM coupling in between the two Co layers. b. MFM images taken before and after a pulse of 4.95 ns with a current density of 6.95×10^{11}A/m^2. c. MFM images taken before and after a pulse of 5.01 ns with a current density of -6.70×10^{11}A/m^2. For the measurement in b. and c. an external OOP field of 15 mT is applied. d. Pt/Co/Ru trilayer stack. e. Sequence of MFM images taken before and after a pulse of 5.05 ns with a current density of 4.36×10^{11}A/m^2. f. Sequence of MFM images taken before and after a pulse of 4.99 ns with a current density of -5.14×10^{11}A/m^2.

two images taken with an MFM. Similar experiments were conducted on a SF and in a Pt/Co/Ru trilayer, stacks that are sharing most of their magnetic properties with the SAF. They confirmed the major impact of the cancellation of the topological charge in the enhancement of the velocity and in the cancellation of the skyrmion Hall effect. The large increase of the velocity, other than from the cancellation of the topological charge, can be explained due to the presence of a large SOT field which suggests an efficient Spin Hall effect, larger than what measured in the single Pt/Co/Ru trilayer. The large SOT thus, cannot be explained just by the Pt/Co interface contribution, but suggests a second contribution coming from the Ru/Pt bilayer [197, 198, 199]. Similar enhancement in the SOT in multiple repetitions rather than in single trilayers were already reported in literature [200, 201]. A third contribution to the velocity increase comes from the magnetic damping, which was proved to be lower in the SF than in the trilayer stack. This could be accounted for by the increased effective magnetic thickness.
The experimental results we obtained have been compared to analytical models and simulations, that allow to both reproduce them and understand better the underlying dynamics of the phenomenon of current-induced motion in SAF.
My group had already started working on the experiments when I started my PhD. I first performed the MFM measurement on the two FM systems and analyzed the experimental data. I also analyzed the data from the MFM measurement on the SAF stack, taken by a previous PostDoc in my group. I contributed to the performing of the micromagnetic simulations in the SAF stack, mainly working on understanding the deformation mechanisms generated by the current.

Chapter 4

Bipolar control of skyrmions in magnetic tunnel junctions for memory applications

Contents

4.1 Introduction . . . 70
4.2 Optimized low RA stack . . . 70
4.3 Device characterization . . . 71
4.4 Operando-STXM experiments in MTJs . . . 72
4.5 Control of a skyrmion using external magnetic field . . . 73
4.6 Bipolar nucleation and annihilation of a skyrmion in an MTJ using a DC current . . . 75
4.7 Bipolar control of a skyrmion in an MTJ using current pulses . . . 76
4.8 Time-resolved bipolar control of skyrmion in a MTJ . . . 77
4.8.1 System excitation . . . 78
4.8.2 Results . . . 78
4.9 Conclusions . . . 81

4.1 Introduction

Skyrmion based memory was first proposed by Fert *et al.* [13]. The author suggested the idea of a racetrack memory, in order to exploit the particle-like properties of skyrmions, which consisted in encoding the bit of information 1 in the skyrmion presence and the bit of information 0 in the skyrmion absence. To achieve a racetrack memory it is fundamental to obtain high-speed current-induced motion of skyrmions as well as their electrical nucleation and detection for the read and write operations. On the way toward the achievement of skyrmion racetrack memory devices, several milestones were reached: the stabilization of skyrmions at room temperature [119], the current-induced motion of ferromagnetic skyrmions [14, 15] and the detection of skyrmions in ultra-thin film exploiting the anomalous Hall effect [20, 21]. However, several key problems were also highlighted: the limited velocity of skyrmions in FM thin films, the arising skyrmion Hall effect directly related to the skyrmion topology that would cause a loss of information [16] and the limited electrical signal obtained from anomalous Hall effect measurements.
The low electrical signal using anomalous Hall effect measurements can be mitigated by considering magnetic tunnel junctions exploiting the TMR signal. Several studies observed the change in resistance of the MTJ which was claimed to be associated with the skyrmion nucleation either by external magnetic fields [134] or currents [148]. Skyrmions have also been nucleated in MTJ pillars by using external gate voltage pulses [150, 22, 23]. From these studies arose the idea of another type of memory device exploiting magnetic skyrmions, different from the racetrack memory. It consists in a MTJ pillar were, instead of having two resistance states that are associated to the bits 0 and 1, like in MRAM technology, a third memory state would be given by a skyrmion state, electrically reachable from the two classic states. To achieve this goal it is necessary to fulfill the full bipolar control of the electrical nucleation and annihilation of magnetic skyrmions in MTJ devices for the reading and writing operations in the memory. The breakthrough brought by the works of Urrestarazu *et al.* [23] and Chen *et al.* [22] is the possibility of combining the electrical detection with an imaging technique (XMCD-STXM for the former and MFM for the latter) to provide a direct correlation between the observed magnetic texture and the measured electrical signal. An *operando* imaging of the process is indeed important to understand, in terms of change of the magnetization, the electrical reading coming from the TMR of the device.

Here, we present the experiments performed to obtain a full bipolar electrical control of skyrmions in MTJ. In the works of Chen *et al.* [22] and Urrestarazu *et al.* [23], the authors show the possibility to achieve the electrical nucleation of the skyrmion. However, the full bipolar control of the skyrmions, namely their electrical nucleation and annihilation, which is a key for devices, was not demonstrated. Instead of exploiting gate voltage, the devices were optimized to exploit spin transfer torque, providing a more effective mean to manipulate spin textures. In this chapter, I will present the *operando* XMCD-STXM experiments performed to demonstrate the electrical nucleation and annihilation of skyrmions in MTJs. We demonstrate that the use of either DC current or current pulses allow a reproducible nucleation and consequent annihilation of a spin texture in a MTJ. In the last part of the chapter I will also present the time-resolved STXM experiments performed to better understand the dynamics of the switching process. I will propose some interpretations for the observed image sequences in the movies.
The demonstration of the nucleation/annihilation process in an MTJ exploiting STT via external current is an important milestone toward the realization of multi-state, skyrmion based memory devices.

4.2 Optimized low RA stack

The optimized MTJ stack designed to achieve the electrical bipolar control of the skrymions using external current is the following: Si/Si_3N_4/Ta/Cu/Ta/Pt/[Co/Pt]×6/Co/Ru/[Co/Pt]×3/Co/W/FeCoB/MgO/FeCoB/W/Pt (see Figure 4.1 for a schematic of the stack with the specified thicknesses for each layer). The FeCoB free layer is deposited as a wedge with nominal thicknesses ranging from 1.7 nm to 1.9 nm. The thickness has been optimized in order to cover at best the thicknesses around the OOP/IP spin reorientation transition, where, due to the low PMA, lower energy is needed to nucleate skyrmions. The hysteresis loops of the FeCoB free layer along the 50 mm wafer measured by nanoMOKE can be observed in Figure 4.1b. For negative thicknesses value the FeCoB layer is thicker, therefore more IP, while for positive values the FeCoB is thinner. The transition from OOP to IP magnetization is clearly visible around 3 mm, which corresponds to a nominal thickness of around 1.8 nm. The magnetization of the FeCoB reference layer is stabilized by the presence of the [Co/Pt]/Ru/[Co/Pt] SAF. The SAF increases the coercive field needed for the switching of the reference layer, making its magnetization more stable to the external magnetic fields and currents used to switch the free layer. The MgO barrier is chosen to be thin (a total thickness of MgO around 1.25 nm) in order to maintain a low resistance × area product (RA). Having a low RA improves the STT control of the magnetization of the free layer over the VCMA control. The bottom electrode (BE) structure made of Ta/Cu/Ta/Pt was optimized for low resistivity to maintain a

low RA and to reduce the heat dissipation during STXM experiments, that could bring to the breaking of the MTJ pillars. The Cu layer provides low resistivity while the Ta layer below the Cu layer is needed in order to improve the adherence during the growth on top of the SiN substrate. The Cu layer cannot risk to get oxidized during the etching process as it would degrade the properties of the MTJ, therefore it has to be protected by a Pt layer, which is more resistant to the oxidation. The Pt layer does not grow well directly on top of a Cu layer, hence a second Ta interlayer is used on top of the Cu layer. The Pt is fundamental not only for protecting the BE from the oxidation, but it is needed to generate the PMA in the adjacent Co layer through the Co/Pt interface. The higher the thickness of Pt, the stronger the PMA; the chosen thickness of 7 nm is a good balance in between a strong PMA and the cost of using Pt.
The SAF is composed of 6 and 3 repetitions of the Co/Pt bilayer in order to reduce the effect of its stray field on the magnetic layers of the MTJ. This configuration has been previously optimized by the "MRAM group" at Spintec. The Co layer between the two magnetic blocks of the SAF enhances the RKKY coupling within the SAF. The two W layers in contact with the FeCoB layers are necessary to make the B, from the FeCoB magnetic layers, to migrate inside them rather than inside the MgO, as this would destroy the oxide barrier. The top Pt layer is used as a protection from the oxidation.
Once deposited, the stack was annealed at 300° C for 10 minutes in order for the MgO to crystallize in the (100) orientation.

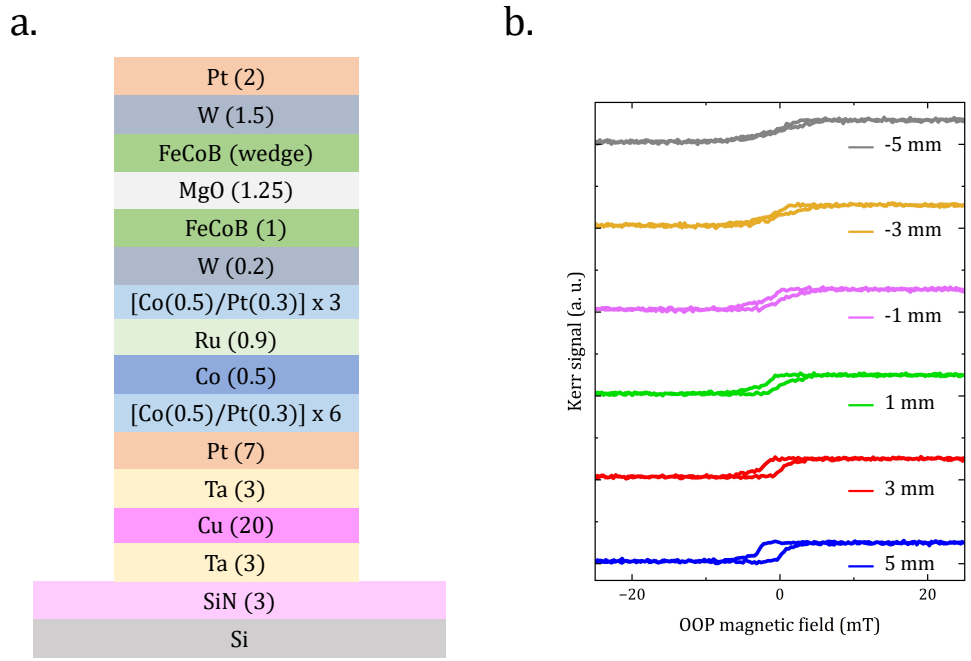

Figure 4.1: **Low RA MTJ stack and OOP hysteresis loops of the FeCoB wedged free layer** | a. Schematic of the low RA MTJ stack composition (thicknesses in nm). b. NanoMOKE OOP hysteresis loops along the wedged FeCoB free layer. The transition from PMA to IP magnetization is clearly visible going from the blue loop at the bottom to the grey one on top.

4.3 Device characterization

An electrical characterization of the fabricated devices is performed in the laboratory before the beamtime. The hysteresis loops of several devices are measured using the manual prober setup described in section 2.2.1. The characterization is performed in order to know which devices should be selected depending on the planned experiment in the synchrotron, as the time we have during the beamtime is limited. In particular, we focused on devices exhibiting intermediate resistance states in their hysteresis loops in order to try to access them also with current.
Figure 4.2 shows the hysteresis loops of the device that was used later in the beamtime for the STXM measurement. The hysteresis loops were measured at different applied currents. Several intermediate resistance states in between the P and AP resistance states are observed over a certain range of magnetic field. The DC current used for the electrical characterization in the laboratory is maintained low because we do not want to risk breaking devices before the beamtime, as we only have a limited number of them.

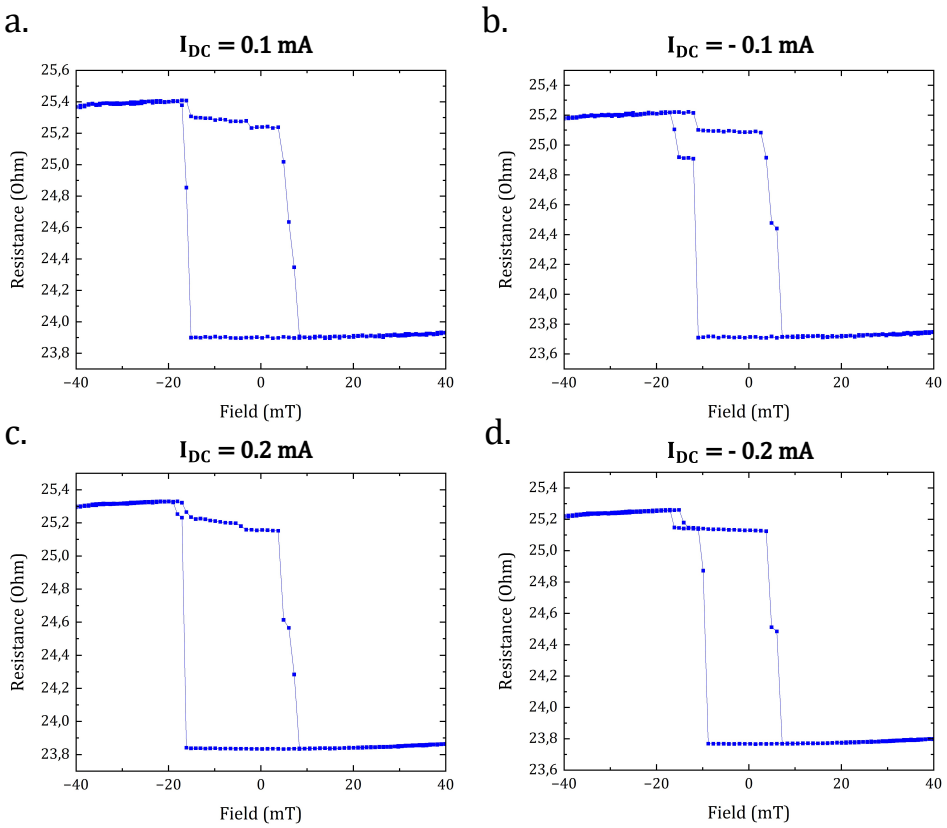

Figure 4.2: **Hysteresis loops of resistance versus external magnetic field applied perpendicular to the sample plane measured on the MTJ pillar used for the STXM experiments for different DC currents** | Hysteresis loops of resistance vs magnetic field. The hysteresis loops are measured for I_{DC} = 0.1 mA, -0.1 mA, 0.2 mA and -0.2 mA in respectively a., b., c. and d.

4.4 Operando-STXM experiments in MTJs

To understand what is happening in the experiments it is important to unambiguously detect nucleated skyrmions inside MTJs. To this end, it is fundamental to perform an *operando* imaging of the spin textures. This allows to associate the MTJ resistance value to an image of the spin texture within the device. Using an imaging technique that could be directly performed in the laboratory like MOKE or MFM is not possible, since they only allow to probe the magnetization a few nm from the surface of the sample, which is not compatible with the fabrication process of MTJs. Indeed, only the metal used to electrically contact the pillars from the top is a several hundreds of nm thick. STXM, on the other hand, allows for an imaging of the magnetization of the MTJs due to the deep penetration of soft x-rays inside materials while at the same time maintaining the pillar electrically contacted. The process explained in section 2.1.3 was followed to fabricate the MTJ devices on top of SiN membranes.
What makes STXM even more interesting is the possibility to focus on different materials inside the pillar by tuning the x-ray energy. The magnetic materials inside our MTJ stack are both FeCoB, in the free and reference layers of the MTJ, and Co in the SAF, used to stabilize the magnetic layers. When imaging a spin texture at the Fe L_3 edge and comparing it with images acquired at the Co L_3 edge, we can confirm that it is actually nucleated only in the free layer of the MTJ and not in the SAF. If the spin textures were also nucleated in the SAF we would see it also by performing an XMCD-STXM image on the Co edge since the contrast is dominated by the repetitions of Co in the SAF layer rather than by the smaller quantity of Co contained in the magnetic layers of the MTJ.
To reconstruct the magnetic contrast, XMCD-STXM images are obtained by taking two images in the same configuration, one with left-circularly polarized x-rays (that we will refer to as positive helicity from now on) and one with right-circularly polarized x-rays (that we will refer to as negative helicity from now on), and subtracting one to the other. Figure 4.3b shows the XMCD-STXM contrast obtained for a device in the AP state (left image). The background and the device present the same grey contrast when the MTJ is in the AP state. This happens because the x-rays that do not get absorbed in the first magnetic layer get absorbed in the second one which presents an opposite magnetization. The result is no change in the XMCD contrast when subtracting right and left polarized x-rays (see section 2.5.1 for more detailed explanation of the XMCD

absorption process). In the P state instead (see the two images in Figure 4.3b on the right) the contrast with respect to the background is visible. If we reconstruct the XMCD-STXM image by performing positive (p) helicity image - negative (n) helicity image we obtain a whiter contrast inside the pillar with respect to the background. If the reconstruction of the XMCD contrast is obtained with the opposite subtraction, therefore performing n - p, in the final image we observe a darker contrast inside the pillar with respect to the grey background.
For the whole chapter I will follow the convention that XMCD images are reconstructed by performing the subtraction p - n.

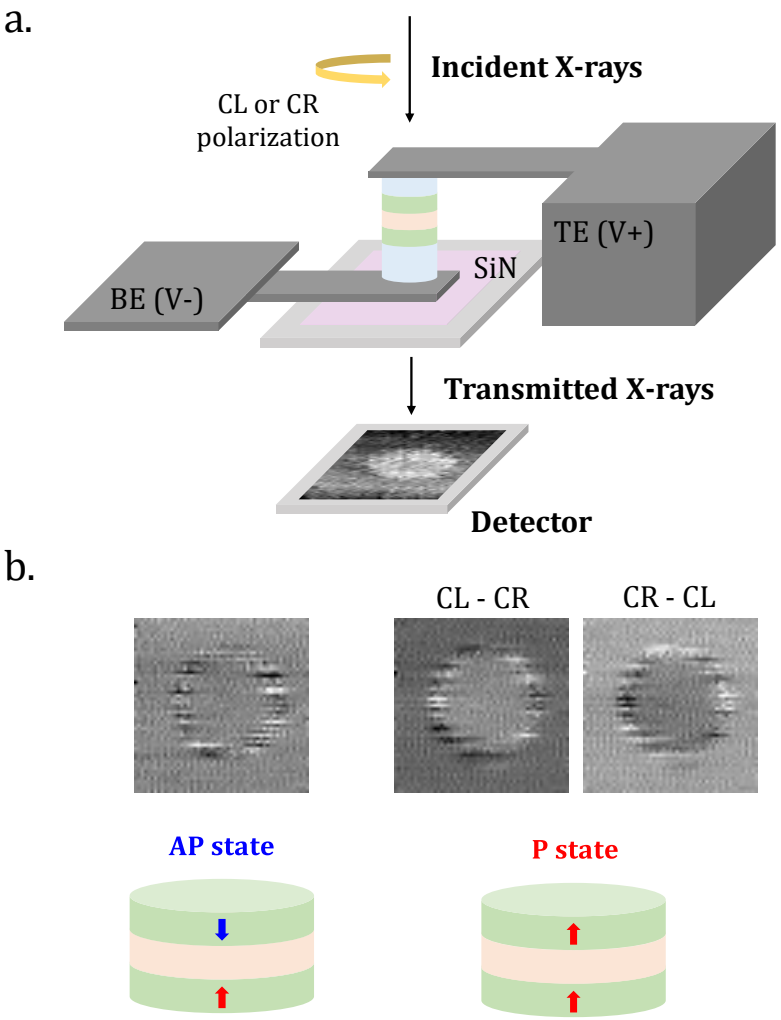

Figure 4.3: **XMCD-STXM contrast for an MTJ in the AP and P states** | a. Schematic of the XMCD-STXM *operando* measurements on an MTJ. b. XMCD contrast in an MTJ for respectively an AP configuration on the left and a P configuration on the right. For the P configuration, opposite contrast is obtained whether the XMCD image is reconstructed by performing the subtraction positive minus negative (p - n) helicity, whiter contrast inside the pillar, or n - p, darker contrast inside the pillar.

4.5 Control of a skyrmion using external magnetic field

To demonstrate full bipolar electrical control of a skyrmion state in the MTJ, we chose a device which features intermediate resistance states in the hysteresis loops (see Figure 4.2). The MTJ has a diameter of 500 nm and is located around the center of the wafer, where the PMA is low and it is therefore easier to nucleate skyrmions. The XMCD-STXM measurements were performed using an x-ray energy of 709.8 eV, i.e. the L_3 Fe-edge, to image the respective magnetization configurations of the free and reference layers made of FeCoB, Fe rich.
The first step of the experiment consisted in finding intermediate resistance states by sweeping the external magnetic field and measuring the electrical resistance before performing STXM imaging. We first measured the resistances of the AP and P states, corresponding respectively to 29.2 Ω and 27.8 Ω with an applied DC current of 2 mA. Then, by sweeping the external magnetic field starting from the AP state at 20 mT, at -5 mT we saw the appearance of an intermediate resistance state with a corresponding resistance of 28.54 Ω. Figure 4.4

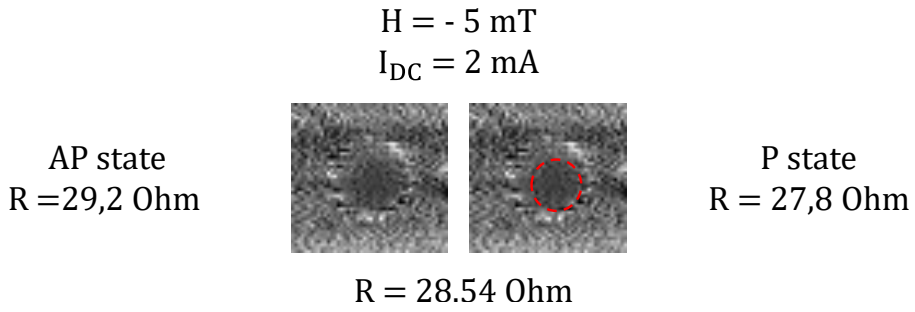

Figure 4.4: **Magnetic field induced skyrmion nucleation in a MTJ pillar** | XMCD-STXM image of a skyrmion nucleated in a 500 nm diameter MTJ pillar under an external field of -5 mT. The image was taken at the Fe L_3 edge energy of 709.8 eV. The measured resistance of the intermediate state corresponds to 28.54 Ω for an external DC current of 2 mA. The skyrmion (highlighted by a red dotted line in the image on the right) presents the same contrast as the background, while the contrast in the remaining part of the pillar is brighter. This means that the skyrmion magnetization is aligned AP to the reference layer, while the surrounding region is parallelly aligned.

shows the corresponding XMCD-STXM images of the nucleation of the skyrmion in the MTJ (the skyrmions is highlighted by the red dotted line in the image on the right). The skyrmion presents a magnetization AP aligned to that of the reference layer as it can be inferred from the grey contrast, while the area around it shows a brighter contrast, meaning a parallel orientation of the magnetization with respect to the reference layer.
To see whether the jump in resistance matches with the area of the nucleated skyrmion we use the following formula for the conductance in a MTJ:

$$G = x \cdot G_P + (1 - x) \cdot G_{AP} \tag{4.1}$$

where G_P and G_{AP} represent respectively the conductance of the MTJ in the P and AP states, and x is the fraction of the magnetization in the AP state. The lengths of the major and minor axes of the nucleated skyrmion measured from the image in Figure 4.4 correspond respectively to 0.4 µm and 0.34 µm. Assuming the diameter of the pillar of 500 nm we obtain a resistance of 28.54 Ω using the equation in 4.1, in agreement with the experimental measurement.
We repeated the same process to characterize the intermediate skyrmion states for different applied DC currents. Once the skyrmion was nucleated, we noticed that it was possible to shrink it by decreasing the amplitude of the external magnetic field, driving the system toward the AP state. Figure 4.5 presents a sequence of XMCD-STXM images showing the shrinking of the white contrasted area surrounding the skyrmion after its nucleation. The resistance was measured for an applied DC current of 0.8 mA. The initial skyrmion expands sweeping the field from -3.8 mT to -2.2 mT, as it can be observed by both the change in resistance from 28.47 Ω to 28.7 Ω and the decrease of the white contrasted area in the XMCD images, that remains at the end only on the top edge of the pillar.

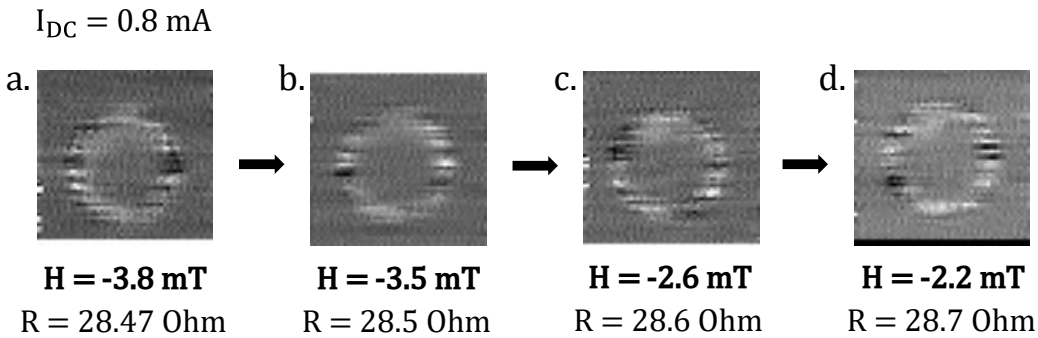

Figure 4.5: **Expansion of a skyrmion in a MTJ pillar under external magnetic field** | XMCD-STXM images of a 500 nm diameter MTJ pillar taken at the Fe L_3 edge energy of 709.8 eV. The external DC current to measure the resistance is 0.8 mA. a. The MTJ magnetization is initially in the intermediate state for an external applied field of -3.8 mT and has a resistance of 28.47 Ω. b. When the magnetic field is slightly increased to -3.5 mT, the skyrmion remains almost the same and the measured resistance is 28.5 Ω. c. At -2.6 mT, the skyrmion expands and the new resistance value measured is 28.6 Ω. d. Further increasing the field to -2.2 mT, leads to an additional expansion of the skyrmion, with a measured resistance of 28.7 Ω.

4.6 Bipolar nucleation and annihilation of a skyrmion in an MTJ using a DC current

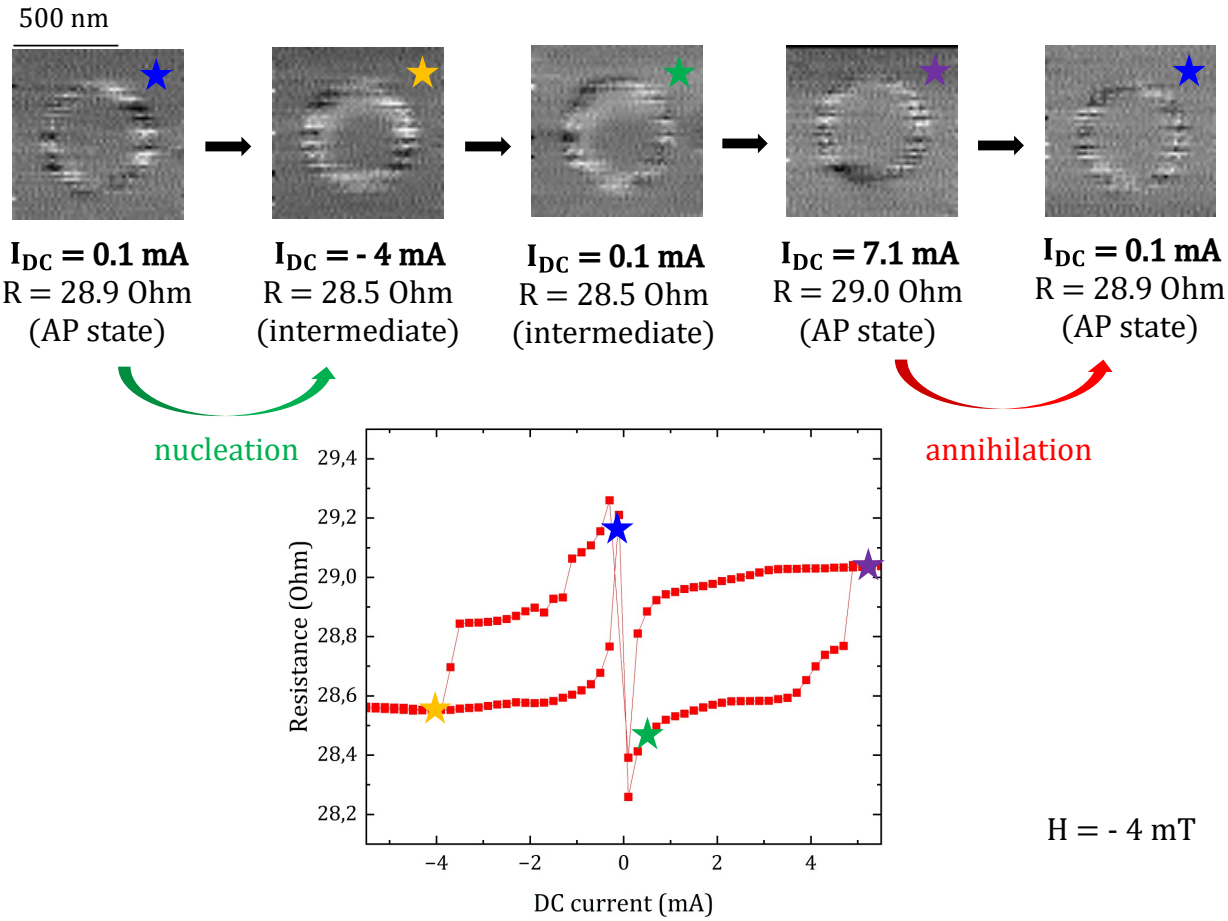

Figure 4.6: **Bipolar electrical control of the nucleation/annihilation process of a skyrmion in a MTJ using DC current** | XMCD-STXM images obtained on a 500 nm diameter MTJ pillar on the Fe L_3 edge at an energy of 709.8 eV. The external applied magnetic field is -4 mT. The first image on the left (blue star) shows the pillar in the AP state with a corresponding R = 28.9 Ω measured with I_{DC} = 0.1 mA. By applying an external DC current of -4 mA a skyrmion is nucleated inside the pillar, as observable by both the change in contrast and the change in resistance that goes to 28.5 Ω in the image marked by a yellow star. In the third XMCD image (green star) the skyrmion is still stable when the current is brought back to I_{DC} = 0.1 mA and the resistance of 28.5 Ω remains unchanged. The current is then brought to I_{DC} = 7.1 mA and the skyrmion gets annihilated. In the XMCD-STXM image the whiter contrast is no longer observable (purple star) and the resistance has jumped back to 29 Ω. Bringing the current back to 0.1 mA the magnetization remains in the AP configuration and the resistance stays unchanged (last image on the right with the blue star). Below the XMCD-STXM images the resistance versus DC current loop shows the nucleation and the annihilation processes. Colored stars mark the corresponding image positions. Note that this is the same device used for field-induced skyrmion nucleation shown in Figure 4.4.

We then addressed the bipolar control of the nucleation/annihilation process induced by an external DC current. To this end, we first saturated the device in the AP configuration with an external magnetic field of 20 mT. Then, we approached the magnetic field at which the intermediate state was nucleated and confirm with an XMCD-STXM image that the device remained in the AP state. The first XMCD-STXM image on the left in Figure 4.6 was taken at an external field of -4 mT, with an applied DC current of 0.1 mA. There is no visible contrast with respect to the background, as expected from the AP state. The associated resistance measured is 28.9 Ω. Then, by applying a DC current of -4 mA we nucleated a skyrmion, similar to the one observed when sweeping the magnetic field (Figure 4.6, I = 4 mA). A white crown around a circular area appears, meaning that during the nucleation process from the AP state the magnetic area reversed is the one around the skyrmion which aligns parallelly to the reference layer magnetization. The measured resistance of the skyrmions state is 28.5 Ω, for a total jump in resistance from the AP state of 0.4 Ω. By removing the external DC current (back to 0.1 mA) the spin texture was still stable (Figure 4.6, I = 0.1 mA) and neither a jump in resistance nor a

change in the shape of the skyrmion can be observed. Starting from this state, the application of a current of 7.1 mA, with reversed polarity, leads to the annihilation of the spin texture (Figure 4.6, I = 7.1 mA) and the MTJ goes back to the AP state with a resistance of 29 Ω. Now, by removing once again the current, we closed the loop and we observed that the AP state was maintained (see Figure 4.6, I = 0.1 mA). We show in Figure 4.6, bottom panel, the corresponding hysteretic change in the resistance while sweeping the DC current. The position of the XMCD images associated to the resistance vs current loop are highlighted with stars of different colors. The back and forth nucleation and annihilation starting from the AP state are clearly observed resulting in an hysteretic resistance versus DC current curve.
We therefore demonstrated a full bipolar control of the nucleation/annihilation process of a skyrmion by using DC current, hence by exploiting the STT control of the magnetization.

4.7 Bipolar control of a skyrmion in an MTJ using current pulses

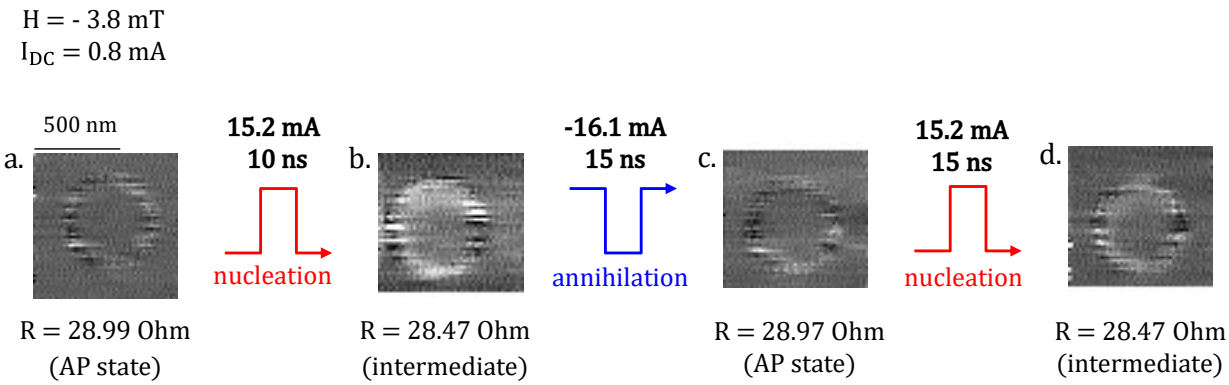

Figure 4.7: **Bipolar electric control of the skyrmion nucleation and annihilation with current pulses** | XMCD-STXM images obtained on a 500 nm pillar at the Fe L_3 edge at the energy of 709.8 eV for an external applied magnetic field of -3.8 mT and a current I_{DC} = 0.8 mA. a. Image showing the pillar in the AP state, no contrast is observable. The corresponding measured resistance is 28.99 Ω. A pulse of 15.2 mA for 10 ns is applied. In b. one observes the nucleation of a skyrmion by the current pulse evidenced by the emergence of a bright ring encircling a gray core. It means that the nucleation proceeds by inverting the magnetization along the edges. The corresponding measured resistance is 28.47 Ω. A second -16.1 mA, 15 ns pulse is applied to the skyrmion state that annihilates it and restore the AP state, in c. Once again, no magnetic contrast is observable and the resistance is back to 28.97 Ω. d. A 15.2 mA, 15 ns pulse re-nucleates the skyrmions, recovering R = 28.47 Ω. The device used for these experiments is the same 500 nm pillar exploited in the precedent experiments.

After demonstrating the nucleation and annihilation of the intermediate skyrmionic state with DC current, we performed a similar experiment using current pulses. The sample was connected to a pulse generator in order to send the current pulses through the MTJ device, and to an oscilloscope to measure the transmitted pulse.
First, the device magnetization was saturated once again in the AP state applying an external field of 20 mT. Following the same pattern for the DC current nucleation experiment, we approached now the coercive field for the intermediate state, while still maintaining the MTJ in the AP state. Figure 4.7a, shows an XMCD-STXM image of the device for an external magnetic field of -3.8 mT and a DC current of 0.8 mA. The pillar is in the AP state as confirmed by both the absence of contrast with the background in the XMCD image and the resistance value of 28.99 Ω associated to the state. We then injected a 15.2 mA, 10 ns current pulse, as measured with the oscilloscope. This leads to the nucleation of a skyrmionic intermediate state (see Figure 4.7b) with a white contrasted ring around the skyrmion. The corresponding resistance measured is 28.47 Ω, for a total jump in resistance of 0.52 Ω. This confirms that the intermediate state reached is the same as the one nucleated with DC current. Once again the magnetization reversal from AP to P happens from the edges of the MTJ, as evidenced by the bright ring in the XMCD image. Now, we applied a current pulse with the opposite polarity, -16.1 mA, measured with the oscilloscope, for 15 ns. This leads to the skyrmion annihilation (see Figure 4.7c) with a disappearance of the white ring. The resistance value of 28.97 Ω corresponds to the AP state. By applying again a positive current pulse of 15.2 mA for 15 ns the skyrmion is nucleated again and the intermediate resistance value of 28.47 Ω is recovered (see Figure 4.7d). The process was indeed reproducible. We demonstrated, therefore, the ability to perform the bipolar electric control of the skyrmion nucleation and annihilation process with current pulses exploiting the STT control of the magnetization of the MTJ.
The same experiment was performed starting from the P state rather than from the AP state. We saturated first the device in the P state by applying an external field of -10 mT. Then we reduced the external field to

-5 mT, where the device was still in the P configuration. In Figure 4.8a the XMCD contrast of the pillar is brighter than the background. By applying now a -14.5 mA, 10 ns current pulse, we nucleated a skyrmion in the pillar (see Figure 4.8b). The nucleation process happens this time from the center of the pillar: the skyrmion magnetization is aligned AP to the reference layer magnetization as can be observed from the darker contrast with respect to the white ring surrounding it. The measured resistance is 28.2 Ω, i.e. an increase of 0.8 Ω compared to the P state.

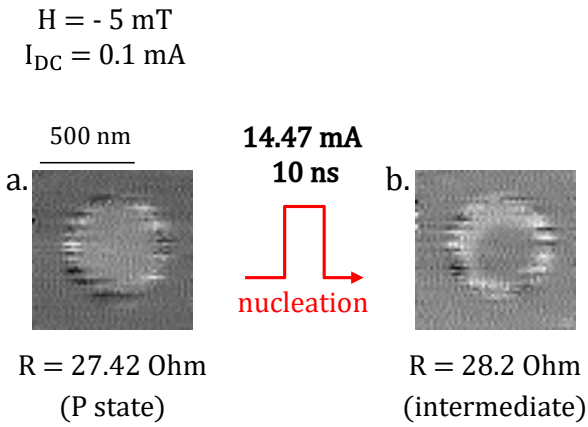

Figure 4.8: **Nucleation of a skyrmion with current pulses from the P state** | XMCD-STXM images obtained on a 500 nm pillar at the Fe L_3 edge at the energy of 709.8 eV for an external applied magnetic field of -5 mT and a current $I_{DC} = 0.1$ mA. a. The image shows the pillar in the P state. One can observe the brighter contrast with respect to the background inside the pillar. The corresponding measured resistance is 27.42 Ω. A -14.47 mA, 10 ns pulse is applied. b. A skyrmion is nucleated with the current pulse. The nucleation occurs now from the center of the pillar whose magnetization switches to the AP state while the crown surrounding the texture remains in the P state. The corresponding resistance is measured to be 28.2 Ω.

We tried several times to send back the pillar to the initial P state by using opposite current pulses, but we could never observe the annihilation of the skyrmion. Therefore, starting from the P state only the skyrmion nucleation process was possible, not the full bipolar control.

4.8 Time-resolved bipolar control of skyrmion in a MTJ

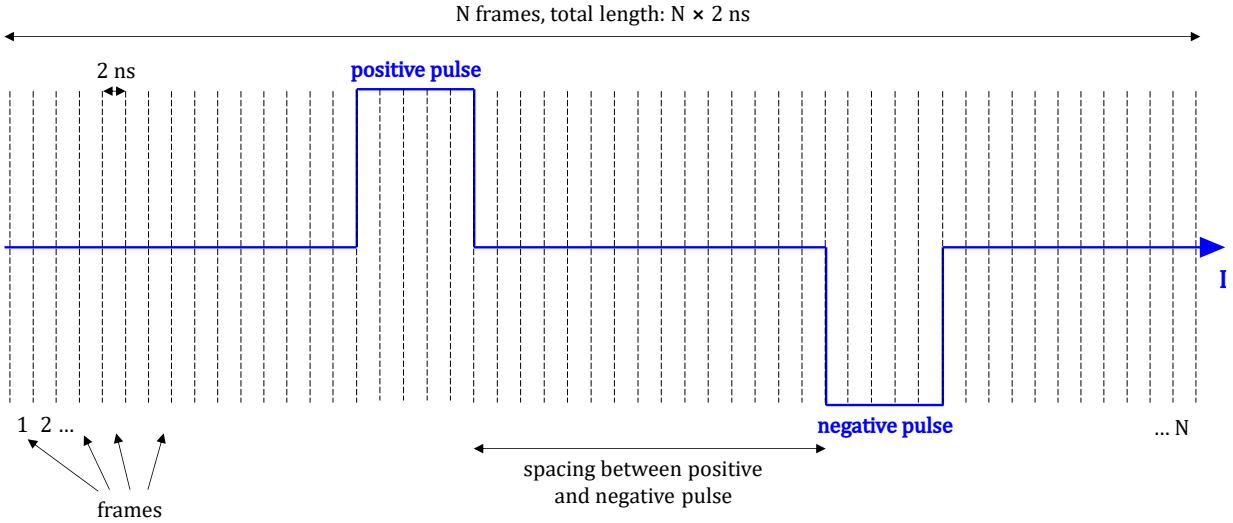

Figure 4.9: **Schematic of the excitation for time-resolved STXM** | Schematic of the excitation provided to the system and the acquisition of the dynamics. The obtained movie is composed of N frames, separated by 2 ns, for a total length of N × 2 ns. The frames at which the pulses arrive can be easily identified looking at the change in contrast in the movies. The number N and the spacing between pulses was changed from movie to movie.

4.8.1 System excitation

Since the electrical bipolar nucleation and annihilation of the skyrmion from the AP state was found to be reproducible, we decided to characterize the nucleation/annihilation dynamics by performing time-resolved pump-probe STXM measurement (see section 2.5.3). The time resolution was set to 2 ns by picking M = 1, as discussed in section 2.5.3. The excitation is given by a sequence of two successive current pulses, one positive and one negative, separated by a given spacing time. Several experiments were performed by changing either the total length of the excitation, 2 ns × N, the length of the pulses used for the excitation or the spacing in between them. The result obtained from a time-resolved experiment is a movie showing the dynamics of the magnetization undergoing a first excitation generated by the positive current pulse and a second excitation generated by negative current pulse. A schematic of the excitation process can be seen in Figure 4.9.

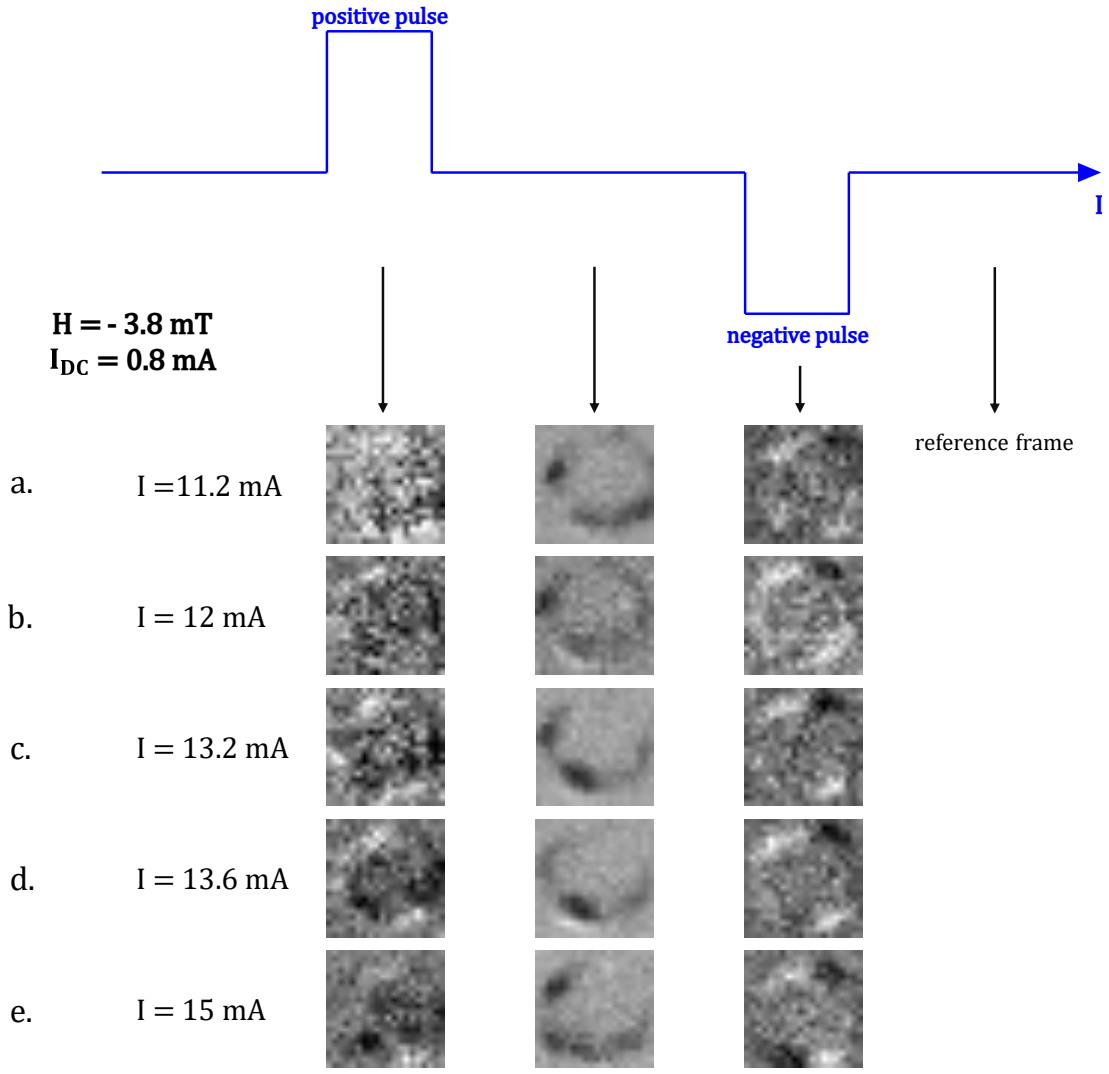

Figure 4.10: **Captures from time-resolved STXM for an external magnetic field of -3.8 mT and an applied DC current of 0.8 mA, normalized with a reference frame taken after the negative pulse** | Frames from different time-resolved STXM movies acquired under identical conditions (magnetic field of -3.8 mT and DC probe current of 0.8 mA), using x-ray photons of negative helicity. To normalize the movies the reference frame used is an averaged intensity of the frames taken after the negative pulse. The frames in the left column are taken at the peak of the positive current pulse, those in the right column are taken at the peak of the negative pulse and those in the central column are obtained averaging the intensity over different frames in between the two pulses to obtain a clearer contrast. The amplitude of the applied current pulses increases from a. to e.: 11.2 mA, 12 mA, 13.2 mA, 13.6 mA and 15 mA.

4.8.2 Results

Time-resolved STXM movies differ from static XMCD because they are typically acquired with a single photon helicity. So, in order to visualize the magnetic contrast it is necessary to normalize all the frames to a reference,

either a given frame or an average intensity obtained from several frames chosen from the movie itself. The contrast obtained represents therefore a change relative to this reference. In other words, the normalized frame at time t is given by $\text{Frame}_{\text{norm}}(t) = \text{Frame}(t) - \text{Frame}_{\text{ref}}$, where Frame(t) and $\text{Frame}_{\text{ref}}$ are respectively the measured frame at time t and the reference.
It is important to highlight how, in this situation, the visible magnetic contrast itself does not give a direct explanation about the process happening. This is because the magnetic configuration associated to the reference is unknown, so seeing a white, grey or black contrast can have different meaning. For example, an absence of contrast can result from subtracting two images in the AP state, so from a real situation of no magnetic contrast, or from subtracting two frames where the magnetization is aligned P in the same direction, resulting in an only apparent lack of magnetic features, that are actually hidden by the normalization. A more detailed explanation on how the contrast resulting from x-rays absorption works in the case of one or two magnetic layers, such as in a MTJ, is presented in Appendix B.

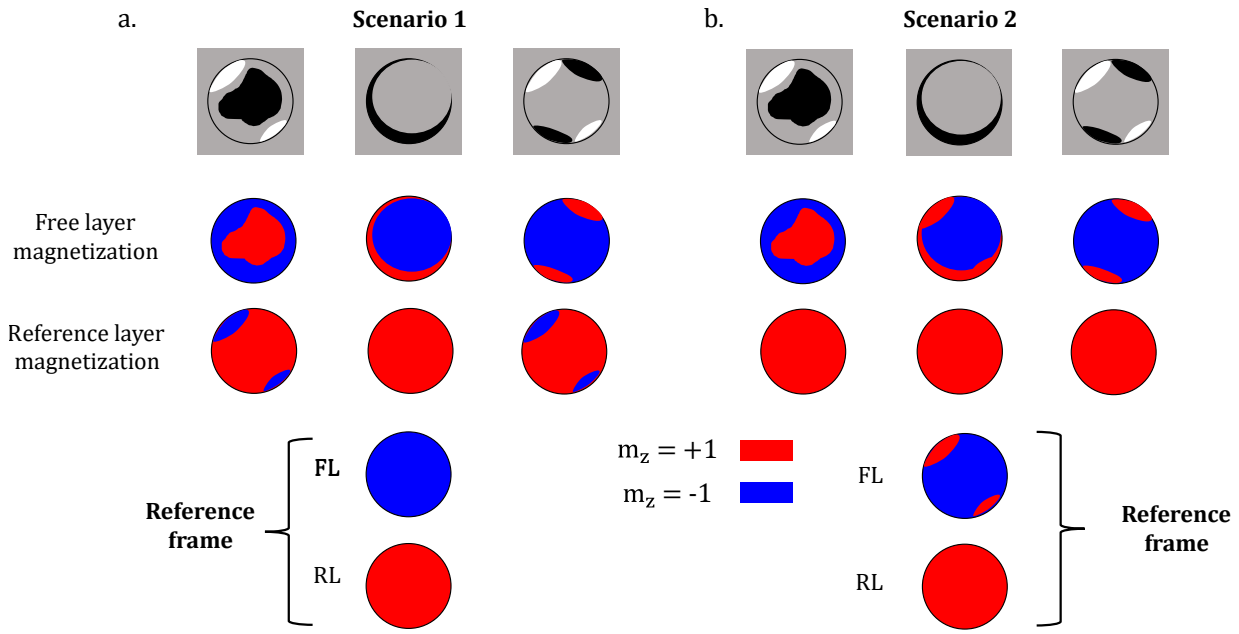

Figure 4.11: **Schematic of the possible dynamic frame and reference frame giving rise to the time-resolved movie in Figure 4.10** | In the first row is presented a sketch of the contrast observable in the frames in Figure 4.10. The second and third rows present respectively the magnetizations of the free and the reference layers of the MTJ, depending on the scenario. Below the third row the expected magnetizations of the FL and RL for the reference frame used for the normalization of the movies are shown. The red contrast stands for a magnetization along +z and the blue for a magnetization along -z. a. Scenario 1: white contrast due to the reversal of the reference layer magnetization. b. Scenario 2: white contrast due to reversed domains always present in the reference frame, which are annihilated during the current pulse injection.

4.8.2.1 First time-resolved STXM movie

We present here some of the results obtained from the time-resolved STXM measurements, exploiting the same field and current conditions as those used for static STXM measurement described in section 4.7. Figure 4.10 shows a series of frames acquired with negative helicity photons. All the movies are normalized to the average of the frames taken after the negative pulse. According to the static experiments, this reference is expected to be a spatially homogeneous AP state with the magnetizations in the free and reference layer pointing respectively along -z and +z. The amplitude of the applied current pulses increases from Figure 4.10a to 4.10e, from 11.2 mA to 15 mA. The frames in the left and right columns are acquired during the peak of the positive and negative current pulses, respectively. The images in the central column show the magnetic state between the positive and the negative pulses.
Similarly to the static experiments (Figure 4.7), one sees that the positive pulse leads to the nucleation of a magnetic skyrmion, via the nucleation of a reversed domain on the edge of the MTJ, as it can be observed by the black ring (P configuration) around a grey core (AP configuration) in the central-column frames, corresponding to a P configuration. The skyrmion magnetization remains in the AP configuration with respect to the reference layer magnetization. The predominantly black contrast observed across the dot during the positive pulse injection (left column) suggests that the skyrmion nucleation occurs via a transient excitation of the whole free

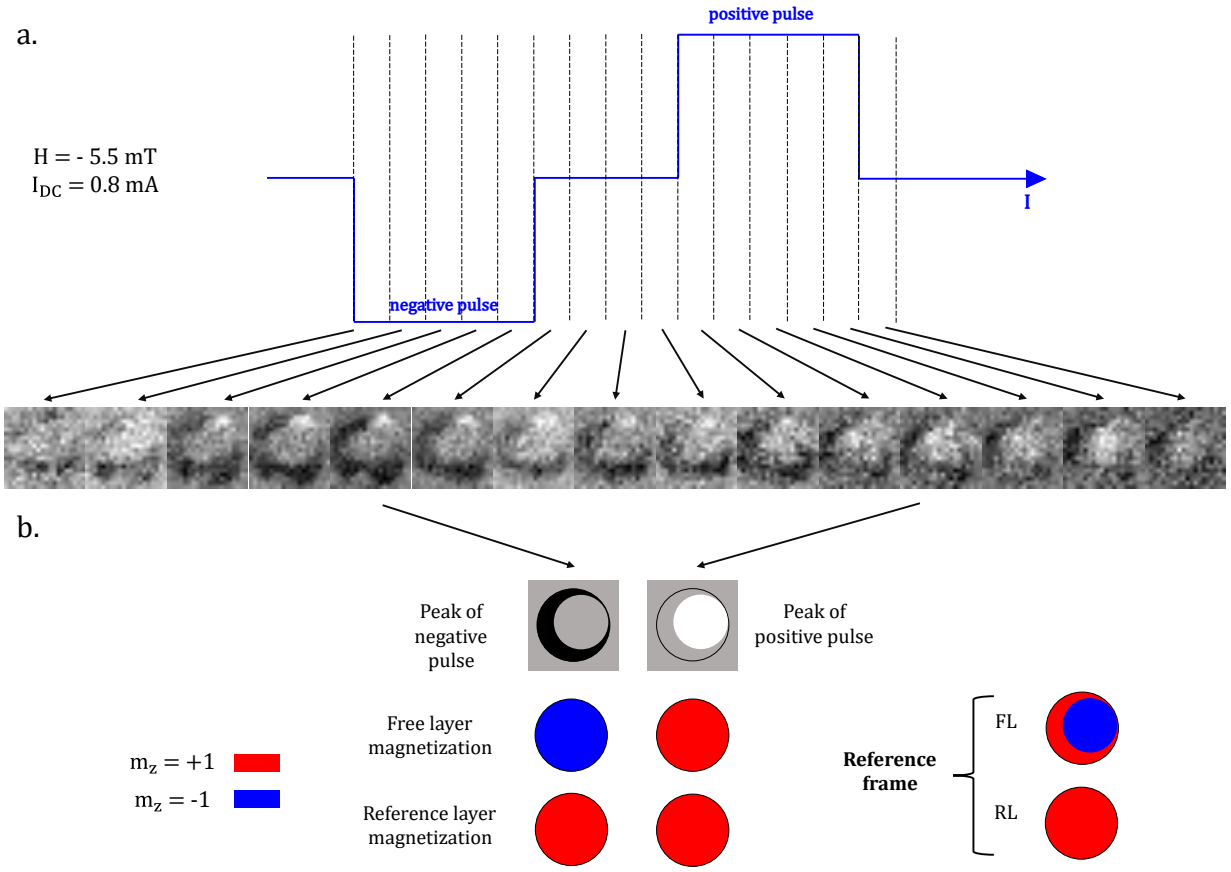

Figure 4.12: **Time-resolved sequence at -5.5 mT and schematic of the free and reference layer magnetization** | a. Excitation consisted of a negative followed 18 ns later by a positive pulse. The frames taken from the beginning of the negative pulse until the end of the positive pulse are shown. The reference frame used for the normalization is given by an average of the frames in between the positive and the negative pulses. The movie is taken using positive helicity photons. b. Schematic of the observed contrast in a. in terms of magnetization of the free and reference layers of the MTJ. Red represents $m_z = +1$ and blue represents $m_z = -1$.

layer magnetization toward the P state due to STT. After the pulse, the edges stay in the P state, while the center reverses back to the AP state, resulting in the skyrmion nucleation.

Unexpected domain contrast during pulse injection More complicated is to explain the presence of both black and white contrasts at pulse maxima (left and right column). A black contrast is explained by a P magnetization of the free and reference layer along +z, whereas white contrast could be explained by magnetization along -z. Therefore, a possible explanation would be a current induced switching of the reference layer magnetization along -z during the pulse as the free layer magnetization is already expected to be along -z (see Figure 4.11a). The pinning of the RL magnetization provided by the SAF would then bring it back to +z, making the white contrast to vanish. This scenario, for the negative pulse, can be explained by the effect of STT on the reference layer magnetization. Current-induced dynamics of the reference layer was already reported in literature [202] and was found to be responsible for back hopping in STT-MRAM.
However, for the positive pulse, the white contrast domain observed cannot be explained by STT, since the mechanism is not expected to favor P state along -z for this polarity. The black contrast observed during the negative current pulse is also unexpected. It could be explained by the switching of some areas of the free layer to the P state. However, cannot be explained by STT since it promotes a switching to the AP state for this current polarity. So, in both cases, other mechanisms have to be involved. One can speculate of a domain nucleation triggered by Joule heating and/or Oersted field which is favoured by a dipolar coupling with the reversed domain in the reference layer.
A second possible scenario for the presence of the unexpected white contrast during the current pulses is that it could result from the presence of a small reversed domains in the P configuration in the frame used for the normalization (see Figure 4.11b). This would mean that the reference state, the one after the negative pulse, is not fully AP: two small regions remain P, with the free-layer magnetization along +z, parallel to the

reference. During the current injection the domains would momentaneously disappear as the magnetization of the free layer switches to -z, such that the domains appear as a white contrast coming from the reference frame. However, STT is supposed to annihilate this domain only for negative current pulses, so that it does not explain its annihilation for positive current pulses.
In Appendix A.2 we present the same movie as Figure 4.10, but using as a reference frame the averaged frames between the positive and negative pulses, i.e. where the skyrmion is expected to be nucleated.
To conclude, unexpected domains nucleation and annihilation are observed on the dot edge during the negative and positive pulses injection. The phenomenon can be explained either by the nucleation of a reversed domain in the reference layer or by the annihilation of a domain in the free layer during the pulses. The physical mechanism behind the nucleation (annihilation) of these small edge domains still remains elusive.

4.8.2.2 Second time-resolved STXM movie

Figure 4.12a shows a sequence of frames obtained from another movie with a short delay between the positive and negative pulses: 9 frames corresponding to 18 ns in time. The movie is obtained under an external magnetic field of -5.5 mT. The reference frame is the average of the frames between the positive and negative pulse. The other type of normalization (the post-negative pulse normalization) is not possible as the two pulses are too close to each other. Since the observed sequence is the difference between the actual magnetization profile and a reference, the nucleated skyrmion is observed in the sequence when it is actually annihilated, meaning when the magnetization is saturated. The images are taken using positive helicity photons.
As a result, the observed sequence can be described as follow (see Figure 4.12b for a sketch explaining the actual magnetization texture): when the negative pulse comes, a black magnetic contrast starts to appear in the images, and reaches its peak, in terms of black area surface, in the frame at the center of the pulse, generating a half ring. The black contrast, for positive helicity, comes from the frame used as a reference. This would mean that, when the negative pulse is injected, the magnetization of the free layer switches along -z to align AP to that of the reference layer and reveals the P ring (black) from the reference frame. When the positive pulse is injected, the black ring starts to fade until fully disappearing and at the same time a white contrast appears. This can be explained by the free layer magnetization going fully P along +z when the pulse arrives, generating a white contrast. The positive pulse however does not succeed in the full switching, therefore the center of the pillar goes back to the AP state while the P state crown, that of the reference frame, remains.
To sum up, this sequence suggests the following dynamics: the negative current pulse leads to the skyrmion annihilation, with the magnetization in the AP state, while the positive current pulse leads to a magnetization reversal toward the parallel state (white contrast in the dot's center), followed by the skyrmion nucleation.
The dynamics highlighted by the movie in Figure 4.12 seems to be generated by a scenario that is similar to the one proposed as scenario 1 in the previous section, a full skyrmion nucleation and annihilation starting from the AP state with a transient toward the P state.

4.9 Conclusions

To conclude, we have demonstrated the bipolar electrical control of a skyrmion in an MTJ using *operando* magnetic microscopy experiments. The nucleation and annihilation process was performed exploiting the STT in the MTJ by injecting both DC current and current pulses.
Time-resolved pump-probe STXM experiments demonstrate the highly reproducible back and forth skyrmion nucleation and annihilation induced by successive positive and negative current pulses. The dynamical experiments suggest that the skyrmion nucleation occurs via a full reversal of the dot magnetization during the current pulse, which eventually relaxes to a skyrmion via a second reversal in the center of the dot when the pulse is off. Domains with unexpected contrast during the pulse injection suggest additional transient reversal of the reference layer or non-complete reversal of the magnetization. Micromagnetic simulations and electrical measurements are currently in progress to further clarify the observed dynamics.

Chapter 5

Introduction on neural networks and reservoir computing

Contents

5.1 Introduction . . . 84
5.1.1 Human brain . . . 84
5.1.2 Artificial neural networks . . . 85
5.1.3 Recurrent neural networks . . . 88
5.2 Reservoir computing . . . 89
5.2.1 Echo state networks . . . 89
5.2.2 Liquid state machines . . . 90
5.3 Physical reservoir computing . . . 91
5.4 Multiplexing . . . 92
5.4.1 Time multiplexing . . . 92
5.5 Implementation of spintronics PRC . . . 92
5.6 Conclusions . . . 97

5.1 Introduction

The Von Neumann architecture is at the foundation of the modern computers architecture [203]. The basic principle of this architecture is to have a memory, where data and instructions are stored, physically separated from the computational unit, the CPU, which enables the computer to perform several tasks. When executing a task, the CPU reads and retrieves data and instructions from the memory, generating a continuous flow of information between the two main units. The Von Neumann architecture is ideal to perform sequential tasks and algorithms. However, the sequential fetching of data between the CPU and the memory is hindered by the so-called "Von Neumann bottleneck", i.e. the fact the throughput of data transfer is lower than the computational rate of the CPU. This occurs because in the last years the data transfer efficiency has not improved as much as processing and storaging technologies [204, 205].
These considerations have driven researchers in the field to seek ways of combining memory and logic within the same component, following a logic-in-memory approach. Moreover, although conventional computers demonstrate extreme efficiency in performing complex calculations, they have lower performances when computing tasks that appear simple to humans, such as image or voice recognition. The situation has motivated the research for new type of hardware architectures inspired by the human brain, for which such tasks are naturally performed. Neural networks, a type of artificial intelligence (AI) models inspired by the brain, have a massively parallel architecture and a high number of parameters to be used for modelling. Neural networks intrinsically merge the computation (performed by the neurons) and the memory (performed by the synapses). As neurons are interconnected by the synapses the information does not need to be transferred, but is directly processed where it is. The Von Neumann architecture is not suitable to emulate the type of computation performed by neural networks, as the energy and time consumption would be too high due to the continuous fetching of information between the CPU and the memory, and anyway orders of magnitude larger than that of the brain. The research is focusing then not only in developing algorithms that are inspired by the brain behaviour, but also physical circuits to solve tasks in a more efficient way than modern computers do. Spintronic devices are promising for this type of application because they have several features, such as non-volatility, plasticity, stochastic behaviour, that could be exploited to mimic biological neural systems.
In this chapter I will provide an overview of neural networks and I will focus on a specific type of neural network, the reservoir computing, for which spintronic devices can be quite suitable [24].

5.1.1 Human brain

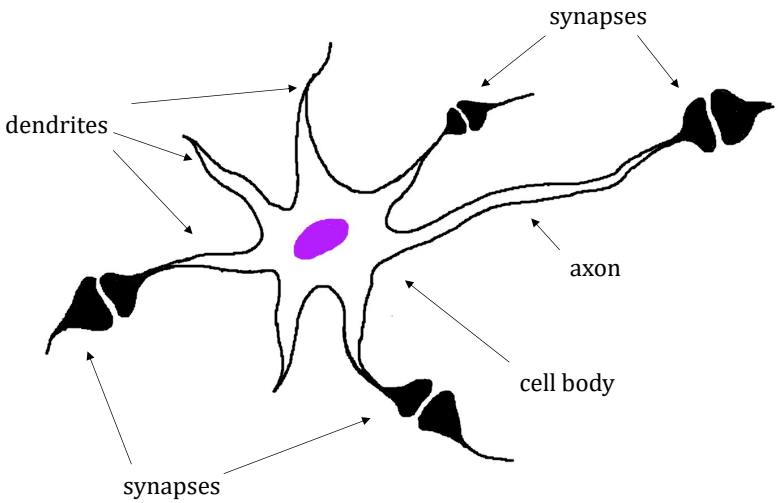

Figure 5.1: **Schematic of a biological neuron** | Schematic of a biological neurons with its synapses that allow the connections with other neurons.

The human brain has always attracted a major interest for its ability of solving pattern recognition problems and for its ability to memorize information. The human brain is able to recognize the same person in different pictures, with different haircuts, clothes, facial expression, age. The human brain is also able to memorize the face of a person and recognize it after time. The brain can also identify the same phoneme pronounced by different people and it is able to learn languages, hence to associate a meaning to new sounds, and to succeed in recognizing them when listening, and in recalling them when talking. In the human brain, the processes of learning and memorizing are dynamically interconnected. This property enables organisms to keep refining their abilities and quickly adapt to change in environmental conditions. While enabling all the cognitive abilities of thinking, memory, feeling emotions, having conscience of the surrounding, the brain also regulates all the

body functionalities. Furthermore, it is extremely efficient in executing all these activities as it processes all the received information and generates a response extremely fast [206] and with a low power consumption [207]. The human brain is really the highest peak of biological complexity.

The basic description of the brain architecture arrived only at the end of the 19th century. In 1906 C. Golgi and S. Ramon y Cajal were jointly awarded for the Nobel prize in medicine for their work on the visualization of nervous cells [208, 209]. The basic unit cell of the brain is the neuron. Each neuron is connected to several other neurons (around 1000), for a total of around 10^{11} neurons in the brain. The neuron connects to other neurons through an axon that terminates with a synapse. The synapses connect to the dendrites of other neurons to send signals. Each synapse has a different weight depending on how much that connection is used. A schematic of a biological neuron can be observed in Figure 5.1.

The synapses send an electro-chemical stimulus to the other neurons, that gets integrated in the nucleus of the neuron. The functioning is explained in simple terms in the following lines [210]. Inside the neuron cell, there is a high concentration of potassium ions K^+, while outside there is a high concentration of sodium ions Na^+, thus generating a ionic imbalance. Naturally, the K^+ and Na^+ ions tend to respectively exit and enter the cell through selective channels to down the electrochemical gradient. The resting membrane potential arises primarily from the membrane's greater permeability to K^+ ions than to Na^+ ions, while some pumps in the membrane maintain the ionic gradient by pumping $3Na^+$ outside the cell for every $2K^+$ brought inside. As a result, the intracellular side becomes negative relatively to the extracellular environment, establishing the resting potential. The membrane receives inputs from multiple synapses and behaves as a leaky integrator: each excitation input produces a small local depolarization that transiently raises the membrane potential. If inputs are separated in time and space, the potential relaxes back to resting one. By contrast, when the depolarizations sum sufficiently, the membrane potential reaches a negative threshold. This causes the opening of the selective sodium channels generating a massive entrance of Na^+ inside the neuron in order to re-balance the membrane potential, this is the so-called depolarization phase. The potential of the membrane becomes positive on the inside due to the entrance of sodium ions, until it reaches a second threshold for which the channels regulating the potassium circulation open and the K^+ ions exit the cell. The potential is slowly rebalanced, this is the repolarization phase. Finally, the channels close again and the ionic concentrations go back to their initial levels, the so-called refractory phase. The schematic of the different phases of the membrane potential is presented in Figure 5.2.
The mechanism of a permeable membrane that spikes when reaching a certain threshold potential has been modeled in the Leaky-Integrate and Fire (LIF) neuron [211]. In the LIF model the membrane potential is described by the following equation:

$$C\frac{du(t)}{dt} = -\frac{1}{R}u(t) + \left(i_0(t) + \sum w_j i_j(t)\right) \tag{5.1}$$

where C is the capacitance of the neuron membrane, u(t) is the membrane potential, R is the input resistance, $i_0(t)$ is the external current driving the neural state, $i_j(t)$ is the input current from the j-th synaptic input and w_j is the strength of the j-th synapse. Whenever the membrane potential reaches the potential threshold value u_{th} due to the summation of the incoming input currents, the neuron spikes [212]. Figure 5.3 illustrates the process: when the input current is not large enough for the membrane potential to reach the threshold, nothing happens, while the neuron spikes when the input overcomes the threshold amplitude. The leaking time is given by the time constant $\tau = RC$. Just after reaching the threshold potential, the membrane potential goes back to its initial level u_{res} and hold it for a time that represents the refractory period. When the input reaches the threshold and maintain the level, the neuron spikes periodically, depending on its integration and refractory time. The key properties of a neuron are its non linearity and its memory, that is coming from the integration. The LIF model and its relation to the different phases of the membrane potential due to the motion of sodium and potassium ions is shown in Figure 5.2.

Starting from this first initial knowledge, research has been focusing on developing theories, models and technologies to better understand and reproduce the brain behaviour. Machine learning aims at understanding rules from provided existing data in order to produce classification and prediction when fed with unknown data. The so called artificial neural networks try to emulate the brain behaviour to solve specific tasks. Emulating the behaviour of the neurons can allow to solve tasks like image or speech recognition in a more efficient way than a normal computer would.

5.1.2 Artificial neural networks

The first model of an artificial neuron was designed in 1942 by McCulloch and Pitts [213] based on the biological one. This model still forms the basis of most neural networks. They assumed a fixed voltage threshold for the

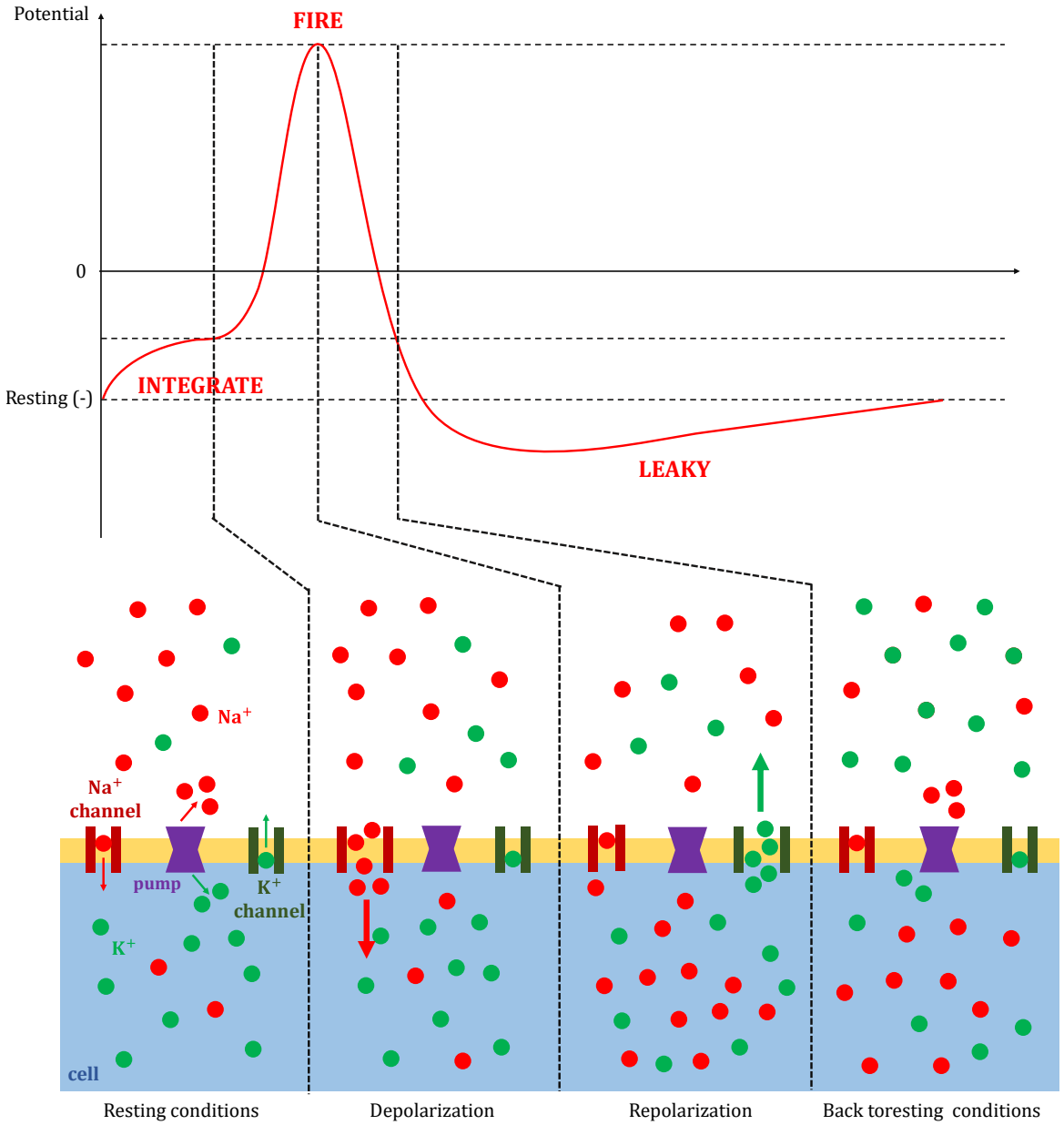

Figure 5.2: **Evolution of the membrane potential and its relation to the LIF neuron approach** | Schematic of the evolution of the membrane potential related to the LIF neuron approach. In resting conditions the membrane potential is negative. If the summation of the small depolarization signals from interconnected synapses has brought the membrane potential to the initial threshold, the depolarization phase starts. Here, high amount of Na^+ enters the neuron cellular environment bringing the potential to a positive value. This process is similar to the integrate phase for a LIF neuron. When a positive potential is reached the LIF neuron fire. In the biological neuron framework the repolarization phase starts, when high amount of K^+ ions are expelled from the cell to decrease the potential until the membrane potential is brought back to a negative value and the cell goes slowly back to initial conditions. In the LIF neuron approach this is the leaky phase.

membrane potential and that inputs coming from synapses connected to the neuron dendrites produce changes in the potential. Multiple excitations coming from the synapses are needed to activate the neuron and make it fire. In the model a set of inputs (the dendrites) is mapped to a set of variable weights (the synapses). The inputs coming from the dendrites are multiplied by their synaptic weights and summed. If weighted sum exceeds a threshold the neuron spikes and produces one single output. The model also includes a synaptic delay that was meant as the time between the arrival of impulses and the spiking, applied equally to all the connections. It is also assumed a fixed window for the summation of the incoming inputs, the integration time, that is intended as the maximum interval of time over which the incoming inputs can summate to reach the threshold to make the neuron fire. The schematic of an artificial neuron is shown in Figure 5.4a. Mathematically, an artificial neuron can be modelled as:

$$y = f\left(\sum_{i=1}^{n} w_i x_i - b\right) \tag{5.2}$$

where y is the output signal, b is the activation threshold of the neuron, x_i are the inputs from the dendrites and w_i are the synaptic weights. The summation is over n, that corresponds to the number of dendrites. f is the so called activation function of the neural network that can take different shapes.
The first artificial neural network (ANN) was proposed by Rosenblatt in 1957 [214]. It is called the single layer perceptron and it was implemented to solve a binary classification problem. It is essentially an artificial neuron with an Heaviside step function as an activation function. When the input is greater than a certain threshold the output of the network is 1, otherwise -1. It is a first example of supervised learning [205], in which the network is trained on input examples with known target outputs. The training consists in calculating the best synaptic weights in order to obtain the desired outputs for the given inputs. Once the weights are determined the machine is used to infer outputs for new unknown examples, the testing part. The counterpart of supervised learning is the unsupervised learning for which the ANN has to detect regular patterns in the data without having any a priori knowledge. Unsupervised learning neural networks are not the focus of this thesis, so I will not deepen the explanation, while I will focused on supervised learning neural networks.

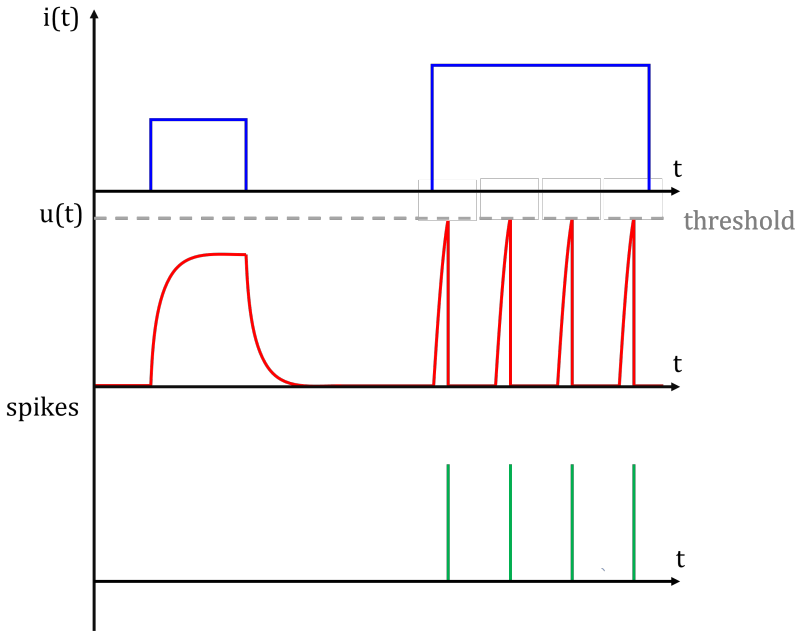

Figure 5.3: **Schematic functioning of a LIF neuron** | Schematic of the LIF neuron functioning. Top: input current versus time. Middle: membrane potential. Bottom: spiking response of the neuron. In the first case, the input current is not sufficient for the membrane potential to reach the threshold. The second current input is large enough for the potential to reach the threshold so the neuron spikes several times. Adapted from [212].

5.1.2.1 Feed forward neural networks

The perceptron falls in the category of feedforward neural networks (FNN). The single layer perceptron could not solve complex tasks, but its improved version, the multilayer perceptron, can. FNN are composed of an input layer, an output layer and one or more hidden layers in between (see Figure 5.4b). The flow of data is unidirectional, and the size of the network depends on the number of hidden layers. A neuron in one layer is connected to all the neurons in the following layer. The connection between two neurons i and j is characterized by a weight coefficient w_{ij} that represents the importance of the connection. The output value of the i-th neuron x_i is determined by:

$$x_i = f(\xi_i) \tag{5.3}$$

where ξ_i is the potential function of the neuron and f is the activation function. The potential function is given by:

$$\xi_i = \vartheta_i + \sum_{j \neq i} w_{ij} x_j \tag{5.4}$$

where ϑ_i is the threshold coefficient for the i-th neuron. The second term is a sum over the contributions of all preceeding neurons connected to the i-th one. The most popular algorithm to train FNN is back-propagation. It uses the steepest-descent method to minimize the error in between the obtained output and the desired output by modifying the weights and the threshold coefficients layer by layer. The algorithm starts from the last layer and iterates backward to the first layer [215, 205]. For each of the layers it calculates the gradient of the loss function with respect to the parameters of the network, and finds the values of those parameters that minimize it. When the loss function converges to a predefined tolerance, the training of the network is considered completed. Due to its complexity, a FNN can be used to solve difficult tasks, and it is in general quite suitable for image classification. One of the critical aspects of FNN is the choice of an appropriate size, in terms of hidden layers, depending on the task. There is not a clear answer to this problem because there is no way to determine a good topology for the network just by looking at inputs and outputs [216, 215]. The size needed strongly depends on the amount of training examples available, the noise and the complexity of the classification. The best way is to try different sizes and evaluate the error in the classification for each of them. The drawback of using FNN with a large number of hidden layers is the growth of the training complexity and hence its energetic cost.
While FNNs work well for classification tasks, they are not inherently suited to learn from sequential data arranged in a chronological order, like an audio clip, a video clip or a text stream. For these types of data, temporal neural networks have been developed.

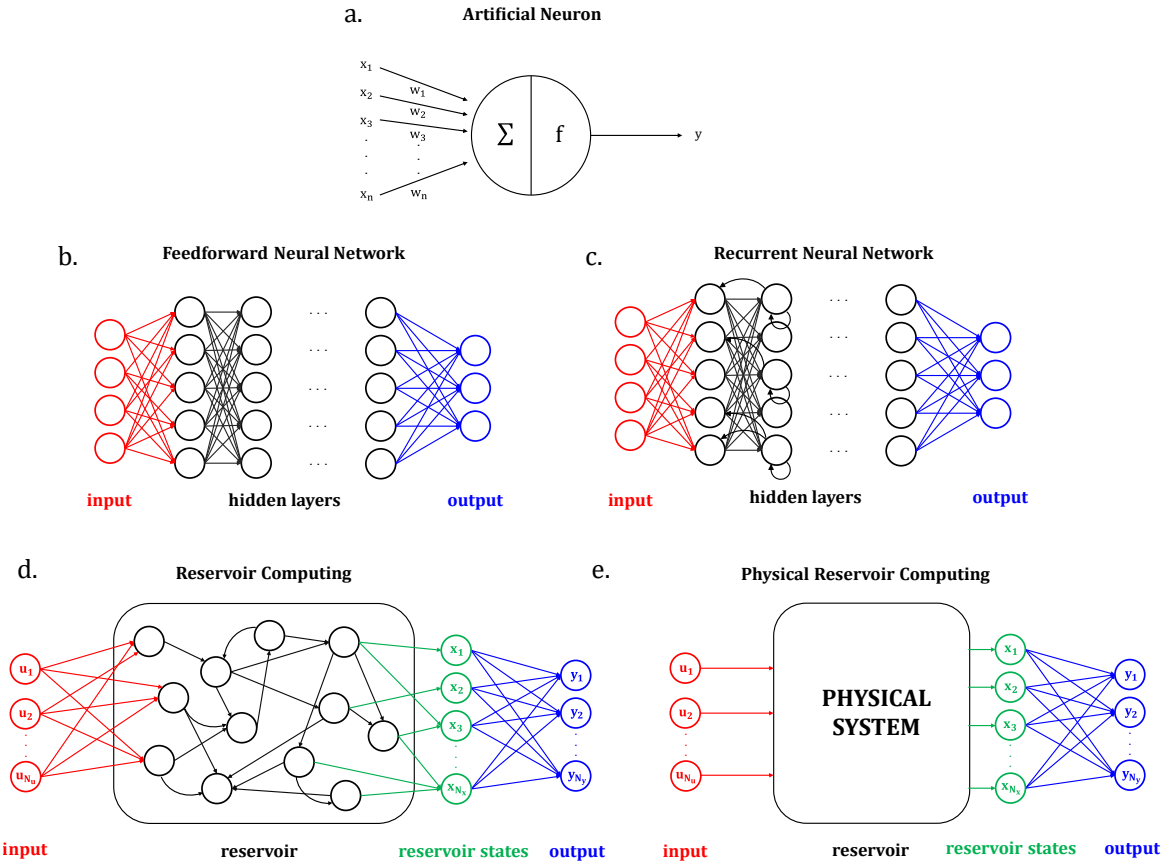

Figure 5.4: **Schematic of an artifical neuron and different types of neural networks** | a. Schematic of a single artificial neuron. b. Schematic of a feed-forward neural network. c. Schematic of a recurrent neural network. d. Schematic of a RC system. e. Schematic of a PRC system.

5.1.3 Recurrent neural networks

For the processing and prediction of sequential data, the most suitable type of neural network is the recurrent neural network (RNN) [217, 218, 219, 220, 205]. RNN approximates dynamical systems by introducing an explicit temporal dimension: the same input can result in different output for different time steps. The information in RNN does not only propagate in one direction, but it is recurrent due to introduction of feedback loops, in order for the past data to act on the present input (schematic of a RNN can be observed in Figure 5.4c). RNN have the ability of "memorizing" past inputs for some time. Because of the feedback loops, the output layer affects the input layers, generating a big improvement in the learning ability. All the neurons

become computing neurons and the type of connection can be various, from fully interconnected networks to networks where areas are still belonging to a feedforward structure. A feedback loop to the node itself is also possible. The output of one node does not depend anymore only on the node itself but on the state of the system in previous moments. Due to this ability, RNNs can process data of uncertain length and can capture complex time dependencies.
The training of RNN can be hard as the complexity of the connections in the hidden layers has increased with respect to the FNN. When using a similar training approaches to the one used for FNN, the gradient minimization, one of the fatal problems that can occur is the inability to complete the training due to vanishing or exploding gradients. This makes the gradient minimization method not efficient for training RNN. RNN can also suffer from short term memory, meaning that for long sequences, the information from earlier steps can be left out. To handle the training of RNN two main models have been developed: the Long Short Term Memory (LSTM) [221] and the Gate Recurrent Unit (GRU) [222]. Both are based on the idea of developing an activation function more sophisticated than conventional ones, introducing a "gate" that modulates the flow of the previous information. LSTM can well model long range dependencies as it also includes a cell state in which information coming from previous levels are stored, and gates decide whether new information coming should pass through later steps or not. The GRU uses a gate to determine the current hidden state level, making the training fast.

5.2 Reservoir computing

In 2001 two new approaches to RNN were proposed independently by W. Mass [223, 224] and and by H. Jaeger [225, 226], respectively under the name of Liquid State Machine (LSM) and Echo State Networks (ESN). Nowadays, they are in general referred to as the Reservoir Computing (RC) paradigm. The fundamental difference in the RC approach with respect of a RNN is that only the output layer weights are trained while the weights in the hidden layers are fixed. The fundamental idea of RC is based on an observation made by Schiller and Steil in 2005 [227, 228]. They noticed that when training a neural network, the dominant changes were happening in the weights of the output layer, while the other weights were converging slowly. In RC, differently than in traditional RNN, it is done a conceptual and computational separation between the reservoir, the inner neurons and the weights of the network, and the readout layer, the neurons and the weights that produce the output. The error of the network influences only the readout layer as the weights of the connection inside the reservoir are set and they do not change during the learning. A schematic of the reservoir is shown in Figure 5.4d.

5.2.1 Echo state networks

The ESN model proposed by Jaeger [226, 229] consists in a discrete-time artificial neuron. Three units are distinguished: the input, the internal units and the output. For a given input $\mathbf{u}(n) \in \mathbb{R}^{N_u}$ where n represents the discrete time input n = 1, ..., T, where T is the number of datapoints of the training dataset, an output $\mathbf{y}^{target}(n) \in \mathbb{R}^{N_y}$ is known. The task consists in finding a model with an output $\mathbf{y}(n) \in \mathbb{R}^{N_y}$, where $\mathbf{y}(n)$ minimizes the error with respect to $\mathbf{y}^{target}(n)$. $\mathbf{x}(n) \in \mathbb{R}^{N_x}$ is the state vector of the reservoir units and it is updated according to the relation:

$$\mathbf{x}(n) = \mathbf{f}\big(W^{in}\mathbf{u}(n) + W\mathbf{x}(n-1)\big) \tag{5.5}$$

where W^{in} is the weight matrix that connects the input to the reservoir and W is the matrix for the recurrent connections inside the reservoir. $\mathbf{f} = (f_1, ..., f_{N_x})$ are the activation functions of the internal units. The recurrence is present as the state $\mathbf{x}(n)$ depends on the input but also on the previous state $\mathbf{x}(n-1)$. The output is in general given as:

$$\mathbf{y}(n) = W^{out}\mathbf{x}(n) \tag{5.6}$$

where W^{out} is the output weight matrix, that is computed by linear regression, minimizing the mean square error between $\mathbf{y}(n)$ and $\mathbf{y}^{target}(n)$. The performance of the ESN depends on the design of the reservoir part. It consists in choosing the size N_x of the reservoir, the matrices W and W_{in} and the activation function $\mathbf{f}$ for the internal units [226]. For the reservoir to function properly, it must satisfy the echo state property (ESP), meaning that the influence of the initial conditions should vanish over time [230]. The echo state property is satisfied if the spectral radius of the matrix W (that is the maximum eigenvalue of the matrix, λ_{max}) is smaller than 1. The echo state property can be seen as a form of fading memory, meaning that the outputs for two inputs that are close in the recent past have to be close, even if the two inputs are not close in the distant past. Another important property is that the reservoir must provide a non-linear expansion of the input space. For some classification tasks for which the inputs are non-linearly separable, the reservoir maps them into a

space where they can be linearly separated at the output. When choosing the parameters of the reservoir it is important to find the good trade-off between the non linearity and the echo state property [231].

5.2.2 Liquid state machines

Liquid state machines [223, 224] use as a model the spiking neural networks (SNNs), a type of neural network where neurons communicate through spikes (LIF neurons), and implement a recurrent connectivity. LSM are composed of an input layer, a reservoir or liquid unit and a readout circuit, similarly to ESN. The reservoir is made of several leaky-integrate and fire neurons connected to each other. The connection follows biologically inspired rules, the probability that two neurons are connected decreases with their distance. The readout layer is also made of LIF neurons but they are not interconnected unlike those inside the reservoir. The "liquid" term comes from a similarity with a liquid media that gets excited by an external stimulus.
The idea behind the LSM is that the availability of a sufficient amount of training data for a neural network is a primary bottleneck. The readout neurons are taking care of the learning in a single and trivial stage while the liquid serves as a pre-processor for the readout neuron. The liquid expands the range of the possible functions of the input u(t). The readout neurons can extract different summaries of the information coming from the input processed by the same liquid [224]. The input and the output are continuous function in time u(t) and y(t) respectively. The dynamics of the liquid or reservoir can be modeled as:

$$x^M(t) = (L^M u)(t) \tag{5.7}$$

where x^M is the reservoir state, u is encoded as a sequence of spikes and L^M is a filter that transforms the input into the reservoir state. The output is obtained by:

$$y(t) = f^M(x^M(t)) \tag{5.8}$$

where f^M is a memory-less readout map. The state $x^M(t)$ is *liquid* as it changes continuously while it receives the input function u. It is up to the readout map f^M to select at which temporal resolution the state of $x^M(t)$ is sampled and transformed into an output [223]. The filter L^M has to satisfy some properties. First of all, it must be time-invariant, meaning that a temporal shift t_0 in the input will cause a temporal shift t_0 in the output as well. Secondly, the filter needs to have a fading memory, as already required for the reservoir of an ESM. This means that the current output primarly depends on the recent history of the input function within a finite interval [-T,t], where t is the actual time.

The term reservoir computing can be traced back to the work of Verstraeten *et al.* [232] where it was proposed a first unified framework of reservoir-based method like ESN and LSM. We give now the general framework of reservoir computing, following [233]. RC is a dynamical system that implements a desired mapping from inputs to outputs. A dataset demonstrating the desired relation between input and output is provided to the system to train it. The task can be a time series, where the input is a time trace and the output its continuation, or a classification task where the input is a signal and the output is the classification of different parts of it in different categories. The desired RC system receives an input $\mathbf{u}^{\text{train}}(t) \in \mathbb{R}_u^N$ and produces an output $\hat{\mathbf{y}}(t) \approx \mathbf{y}^{\text{train}}(t)$, where $\mathbf{y}^{\text{train}}(t) \in \mathbb{R}_y^N$ is the target output. The reservoir is represented by a high dimensional state X(t) driven by the input signal $\mathbf{u}^{\text{train}}(t)$. The state variables of the reservoir $\mathbf{x}(t) \in \mathbb{R}_x^N$ are accessible to read. When the reservoir is driven by the training input $\mathbf{u}^{\text{train}}(t)$ we can read its state as $\mathbf{x}^{\text{train}}(t)$. A readout function F maps the reservoir state variables to the output according to:

$$F\big(x_1^{\text{train}}(t), ..., x_N^{\text{train}}(t)\big) = \hat{\mathbf{y}}(t) \tag{5.9}$$

The F function is obtained by minimizing a loss function $L(\mathbf{y}, \hat{\mathbf{y}})$ which evaluates the difference in between the obtained and the desired output. In general F is obtained with a simple linear regression. The F function is the one containing the adjustable weights to be trained in order to connect the reservoir and the output. After the training procedure, F is fixed and the reservoir can be used to make predictions on new data that were not used in order to test its performances.
The advantages of a system like RC are several. Firstly, it can be used for any temporal task which can provide an input and an output. Secondly, any non-linear, dynamical system can be used as a reservoir. The system has to provide some characteristics that are explained in detail in the following section. The system chosen as a reservoir does not need to be trained or modified. This makes the training of the neural networks highly efficient and computationally inexpensive as only the last layer has to be trained. Also RC can be used to learn different mapping to the same input signal. The original motivations that gave rise to reservoir computing, i.e. the need of a more efficient training for RNN has been surpassed by new deep learning methods, like Backpropagation Through Time [234], but due to its simple characteristics RC its still flourishing in a variety of field (see section 5.5).

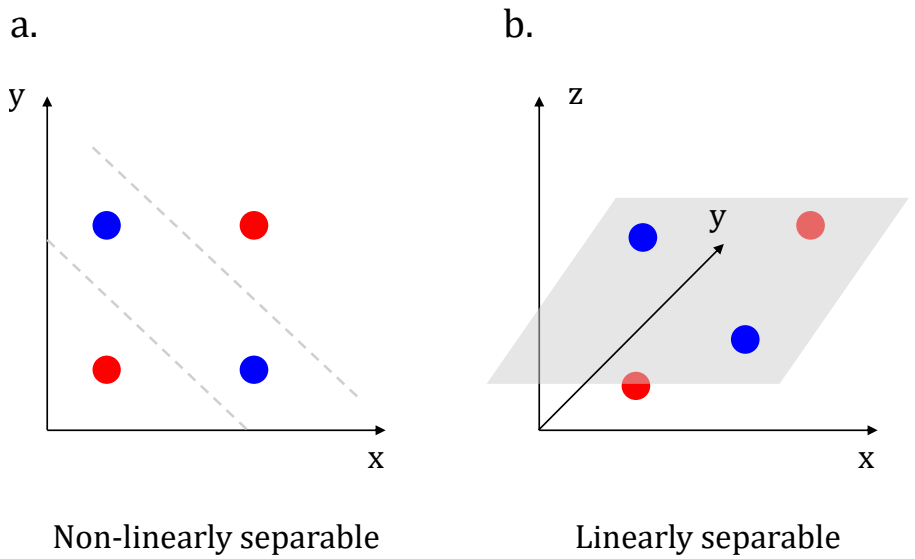

Figure 5.5: **Linear separability** Illustration of the mapping a problem into a higher-dimensional space to make a problem linearly separable. adapted from [235]. a. In two-dimensional space there is no single straight line that can separate the blue dots from the red dots. b. If the problem is non-linearly mapped into a three-dimensional space, now it exists a plane that can separate the blue dots from the red dots, so the problem has become linearly separable in the new space.

5.3 Physical reservoir computing

An extension to the concept of reservoir computing is physical reservoir computing (PRC), in which the reservoir part of the network is substituted by an actual dynamical physical system (see Figure 5.4e). Any dynamical system has the potential to serve as a reservoir computing as long as it fulfills some requirements. The first is high dimensionality: the reservoir computing has to map the input into a high dimensional space, in order to facilitate the separation of originally inseparable inputs and to capture spatio-temporal dependencies. The second is the non-linearity, the reservoir has to operate as a non linear map of the input. This property allows for transforming non-linearly separable input into linearly separable inputs in order to solve classification tasks. A schematic of the non-linearity property is represented in Figure 5.5. The problem shown is non-linearly separable in two dimensions, but when mapped in a state with 3 dimensions, it becomes linearly separable. The third requirement is the fading memory property. As already explained for both ESN and LSM, it is necessary that the output of the reservoir presents a memory, a dependency, on recent previous inputs, but not on distant inputs. The fading memory can be also expressed as a short term memory, because the output shows an influence on inputs just within a short interval in time [235, 236]. Also, PRC should present separation property, meaning that it has to produce a sufficiently different response to input belongings to different classes. Last but not least, the reservoir needs to be insensitive to small fluctuations and noise, in order to be able to classify correctly similar inputs. If the system does not show resilience to noise, two same inputs slightly modified by a noise component could be assigned to two different outputs.
Once a system that satisfies these requirements is found, the computing is operated as explained in the section 5.2. Inputs are provided to the physical system and the state of the reservoir is read. The inputs and the outputs of the reservoir could be different types of signals depending on the physical system itself. The state of the reservoir $\mathbf{x}^{\text{train}}(t)$ as a response to an input training signal $\mathbf{u}^{\text{train}}(t)$ is collected and put into a matrix $S = [x^{\text{train}}(1), ..., x^{\text{train}}(N_{\text{train}})] \in \mathbb{R}^{N_x \times N_{\text{train}}}$ where N_{train} is the temporal length of the training signal. The desired output is also collected into a matrix $D = [y^{\text{train}}(1), ..., y^{\text{train}}(N_{\text{train}})] \in \mathbb{R}^{N_y \times N_{\text{train}}}$. The optimal weights to get the desired output from the input signal are obtained by performing a linear regression. The relation between the reservoir state and the output is the following:

$$\mathbf{y} = W^{\text{out}}\mathbf{x} \tag{5.10}$$

The matrix W^{out} that satisfies the relation for a given task is computed through the least square approximation as:

$$W^{\text{out}} = \min \sum_{i=1}^{N_x} (W^{\text{out}'} x_i - y_i)^2 \tag{5.11}$$

where $W_{\text{out}'}$ represents all the possible matrices that satisfy the relation between x and y. The solution to this

problem is given by:

$$W^{out} = \left(S^{\dagger}D\right)^{T} \tag{5.12}$$

where $S^{\dagger}$ is the Moore-Penrose pseudo-inverse matrix [237] of the collection matrix of the states of the reservoir. Once the parameters are learned, the system is evaluated on new samples that were never seen before by the network.
The parameters of the physical system chosen to perform the PRC can be adjusted within the range of the demanded constraints in order to perform the best classification/prediction depending on the provided input signal.

5.4 Multiplexing

As just explained, one of the main requirements for a reservoir computing system is to provide a high dimensionality. The vector $\mathbf{x}(t) \in \mathbb{R}^{N^x}$ is the state vector of the reservoir and it has a dimensionality N_x. In a neural network, each neuron i is a single state variable $x_i(t)$ of the reservoir's state vector, so the dimensionality of the system can be expanded by increasing the number of neurons. For a PRC, we can imagine that different neurons can be represented by separated physical systems, each one with its own dynamics, to provide several degrees of freedom to solve the initial problem. This scenario is called spatial multiplexing. In this case, a single physical system can also be used, with its parameters systematically varied to produce different dynamical responses to the same input. The single system can be used in different regimes to augment the dimensionality to the input response. All dynamical responses to the same system, driven in different dynamical regimes, are gathered to provide the dimensionality, and the output is reconstructed by reading the state of the reservoir in each regime. Examples of spatially multiplexed reservoir computing systems are presented in the following section 5.5. Another solution is to implement the so-called temporal multiplexing, in which the usual structure of multiple connected nodes is substituted by a single node subjected to delayed feedback.

5.4.1 Time multiplexing

Temporal multiplexing was proposed by Appeltant *et al.* [235], where it was tested for a photonics RC. We follow here the description given by Appeltant *et al.* of the time multiplexing which has been widely accepted by the reservoir computing community. Instead of creating several spatially separated nodes, they exploit the potential of a single node, that is a single physical system which provides the characteristics demanded for a reservoir. The physical system is characterized by an instrinsic timescale T, that can be thought of as a relaxation time in response to changes in the input. A delay time τ is then introduce and divided into N intervals of duration $\theta = \frac{\tau}{N}$. N is the number of virtual nodes or virtual neurons, called like this because they have the same function of nodes or neurons as in a traditional reservoir. The time θ is chosen in order to be shorter than the characteristic time of the single node, hence $\theta < T$. θ is the characteristic time that separates the virtual nodes, therefore such a choice of θ ensures that the state of one node is dependent on that of its neighbour. A schematic of the idea of the reservoir computing with temporally delayed nodes is presented in Figure 5.6a. The input to a temporally delayed system has to be temporally multiplexed. To this end, the input $\mathbf{u}(t)$ or $\mathbf{u}(k)$, depending if it is time continuous or discrete in time respectively, undergoes an operation of "sampling and hold" resulting in a pre-processed signal I(t) that is constant for a time delay τ, before it gets updates to the following value. Therefore, the signal I(t) is discretized in time, no matter whether the initial input was discrete or continuous in time. Now the pre-processed signal is multiplied by a random matrix M, whose size is $(N \times Q)$, where N is the number of virtual nodes, in order for the input to be coupled with the virtual neurons. The random matrix transforms the constant value held during each delay time τ into N different values, each one maintained for a time $\theta = \tau/N$. The pre-processed signal, that we can call $\mathbf{J}(t) = M \times \mathbf{I}(t)$, is then fed into the reservoir. Schematic of the pre-processing of the signal is represented in Figure 5.6b. After a period τ, all the virtual nodes have been updated and, at the end of each period, the states of the nodes are read out to be processed. The output of the reservoir at time t is given by:

$$y(t) = \sum_{i=1}^{N} w_i \mathbf{x}\left(t - \frac{\tau}{N}(N - i)\right) \tag{5.13}$$

The training uses the standard procedure for the RC previously explained in section 5.2.

5.5 Implementation of spintronics PRC

Since the proposal of PRC and the idea of a time-delayed PRC to implement the RC using a single node, several works and ideas on how to implement it experimentally were proposed. In recent years, there has been

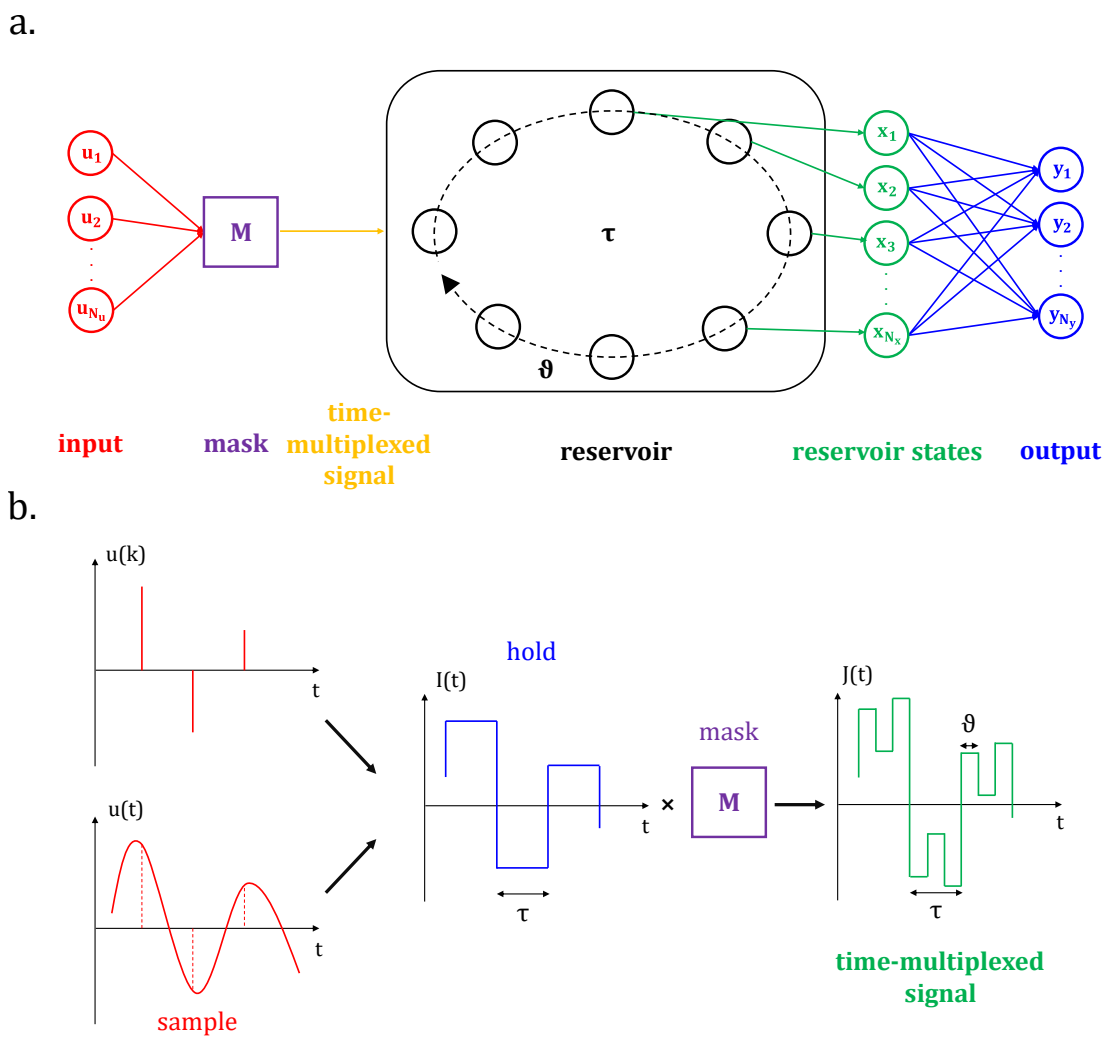

Figure 5.6: **Implementation of time-delayed virtual nodes** | a. RC using time-delayed virtual nodes. The input signal is time multiplexed in order to generate the temporal delay. The time multiplexed input signal is provided to the single node reservoir. In the schematic, inside the reservoir, the N virtual nodes separated by the time θ are shown. The output is the weighted sum of the states of the virtual nodes over a time delay τ as shown in equation 5.13. b. Input signal preparation for a TC with a delay line. The input is sampled (in case of a continuous signal u) and every time step is held for a time τ, obtaining the signal I(t). The signal I(t) is multiplied by a random matrix M that couples it with the virtual nodes inside the reservoir. Every sequence of a length τ is divided into N sequence of length θ. The input signal to the reservoir J(t) is hence obtained as $J(t) = M \times I(t)$. Both adapted from [235].

an extensive research focused on how to exploit different physical systems for RC and how to use them to solve practical problems involving real data. The simplicity of the training methods allowed people from outside the neural network community to participate in the research without having a large expertise in the field. PRC has been implemented in different research topics, ranging from electronics, biology, photonics, spintronics, mechanics and others [236]. I will focus here on the advances of the research for a RC systems in the spintronics field, as during my thesis I only worked with spintronic devices.

Spintronic devices are promising for neuromorphic computing applications as they can exploit several materials and properties in order to obtain complex dynamics. They can have oscillatory or stochastic behaviours, they can store information and also transport it using spin currents, magnetic textures and spin waves. Furthermore, spintronic devices can be small and compact, increasing the energy efficiency for applications while decreasing the area of the circuits. Of all the possible devices, magnetic tunnel junctions are particularly interesting for applications as they are compatible with CMOS technology, so they can be easily incorporated in industrial processes [24].

Spin torque oscillators RC

A first element that was exploited to generate spintronics PRC is the spin torque oscillator (STO). STO are nanoscale pillars, composed of two ferromagnetic layers separated by a non-magnetic spacer. When current flows through the first ferromagnetic layer with a fixed orientation of the magnetization, it becomes spin polarized. The spin polarized current due to STT generates a torque on the magnetization of the free layer, that is sent to a precessional state. The frequency of the oscillation of the magnetization can be tuned by varying the applied DC current and the external magnetic field. The amplitude of the oscillation has a non-linear dependency on the applied driving current and the magnetization relaxes with a time constant when the input is varied. These devices therefore show the key properties to be used as PRC, non-linearity and fading memory. In the work of Torrejon *et al.* [238], the dynamics of a STO was used to perform spoken digit recognition by performing time-multiplexing of the input signal. The pre-processed input was sent to the system as a current with a varying amplitude that would generate a dynamical response of the device which gets read as a voltage signal with amplitude variations. Recognition rates up to 99.6 % were obtained after the training, a consistently improved value with respect to those obtained without STO. In the work of Riou *et al.* [239, 240] the same STO system was used to solve the sine and square recognition task (explained in detail in section 6.4). Once again the time-multiplexing technique was chosen to exploit the dynamics of a single oscillator. They reported increased performances on the recognition task by adding an external electronic feedback line with the same time-delay τ chosen for the time-multiplexed signal to enhance the coupling in between virtual neurons (schematic of the setup with the external delay line can be observed in Figure 5.7b). Markovic *et al.* [241] reported that not only the amplitude of the STO response can be used as a RC but also its frequency and phase. They locked the frequency and phase of the oscillator with the external input signal. This can be done for a range of microwave frequencies close to the natural frequency of the STO. They tested the idea with a sines and squares classification task using a single node STO, therefore performing time-multiplexing. They encoded the amplitude of the time-multiplexed input signal in microwaves at different frequencies. They showed that the recognition rate strongly depends on the central frequency used for the encoding. Williame *et al.* [242] studied the delayed feedback in STO and they showed the possibility to obtain complex chaotic dynamics that could be exploited for different tasks. Furuta *et al.* [243] simulated the behaviour of single MTJ and multiple connected MTJs used as STO for short-term memory and parity check tasks and reported that the observed performances are similar to those obtained by ESN with higher number of nodes. Kanao *et al.* [244] simulated several STOs inside a square array. They showed that the devices are coupled due to the emission of large microwave dipolar fields. To perform RC they exploited the power and the amplitude of the oscillations in the waveforms induced by the input signal. They tested the performances on short-term memory and parity checks tasks.

Skyrmions RC

Other spintronics-base RC approaches have focused on magnetic skyrmions. Prychencko *et al.* [249] first proposed to exploit skyrmion fabrics in ferromagnetic films for RC. They started by analyzing the trajectories of a single skyrmion in a ferromagnetic film when applying an external voltage by measuring the anisotropic magnetoresistance effect. They observed non-linear current-voltage characteristic due to the interplay of current-induced dynamics and pinning effects. They reported that the type of magnetoresistive effect used for detection is not crucial, as the non-linear behaviour is a general property of the system. Bourianoff *et al.* [250] also proposed the use of a "skyrmion fabrics" in magnetic substrates with broken inversion symmetry as a RC system. They showed that the current flowing through a skyrmion fabric is strongly perturbed compared to that flowing through a uniformly magnetized substrate. They reported that the first situation would meet the required properties to use the systems for PRC. Msiska *et al.* [248] simulated a square magnetic thin film hosting skyrmions in a random configuration with 78 electrical contact, 39 per side. They tested on this system the spoken digit classification task by pre-processing the audio samples into 39 frequency channels. The intensity of each frequency channel was converted into a voltage signal and applied as input to the reservoir, while the opposite contacts on the other side received the negative value of the corresponding input channel, in order to create a steep gradient (see Figure 5.7e for a schematic of the setup). For the readout of the reservoir state they exploited a spatially resolved method by dividing the film into non-overlapping discrete cells and by looking at the magnetization dynamics inside each of them. The digits were identified with an overall accuracy of 97.4 %. Pinna *et al.* [251] simulated a skyrmion fabric and investigated its response to sinusoidal and square voltage pulses as a function of the frequency of the input signal. The skyrmion fabric was excited by time-varying voltage patterns applied between two contacts and the output measured via its AMR response. They observed that at high frequencies the system response is linear, so it cannot be employed for RC, while for driving frequency closer to the natural one of the system a strong non-linear response occurred. They tested the system to see if the reservoir state was showing differences for sine-square, square-square, sine-sine or square-sine sequences. They observed that the responses were visually distinct, meaning that the reservoir state does not depend only on the last input, but also on the previous ones, i.e. the system shows a fading memory. They extended the

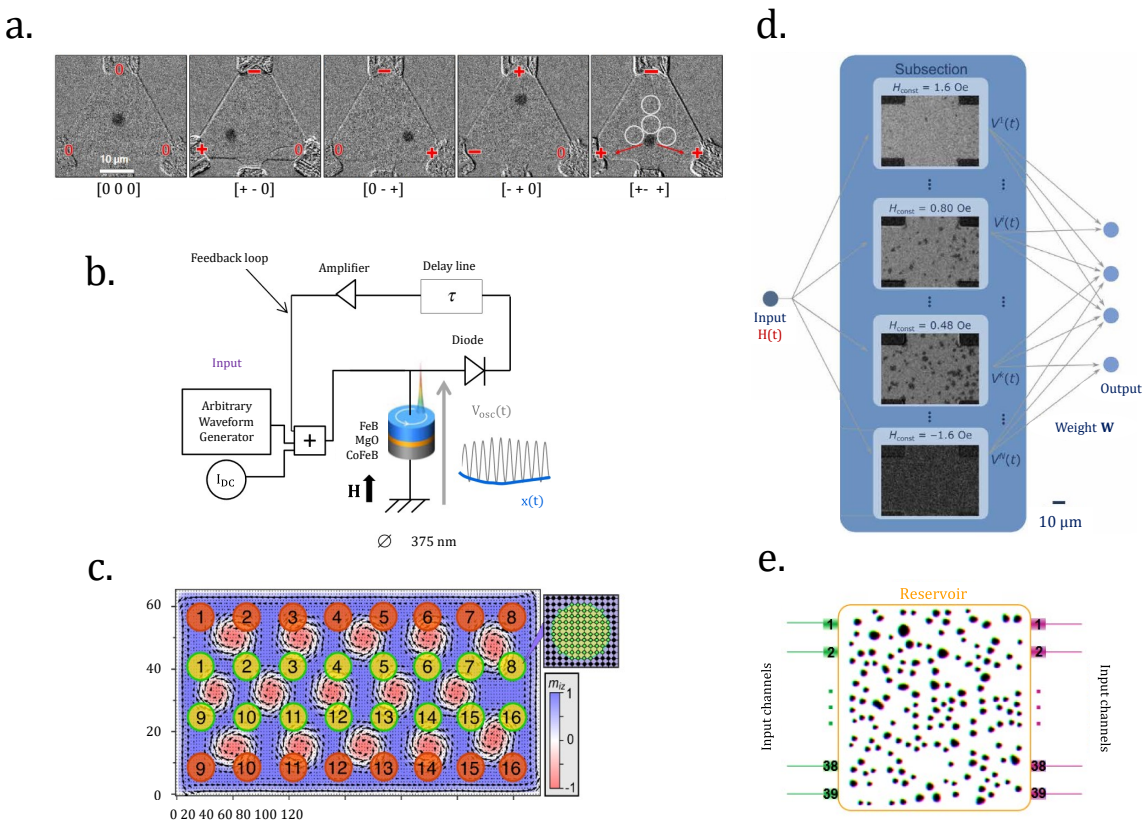

Figure 5.7: **Examples of PRC implemented using spintronics systems.** a. Kerr microscopy images of the equilateral triangle containing a single skyrmion used as a reservoir by Raab *et al.* [245]. The skyrmion moves depending on the applied electrical input configuration. In the last image on the right the circles show the four regions used to evaluate the skyrmion position probability. b. Experimental setup used by Riou *et al.* [240] to implement temporal-multiplexing with an external delayed feedback line to perform PRC with a single spin-torque oscillator. c. Configuration of the skyrmion reservoir used for spin waves excitation by Lee *et al.* [246]. The red and yellow circles represent the input and readout nodes respectively. d. Schematic illustration of the skyrmion-based RC implemented by Yokouchi *et al.* [247]. The magnetic textures are modified in each section by an external magnetic field. The reservoir state response to the input in each section is recorded as a Hall voltage. e. Schematic of the multi-contact skyrmion reservoir with 39 electrical contacts per side used to send the input. The system is used to perform a spoken-digit recognition task. By [248].

testing to longer sequences of three randomly assigned sines and squares.
Raab *et al.* [245] experimentally demonstrated a RC system exploiting the brownian motion of a geometrically confined skyrmion. An equilateral triangle geometry patterned on a thin film is hosting in its center a confined skyrmion (see Figure 5.7a). At the three corners, gold electrical contacts allow to apply voltage potentials. The skyrmion position inside the triangle depends on a balance between the current-induced motion due to the applied potential, the repulsion from the edges and its thermally diffusive dynamics. The skyrmion position is tracked with a MOKE microscope. Boolean operation are performed by applying different voltage potentials at the edges and evaluating the probability for the skyrmion to be in a certain position (various input configurations and their corresponding skyrmion responses are presented in Figure 5.7a). The probability of the skyrmion to be in a certain position represents the state of the reservoir, which is used to train the readout layer. The RC can perform different Boolean operations depending on the chosen weights of the readout layer. Later, Beneke *et al.* [252] employed the same system to perform a different task, hand gesture recognition. For this type of task, different hand gestures were captured by a Doppler radar and fed into the skyrmion reservoir as time dependent voltage signals. At each hand gesture a classification number is assigned. The readout in the proof of concept is still performed by MOKE microscopy, but they simulated the presence of MTJs on top of the triangle to find the best number of devices and position in order to have the highest recognition.
Yokouchi *et al.* [247] developed a RC system exploiting the non-linear response arising from magnetic field-induced dynamics of skyrmions. They built Hall bar shaped subsections on Pt/Co/Ir films that host skyrmions. The input signal was encoded as an OOP magnetic field that was applied to each subsection. The response of the reservoir to the input magnetic field is read as a Hall voltage variation. For the actual experiment a single Hall bar section was used. The technique adopted to increase the dimensionality of the response is to drive the

reservoir into different dynamical states by modifying the amplitude of the applied magnetic field, which alters the magnetic state of the thin film. What they performed is therefore a spatial multiplexing as they collected the reservoir response in different dynamical states into a matrix that is used for the readout layer training. A schematic of the performed experiment is presented in Figure 5.7d. The systems is used to test first a simpler task, the sine and square recognition, and later a more complex task, the handwritten digit recognition provided by the MNIST [253]. They obtained a recognition accuracy up to 94.7 % compared to a value of 9.9 % when the skyrmion reservoir is not present.
Lee *et al.* [246] exploited the complex dynamics of the chiral magnet Cu_2OSeO_3 that can either host skyrmions, or be in a conical or in an helical magnetic phase, to perform a task adaptive approach to RC. By tuning temperature and external magnetic field they controlled the magnetic phase of the material and thus its dynamic response. They tested a forecasting task using the Mackey-Glass series signal [254]. They observed better performances if the system was driven into the skyrmion phase with respect to the conical phase. The best results in the prediction task were obtained for an intermediate magnetic phase in between the two, obtained by changing the external magnetic field. For a transformation task, in which the input signal, for example a sine wave, has to be transformed in a different function by the network, they observed that on the opposite the conical phase was performing better than the skyrmion phase. They demonstrated that different tasks can be better performed by different magnetic phase spaces.

Spin-waves based RC

Other approaches to spintronics RC exploited spin waves. Nakane *et al.* [255] proposed a system made of an Yttrium iron garnet (YIG) film between a magneto-electric coupling layer and a conductive substrate. Spin waves in the YIG are excited by the application of voltage inputs through metal electrodes. The detection is also operated through voltage reading on other electrodes. The interference of spin waves has non-linear dynamics and the spin-dynamics is observed to be history dependent. Still Nakane *et al.* [256], in another work, proposed a similar YIG substrate as the one just described but where instead they excited spin waves in a stripe domains structure. The stripe domains structure was incorporated in order to spatially control the spin dynamics. They tested the reservoir system by solving a temporal XOR task [257] and the Mackey-Glass chaotic prediction task [254]. Lee *et al.* [258] proposed to exploit the dynamics of spin waves in a skyrmion crystal to perform RC. In the simulated system, the input signal was provided to the skyrmion reservoir as OOP microwave magnetic field generated by injecting electrical current in a metallic ring that represents the input node. The microwave pulses induce oscillations in the skyrmions magnetization that propagate as spin waves. The propagation shows a non-linear dynamics due to the internal configuration of the skyrmion crystal. The output is measured in the regions corresponding to the readout nodes, as a time profile of the induced electric current. The skyrmions are expected to act as a series of STO interacting via magnetic dipole-dipole interaction. The magnetization dynamics is measured at N different readout points, which together formed the N-dimensional reservoir state vector. They tested the system with a duration-estimation task, short-memory task and parity check task to investigate the required characteristics of a RC. They demonstrated that the skyrmion system excited by spin-waves has the characteristics to perform information processing as a reservoir.
In another work Lee *et al.* [246] tested handwritten digit recognition task from MNIST using once again spin waves in a skyrmion reservoir. The input was provided using sixteen input nodes where current loops where used to apply magnetic fields. Other 16 output nodes where used to detect current generated by the spin waves propagation (see Figure 5.7c). The recognition rate obtained with the skyrmion reservoir went up to 88.2%, around 10% higher than those obtained using an ESN.
Namiki *et al.* [259] created a PRC system utilizing non-linear spin wave interference in YIG single crystal. The input and output from the YIG crystal are sent and detected using two antennas. The input signal is sent to the device in the form of a microwave Oersted field which drives the precession of the magnetic moments. The output signal is detected through an oscilloscope. The spin waves interfere during their propagation generating a non-linear dynamics and at the same time a fading memory due to a remanent spin precession. The system was first tested using the handwritten digit recognition task where they achieved a recognition accuracy of 89.31 %. A second test was performed using a second-order non-linear prediction task that is "easy" as it only requires the physical system to show non-linearity. They also tested the system on NARMA2 and NARMA10 tasks [260] which require the system to not only perform a non-linear transformation, but also to exhibit a fading memory over respectively 2 and 10 time steps. They reported that the normalized mean square error, as a mark of accuracy in the testing of both tasks, was lower than that of any other RC system available at the date of the publication of the paper. In another work, Namiki *et al.* [261] used the same YIG systems, but instead of performing a multi-detection of the signal they used the time-multiplexing technique.

5.6 Conclusions

In this chapter I presented an introduction on neural networks and their possible declination. I then focused my attention on the reservoir computing paradigm, highlighting the requirements for a physical system to be exploited as a reservoir. I then presented a state of the art work on the use of spintronics systems for reservoir computing applications.

Chapter 6

Physical reservoir computing exploiting spin textures in magnetic tunnel junctions

Contents

6.1 Introduction . . . 100
6.2 Electrical characterization of the device . . . 101
6.3 Temporal characterization of the device . . . 102
6.4 Sine and square classification task . . . 104
6.4.1 Protocol . . . 105
6.4.2 Results . . . 106
6.4.3 Reservoir metrics . . . 111
6.4.4 Saturated states . . . 112
6.5 NARMA task . . . 112
6.5.1 Results . . . 113
6.6 Mackey-Glass task . . . 115
6.6.1 Results . . . 115
6.7 Conclusions . . . 115

6.1 Introduction

Spintronics has raised a large interest in recent years for its application in the field of neuromorphic computing [24], where the goal is to create hardwares which can emulate the brain behaviour by performing the operations of calculation and memorization in the same place. Spintronic devices combine unique properties like non-volatility, stochasticity, plasticity, with the ability to transfer information over distances exploiting various phenomena, capabilities which can be exploited for compact and energy efficient non-conventional computing applications. In this framework, several works have been proposed on how to exploit magnetic skyrmions for neuromorphic applications [249, 248, 251]. The small dimension of skyrmion textures and the possibility to control them with electrical current make them very interesting candidates for these types of applications.
Our idea of a device to perform non-conventional computing using magnetic skyrmions or, more in general, spin textures, comes from the work of Urrestarazu *et al.*. [23]. In this work, that was carried out in my group at Spintec, the authors demonstrated the possibility of nucleating spin textures inside MTJ devices using voltage pulses, exploiting VCMA. They also showed the possibility to tune and modify the intermediate states in MTJs by using either an external DC voltage or an external magnetic field. Starting from this toolbox to control intermediate states, we thought of using a similar MTJ system as a physical reservoir computing. The idea consists in the nucleation of intermediate states and the modification of their magnetization using an external DC voltage. The reading of the reservoir is done by exploiting the TMR changes generated by the changes in the magnetization of the intermediate state.

Here, we present the measurements that we performed to show that an MTJ device can present the necessary characteristics of non-linearity and short-term memory to be used as a physical reservoir computing system. We describe the behaviour of the device which shows stochastic jumps in between several intermediate resistance states and how these are depending on the external magnetic field. We show how we exploited the device as a reservoir computing system using the technique of temporal multiplexing. We then present the results obtained on some of the standard benchmarks used to evaluate the quality of a reservoir computing system. First, we discuss the sines and squares classification task and the impact of the short-term memory and of the non-linearity of the the reservoir to successfully perform it. Second, we present some initial results on the Mackey-Glass chaotic time-prediction task and on different types of NARMA-N tasks. We conclude with a discussion about the possible adjustments to improve the reservoir performances based on the experimental results.

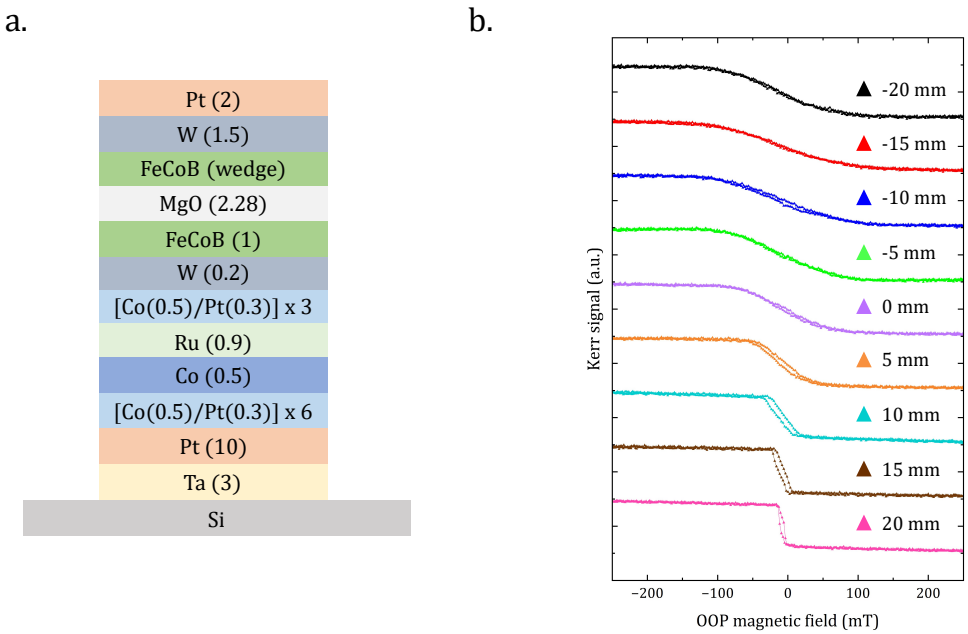

Figure 6.1: **High RA MTJ stack and the OOP hysteresis loop of the FeCoB wedge** | a. The stack of the MTJ device with the corresponding thicknesses for each layer expressed in nm. b. OOP hysteresis loops of the sample measured with the nanoMOKE. Along the wedge, the film thickness decreases from negative to positive positions. A clear transition from IP to OOP is observed around 5/10 mm.

6.2 Electrical characterization of the device

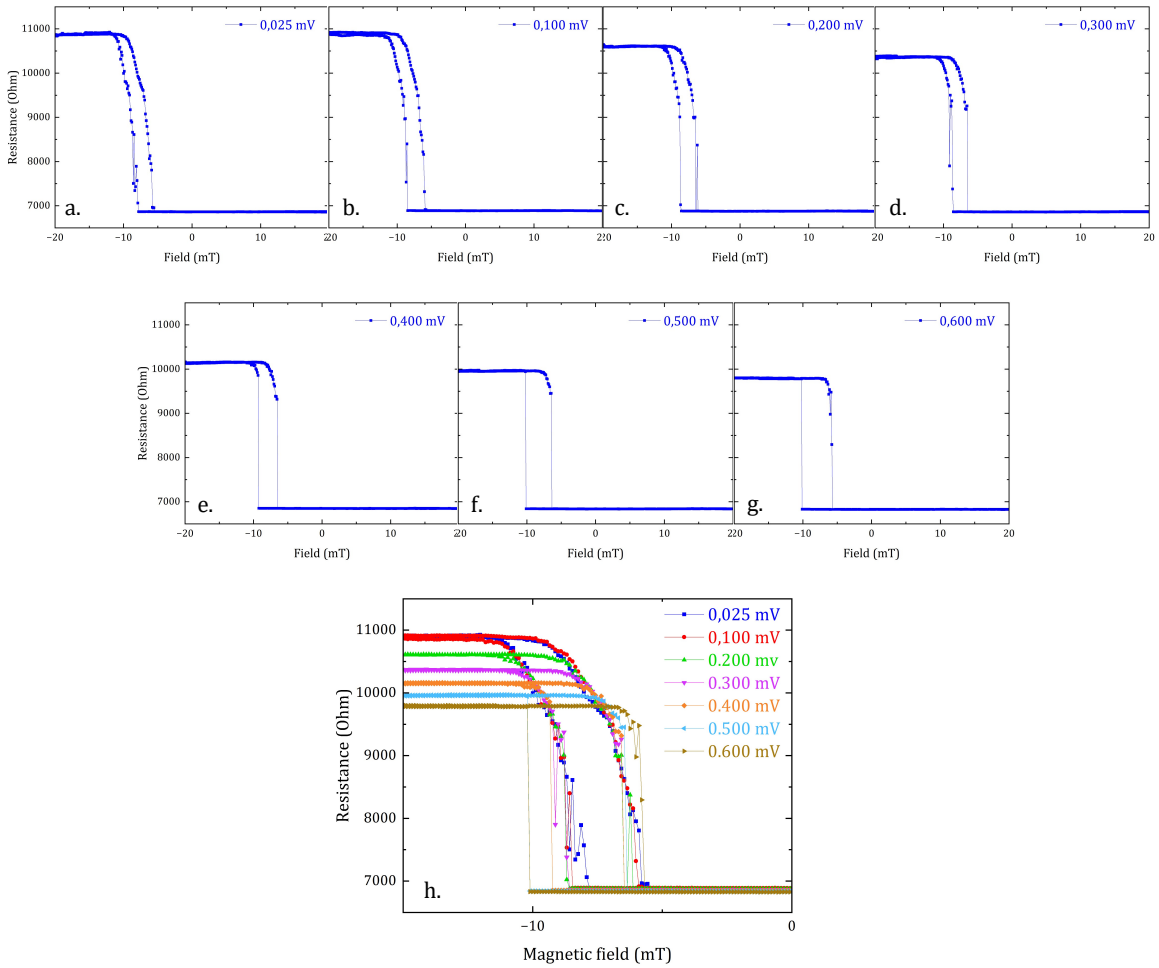

Figure 6.2: **Hysteresis loops of the device for different applied DC voltage** | Hysteresis loop measured at V_{DC} = 0.025 mV, 0.100 mV, 0.200 mV, 0.300 mV, 0.400 mV, 0.500 mV and 0.600 mV respectively in a., b., c., d., e., f. and g. In h. the different hysteresis loops are plot together to better observe the effect of the external DC voltage on the intermediate states resistances, on the TMR and on the coercive field.

The device chosen for the experimental demonstration of physical reservoir computing is a high-RA MTJ, like the one used by Urrestarazu *et al.* for their work. The stack is the following: Si/Ta/Pt/[Co/Pt]×6/Co/Ru/[Co/Pt]×3 /Co/W/FeCoB/MgO/FeCoB/W/Pt. Figure 6.1a presents a schematic of the stack along with the thicknesses of the material per each layer. It is similar to the device used and described in chapter 4, with a difference consisting in a thicker MgO barrier to obtain a higher RA product and a different bottom electrode. The higher RA allows a control of the magnetization of the free layer exploiting the VCMA effect while keeping low current, and thus low STT. The thickness of the FeCoB free layer is chosen in order to target the OOP/IP transition which allows easier skyrmion nucleation.
Figure 6.1b shows the hysteresis loops measured via Kerr effect for different thicknesses along the wedge. Along the wedge, the film thickness decreases from negative to positive positions. The transition from IP to OOP behaviour is observable around 5/10 mm.
For this experiment, the magnetic stack was deposited on a standard Si wafer as we did not need to perform any transmission microscopy experiment exploiting x-rays. The fabrication process is the same as the one described in chapter two, without the SiN membranes. The device chosen for the reservoir computing experiment is a 200 nm pillar that presents intermediate resistance states as can observed on the hysteresis loops shown in Figure 6.2. The hysteresis loops are measured for different external applied voltages (respectively from 0.025 mV to 600 mV from a. to g. in Figure 6.2) and one can observe the changes in the number and in the resistance values of the intermediate states depending on the applied voltage. Figure 6.2h compares hysteresis loops at different DC voltages. A reduction of the resistance of the AP state is observed, and therefore of the total TMR, due to the applied voltage, a well know effect of the TMR in magnetic tunnel junctions [262]. One observes also squarer loops with less intermediate states and an increase in the coercivity with increasing voltage.

We then characterized the resistance response to variable DC voltage for a fixed magnetic field to see whether we could observe a non-linear response of the intermediate resistance states, as needed for the reservoir computing. In Figure 6.3 some examples are presented. We observed that the sample presents a hysteretic behaviour such that the resistance response to the DC voltage is strongly history dependent. Furthermore, we saw that the response to the applied DC voltage for a certain range of magnetic fields was consisting in a series of stochastic jumps in between different intermediate states. The examples presented in Figure 6.3 are obtained by averaging the resistance response to the same input DC voltage range over several loops. In red is highlighted the averaged resistance response while the error bars due to the stochasticity are plot in grey. A more detailed discussion of the temporal behaviour of the stochastic jumps is presented in the following section.
The non-linear behaviour is clear in all the examples and its contribution is coming from both the stochasticity of the magnetization and the TMR change due to applied external voltage.

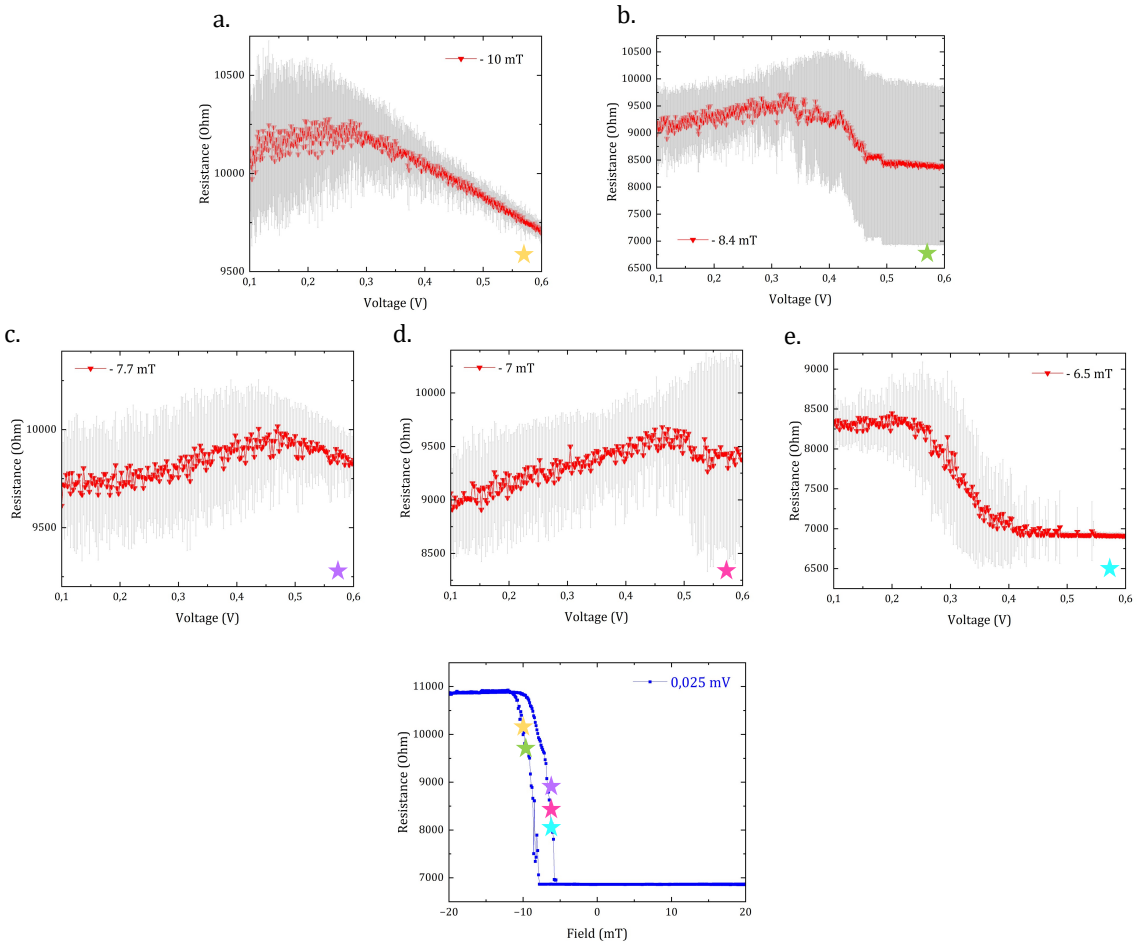

Figure 6.3: **Resistance versus applied DC voltage curves at different external magnetic fields** | Measured resistance as a function of applied DC voltage for different values of external applied magnetic field. The loops are measured for -10 mT and -8.4 mT in a and b, after saturation in the P state, and for -7.7, -7 and -6.5 mT respectively in c, d, and e, after saturation in the AP state. Each resistance point is averaged over 50 measurements to account for stochastic jumps between intermediate resistance states. The red trace is the average resistance value, and grey error bars show the standard deviation. Measurement positions are indicated on the hysteresis loop of the device in f by mean of a star of the same color.

6.3 Temporal characterization of the device

The setup used to measure the resistance variation as a function of time is the one described in section 2.2.2. Using this setup, we can connect the device to an arbitrary waveform generator (AWG) that we use to inject a voltage signal. At the same time we can measure in parallel, on two different channels of an oscilloscope, the voltage drop across the MTJ device due to the input, and the voltage signal provided by the AWG. In this way we can record in real time on the oscilloscope the variation of the resistance on the MTJ. Since we observed stochastic jumps during the DC measurements, we wanted to better investigate their temporal dependence and

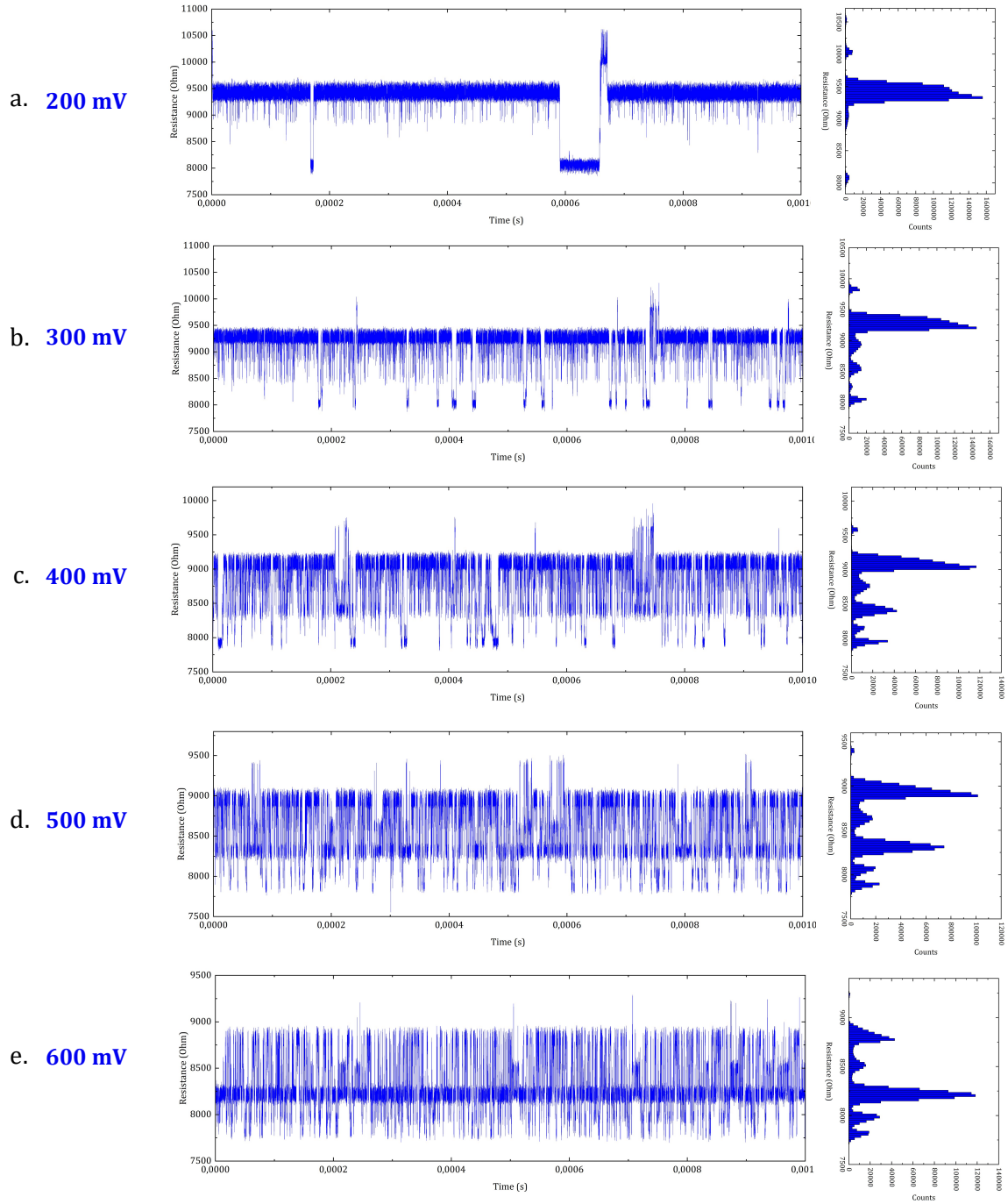

Figure 6.4: **Stochastic jumps among intermediate resistance states as a function of the DC voltage** | Time traces of the resistance of the device for an applied DC voltage of 200 mV, 300 mV, 400 mV, 500 mV and 600 mV, respectively in a., b., c., d. and e. The external magnetic field is fixed at a value of -9.3 mT. The resistance shows stochastic jumps between different intermediate states. Right: histogram obtained from the time trace to better visualize the different intermediate resistance states and how likely they are reached.

evolution. To this end, we recorded the time evolution of the resistance for different DC currents (see Figure 6.4).

The resistance exhibits random jumps among several discrete intermediate states. The histograms on the side of the time traces resolve these intermediate states and how likely they are reached depending on the applied voltage. By mean of these plots we can identify six intermediate states whose probability of occupation depends on the applied DC voltage. The resistance values associated to the intermediate states vary as well with the applied DC voltage because of the changes in the TMR. We further observed that changing the magnetic state via the applied field modulates the dwell times of the stochastic transitions, i.e., the stability of the reached states, leading to complex dynamics. These intermediate states are likely generated by one or several domain

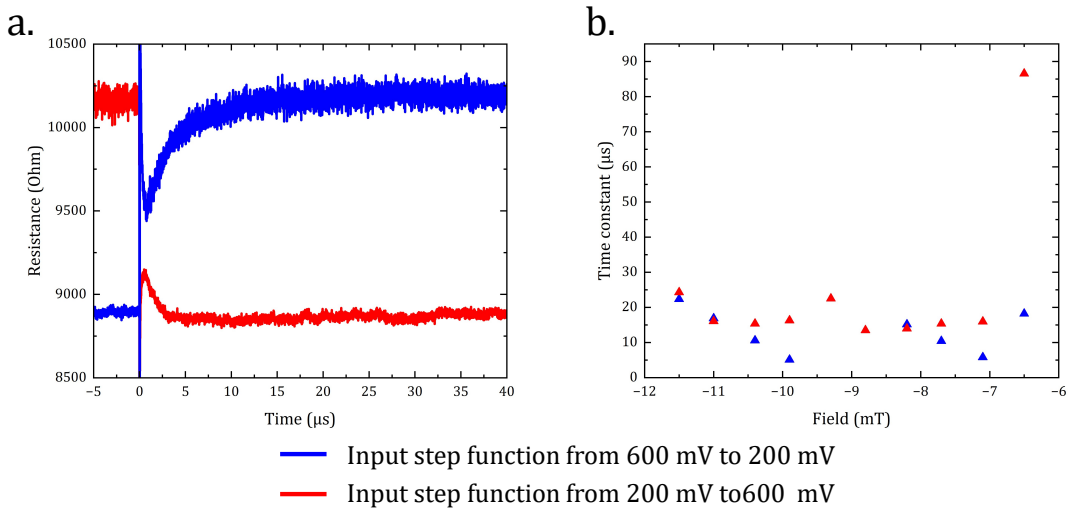

Figure 6.5: **Resistance relaxation in response to step function input pulses averaged 500 times** | a. Resistance response of the device for an external field of -11 mT to a step input function from 200 to 600 mV (red curve) and from 600 to 200 mV (blue curve). The curves are obtained by averaging 500 times the response to the input step function. Single exponential fits give time contants of 4.9 µs (blue) and 2.3 µs (red). b. Relaxation time as a function of the magnetic field (after saturation in the P state) in response to an input step function from 200 to 600 mV (red points) and from 600 to 200 mV (blue points).

walls that get shifted inside the pillar due to applied voltage.
The short-term memory of our device arises from the variation of the occupation of the intermediate states as a function of the applied voltage, revealed after averaging over several identical measurement. The averaged traces exhibit a slow relaxation governed by both changes of the magnetization and the evolving occupancy of intermediate states. The associated time constant is extracted by fitting the mean response.
Figure 6.5a shows the resistance response of the device to input step functions going respectively from 200 to 600 mV (red curve) and from 600 to 200 mV (red curve), where the jump happens at time t = 0. The curves are obtained by averaging 500 times. This allows us to see the mean relaxation effect generated by the stochastic jumps in between different resistance states. Two effects are visible. Firstly, a sudden change in resistance due to the voltage dependence of the TMR effect. Then, after a small delay ($\sim$ 100 ns) due to the electronic circuit, the electrical relaxation caused by the stochastic dynamics between different magnetic states is observed. Last, the main relaxation caused by the averaging of the stochastic jumps is observed. Single-exponential fits of the main relaxation yield time constants of 4.9 µs (blue) and 2.3 µs (red). Figure 6.5b shows the variation of the time constant as a function of the external magnetic field for the two different jumps of 200 to 600 mV (blue dots) and 600 to 200 mV (red dots). For every measured point, the device was first saturated in the P state. The relaxation time does not follow a specific trend but it stays in general in between 5 and 15 µs with a few outliers.

6.4 Sine and square classification task

The sine and square classification is a type of task used to evaluate the performances of a reservoir computing system since it requires both the non-linearity and the short-term memory of previous inputs to be successfully accomplished. The task consists in the following: a random sequence of sine and square waveforms is generated (see Figure 6.6a) and sampled in order to obtain a discrete input sequence that is used as an input to the reservoir system. For every sampled point, the goal of the network is to classify whether it is belonging to a sine or to a square, generating an output that corresponds respectively to a 1 or to a 0. Figure 6.6d shows a waveform made of a sine period followed by a square period with the same amplitude and frequency. The waveforms are both sampled at 8 points. The sampled points are referred to as si1 to si8 for the sine waveform and sq1 to sq8 for the square waveform. They are represented in different colors; the same colours are used when the sampled input value is the same, for example si3 = sq1 = sq2 = sq3 = sq4. Because of the symmetry, the input contains only 5 different values, so in order to correctly classify whether the input is belonging to a sine or to a square both the memory and non-linearity properties are needed. Without the non-linearity the different inputs provide the same output and without memory it would be impossible to distinguish the highest and lowest values of the sine, respectively si3 and si7, from those of the square, since they have the same input value. The differentiation can be provided by the memory since the prior inputs to those inputs sharing the same

value are different, therefore, if the system is able to remember prior inputs, same inputs can be distinguished.

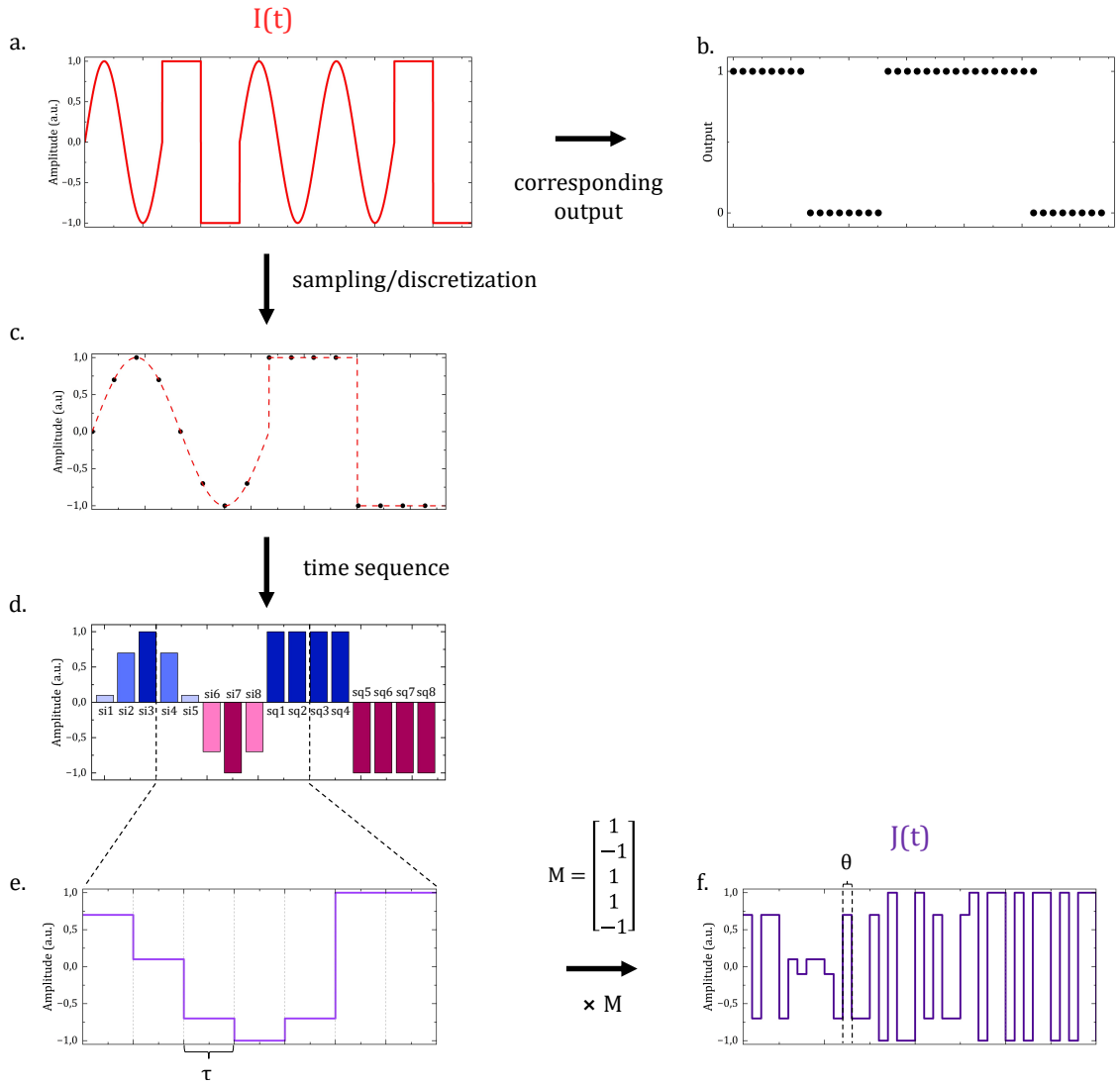

Figure 6.6: **Sine and square classification task performing time-multiplexing** | a. Random continuous sequence of sines and squares functions. b. Corresponding output, 1 for every point belonging to a sine and 0 for every point belonging to a square. c. Sampling of the continuous signal to discretize it. d. Every sampled element is held for a time τ in order to obtain a time sequence from the initial signal. e. Zoom on the time sequence. f. Multiplication of the signal by a random matrix, in this case composed of N = 5 neurons, with values either 1 or -1. J(t) is the final time-multiplexed signal, where every point is held for a time θ given by τ/N.

Since our system is composed of a single MTJ, we increase the dimensionality via the temporal multiplexing technique (section 5.4.1). Figure 6.6e shows the signal where every step in the input is held for a time τ. The signal is then multiplied by a random matrix composed of a sequence of 1 and -1 (in the example the sequence has a length N = 5, where N is the number of virtual neurons). The final time-delayed signal is composed of a sequence of input points, each of them held for a time $\theta = \tau/\mathrm{N}$. The input is then provided to the device as a voltage waveform chosen within the bias window where the system shows a non-linear response to the applied voltage.

6.4.1 Protocol

A random sequence of 400 periods of sine and square waveforms with is generated in the computer. The sequence is then time-multiplexed, still in the computer and provided to the AWG. In the AWG we can select the amplitude voltage to use for the input sequence chosen within the bias window where the device exhibits the strongest nonlinearity for the selected external field. The time step θ is also modified by the AWG when the signal is generated.

When the signal is provided to the device, we measure on two different channels in the oscilloscope the full voltage input and the voltage drop on the MTJ, in order to measure in real time the resistance response of the pillar using the formula 2.2. The voltage input signal is provided and measured 500 times because of the stochastic behaviour of the device. Figure 6.7b shows a part of the resistance time trace of the device as measured in the oscilloscope for the input voltage sequence (still measured in the oscilloscope) in Figure 6.7a, that corresponds to the time-multiplexed sines and squares. The sampling frequency of the oscilloscope is chosen in order to get an integer number of points per period θ, in general around 125 or 250 sampled points. The measured signal is then sampled out in the computer in order to obtain one resistance value per period θ. We split the dataset into training of the network (80%) and testing (20%). The training is performed using a simple linear regression. The output obtained from the linear regression is compared to the true output which was generated together with the input waveform.

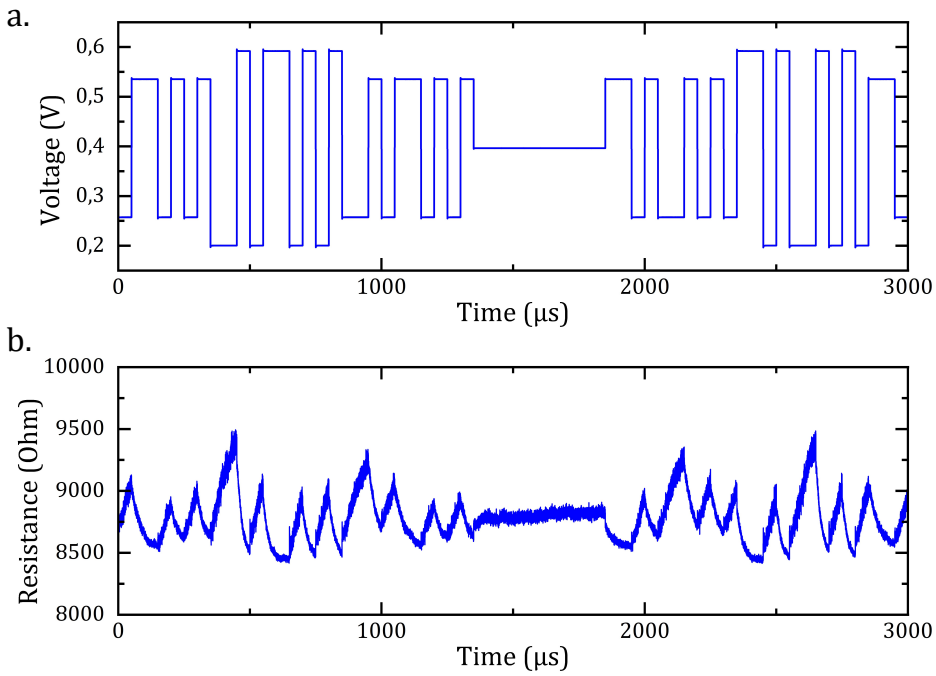

Figure 6.7: **Resistance time trace for the sine and square task** | a. Voltage input signal corresponding to a part of the time-multiplexed random sequence of sines and squares. b. The resistance time trace of a part of the response to the time multiplexed voltage input signal in a as recorded on the oscilloscope. The time step θ corresponds to 50 µs and the number of neurons is N = 10.

6.4.2 Results

I present in this section some experimental results on the testing of the sine and square classification task using the physical reservoir. For all the results presented here we used N = 10 virtual neurons and θ = 2 µs for the time-multiplexing. The input voltage signal goes from a minimum of 200 mV to a maximum of 600 mV.

Choice of theta and voltage range

The choice of the parameter θ = 2 µs comes from the relaxation constant measured. Specifically, for the first case that I discuss in the following lines and in Figure 6.9a, the relaxation curves are those shown in Figure 6.5a. The two measured time constants are around 4 and 2 µs. We therefore decided to test the recognition for a value of 2 µs, around half of the larger time constant. For the other two examples presented in Figure 6.9b and c, the θ is not optimized, but the goal of the experiment was to quantify how much this parameter can affect the classification. Since the time-relaxation was strongly varying due to the applied magnetic field, the protocol we followed in the experiments was to first characterize the relaxation time of the state at the chosen field, and then define the time constant θ depending on the observed relaxation. The input voltage window (200 - 600mV) is chosen to exploit the non-linear response of the device while maintaining a good signal to noise ration (we avoid low value below 100 mV) and device integrity (we avoid voltages higher than 600 mV).
The signal contains 400 periods of sines and squares, for a total of 32000 points since the sines and the squares are each sampled at 8 points as shown in Figure 6.6. The input voltage of the sines and squares after the time-multiplexing, as sent to the device, is presented in Figure 6.8a, while Figure 6.8b shows the resistance response

of the reservoir for an external magnetic field of -11 mT, after the sampling process of the full resistance signal measured. We use 80% of the reservoir reponse for the training and 20% for the test.

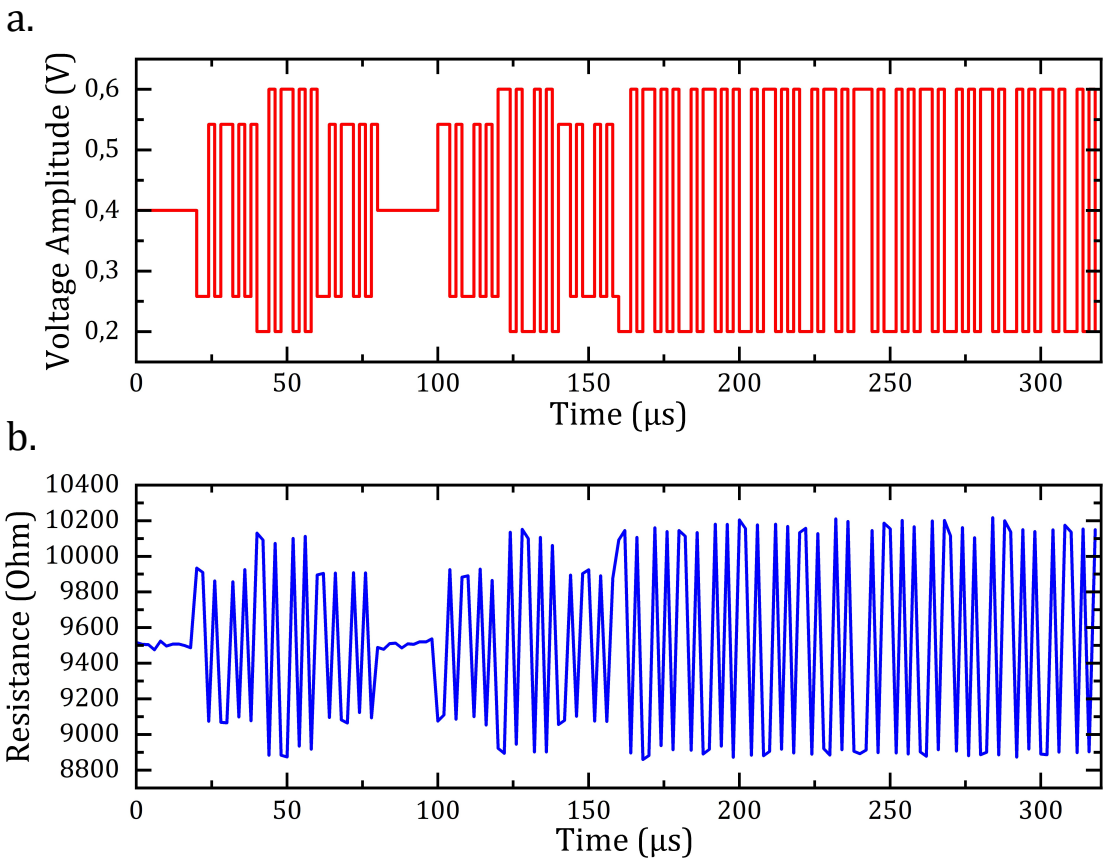

Figure 6.8: **Time-multiplexed voltage input (square/sine) and corresponding sampled resistance output** | a. A sine and a square waveform after the time-multiplexing process as a voltage input signal provided to the system. The chosen values are N = 10 virtual neurons an θ = 2 µs. The amplitude of the input voltage goes from 200 mV to 600 mV. b. Sampled resistance output of the MTJ to the input in a. for an external magnetic field of -11 mT.

Performance at different fields

Figure 6.9 shows the reconstructed output after the linear regression compared to the expected output for external magnetic fields of -11 mT, -11.5 mT and -9.5 mT. The waveform provided in the three cases is identical, only the magnetic field varies. In a. the classification accuracy reaches 98.28%, in b. 94.02% and in c. 89.69%. The accuracy is calculated as the number of time the classification output is matching the real output, divided by the total number of samples used for the testing. We observe that the number of points for which the output gets wrongly classified increases from a. to c.
On the right side of the plot, the confusion matrix related to reconstructed output is presented. A confusion matrix is a specific table layout that allows the visualization of the performances of an algorithm. In this case, the rows represent the true 0 and 1 output and the columns represent the 0 and 1 expected output. The diagonal of the confusion matrix gives the instances for which the true and the predicted output matches, so 0-0 and 1-1, while the top-right box gives the number of times for which a true 0 output has been mistaken for a 1 and viceversa for the bottom-left box. It can be observed that for the case in Figure 6.9a the two types of error are obtained with similar probabilities, while for b. and c. the most likely error is that of an expected output 1 (sine) gets misclassified as a 0 (square).

Error analysis

Starting from the confusion matrix we can analyze more in depth the results in order to understand the reasons behind the differences in the recognition accuracy. First of all, we checked if there was a trend in the errors. For the waveform in Figure 6.9a, the points which got badly classified are si3, si7 (maximum and minimum of

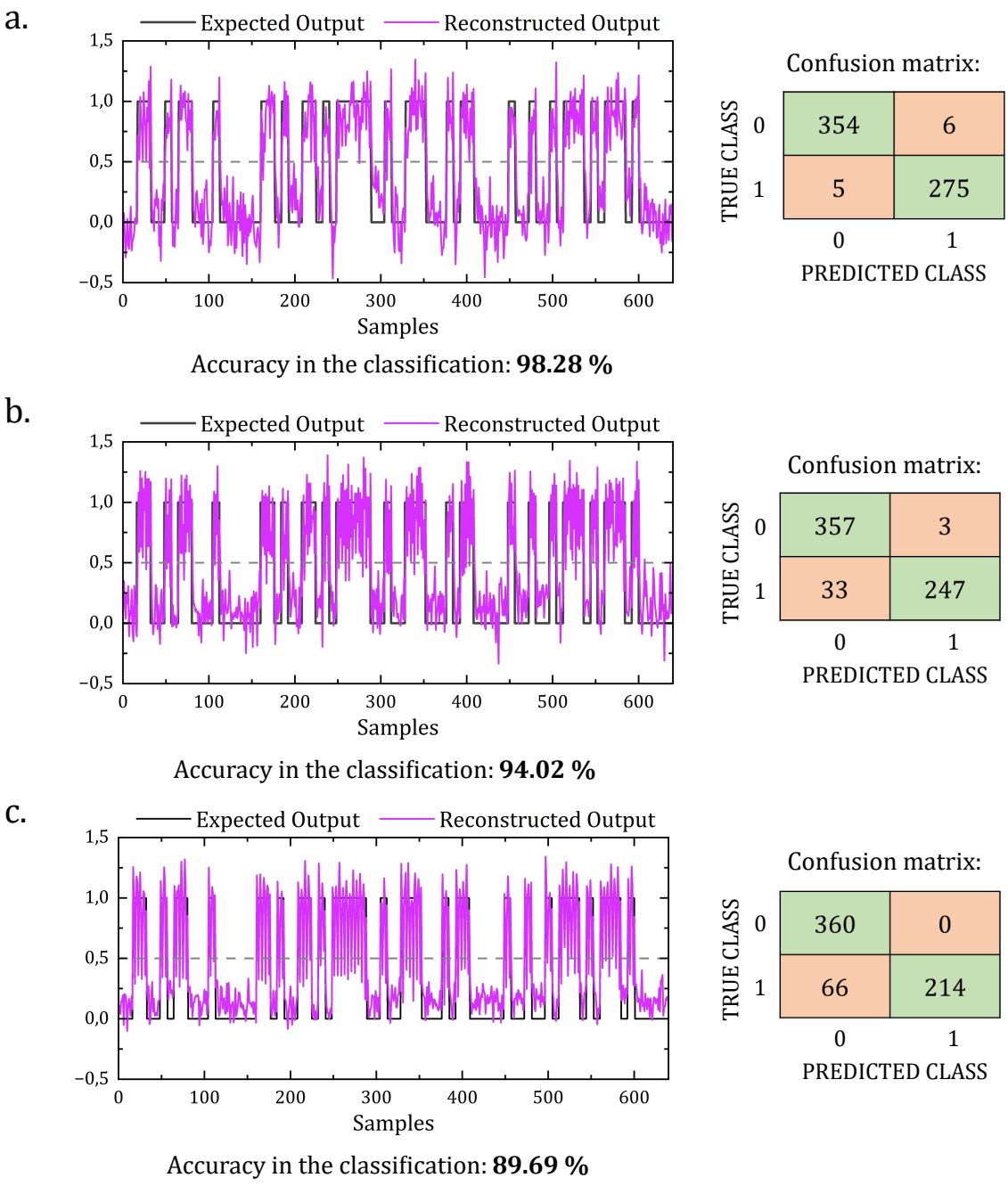

Figure 6.9: **Expected and reconstructed outputs from the testing of the sines and squares classification task** | a. Compared expected and reconstructed output with relative confusion matrix for an external field of -11 mT. The accuracy in the classification is 98.28%. b. Compared expected and reconstructed output compared with relative confusion matrix for an external field of -11.5 mT. The accuracy in the classification is 94.02%. c. Compared expected and reconstructed output compared with relative confusion matrix for an external field of -9.5 mT. The accuracy in the classification is 89.69%.

the sine respectively), sq1 and sq8 (first and last points of the square, see Figure 6.6 for the definition of the points). For the one in Figure 6.9b the points of the sine that get wrongly classified are always si3 and si7, but not all of them, while for the squares there are just three errors in the classification corresponding to the points sq1 and sq7 (twice). For the curve in Figure 6.6c, the points that get wrongly classified are the si3 and si7, all of them but four, for the length of the signal used for testing. As already highlighted in section 6.4, the input value of si3 is exactly the same as sq1, sq2, sq3 and sq4, and the input for si7 is the same as sq5, sq6, sq7 and sq8. This means that to correctly classify si3 and si7 as 1s and not as 0s, the system has to provide enough short-term memory as the non-linearity on its own is not enough. For a correct classification of the other points the non-linearity is sufficient. If the system was absolutely linear the recognition rate would be that given by a random choice, so around 50-60% [263]. The non-linearity increases the classification depending on the specific waveform used. In our case, the part of the waveform used for the testing contains 45 squares and 35 sines,

for a total of 640 points to classify (8 per waveform period). With the non-linearity only, counting that the si3 and si7 will get badly classified, for a total of 70 points out of 640, the maximum accuracy in the recognition that we can obtain is around 89%. It means that for case presented in Figure 6.9c the memory of the system is too short (or too long) to provide a higher recognition. For the case in Figure 6.9b some short-term memory is provided by the reservoir, but not enough to get as good accuracy as the case in a.

Principal Component Analysis

To better understand how the classification works for different situations we can perform the so called Principal Component Analysis (PCA), that is a statistical tool that can help in the visualization of high-dimensional data [264]. The data are linearly transformed using a system of coordinates that are those along which the data show a larger variance. To better visualize our data we can use as a first coordinate the classification scores coming from the regression, meaning $\hat{\mathbf{y}} = \mathrm{W}^{\mathrm{out}}\mathbf{x}$, using the terminology from sections 5.2 and 5.3. This is the same y-axis used in the plots in Figure 6.9. As a second coordinate for the PCA we use the projection of the data in the subspace orthogonal to $\mathrm{W}^{\mathrm{out}}$. In this way we can visualize the clusters of data that will be separated by the vertical line x = 0.5 into squares (for x < 0.5) and sines (x > 0.5).

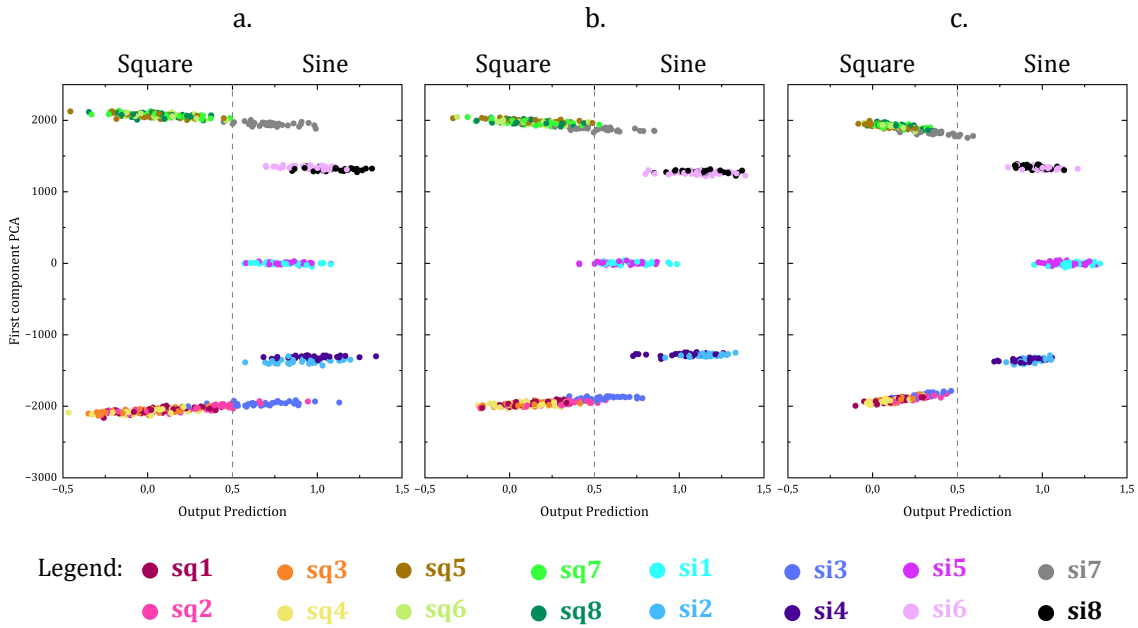

Figure 6.10: **Principal component analysis of the reconstructed outputs** | PCA of the reconstructed outputs of the case shown in Figure 6.9a, b and c respectively. The x-axis is given by the reconstructed output from the linear regression and the y-axis is given by the projection of the data in the subspace orthogonal to $\mathrm{W}^{\mathrm{out}}$. The color of the points in the plot is explained in the legend below the graphs.

Figure 6.10 shows the higher dimension mapping resulting from the PCA for the three cases shown in Figure 6.9, following the same letters a., b. and c. It can be observed that for the case in a., for which the classification accuracy reaches 98.28%, there are several different clusters resulting from the analysis. For the square side there are two clusters, one for sq1-sq2-sq3-sq4 and one for sq5-sq6-sq7-sq8, having the same input point. There is then a cluster for si3, close, but well separated from that of sq1 and others, and a second cluster for si7 separated from the one of sq5 and others. This shows that the short-term memory is sufficient to differentiate the points with identical inputs but belongings to different waveforms. For the sine part, there are then three other clusters for the three groups of points sharing the same input value. One can observe that within the clusters the points are divided in two sub-clusters that are not perfectly overlapping, showing some short-term memory effect. A similar situation is observed for the case in 6.10b, where the si3 and si7 clusters overlap more with sq1-sq4 and sq5-sq8, respectively, and the si1/si5 cluster contains some points misclassified as square. This can explain the reduction of accuracy from the case in a.
For the last case shown in Figure 6.10c, all the points belonging to si3 get badly classified and indeed there is just one cluster for sq1-sq2-sq3-sq4-si3. Similar situation happens for si7 where almost all the points get badly classified and the cluster they generate overlaps more with that of sq5-sq8 and others. In this case the memory was not enough to differentiate points with the same input value, explaining the accuracy of only 89%.

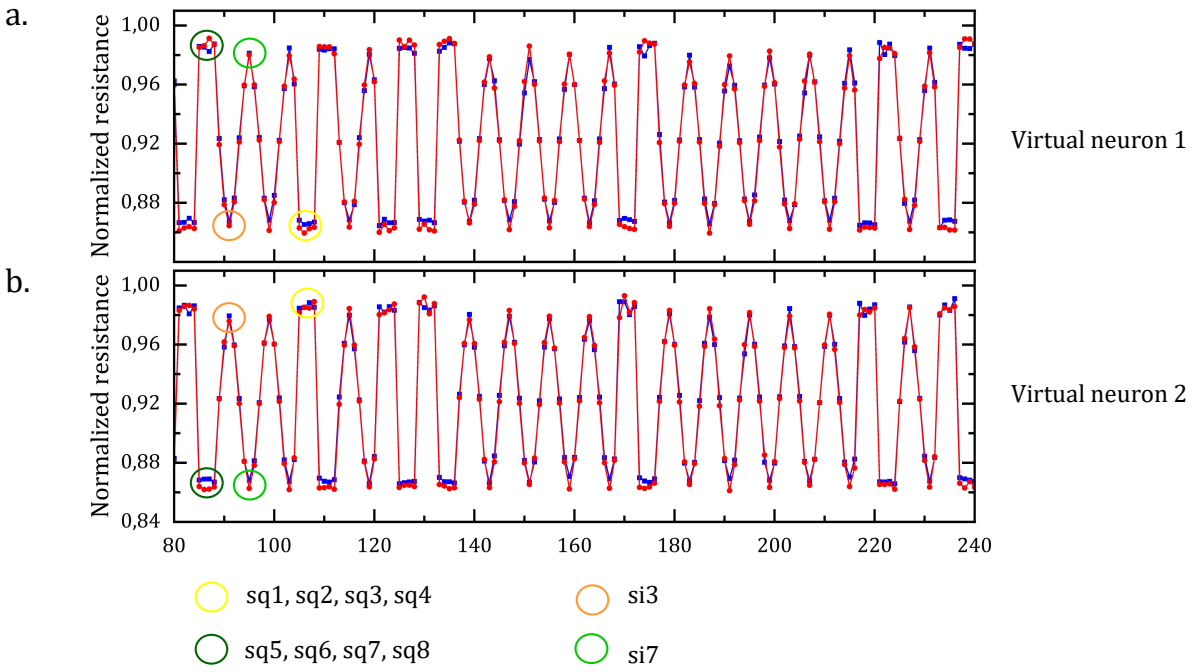

Figure 6.11: **Response of two virtual neurons to the input signal** | Responses of the two first virtual neurons generated in the time-multiplexing process respectively in a. and b. In red is the curve coming from the case presented in Figure 6.9a and in blue that coming from 6.9b. With a dark green circles are highlighted the points sq1, sq2, sq3 and sq4, with a light green circle the point si3, with an orange circle the point si7 and with a yellow circle the points sq5, sq6, sq7 and sq8.

	Blue curve (94.02%)	**Red curve (98.28%)**
$\sum_{N=1}^{10}\sum_{i=1,2,3,4}(si3_N - sqi_N)$	-0.0939	-0.10252
$\sum_{N=1}^{10}\sum_{i=5,6,7,8}(si7_N - sqi_N)$	-0.10145	-0.14145

Table 6.1: Average difference in the response for points having the same input in the sines and squares classification task.

Neuronal level view

To better understand how the memory affects the recognition we can analyze the responses of the single neurons for the two cases presented in Figure 6.9a and b. Figure 6.11 compares the responses of the first two virtual neurons for selected points. The resistances measured in the two cases are similar, but for better comparison and visualization they have both been normalized using the same value. The points circled in orange correspond to si3 and those circled in yellow correspond to sq1, sq2, sq3 and sq4. The points circled in light green correspond to si7 while those circled in dark green correspond to sq5, sq6, sq7 and sq8. Those two groups of points (yellow-orange and light green-dark green) have to be distinguished during the regression process in order to obtain a high accuracy. Just by looking at the plot, it is difficult to judge whether on average the si3 and sq1, sq2, sq3 and sq4 are more separable for the blue or for the red curve and likewise for si7 and sq5-sq8. We can therefore calculate the average difference between si3 and sq1-sq4 circled in yellow for both the blue and the red curves, and the same for si7 and sq5-sq8 circled in dark green. We then sum all these differences, between si3 and the sq1-sq4, and between si7 and sq5-sq8. By then summing over all the neurons we obtain the values presented in table 6.1.
Table 6.1 shows that the difference between the si3 and si7 with respectively sq1-sq4 and sq5-sq8 is slightly larger for the red curve (the one corresponding to 98.28% of accuracy in the classification) than for the blue curve (the one corresponding to 94.02% of accuracy in the classification). The larger the difference in between the measured points, the higher the chance that after the linear regression they fall into two different categories. From this analysis we can observe that just small differences in the reservoir properties can change the recognition accuracy of few points percentage. This shows that the reservoir is very dependent on the external parameters, in this case the magnetic field, that directly affects the short-term memory property, as well as the input voltage amplitude used to encode the signal.

6.4.3 Reservoir metrics

A way to quantify the performances of a physical reservoir computing is the calculation of the reservoir metrics [265, 266, 267]. The two metrics we calculate are the non-linearity metric (NL) and the memory capacity metric (MC). These metrics can be calculated using the same set of input and output data used for a task, and they are task independent. In our case, to calculate these metrics, we can directly use the reservoir output data from the sine and square classification task. The two metrics are calculated by evaluating the reservoir's response to lagged inputs over a number of time steps exceeding the relaxation time. We use 8 steps, following the work of Lee *et al.* [266]. To compute the NL metric, we first assess the quality of reconstructing the network output when the reservoir is driven by lagged inputs. This is expressed by the following equation:

$$\hat{y}(t) = \sum_{i=0}^{8} w_i x(t-i) \tag{6.1}$$

where t is the timestep, w_i are the weights obtained by linear regression using 80% of the lagged reservoir states for the training and the real expected output, and x(t-i) is the lagged reservoir state, the remaining 20% part used for the testing. To assess the quality of the estimator in equation 6.1, we use the coefficient of correlation R^2, defined as:

$$R^2[\hat{y}, y] = 1 - \frac{\sum_{j=1}^{n_{test}} (y_j - \hat{y}_j)^2}{\sum_{j=1}^{n_{test}} (y_j - \bar{y})} \tag{6.2}$$

where $\bar{y}$ is the average of the expected outputs y_j (the 20% used for the testing) and n_{test} is the number of points used for the testing. The NL metric is given by:

$$NL = 1 - R^2[\hat{y}, y] \tag{6.3}$$

NL has a value in the interval [0,1] and represents the fraction of the output that cannot be explained by a linear transformation of the lagged input, where 0 indicates a linear relationship in between input and output and 1 indicates a highly non-linear relationship.
The MC metric is used to evaluate the capacity of the reservoir to remember previous inputs. To calculate it, we first use the output of the reservoir to predict past inputs, as follows:

$$\hat{x}(t-i) = w_i y(t) \tag{6.4}$$

where y(t) is the actual output from the network, $\hat{x}(t-i)$ is the predicted input of the reservoir lagged of i timesteps and w_i are the coefficients determined from linear regression using $x(t-i)$, the real lagged input, as training. We can now define the MC metrics as:

$$MC = \sum_{i=0}^{8} R^2[\hat{x}(t-i), x(t-i)] \tag{6.5}$$

A high MC means that the system retains the information about past input in its current data input.
In table 6.2 we calculated the two metrics for the dataset corresponding to the output presented in Figure 6.9.

	Case in Fig. 6.9a. (98.28%)	**Case in Fig. 6.9b. (94.02%)**	**Case in Fig. 6.9c. (89.69%)**
NL	0.405	0.409	0.505
MC	2.798	1.893	1.573

Table 6.2: Calculation of the NL and MC metrics for the three cases presented in Figure 6.9.

The reservoir metrics confirm what was observed in the PCA and in the analysis of the virtual neurons: in the case of Figure 6.9a the MC has a higher value than in the other two cases, shown respectively in Figure 6.9b and in Figure 6.9c, where the MC presents the lowest value, meaning that the system in a. has a better memory of previous inputs. For the NL metric, the values are quite similar, especially for the case in a. and b., that are almost identical. The highest value of NL is observed for the case in c. In the case in a. the MC and the NL, even if not extremely high, combined, still provide a very good accuracy in the classification. This highlights even more how the performances of the reservoir system are highly dependent on the combination of the memory and the non-linearity and not on their separated effect.

6.4.4 Saturated states

Even in magnetically saturated states, the tunneling transport leads to a non-linear dependence of the resistance on voltage. The resistance vs applied DC voltage curves measured in the saturated states, respectively AP and P, are presented in Figure 6.12: a large change of resistance with voltage is observed in the AP state, while the P state exhibits a smaller non-linear variation.
To evaluate the impact of the non-linear voltage dependence of the resistance, we tested the sine and square recognition task in the magnetically saturated states. We observed that the change in the resistance due to the applied voltage in the measurement bring the classification accuracy up to 89% in the AP state, provided by the non-linearity of the system only. In the P state, a lower accuracy around 82% still provided by a non-linear resistance reading.
We calculated also for these two scenarios the reservoir metrics starting from the input and output of the sine and square tasks and using the same input voltage values and the same θ in the examples just discussed. We obtained for the P state NL = 0.692 and MC = 0.687 and for the AP state NL = 0.612 and MC = 0.883. We can observe that the MC decreases from the values presented in table 6.2, while the non-linearity is actually higher than in these examples, but on its own not sufficient to increase the accuracy. What matters is the combination of these two metrics (or reservoir properties) rather than just one, even if apparently good.

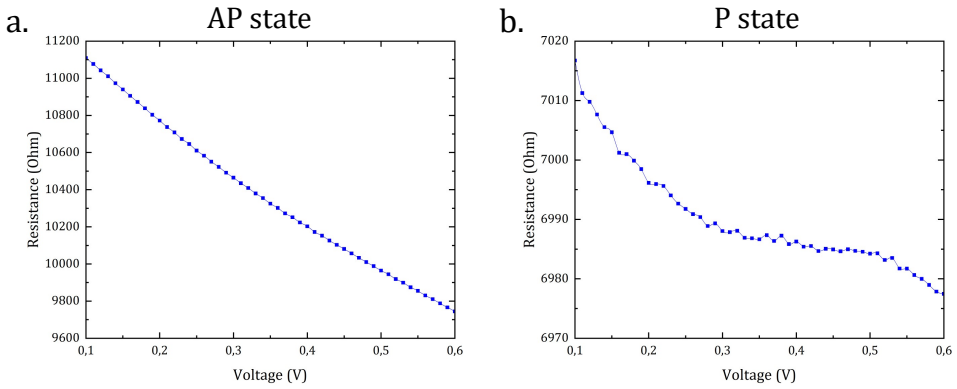

Figure 6.12: **R vs V for the saturated states** | a. Resistance as a function of the applied voltage in the AP state. b. Resistance as a function of the applied voltage in the P state.

6.5 NARMA task

The NARMA (Normalised Auto-Regressive Moving Average) is another type of task used as a benchmark for RC and dynamical systems, as it requires non-linearity and memory properties to be successfully performed. It is an imitation task, meaning that the neural network is expected, once trained, to be able to recreate the target output sequence [260]. The NARMA-N is a time series whose form can be generalised as:

$$x(t+1) = \alpha x(t) + \beta x(t)\Big(\sum_{i=0}^{N-1} x(t-i)\Big) + \gamma u(t-N+1)u(t) + \delta \tag{6.6}$$

where N represents the order of the equation, in terms of number of previous states that must be remembered. The non-linearity comes from the x(t)x(t-i) and the u(t-N+1)u(t) terms. The parameters α, β, γ and δ are tuned depending on N in order for the time series not to diverge. The input u(t) for the time series is generated from a random distribution in the range of [0, 0.5] or [0, 0.2], depending on the chosen parameters for the task. In the following table (6.3) the three NARMA tasks used to test our RC systems are listed with their corresponding parameters found in literature:

N	α	β	γ	δ	Introduced in:
5	0.3	0.05	1.5	0.1	[268]
10	0.3	0.05	1.5	0.1	[269]
30	0.2	0.04	1.5	0.001	[270]

Table 6.3: Parameters for different NARMA-N tasks.

The three task require respectively the memory of 5, 10 and 30 previous input time-steps. The same input in the range [0, 0.5] was used for the three tasks. Figure 6.13a shows 200 timesteps from the three different NARMA outputs, respectively the NARMA-5, NARMA-10 and NARMA-30 in red, green and blue. Due to the long-term temporal dependency, the NARMA task is more challenging for a reservoir computing system than the sine and square classification task and requires a higher balance in between the non-linearity and the memory capacity of the system [260].
To perform the task in our system the input was re-normalized to the voltage input using the following formula:

$$u_{PRC} = \frac{u}{0.5} * (max_{PRC} - min_{PRC}) + min_{PRC} \tag{6.7}$$

where min_{PRC} and max_{PRC} represent respectively the minimum and the maximum voltage value applied to the system. Once obtained the correct voltage amplitude to provide to our system, the time-multiplexed technique was applied in order to increase the dimensionality. The input gets multiplied by a random matrix of ±1 with a size N, corresponding to the chosen number of virtual neurons.

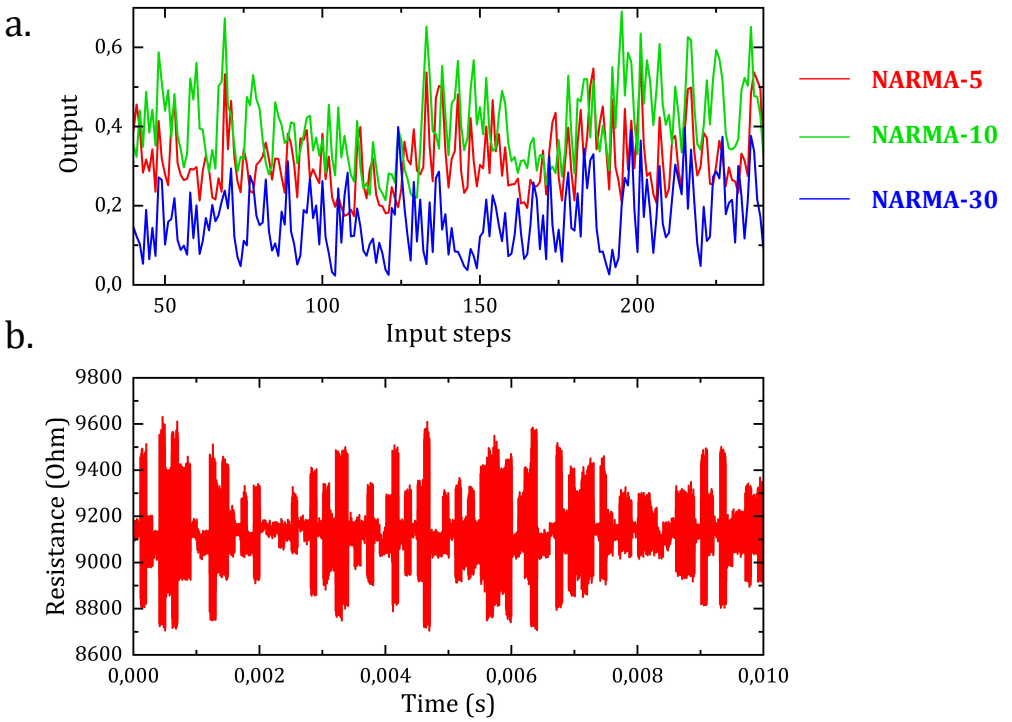

Figure 6.13: **NARMA imitation task** | a. 200 timesteps of the output for the NARMA-5 (red), NARMA-10 (green) and NARMA-30 (blue) imitation tasks. b. Part of the resistance response of the device, measured and sampled, to the random input sequence used for the NARMA tasks.

6.5.1 Results

In Figure 6.13 we show a part of the resistance response of the device for an external magnetic field of -7 mT to the random input sequence used for the three different NARMA tasks. We use N = 50 virtual neurons, θ = 2 µs, and a voltage range of 200 - 500mV. The input length is 3000 points before the time-multiplexing. Of these 3000 points 80% are used for training and 20% for testing.
Figure 6.14 shows 150 samples of the expected output compared to the imitation of the output generated by the reservoir system for the three NARMA tasks presented in table 6.3, respectively NARMA-5 in a., NARMA-10 in b. and NARMA-30 in c. The output generated by the network follows the expected output to some extent, mainly in terms of shape of the signal. However, the amplitude of the expected output varies more than the reconstructed one, meaning probably a lack of memory of the system that produces similar amplitudes, whatever the input. We calculated the normalized mean square error (NMSE) for the three tasks. The NMSE that is calculated as the square of the average difference in between the expected and the measured output, divided by the average squared expected output, point by point (see equation 6.8), is in general used as a parameter to quantify the quality of the reservoir system. The NMSE is expressed by the following equation:

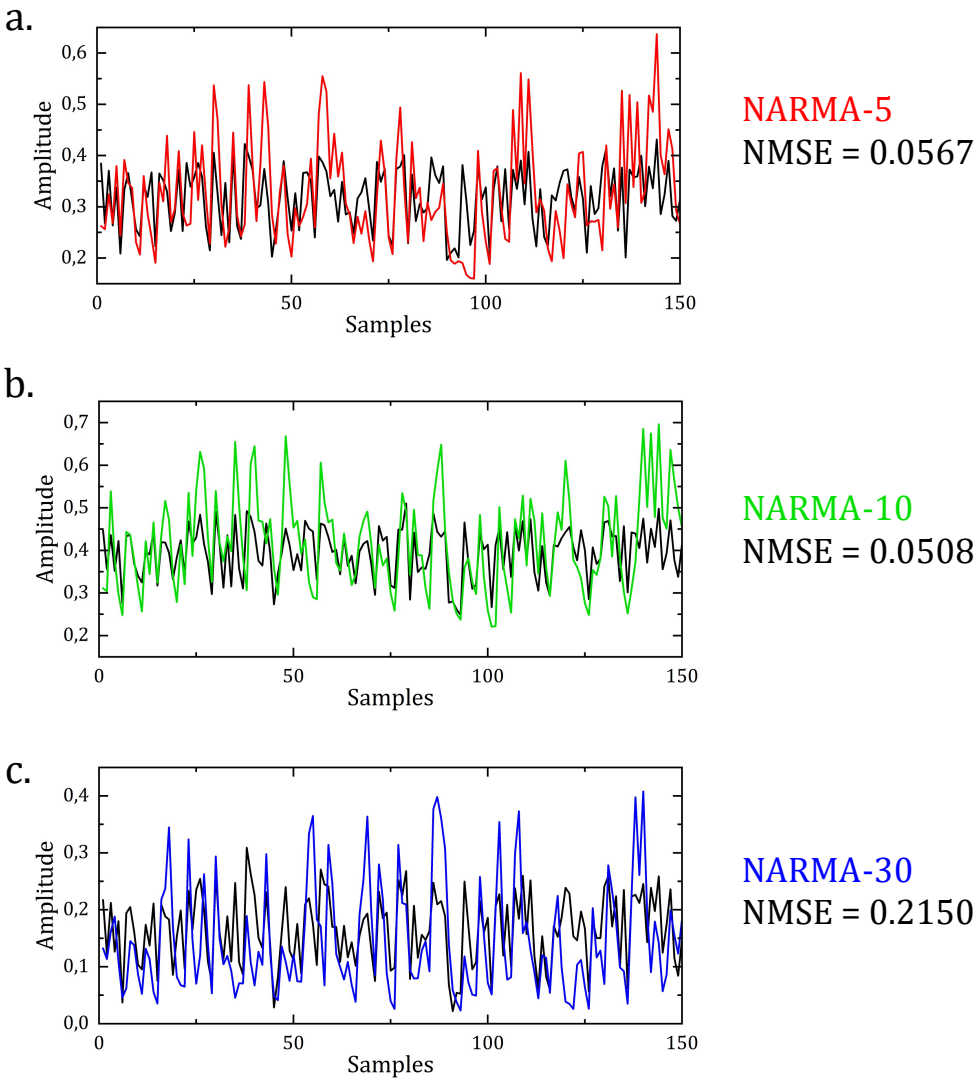

Figure 6.14: **Expected and reconstructed outputs for three different NARMA tasks** | a. 150 timesteps of the reconstructed amplitude for the NARMA-5 task (black) compared to the expected output (red). b. 150 timesteps of the reconstructed amplitude for the NARMA-10 task (black) compared to the expected output (green). c. 150 timesteps of the reconstructed amplitude for the NARMA-10 task (black) compared to the expected output (blue).

$$\mathrm{NMSE} = \frac{\mathrm{mean}(\sum_{i=1}^{\mathrm{len}(y_{test})} \left(y_{test}(i) - y_{pred}(i)\right)^2}{\mathrm{mean}\left(y_{test}(i)\right)^2)} \tag{6.8}$$

where y_{test} is the target output and y_{pred} is the predicted output on the test set. For the NARMA-5 task we obtain a value of NMSE = 0.0567 and for the NARMA-10 task we obtain a value NMSE = 0.0508. The state-of-the-art NMSE for these tasks are is in between 5×10^{-4} and 0.01 for the NARMA-5 task and in between 7.7×10^{-4} and 0.023 for the NARMA-10 task, from [271, 272]. NMSE < 0.05 for the NARMA-5 task and NMSE $<$ 0.1 for the NARMA-10 task are considered acceptable [271, 272]. This means that the results we obtain for the NARMA-5 task are outside the acceptable limits, while those for the NARMA-10 are still acceptable, but we could probably improve the results by tuning the parameters of the network for both presented cases. For the NARMA-30 task as it is high memory demanding (30 steps ahead) it is more complicated to get a low NMSE. It is in general said that a NMSE up to 0.2 indicates good performances of the reservoir system [273]. In our case we obtain a NMSE of 0.2150 that is a bit above the threshold. By looking at the visual differences in between the reconstructed and the expected output for the three tasks, the two curves that seem to better overlap are indeed the ones for the NARMA-30 task. This could mean that with the parameters used, the system showed better performances on tasks requiring longer memory than on task requiring a short-term memory. Still, there could be other reasons to explain these results which are not optimal for any of the three NARMA tasks.
To conclude, more experimental measurements are needed to better understand the response of the system to the

different NARMA tasks. Several parameters can be tuned, the most important being the magnetic field, which directly affects the relaxation time of the system; the number of virtual neurons used for time-multiplexing, chose in relation to the time constant, is another key parameter, to be further investigated.

6.6 Mackey-Glass task

The Mackey-Glass task is another benchmark for reservoir computing. The Mackey-Glass is a model that was developed to describe the physiological control in biological systems. Depending on the parameters used, the equation can show different dynamical behaviours: periodic, aperiodic or chaotic [274]. The model at the basis of the benchmark is based on the growth rates of white blood cells in leukaemia patients. It consists in:

$$\mathrm{P} = \frac{\beta\theta^{\mathrm{n}}\mathrm{P}_{\mathrm{t}-\tau}}{\theta^{\mathrm{n}} + \mathrm{P}^{\mathrm{n}}_{\mathrm{t}-\tau}} - \gamma\mathrm{P}_{\mathrm{t}} \tag{6.9}$$

where $\mathrm{P_t} > 0$ is the concentration of circulating blood cells at time t, τ is the time delay between initiating blood cells production and mature blood cells being released, $\beta > 0$ is the base level production rate of cells, $\theta > 0$ is the baseline concentration, $\gamma > 0$ is the decay rate of cells and $\mathrm{n} > 0$ is a non-linearity parameter. By normalising the concentration with respect to the baseline θ we obtain the classic form of the Mackey-Glass equation [275]:

$$\frac{\mathrm{dx}}{\mathrm{dt}} = \frac{\beta\mathrm{x}(\mathrm{t}-\tau)}{1 + \mathrm{x}(\mathrm{t}-\tau)^{\mathrm{n}}} - \gamma\mathrm{x}(\mathrm{t}) \tag{6.10}$$

To get a discrete sequence we take $\mathrm{dt} = 1$. The parameters chosen in general for the task are $\beta = 0.2$, $\mathrm{n} = 10$, $\gamma = 0.1$ and $\tau = 17$ for which the task is mildly chaotic, as proposed by Jaeger *et al.* [226]. Figure 6.15 shows 1000 timesteps of the Mackey-Glass series resulting from the use of the parameters just listed.
The Mackey-Glass task is a prediction task, meaning that the network get tested on predicting the behaviour of the signal $\mathrm{k_{ahead}}$ steps in the future. The system is fed with the Mackey-Glass time series as an input, and it has to provide the prediction for the time series $\mathrm{k_{ahead}}$ steps ahead. Similarly to what was discussed for the NARMA task, the Mackey-Glass chaotic prediction task is more challenging than sine-squre classification because of the long term dependencies in the signal [260].
For our physical reservoir system the input is re-normalized to the device's voltage input value range where non-linear behaviour is observed and temporal multiplexing is applied to increase the dimensionality of the system.

6.6.1 Results

We present here the results obtained for a signal time-multiplexed with $\mathrm{N} = 100$ virtual neurons and $\theta = 2$ µs. The measurement procedure is the same as for the sine and square task. The time-multiplexed Mackey-Glass input was mapped to a voltage range of 200 - 600 mV. The amplitude of the resistance response does not reflect well the changes in the input amplitude, probably for a lack of short-term memory. This is indeed reflected in the output of the network when compared to the expected output, respectively the red and blue curves in Figure 6.15b. The two are compared performing the task for 10 steps ahead. The output of the network seems to follow in some way the expected one, but both the shapes and the amplitude are not matching well with the signal in blue. The NMSE, already used as an accuracy parameter for the NARMA task, presented in equation 6.8, is in general used also to quantify the quality of the reservoir system used when testing the Mackey-Glass task. For the example in Figure 6.15c we obtain a NMSE of 0.0568 which can be considered an acceptable performance [276]. We expect improved performance by tuning experimental parameters, specifically the magnetic field, the time multiplexing step theta and the number of virtual neurons N.

6.7 Conclusions

In this chapter we studied the potential of spin textures in magnetic tunnel junction (MTJ) to perform the temporal recognition and prediction tasks using the reservoir computing principles. A large resistance × area product MTJ was used for the study, which allows us to achieve low power excitation using VCMA effect. The spin textures were excited using a voltage applied on the MTJ and their dynamics was electrically detected using the magnetoresistive effect. The spin textures were nucleated using an external magnetic field as evidenced by intermediate resistance states in the hysteresis loops. The response of the device to the applied external DC voltage consists in stochastic jumps in between these several states. On average, this creates a non-linear response of the device to the applied excitation. Furthermore, we showed that the different occupations of the

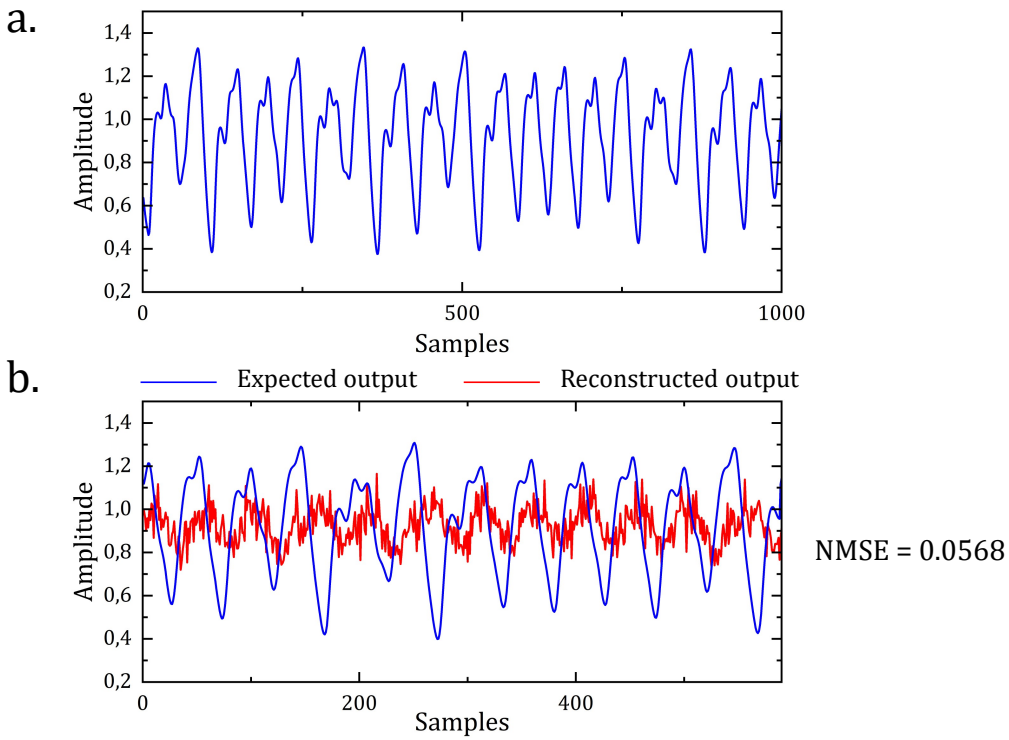

Figure 6.15: **Mackey-Glass prediction task** | a. 1000 timesteps of the Mackey-Glass prediction task time series for the parameters $\beta = 0.2$, n = 10, $\gamma = 0.1$ and $\tau = 17$. series. c. Expected (blue) and reconstructed (red) output from the reservoir for the Mackey-Glass prediction task, 10 steps ahead, for N = 100 virtual neurons and $\theta = 2$ µs.

intermediate resistance states due to the stochasticity are creating a relaxation time that can be used as a short-term memory of the device. To test the efficiency of the reservoir, we first considered a simple classification task, consisting in distinguishing sine and square temporal signals. We observe that the recognition depends significantly on the magnetic field value and history during the reversal, i.e. the nature of the intermediate resistance states. By analysing the responses to the same task under different conditions we showed, via principal component analysis, how the short-term memory of the network can affect the accuracy. We also quantified the respective roles of non-linearity and memory capacity through task-independent reservoir metrics.
We then presented some first results on two other benchmark tasks: the NARMA task and the Mackey-Glass time-series prediction.
Overall, the device shows the necessary qualities to be exploited as a physical reservoir computing for some sets of external parameters. It is anyway complicated to stabilize the parameters of the system due to a hysteretic behaviour in response to the external magnetic field and due to the stochasticity. These behaviours make it difficult to reproduce the good conditions found to solve a specific task. The system need to be studied more in depth, specifically using the Mackey-Glass and NARMA tasks to better understand the effect of the short-term memory of the device. An outlook will be to consider tuning the device properties to achieve a more deterministic behavior, while keeping the non-linearity and short-term memory. This could be performed by playing on the magnetic anisotropy via the thickness of the magnetic layers, pillar diameter to modify the intermediate states, or by using other excitation schemes, such spin transfer torque using lower resistance area product MTJs.

Chapter 7

Summary and perspectives

7.1 Summary

In this section I aim at giving a comprehensive summary of the work presented in this thesis and carried out during the last three years. The main characters of this thesis are magnetic skyrmions; we focused on showing how these magnetic particle-like structure are extremely interesting for a wide range of applications, going from memory to unconventional computing. Since the first discovery of magnetic skyrmions, several milestones toward their exploitation in real device application have been achieved: their stabilization at room temperature, their current-induced motion and their electrical detection. But several challenges still remain to face.
One of the first challenges to be tackled concerns the current-induced motion of skyrmions. Indeed, in ferromagnetic systems, magnetic skyrmions shows a limited velocity (up to around 100 m/s), accompanied by a bending of their trajectory away from the current direction that is caused by their topology, a phenomenon named skyrmion Hall effect. These detrimental effects for applications could be avoided by the use of synthetic antiferromagnets because of their vanishing magnetization and the zero net topological charge that antiferromagnetic skyrmions would carry. Steps toward the realization of current-induced motion experiments of skyrmions in synthetic antiferromagnets have been done, starting from their nucleation and detection, challenging tasks due to the zero magnetization in these systems.

In the first part of my PhD we focused our attention on the demonstration of the fast current-induced motion of magnetic skyrmions in a synthetic antiferromagnet stack. Using magnetic force microscopy (MFM), we experimentally observed the fast velocity (up to 900 m/s) and the cancellation of the skyrmion Hall effect. I also performed additional current-induced motion experiments in ferromagnetic stacks similar to the SAF, which demonstrated much slower motion (100 m/s) with significant skyrmion Hall effect. This shows that the increase in velocity and the cancellation of the skyrmion Hall results form the magnetic compensation.
To better understand the results, the work was complemented by micromagnetic simulations and an analytical modelling. The observed high experimental velocities at high current densities matched well the analytical model and this can be explained by the compensation of the gyrotropic forces. Micromagnetic simulations revealed a dynamical deformation in the skyrmion shape and a tilt in the skyrmion magnetization away from the Néel chirality resulting in a saturation of the velocities for high current densities. We also showed that by increasing the RKKY coupling in between the two ferromagnetic layers or by decreasing the length of the current pulses used to study the dynamics, we could decrease this deformation and reach higher velocities.
These results set a milestone for memory applications based on skyrmions in tracks where a fast motion along the current direction is crucial.

The second part of this thesis was dedicated to the study of the manipulation of the magnetic skyrmions in a magnetic tunnel junction for memory applications. Contrary to MRAM where the bit is composed of two memory levels, the skyrmion state offers an additional degree of freedom, which can be tuned electrically. This opens a promising path for skyrmion base multistate memories.
When I started my PhD, the full bipolar electrical control of the nucleation/annihilation process in a MTJ, a crucial step for the write and erase operation for memories, was still missing. To reach this goal, I considered *operando* x-ray magnetic microscopy which allows the visualisation of the nucleated skyrmions in MTJ together with their electrical characterization. *Operando* scanning transmission x-ray magnetic microscopy experiments allowed me to demonstrate the bipolar electrical control of the nucleation and annihilation process using DC electrical current as well as current pulses. I also performed time-resolved pump-probe magnetic imaging, which shed light on the current-induced skyrmion nucleation and annihilation process. The experiments suggest that the nucleation occurs via a full reversal of the magnetization followed by the skyrmion nucleation after the pulse. Micromagnetic simulations and additional experiments are in progress to support this scenario.

A third project of my thesis work, aimed at exploiting the dynamics of magnetic skyrmions for non-conventional computing applications based on the physical reservoir computing scheme. Reservoir computing proposes to use the dynamics of a complex physical system to achieve classification and prediction tasks. The physical system allows to project linearly inseparable inputs into a higher dimensional space, making them linearly separable. The state of the reservoir is then read and transformed into the output of the neural network system by training one layer of neurons. In our work, we exploited spin textures generating intermediate resistance states in an MTJ system as a physical reservoir. An external applied voltage was used as input which led to spin textures dynamics. The reading of the reservoir state was performed by exploiting the changes in the TMR caused by the modification in the magnetization of the intermediate states.
We first presented in detail the system chosen to perform the reservoir computing, by describing its response to external magnetic field and gate voltage, consisting in a stochastic jumps in between different intermediate resistance states. We showed how we exploited the stochasticity to have the necessary characteristic require from a reservoir system, i.e. the non-linearity response to the input and a short-term memory of previous inputs. We showed the result of standard benchmarks used to evaluate the quality of reservoir computing systems like the sines and squares classification task, the Mackey-Glass chaotic time predictions task and the NARMA imitation tasks. We discussed the obtain results on the different task and how they can be used to evaluate the properties of the reservoir system.

7.2 Perspectives

This thesis' work open several perspectives and possibilities for future developments and applications.
While fast skyrmion motion was demonstrated in SAF, we observed that the effect of pinning is still strongly present. This cause a large variation of the skyrmion velocity observed in response to a pulse and in some cases the depinning energy barrier is not overcome, so no motion of the skyrmions is produced. To move toward applications like the racetrack memory where the skyrmions represent the information bits, a highly controllable and reproducible flow of the magnetic skyrmions due to the current-induced motion has to be achieved, and pinning represents one of the main drawbacks. The pinning could be reduced by the use of more amorphous FM materials rather than Co. Due to the lack of a crystalline structure, amorphous materials should be less subject to pinning, that is in general generated by dislocations, grain boundaries or other defects in the material structure [277, 278]. Materials that could be exploited are alloys like CoB, CoFeB or CoFeBSi, since the presence of B and Si increases drastically the amorphous character of the material [279]. The effect could also be given by alloys of Co and Fe containing Gd or Tb as the disorder is introduced by the high chemical mismatch [280].

Another bottleneck for the achievement of a racetrack memory is the electrical detection of the skyrmions. The electrical signal per skyrmion derived from the Hall resistivity measurement has been shown to be very low [20], while instead exploiting the TMR reading in an MTJ when a skyrmion is nucleated allows for an unambiguous electrical detection, as we observed in the experimental measurements presented in chapter 4. Combining the racetrack with an MTJ device could be the solution. To this end, the FM film hosting the skyrmions should be integrated with the free layer of the MTJ for the detection. This project is under study in my group in Spintec [281].

The experimental work presented in chapter 4 is an important milestone toward the achievement of a multilevel skyrmion memory. To continue in that direction it would be important to successfully perform the nucleation and annihilation process at zero external magnetic field, in order to make the device fully controllable just with current. Furthermore, it is important to achieve the full nucleation and annihilation of the intermediate resistance state both from the AP and P state, as it would be necessary for the writing operation. For instance, during the last experiments we were not able to annihilate the skyrmion once having it nucleated starting from the P state.

Several interesting applications of magnetic skyrmions can be thought, in the field of non-conventional computing. Several works proposed the idea of exploiting skyrmion lattices for reservoir computing [249, 251]. The experimental results in this direction mainly rely on imaging techniques [247, 245], while it would be more interesting for applications to have an electrical readout of the signal generated by the skyrmion reservoir. Also in this case a possibility to have a large electrical readout would be to exploit several MTJs integrated inside the thin film hosting the skyrmions in order to exploit their TMR.
Continuing instead on our idea of spin textures in MTJ to perform a physical reservoir computing, it could be thought of looking for devices showing a more deterministic behaviour in terms of dependence to the external magnetic field and applied voltage. Exploiting current rather than voltage could be a possibility in that direction, but that would make a less power efficient application.

The research is also focusing on skyrmion hosted by more exotic materials. Altermagnets, a recently discovered type of materials [282, 283], are raising a large interest in the spintronics community. Altermagnets are exhibiting a zero net magnetization, similar to antiferromagnets, which is coming from the arrangement of the magnetic atoms in the crystal structure. Differently from antiferromagnets, they exhibit a spin-dependent splitting of the electronic band structure along some of the crystal directions depending on the material. Due to the spin-splitting they exhibit different type of anomalous Hall effects, which promotes them as candidates for possible spintronics applications. Stabilizing magnetic skyrmions in such materials could open the doors for new possible manipulation of spin textures.
Other interesting candidates to host magnetic skyrmions could be two-dimensional (2D) materials, as 2D van der Waals materials, that are composed of one or few atomic layers with strong atomic bonds within the layer and van der Waals interaction between the layers that maintain the structure of the material. It has been shown that these materials can host skyrmions and skymion lattices [284] due to a large DMI interaction that is induced by the breaking of the symmetry at the interfaces [285].

Overall, the research related to magnetic skyrmions and their possible applications is strongly proliferating; new ideas of applications are rising continuously given the large number of materials that which host them and a wide range of interesting properties discovered.

Appendix A

Derivation of Thiele equation

Contents

A.1 From LLG equation to Thiele equation 124
A.2 Thiele equation with DL-SOT 126

A.1 From LLG equation to Thiele equation

Here we derive the Thiele eqaution starting from the expression of the LLG equation by including only the DL-SOT term.

$$\frac{\partial \mathbf{m}}{\partial \mathrm{t}} = -\gamma_0\big(\mathbf{m}\times\mathbf{H_{eff}}\big) + \alpha\bigg(\mathbf{m}\times\frac{\partial \mathbf{m}}{\partial \mathrm{t}}\bigg) - \gamma_0\big(\mathbf{m}\times\mathbf{H_{DL}}\big) \tag{A.1}$$

We take the outer product with $\mathbf{m}$ from the right side of the equation:

$$\frac{\partial \mathbf{m}}{\partial \mathrm{t}} = -\gamma_0\mathbf{m}\times\bigg(\mathbf{H_{eff}} - \frac{\alpha}{\gamma_0}\frac{\partial \mathrm{m}}{\partial \mathrm{t}} + \mathbf{H_{DL}}\bigg) \tag{A.2}$$

where we can call the term in parenthesis multiplying $\mathbf{m}$ the total magnetic field $\mathbf{H_{tot}}$.

$$\mathbf{H_{tot}} = \bigg(\mathbf{H_{eff}} - \frac{\alpha}{\gamma_0}\frac{\partial \mathrm{m}}{\partial \mathrm{t}} + \mathbf{H_{DL}}\bigg) \tag{A.3}$$

and hence it is obtained:

$$\frac{\partial \mathbf{m}}{\partial \mathrm{t}} = -\gamma_0\mathbf{m}\times\mathbf{H_{tot}} \tag{A.4}$$

Now to continue the rearrangement we cross multiply both sides of the equation by $\mathbf{m}$:

$$\mathbf{m}\times\frac{\partial \mathbf{m}}{\partial \mathrm{t}} = -\gamma_0\mathbf{m}\times\mathbf{m}\times\mathbf{H_{tot}} \tag{A.5}$$

We use now the property of the cross product multiplication $\mathbf{A}\times(\mathbf{B}\times\mathbf{C}) = (\mathbf{A}\cdot\mathbf{C})\mathbf{B} - (\mathbf{A}\cdot\mathbf{B})\mathbf{C}$ on the right side of the equation, and we obtain:

$$\mathbf{m}\times\frac{\partial \mathbf{m}}{\partial \mathrm{t}} = -\gamma_0\bigg[(\mathbf{m}\cdot\mathbf{H_{tot}})\mathbf{m} - (\mathbf{m}\cdot\mathbf{m})\mathbf{H_{tot}}\bigg] \tag{A.6}$$

where $\mathbf{m}\cdot\mathbf{m} = 1$, therefore it is obtained:

$$\mathbf{m}\times\frac{\partial \mathbf{m}}{\partial \mathrm{t}} = -\gamma_0\bigg[(\mathbf{m}\cdot\mathbf{H_{tot}})\mathbf{m} - \mathbf{H_{tot}}\bigg] \tag{A.7}$$

Defining now $\lambda = \mathbf{m}\cdot\mathbf{H_{tot}}$ it is obtained:

$$-\frac{1}{\gamma_0}\mathbf{m}\times\frac{\partial \mathbf{m}}{\partial \mathrm{t}} = \lambda\mathbf{m} - \mathbf{H_{eff}} + \frac{\alpha}{\gamma_0}\frac{\partial \mathrm{m}}{\partial \mathrm{t}} - \mathbf{H_{DL}} \tag{A.8}$$

And we can now isolate $\mathbf{H_{eff}}$ obtaining:

$$\mathbf{H_{eff}} = \lambda\mathbf{m} - \frac{1}{\gamma_0}\frac{\partial \mathbf{m}}{\partial \mathrm{t}}\times\mathbf{m} - \mathbf{H_{DL}} + \frac{\alpha}{\gamma_0}\frac{\partial \mathrm{m}}{\partial \mathrm{t}} \tag{A.9}$$

The fundamental assumption in Thiele's model is to consider the skyrmion like a rigid body, so it's magnetization can be written as $\mathbf{m}(\mathbf{r},\mathrm{t}) = \mathbf{m}(\mathbf{r}-\mathbf{v}\mathrm{t})$. The time derivative can be changed into a space derivative using the chain rule $\frac{\partial \mathrm{u(x,y)}}{\partial \mathrm{x}} = \frac{\partial \mathrm{u(x,y)}}{\partial \mathrm{y}}\frac{\partial \mathrm{y}}{\partial \mathrm{x}}$, so it is obtained:

$$\frac{\partial \mathbf{m}}{\partial \mathrm{t}} = -\frac{\partial \mathbf{r}}{\partial \mathrm{t}}\frac{\partial \mathbf{m}}{\partial \mathbf{r}} = -(\mathbf{v}\cdot\nabla)\mathbf{m} = -\sum_{\mathrm{i}}\mathrm{v_i}\frac{\partial \mathbf{m}}{\partial \mathrm{x_i}} \tag{A.10}$$

The total force acting on the magnetization [131] is:

$$\mathbf{F} = \begin{pmatrix}\mathrm{F_x}\\ \mathrm{F_y}\\ \mathrm{F_z}\end{pmatrix},\ \mathrm{F_i} = -\mu_0\mathrm{M_s}\iiint \mathbf{H_{eff}}\cdot\frac{\partial \mathbf{m}}{\partial \mathrm{x_i}}\mathrm{d^3r} \tag{A.11}$$

where i=x,y,z and $\mathrm{d^3r} = \mathrm{dxdydz}$. Now we start the evaluation of the force without the DL-SOT term ($\mathbf{H_{DL}} = 0$), substituting equation A.9:

$$\mathrm{F_i} = -\mu_0 \mathrm{M_s} \iiint \left[\lambda \mathbf{m} - \frac{1}{\gamma_0} \frac{\partial \mathbf{m}}{\partial \mathrm{t}} \times \mathbf{m} + \frac{\alpha}{\gamma_0} \frac{\partial \mathbf{m}}{\partial \mathrm{t}} \right] \cdot \frac{\partial \mathbf{m}}{\partial \mathrm{x_i}} \, \mathrm{d^3r} \tag{A.12}$$

$$= -\mu_0 \mathrm{M_s} \iiint \left[\lambda \mathbf{m} - \frac{1}{\gamma_0} \mathrm{v_j} \frac{\partial \mathbf{m}}{\partial \mathrm{x_j}} \times \mathbf{m} + \frac{\alpha}{\gamma_0} \mathrm{v_j} \frac{\partial \mathbf{m}}{\partial \mathrm{x_j}} \right] \cdot \frac{\partial \mathbf{m}}{\partial \mathrm{x_i}} \, \mathrm{d^3r} \tag{A.13}$$

$$= -\frac{\mu_0 \mathrm{M_s}}{\gamma_0} \iiint \left[\gamma_0 \lambda \mathbf{m} - \mathrm{v_j} \frac{\partial \mathbf{m}}{\partial \mathrm{x_j}} \times \mathbf{m} + \alpha \mathrm{v_j} \frac{\partial \mathbf{m}}{\partial \mathrm{x_j}} \right] \cdot \frac{\partial \mathbf{m}}{\partial \mathrm{x_i}} \, \mathrm{d^3r} \tag{A.14}$$

Assuming the magnetization along $\hat{\mathbf{z}}$ homogeneous across the thickness t of the FM layer it is obtained $\iiint \mathrm{d^3r} = \iiint \mathrm{dxdydz} = \mathrm{t} \iint \mathrm{dxdy}$. Also the vector $\mathbf{m}$ and its spacial derivative are orthogonal, so it is obtained:

$$\mathrm{F_i} = -\frac{\mu_0 \mathrm{M_s t}}{\gamma_0} \iint \left[-\mathrm{v_j} \frac{\partial \mathbf{m}}{\partial \mathrm{x_j}} \times \mathbf{m} + \alpha \mathrm{v_j} \frac{\partial \mathbf{m}}{\partial \mathrm{x_j}} \right] \cdot \frac{\partial \mathbf{m}}{\partial \mathrm{x_i}} \, \mathrm{dxdy} \tag{A.15}$$

$$= -\frac{\mu_0 \mathrm{M_s t}}{\gamma_0} \iint \left[-\frac{\partial \mathbf{m}}{\partial \mathrm{x_j}} \times \mathbf{m} + \alpha \frac{\partial \mathbf{m}}{\partial \mathrm{x_j}} \right] \cdot \frac{\partial \mathbf{m}}{\partial \mathrm{x_i}} \mathrm{v_j} \, \mathrm{dxdy} \tag{A.16}$$

$$\tag{A.17}$$

$\mathbf{H_{eff}}$ does not generate any force on the skyrmion so $\mathrm{F_i} = 0$ which brings the expression to (using $\gamma_0 = \mu_0 \gamma$):

$$-\frac{\mathrm{M_s t}}{\gamma} \iint \left[-\frac{\partial \mathbf{m}}{\partial \mathrm{x_j}} \times \mathbf{m} + \alpha \frac{\partial \mathbf{m}}{\partial \mathrm{x_j}} \right] \cdot \frac{\partial \mathbf{m}}{\partial \mathrm{x_i}} \mathrm{v_j} \, \mathrm{dxdy} = 0 \tag{A.18}$$

The two terms can be separated:

$$-\frac{\mathrm{M_s t}}{\gamma} \iint \left[-\frac{\partial \mathbf{m}}{\partial \mathrm{x_j}} \times \mathbf{m} \right] \cdot \frac{\partial \mathbf{m}}{\partial \mathrm{x_i}} \mathrm{v_j} \, \mathrm{dxdy} - \frac{\mathrm{M_s t}}{\gamma} \iint \left[\alpha \frac{\partial \mathbf{m}}{\partial \mathrm{x_j}} \right] \cdot \frac{\partial \mathbf{m}}{\partial \mathrm{x_i}} \mathrm{v_j} \, \mathrm{dxdy} = 0 \tag{A.19}$$

and by using the cross product properties $(\mathbf{A} \times \mathbf{B}) \cdot \mathbf{C} = \mathbf{A} \cdot (\mathbf{B} \times \mathbf{C}) = (\mathbf{B} \times \mathbf{C}) \cdot \mathbf{A}$ one obtains:

$$-\frac{\mathrm{M_s t}}{\gamma} \iint \left[-\frac{\partial \mathbf{m}}{\partial \mathrm{x_j}} \times \frac{\partial \mathbf{m}}{\partial \mathrm{x_i}} \right] \cdot \mathbf{m} \, \mathrm{v_j} \, \mathrm{dxdy} - \frac{\mathrm{M_s t}}{\gamma} \iint \alpha \frac{\partial \mathbf{m}}{\partial \mathrm{x_i}} \cdot \frac{\partial \mathbf{m}}{\partial \mathrm{x_j}} \mathrm{v_j} \, \mathrm{dxdy} = 0 \tag{A.20}$$

Now we can write the equation in a vectorial form:

$$\mathbf{G} \times \mathbf{v} - \alpha \mathcal{D} \cdot \mathbf{v} = 0 \tag{A.21}$$

where

$$\mathbf{G} = \begin{pmatrix} 0 \\ 0 \\ \mathrm{G} \end{pmatrix}, \, \mathrm{G} = -\frac{\mathrm{M_s t}}{\gamma} \iint \left(\frac{\partial \mathbf{m}}{\partial \mathrm{x_j}} \times \frac{\partial \mathbf{m}}{\partial \mathrm{x_i}} \right) \mathrm{dxdy} \tag{A.22}$$

$$\mathcal{D} = \begin{pmatrix} \mathcal{D}_{\mathrm{xx}} & \mathcal{D}_{\mathrm{xy}} \\ \mathcal{D}_{\mathrm{yx}} & \mathcal{D}_{\mathrm{yy}} \end{pmatrix}, \, \mathcal{D}_{\mathrm{ij}} = \frac{\mathrm{M_s t}}{\gamma} \iint \frac{\partial \mathbf{m}}{\partial \mathrm{x_i}} \cdot \frac{\partial \mathbf{m}}{\partial \mathrm{x_j}} \, \mathrm{dxdy} \tag{A.23}$$

$$\mathbf{v} = \begin{pmatrix} \mathrm{v_x} \\ \mathrm{v_y} \\ 0 \end{pmatrix} \tag{A.24}$$

Equation A.21 is the Thiele equation, where $\mathbf{G} = \mathrm{G}\hat{\mathbf{z}}$ is the gyrotropic vector with $\mathrm{G} = -\frac{\mathrm{M_s t}}{\gamma} 4\pi \mathrm{N_{sk}}$, being $\mathrm{N_{sk}} = \pm 1$ the skyrmion number.

A.2 Thiele equation with DL-SOT

We want to compute now the Thiele equation taking into account the DL-SOT term in the lLG equation, so its generated force on the skyrmion. The effective field associated to the DL-SOT is given by $\mathbf{H_{DL}} = \mathrm{H_{DL}^0}(\mathbf{m}\times(\hat{\mathbf{j}}\times\hat{\mathbf{j}})$ where $\mathbf{J} = \mathrm{J}\hat{\mathbf{j}}$ is the charge current. We $\mathrm{H_{DL}} > 0$, and we also define $\mu_0\mathrm{H_{DL}^0} = \mathrm{C_{DL}J}$, with $\mathrm{C_{DL}}$ the effective magnetic field per unit current density (in $\mathrm{TA/m^2}$). Choosing $\hat{\mathbf{j}} = \hat{\mathbf{x}}$, it is obtained $\mathbf{H_{DL}} = \mathrm{H_{DL}^0}(\hat{\mathbf{y}} \times \hat{\mathbf{m}})$. The Thiele equation considering the DL-SOT terms reads:

$$\mathbf{F_{DL}} + \mathbf{G} \times \mathbf{v} - \alpha\mathcal{D} \cdot \mathbf{v} = 0 \tag{A.25}$$

To define the force generated by the DL torque we use the same procedure followed in A.1 and we substitute $\mathbf{H_{eff}}$ by $-\mathbf{H_{DL}}$ in equation A.11:

$$\mathrm{F_i} = \mu_0\mathrm{M_s}\iiint \mathbf{H_{DL}} \cdot \frac{\partial\mathbf{m}}{\partial \mathrm{x_i}}\mathrm{d^3r} = \mu_0\mathrm{M_s}\mathrm{H_{DL}^0}\iiint(\hat{\mathbf{y}} \times \hat{\mathbf{m}}) \cdot \frac{\partial\mathbf{m}}{\partial \mathrm{x_i}}\mathrm{d^3r} \tag{A.26}$$

Assuming once again homogeneous magnetization all over the thickness t of the FM magnetic film and calculating the product inside the integral for $\mathbf{m} = (\mathrm{m_x}, \mathrm{m_y}, \mathrm{m_z})$ it is obtained:

$$\mathrm{F_i} = \mu_0\mathrm{M_s}\mathrm{H_{DL}^0}\mathrm{t}\iint(\hat{\mathbf{y}} \times \hat{\mathbf{m}}) \cdot \frac{\partial\mathbf{m}}{\partial \mathrm{x_i}}\,\mathrm{dxdy} \tag{A.27}$$

$$= \mu_0\mathrm{M_s}\mathrm{H_{DL}^0}\mathrm{t}\iint\big((0\,1\,0) \times (\mathrm{m_x}\,\mathrm{m_y}\,\mathrm{m_z})\big) \cdot \begin{pmatrix} \frac{\partial \mathrm{m_x}}{\partial \mathrm{x_i}} \\ \frac{\partial \mathrm{m_y}}{\partial \mathrm{x_i}} \\ \frac{\partial \mathrm{m_x}}{\partial \mathrm{x_i}} \end{pmatrix}\mathrm{dxdy} \tag{A.28}$$

$$= \mu_0\mathrm{M_s}\mathrm{H_{DL}^0}\mathrm{t}\iint(\mathrm{m_z}\,0\,-\mathrm{m_x}) \cdot \begin{pmatrix} \frac{\partial \mathrm{m_x}}{\partial \mathrm{x_i}} \\ \frac{\partial \mathrm{m_y}}{\partial \mathrm{x_i}} \\ \frac{\partial \mathrm{m_x}}{\partial \mathrm{x_i}} \end{pmatrix}\mathrm{dxdy} \tag{A.29}$$

$$= \mu_0\mathrm{M_s}\mathrm{H_{DL}^0}\mathrm{t}\iint\Big(\mathrm{m_z}\frac{\partial \mathrm{m_x}}{\partial \mathrm{x_i}} - \mathrm{m_x}\frac{\partial \mathrm{m_x}}{\partial \mathrm{x_i}}\Big)\,\mathrm{dxdy} \tag{A.30}$$

Now we use the spherical coordinates for the magnetization, writing $\mathbf{m}(\mathbf{r}) = \big(\cos\Phi(\varphi)\sin\vartheta(\mathrm{r}), \sin\Phi(\varphi)\sin\vartheta(\mathrm{r}), \mathrm{r}\cos\vartheta(\mathrm{r})\big)$. We consider a Néel skyrmion for that presents a winding number $\mathrm{W} = 1$ and an helicity $\Psi = 0$. Therefore using $\Phi(\varphi) = \mathrm{W}\psi + \gamma$ we obtain for a Néel skyrmion $\Phi(\varphi) = \gamma$. All the angles can be observed in Figure A.1. Furthermore, for a Néel skyrmions we have that $\mathrm{F_{DL,y}} = 0$ and $\mathrm{F_{DL,x}} = \mathrm{F_{DL}}$. With these assumptions we can write: $\mathbf{m}(\mathbf{r}, \varphi) = \big(\sin\vartheta\cos\varphi, \sin\vartheta\sin\varphi, \cos\vartheta\big)$.

$$\mathrm{F_i} = \mu_0\mathrm{M_s}\mathrm{H_{DL}^0}\mathrm{t}\iint\left(\mathrm{m_z}\frac{\partial \mathrm{m_x}}{\partial \mathrm{x}} - \mathrm{m_x}\frac{\partial \mathrm{m_x}}{\partial \mathrm{x}}\right)\mathrm{dx\,dy} \tag{A.31}$$

$$= \mu_0\mathrm{M_s}\mathrm{H_{DL}^0}\mathrm{t}\int_0^{2\pi}\int_0^{\infty}\left(\sin\vartheta\cos\varphi\frac{\partial\cos\theta}{\partial \mathrm{x}} - \cos\vartheta\frac{\partial\sin\theta\cos\varphi}{\partial \mathrm{x}}\right)\mathrm{r\,dr\,d}\varphi \tag{A.32}$$

$$= \mu_0\mathrm{M_s}\mathrm{H_{DL}^0}\mathrm{t}\int_0^{2\pi}\int_0^{\infty}\left(\sin\vartheta\cos\varphi\frac{\partial\cos\theta}{\partial \mathrm{r}}\frac{\partial \mathrm{r}}{\partial \mathrm{x}} - \cos\vartheta\frac{\partial(\sin\theta\cos\varphi)}{\partial \mathrm{r}}\frac{\partial \mathrm{r}}{\partial \mathrm{x}}\right)\mathrm{r\,dr\,d}\varphi \tag{A.33}$$

$$= \mu_0\mathrm{M_s}\mathrm{H_{DL}^0}\mathrm{t}\int_0^{2\pi}\int_0^{\infty}\left(-\sin^2\vartheta\cos^2\varphi\frac{\mathrm{d}\vartheta}{\mathrm{dr}} - \cos^2\vartheta\cos^2\varphi\frac{\mathrm{d}\vartheta}{\mathrm{dr}}\right)\mathrm{r\,dr\,d}\varphi \tag{A.34}$$

$$= -\mu_0\mathrm{M_s}\mathrm{H_{DL}^0}\mathrm{t}\int_0^{2\pi}\int_0^{\infty}\cos^2\varphi\frac{\mathrm{d}\vartheta}{\mathrm{dr}}\,\mathrm{rdrd}\varphi \tag{A.35}$$

The integral $\int_0^{2\pi}\cos^2\varphi\,\mathrm{d}\varphi = \pi$, so it is obtained:

$$\mathrm{F_{DL}} = -\mu_0\mathrm{M_s}\mathrm{H_{DL}^0}\mathrm{t}\pi\int_0^{\infty}\frac{\mathrm{d}\vartheta}{\mathrm{dr}}\,\mathrm{rdr} \tag{A.36}$$

To evaluate this integral we assume that the skyrmion has a 180° Bloch DW profile:

$$\vartheta(\mathrm{r}) = -2\arctan\left(\exp\left(\frac{\mathrm{r}-\mathrm{R}}{\Delta}\right)\right) \tag{A.37}$$

so it can be calculated:

$$\frac{\mathrm{d}\vartheta}{\mathrm{dr}} = -\frac{1}{\Delta}\frac{\exp\left(\frac{\mathrm{r}-\mathrm{R}}{\Delta}\right)}{1+\exp 2\left(\frac{\mathrm{r}-\mathrm{R}}{\Delta}\right)} = -\frac{1}{\Delta}\mathrm{sech}\left(\frac{\mathrm{r}-\mathrm{R}}{\Delta}\right) \tag{A.38}$$

but it also holds $\sin\vartheta(\mathrm{r}) = \mathrm{sech}\left(\frac{\mathrm{r}-\mathrm{R}}{\Delta}\right)$ is is obtained:

$$\mathrm{F_{DL}} = -\mu_0 \mathrm{M_s H^0_{DL} t}\frac{\pi}{\Delta}\int_0^\infty \sin\vartheta \mathrm{r dr} \tag{A.39}$$

for a skyrmion with a radius $\mathrm{R} >> \Delta$ it can be used in the integral $\mathrm{r} = \mathrm{R}$, so it is obtained:

$$\mathrm{F_{DL}} \approx -\mu_0 \mathrm{M_s H^0_{DL} tR}\frac{\pi}{\Delta}\int_0^\infty \sin\vartheta \mathrm{dr} \tag{A.40}$$

$$\approx -\mu_0 \mathrm{M_s H^0_{DL} tR}\frac{\pi}{\Delta}\left[-2\Delta \arctan\left(\exp\left(\frac{\mathrm{r}-\mathrm{R}}{\Delta}\right)\right)\right]_0^\infty \tag{A.41}$$

$$\approx \mu_0 \mathrm{M_s H^0_{DL} tR} 2\pi\left[\frac{\pi}{2} - \arctan(\exp\left(-\frac{\mathrm{R}}{\Delta}\right)\right] \tag{A.42}$$

$$\approx \mu_0 \mathrm{M_s H^0_{DL} tR}\pi^2 \tag{A.43}$$

For the dissipation factor it was calculated the expression in A.23. If we assume rotational symmetry we obtain $\frac{\partial \mathbf{m}}{\partial \mathrm{x}} = \frac{\partial \mathbf{m}}{\partial \mathrm{y}}$ and the two terms are orthogonal to each other, so it is obtained $\mathcal{D}_{\mathrm{xx}} = \mathcal{D}_{\mathrm{yy}} = \mathcal{D}$ and $\mathcal{D}_{\mathrm{xy}} = \mathcal{D}_{\mathrm{yx}} = 0$. the expression obtained is:

$$\mathcal{D} = \frac{\mathrm{M_s t}}{\gamma}\iint\left(\frac{\partial \mathbf{m}}{\partial \mathrm{x}}\right)^2 \mathrm{dxdy} \tag{A.44}$$

To solve this integral we have to transform once again $\left(\frac{\partial \mathbf{m}}{\partial \mathrm{x}}\right)^2$ in spherical coordinates. We remember it holds the relation:

$$\frac{\partial \mathbf{m}}{\partial \mathrm{x}} = \frac{\partial \mathrm{r}}{\partial \mathrm{x}}\frac{\partial \mathbf{m}}{\partial \mathrm{r}} + \frac{\partial \varphi}{\partial \mathrm{x}}\frac{\partial \mathbf{m}}{\partial \varphi} = \cos\varphi\frac{\partial \mathbf{m}}{\partial \mathrm{r}} - \frac{\sin\varphi}{\mathrm{r}}\frac{\partial \mathbf{m}}{\partial \varphi} \tag{A.45}$$

so we obtain:

$$\frac{\partial \mathbf{m}}{\partial \mathrm{x}} = \begin{pmatrix}\frac{\partial \mathrm{m_x}}{\partial \mathrm{x}}\\ \frac{\partial \mathrm{m_y}}{\partial \mathrm{x}}\\ \frac{\partial \mathrm{m_z}}{\partial \mathrm{x}}\end{pmatrix} = \begin{pmatrix}\cos\varphi\frac{\partial(\cos\varphi\sin\vartheta)}{\partial \mathrm{r}} - \frac{\sin\varphi}{\mathrm{r}}\frac{\partial(\cos\varphi\sin\vartheta)}{\partial\varphi}\\ \cos\varphi\frac{\partial(\sin\varphi\sin\vartheta)}{\partial \mathrm{r}} - \frac{\sin\varphi}{\mathrm{r}}\frac{\partial(\sin\varphi\sin\vartheta)}{\partial\varphi}\\ \cos\varphi\frac{\partial(\cos\vartheta)}{\partial \mathrm{r}} - \frac{\sin\varphi}{\mathrm{r}}\frac{\partial(\cos\vartheta)}{\partial\varphi}\end{pmatrix} = \begin{pmatrix}\cos^2\varphi\frac{\mathrm{d}\sin\vartheta}{\mathrm{dr}} + \frac{\sin^2\varphi}{\mathrm{r}}\sin\vartheta\\ \cos\varphi\sin\varphi\frac{\mathrm{d}\sin\vartheta}{\mathrm{dr}} + \frac{\sin\varphi\cos\varphi}{\mathrm{r}}\sin\vartheta\\ \cos\varphi\frac{\mathrm{d}\sin\vartheta}{\mathrm{dr}}\end{pmatrix} \tag{A.46}$$

Now if we compute the square value from equation A.45:

$$\left(\frac{\partial \mathbf{m}}{\partial \mathrm{x}}\right)^2 = \cos^2\varphi\left(\frac{\mathrm{d}\sin\vartheta}{\mathrm{dr}}\right)^2 + \frac{\sin^2\varphi\sin^2\vartheta}{\mathrm{r}^2} + \cos^2\varphi\left(\frac{\mathrm{d}\cos\vartheta}{\mathrm{dr}}\right)^2 \tag{A.47}$$

and we can substitute the value obtained inside A.44 by remembering $\int_0^{2\pi}\cos^2\varphi\,\mathrm{d}\varphi = \int_0^{2\pi}\sin^2\varphi\,\mathrm{d}\varphi\pi = \pi$:

$$\mathcal{D} = \frac{\mathrm{M_s t}}{\gamma}\int_0^\infty\int_0^{2\pi}\left[\cos^2\varphi\left(\frac{\mathrm{d}\sin\vartheta}{\mathrm{dr}}\right)^2 + \frac{\sin^2\varphi\,\sin^2\vartheta}{\mathrm{r}^2} + \cos^2\varphi\left(\frac{\mathrm{d}\cos\vartheta}{\mathrm{dr}}\right)^2\right]\mathrm{r\,dr\,d}\varphi \tag{A.48}$$

$$= \frac{3\pi\mathrm{M_s t}}{\gamma}\int_0^\infty\left[\left(\frac{\mathrm{d}\sin\vartheta}{\mathrm{dr}}\right)^2 + \frac{\sin^2\vartheta}{\mathrm{r}^2} + \left(\frac{\mathrm{d}\cos\vartheta}{\mathrm{dr}}\right)^2\right]\mathrm{r\,dr} \tag{A.49}$$

$$= \frac{3\pi\mathrm{M_s t}}{\gamma}\int_0^\infty\left[\cos^2\vartheta\left(\frac{\mathrm{d}\vartheta}{\mathrm{dr}}\right)^2 + \frac{\sin^2\vartheta}{\mathrm{r}^2} + \sin^2\vartheta\left(\frac{\mathrm{d}\vartheta}{\mathrm{dr}}\right)^2\right]\mathrm{r\,dr} \tag{A.50}$$

$$= \frac{3\pi\mathrm{M_s t}}{\gamma}\int_0^\infty\left[\left(\frac{\mathrm{d}\vartheta}{\mathrm{dr}}\right)^2 + \frac{\sin^2\vartheta}{\mathrm{r}^2}\right]\mathrm{r\,dr} \tag{A.51}$$

Now we can use once again the relation $\sin\vartheta = \Delta\frac{\mathrm{d}\vartheta}{\mathrm{dr}}$ for the first term in the integral:

$$\mathcal{D} = \frac{3\pi M_s t}{\gamma} \int_0^\infty \left[\left(\frac{\sin\vartheta}{\Delta} \right)^2 + \frac{\sin^2\vartheta}{r^2} \right] r\, dr \tag{A.52}$$

$$= \frac{3\pi M_s t}{\gamma} \int_0^\infty \sin^2\vartheta \left[\frac{1}{\Delta^2} + \frac{1}{r^2} \right] r\, dr \tag{A.53}$$

Now as for the calculation of F_{DL} we can use once again the assumption $R >> \Delta$ and we can assume $r = R$:

$$\mathcal{D} \approx \frac{\pi M_s t}{\gamma} \left(\frac{1}{R} + \frac{R}{\Delta^2} \right) \int_0^\infty \sin^2\vartheta\, dr \tag{A.54}$$

$$\approx \frac{\pi M_s t}{\gamma} \left(\frac{1}{R} + \frac{R}{\Delta^2} \right) \left[2\Delta \frac{\exp(\frac{2R}{\Delta})}{\exp(\frac{2R}{\Delta} + 1)} \right] \tag{A.55}$$

$$\approx \frac{\pi M_s t}{\gamma} \left(\frac{1}{R} + \frac{R}{\Delta^2} \right) 2\Delta \tag{A.56}$$

$$\approx \frac{\pi M_s t}{\gamma} 2 \left(\frac{\Delta}{R} + \frac{R}{\Delta} \right) \tag{A.57}$$

$$\approx \frac{2\pi M_s t}{\gamma} \frac{R}{\Delta} \tag{A.58}$$

To conclude the expression of G for a Néel skyrmion, so $N_{sk} = 1$ it is:

$$G = -4\pi \frac{M_s t}{\gamma} \tag{A.59}$$

Now that we have the expressions for all the terms we can calculate the velocity. From writing Thiele equation A.25 in vectorial form we obtain:

$$\begin{pmatrix} F_{DL,x} \\ F_{DL,y} \\ 0 \end{pmatrix} + G \begin{pmatrix} -v_y \\ v_x \\ 0 \end{pmatrix} - \alpha\mathcal{D} \begin{pmatrix} v_x \\ v_y \\ 0 \end{pmatrix} = 0 \tag{A.60}$$

so solving separately for the x and y component, one obtains:

$$v_x = \frac{\alpha\mathcal{D}F_{DL,x} - GF_{DL,y}}{G^2 + \alpha^2\mathcal{D}^2} \tag{A.61}$$

$$v_y = \frac{\alpha\mathcal{D}F_{DL,y} + GF_{DL,x}}{G^2 + \alpha^2\mathcal{D}^2} \tag{A.62}$$

As we already assumed $F_{DL,y} = 0$, it is obtained:

$$v_x = \frac{\alpha\mathcal{D}F_{DL}}{G^2 + \alpha^2\mathcal{D}^2} \tag{A.63}$$

$$v_y = \frac{GF_{DL}}{G^2 + \alpha^2\mathcal{D}^2} \tag{A.64}$$

Now can calculate the velocity and plug the values found fro F_{DL}, G and $\mathcal{D}$:

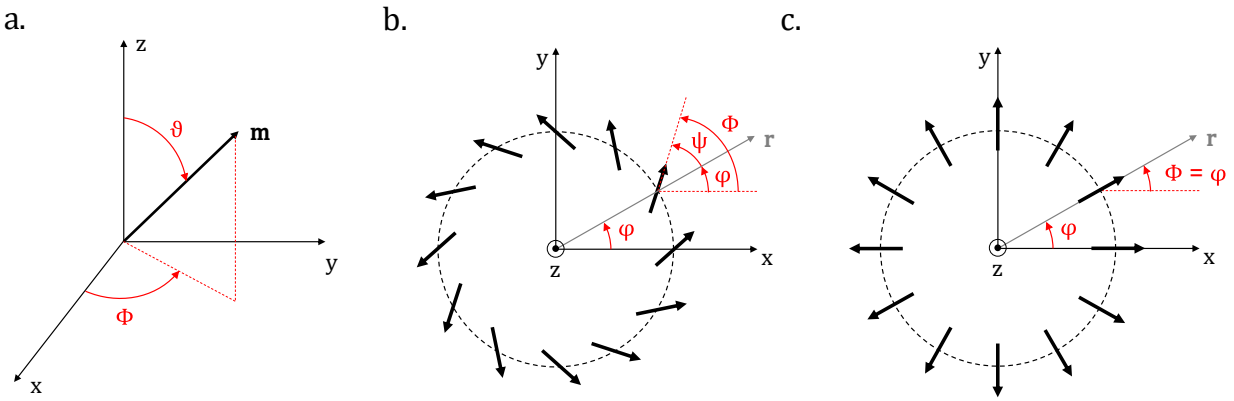

Figure A.1: **Demagnetizing field** | a. Spherical coordinates. b. Schematic top view of a skyrmion Bloch-Néel type. The angles φ and the helicity ψ are defined. c. Schematic top view of a Néel skyrmions, for which the helicity is 0 and hence Φ coincides with φ.

$$v = \sqrt{v_x^2 + v_y^2} \tag{A.65}$$

$$= \sqrt{\left(\frac{\alpha \mathcal{D} F_{DL}}{G^2 + \alpha^2 \mathcal{D}^2}\right)^2 + \left(\frac{G F_{DL}}{G^2 + \alpha^2 \mathcal{D}^2}\right)^2} \tag{A.66}$$

$$= \frac{1}{G^2 + \alpha^2 \mathcal{D}^2} \sqrt{\alpha^2 \mathcal{D}^2 F_{DL}^2 + G^2 F_{DL}^2} \tag{A.67}$$

$$= \frac{F_{DL}}{\sqrt{G^2 + \alpha^2 \mathcal{D}^2}} \tag{A.68}$$

$$= \frac{\mu_0 M_s H_{DL}^0 t R \pi^2}{\sqrt{\left(-4\pi \frac{M_s t}{\gamma}\right)^2 + \alpha^2 \left(\frac{M_s t}{\gamma} 2\pi \frac{R}{\Delta}\right)^2}} \tag{A.69}$$

$$= \frac{\mu_0 M_s H_{DL}^0 t R \pi^2}{2\pi \frac{M_s t}{\gamma} \sqrt{\alpha^2 \frac{R^2}{\Delta^2} + 4}} \tag{A.70}$$

$$= \frac{\mu_0 H_{DL}^0 R \pi \gamma}{4\sqrt{1 + \left(\frac{\alpha R}{2\Delta}\right)^2}} \tag{A.71}$$

$$= \frac{R \pi \gamma}{4\sqrt{1 + \left(\frac{\alpha R}{2\Delta}\right)^2}} C_{DL} J \tag{A.72}$$

And regarding the angle in between the x and y component of the velocity, identified experimentally as the skyrmion Hall angle, it can observed that it holds:

$$\tan \theta_{SkH} = \frac{v_y}{v_x} = \frac{G}{\alpha \mathcal{D}} \tag{A.73}$$

$$= \frac{-4\pi \frac{M_s t}{\gamma}}{\alpha \frac{2\pi M_s t}{\gamma} \frac{R}{\Delta}} \tag{A.74}$$

$$= \frac{-2\Delta}{\alpha R} \tag{A.75}$$

Appendix B

XMCD contrast

Contents

B.1 Contrast generated by x-ray absorption in one magnetic and two layers 132
B.2 Normalization in time-resolved STXM movies 132
B.3 Time-resolved image 132

B.1 Contrast generated by x-ray absorption in one magnetic and two layers

Figure B.1 shows a schematic of how the contrast resulting from x-ray absorption in one and two magnetic layers works. For positive (negative) helicity the absorption for a single magnetic layer is 0 when the magnetization is IP, is 1/2 (-1/2) when the magnetization is OOP in one direction and -1/2 (1/2) for the opposite direction. When the magnetic layers are two, like in an MTJ, the contrast sums up. Hence, if the two magnetic layers are parallelly oriented one obtains either 1 or -1, depending on the helicity and on the magnetization direction, and 0 when they are oriented AP. If one of the two layers presents an IP magnetization the contrast will remain either 1/2 or -1/2 as this scenario is the same as having only one effective magnetic layer counting for the absorption process. 1 represents a white contrast on the image and -1 represents a black contrast.

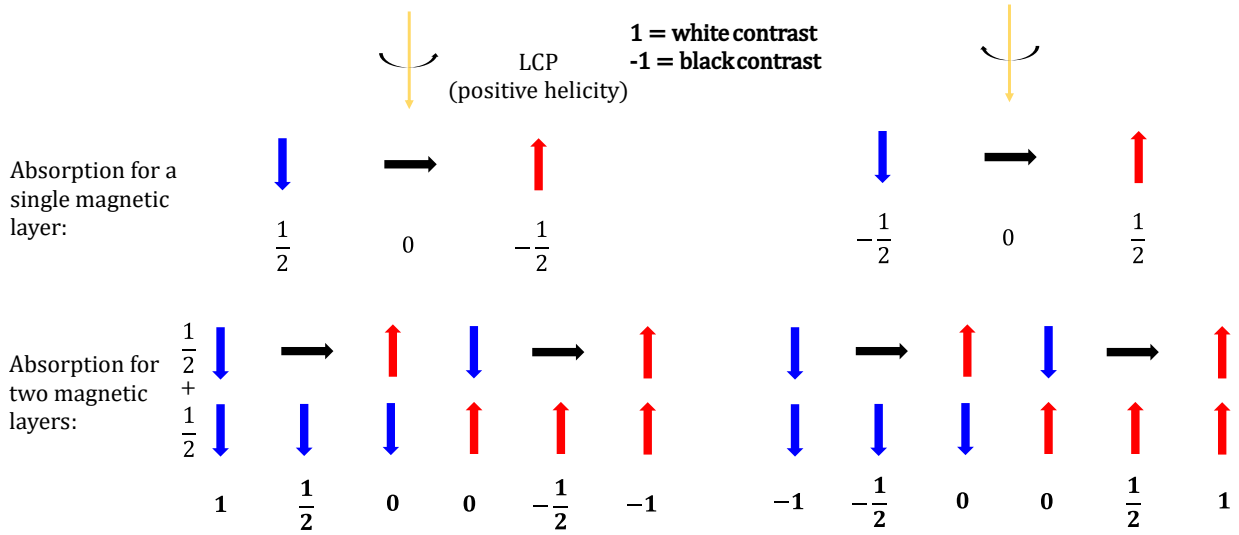

Figure B.1: **Schematic of the contrast resulting from x-ray absorption process** | Schematic of the absorption process for one or two magnetic layers. The contrast is inverse for the opposite helicities. For one magnetic layer the possibilities are either 1/2 or -1/2 as absorption values. When the system includes two magnetic layers, like an MTJ, the contrast deriving from the two layers sums up obtaining a wider range of cases.

B.2 Normalization in time-resolved STXM movies

To see magnetic contrast in time-resolved movies obtained exploiting only one helicity of the x-ray photons, as explained in chapter 4, a reference image has to be used for normalization. The normalized frame at time t is given by $\text{Frame}_{\text{norm}}(t) = \text{Frame}(t) - \text{Frame}_{\text{ref}}$, where Frame(t) and $\text{Frame}_{\text{ref}}$ are respectively the measured frame at time t and the reference frame.
Several possible scenarios are depicted in Figure B.2 and Figure B.3, deriving from the subtraction of two different frames acquired with the same helicity, respectively for positive helicity photons and negative helicity photons. To each scenario is associated a number resulting from the subtraction of the contrast provided by the reference to that of the main frame. The numbers go from 2 to -2, where positive numbers represent white contrast and the negative numbers represent black contrast, for both of them with an intensity that can be scaled, while 0 represent no contrast.

B.3 Time-resolved image

Figure B.4 shows the same set of frames presented in Figure 4.10 in chapter 4, but now the frames used as a reference for the normalization process are the averaged intensity in between the positive and negative pulse, therefore in the likely skyrmionic state. This is why one can observe a crown presenting a white contrast in the right column, the system is in AP state after the negative pulse, hence the reference frame generates the white contrrast by subtraction. The white contrast is the same observed in black for the central column frames in Figure 4.10.

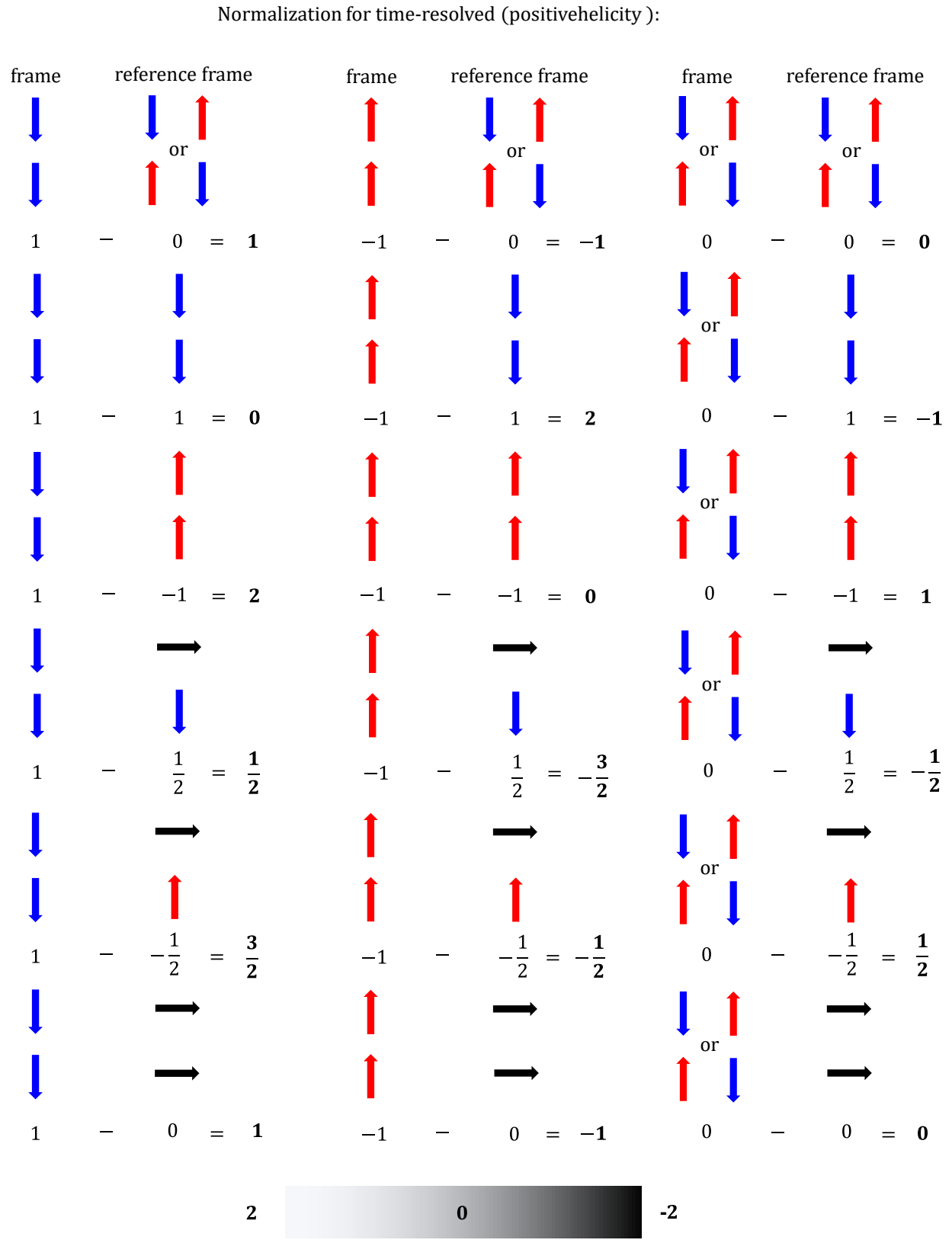

Figure B.2: **Schematic of the normalization process with a reference frame for time-resolved STXM for positive helicity photons** | Several possible scenarios resulting from the normalization of a frame with a reference one are presented in the case of an MTJ for the case of LCP photons. The contrast results from the subtraction of the reference frame to the main one, and can range from 2 to -2.

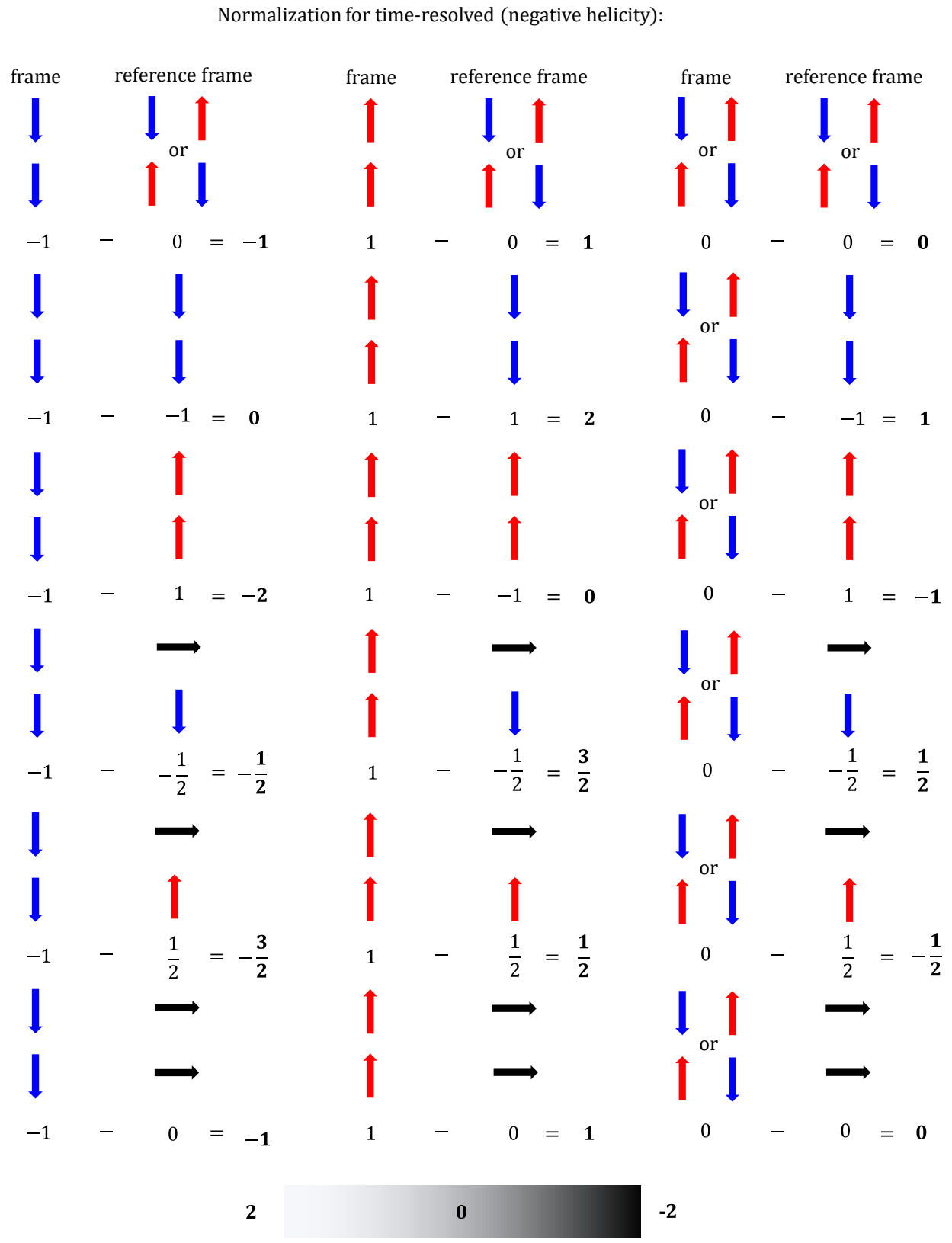

Figure B.3: **Schematic of the normalization process with a reference frame for time-resolved STXM for negative helicity photons** | Several possible scenarios resulting from the normalization of a frame with a reference one are presented in the case of an MTJ for the case of RCP photons. The contrast results from the subtraction of the reference frame to the main one, and can range from 2 to -2.

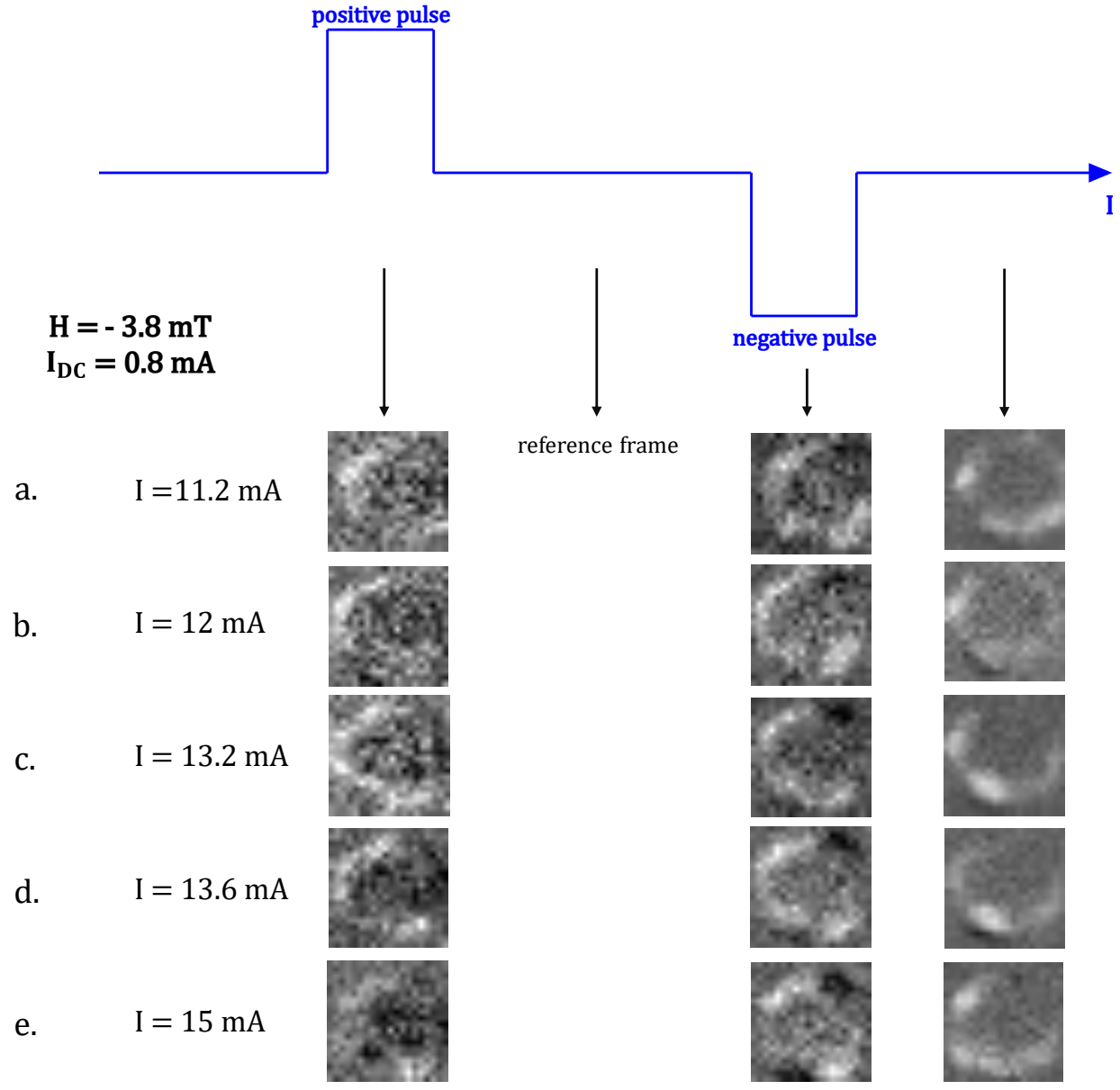

Figure B.4: **Captures from time-resolved STXM for an external magnetic field of -3.8 mT and an applied DC current of 0.8 mA, normalization with a reference frame taken after the positive pulse** | Frames taken by different time-resolved STXM movies obtained in the same external conditions of -3.8 mT magnetic field and 0.8 mA of DC current applied. All the movies are obtained using x-ray photons with negative helicity. To normalize the movies the reference frame used is an averaged intensity of frames acquired after the positive pulse. The frames on the left column are taken at the peak of the positive current pulse, those on the central column are taken at the peak of the negative pulse and those on the right column are after the positive pulse. The amplitude of the applied current pulses increases: 11.2 mA in a., 12 mA in b., 13.2 mA in c., 13.6 mA in d. and 15 mA in e.

References

[1] E. Mansfield, B. Barnes, R. J. Kline, A. E. Vladar, Y. S. Obeng, and A. Davydov. *INTERNATIONAL ROADMAP FOR DEVICES AND SYSTEMSTM 2023 EDITION METROLOGY*. Dec. 8, 2023. URL: `https://tsapps.nist.gov/publication/get_pdf.cfm?pub_id=956664` (cit. on p. 2).

[2] "Spintronics for ultra-low-power circuits and systems". *Nature Reviews Electrical Engineering*, 1 11, 2024, pp. 691–691.

[3] H. Ohno, M. D. Stiles, and B. Dieny. "Spintronics". *Proceedings of the IEEE*, 104 10, 2016, pp. 1782–1786.

[4] M. N. Baibich, J. M. Broto, A. Fert, F. N. V. Dau, F. Petroff, P. Etienne, G. Creuzet, A. Friederich, and J. Chazelas. "Giant Magnetoresistance of (001)Fe/(001)Cr Magnetic Superlattices". *Physical Review Letters*, 61 21, 1988, pp. 2472–2475.

[5] P. Grünberg, R. Schreiber, Y. Pang, M. B. Brodsky, and H. Sowers. "Layered Magnetic Structures: Evidence for Antiferromagnetic Coupling of Fe Layers across Cr Interlayers". *Physical Review Letters*, 57 19, 1986, pp. 2442–2445.

[6] M. Julliere. "Tunneling between ferromagnetic films". *Physics Letters A*, 54 3, 1975, pp. 225–226.

[7] L. Berger. "Emission of spin waves by a magnetic multilayer traversed by a current". *Physical Review B*, 54 13, 1996, pp. 9353–9358.

[8] J. Slonczewski. "Current-driven excitation of magnetic multilayers". *Journal of Magnetism and Magnetic Materials*, 159 1, 1996, pp. L1–L7.

[9] I. Dzyaloshinsky. "A thermodynamic theory of "weak" ferromagnetism of antiferromagnetics". *Journal of Physics and Chemistry of Solids*, 4 4, 1958, pp. 241–255.

[10] T. Moriya. "Anisotropic Superexchange Interaction and Weak Ferromagnetism". *Physical Review*, 120 1, 1960, pp. 91–98.

[11] A. Neubauer, C. Pfleiderer, B. Binz, A. Rosch, R. Ritz, P. G. Niklowitz, and P. Böni. "Topological Hall Effect in theAPhase of MnSi". *Physical Review Letters*, 102 18, 2009.

[12] S. Mühlbauer, B. Binz, F. Jonietz, C. Pfleiderer, A. Rosch, A. Neubauer, R. Georgii, and P. Böni. "Skyrmion Lattice in a Chiral Magnet". *Science*, 323 5916, 2009, pp. 915–919.

[13] A. Fert, V. Cros, and J. Sampaio. "Skyrmions on the track". *Nature Nanotechnology*, 8 3, 2013, pp. 152–156.

[14] A. Hrabec, J. Sampaio, M. Belmeguenai, I. Gross, R. Weil, S. M. Chérif, A. Stashkevich, V. Jacques, A. Thiaville, and S. Rohart. "Current-induced skyrmion generation and dynamics in symmetric bilayers". *Nature Communications*, 8 1, 2017.

[15] R. Juge, S.-G. Je, D. d. S. Chaves, L. D. Buda-Prejbeanu, J. Peña-Garcia, J. Nath, I. M. Miron, K. G. Rana, L. Aballe, M. Foerster, F. Genuzio, T. O. Menteş, A. Locatelli, F. Maccherozzi, S. S. Dhesi, M. Belmeguenai, Y. Roussigné, S. Auffret, S. Pizzini, G. Gaudin, J. Vogel, and O. Boulle. "Current-Driven Skyrmion Dynamics and Drive-Dependent Skyrmion Hall Effect in an Ultrathin Film". *Physical Review Applied*, 12 4, 2019, p. 044007.

[16] W. Jiang, X. Zhang, G. Yu, W. Zhang, X. Wang, M. Benjamin Jungfleisch, J. E. Pearson, X. Cheng, O. Heinonen, K. L. Wang, Y. Zhou, A. Hoffmann, and S. G. E. te Velthuis. "Direct observation of the skyrmion Hall effect". *Nature Physics*, 13 2, 2017, pp. 162–169.

[17] K. Litzius, I. Lemesh, B. Krüger, P. Bassirian, L. Caretta, K. Richter, F. Büttner, K. Sato, O. A. Tretiakov, J. Förster, R. M. Reeve, M. Weigand, I. Bykova, H. Stoll, G. Schütz, G. S. D. Beach, and M. Kläui. "Skyrmion Hall effect revealed by direct time-resolved X-ray microscopy". *Nature Physics*, 13 2, 2017, pp. 170–175.

[18] W. Legrand, D. Maccariello, F. Ajejas, S. Collin, A. Vecchiola, K. Bouzehouane, N. Reyren, V. Cros, and A. Fert. "Room-temperature stabilization of antiferromagnetic skyrmions in synthetic antiferromagnets". *Nature Materials*, 19 1, 2020, pp. 34–42.

[19] R. Juge, N. Sisodia, J. U. Larrañaga, Q. Zhang, V. T. Pham, K. G. Rana, B. Sarpi, N. Mille, S. Stanescu, R. Belkhou, M.-A. Mawass, N. Novakovic-Marinkovic, F. Kronast, M. Weigand, J. Gräfe, S. Wintz, S. Finizio, J. Raabe, L. Aballe, M. Foerster, M. Belmeguenai, L. D. Buda-Prejbeanu, J. Pelloux-Prayer, J. M. Shaw, H. T. Nembach, L. Ranno, G. Gaudin, and O. Boulle. "Skyrmions in synthetic antiferromagnets and their nucleation via electrical current and ultra-fast laser illumination". *Nature Communications*, 13 1, 2022, p. 4807.

[20] D. Maccariello, W. Legrand, N. Reyren, K. Garcia, K. Bouzehouane, S. Collin, V. Cros, and A. Fert. "Electrical detection of single magnetic skyrmions in metallic multilayers at room temperature". *Nature Nanotechnology*, 13 3, 2018, pp. 233–237.

[21] K. Zeissler, S. Finizio, K. Shahbazi, J. Massey, F. A. Ma'Mari, D. M. Bracher, A. Kleibert, M. C. Rosamond, E. H. Linfield, T. A. Moore, J. Raabe, G. Burnell, and C. H. Marrows. "Discrete Hall resistivity contribution from Néel skyrmions in multilayer nanodiscs". *Nature Nanotechnology*, 13 12, 2018, pp. 1161–1166.

[22] S. Chen, J. Lourembam, P. Ho, A. K. J. Toh, J. Huang, X. Chen, H. K. Tan, S. L. K. Yap, R. J. J. Lim, H. R. Tan, T. S. Suraj, M. I. Sim, Y. T. Toh, I. Lim, N. C. B. Lim, J. Zhou, H. J. Chung, S. T. Lim, and A. Soumyanarayanan. "All-electrical skyrmionic magnetic tunnel junction". *Nature*, 627 8004, 2024, pp. 522–527.

[23] J. Urrestarazu Larrañaga, N. Sisodia, R. Guedas, V. T. Pham, I. Di Manici, A. Masseboeuf, K. Garello, F. Disdier, B. Fernandez, S. Wintz, M. Weigand, M. Belmeguenai, S. Pizzini, R. C. Sousa, L. D. Buda-Prejbeanu, G. Gaudin, and O. Boulle. "Electrical Detection and Nucleation of a Magnetic Skyrmion in a Magnetic Tunnel Junction Observed via *Operando* Magnetic Microscopy". *Nano Letters*, 2024, acs.nanolett.4c00316.

[24] J. Grollier, D. Querlioz, K. Y. Camsari, K. Everschor-Sitte, S. Fukami, and M. D. Stiles. "Neuromorphic spintronics". *Nature Electronics*, 3 7, 2020, pp. 360–370.

[25] A. Fert, M. Chshiev, A. Thiaville, and H. Yang. "From Early Theories of Dzyaloshinskii–Moriya Interactions in Metallic Systems to Today's Novel Roads". *Journal of the Physical Society of Japan*, 92 8, 2023.

[26] T. Moriya. "New Mechanism of Anisotropic Superexchange Interaction". *Physical Review Letters*, 4 5, 1960, pp. 228–230.

[27] A. Fert and P. M. Levy. "Role of Anisotropic Exchange Interactions in Determining the Properties of Spin-Glasses". *Physical Review Letters*, 44 23, 1980, pp. 1538–1541.

[28] A. Crépieux and C. Lacroix. "Dzyaloshinsky–Moriya interactions induced by symmetry breaking at a surface". *Journal of Magnetism and Magnetic Materials*, 182 3, 1998, pp. 341–349.

[29] M. Bode, M. Heide, K. von Bergmann, P. Ferriani, S. Heinze, G. Bihlmayer, A. Kubetzka, O. Pietzsch, S. Blügel, and R. Wiesendanger. "Chiral magnetic order at surfaces driven by inversion asymmetry". *Nature*, 447 7141, 2007, pp. 190–193.

[30] H. Yang, A. Thiaville, S. Rohart, A. Fert, and M. Chshiev. "Anatomy of Dzyaloshinskii-Moriya Interaction atCo/PtInterfaces". *Physical Review Letters*, 115 26, 2015.

[31] A. Belabbes, G. Bihlmayer, F. Bechstedt, S. Blügel, and A. Manchon. "Hund's Rule-Driven Dzyaloshinskii-Moriya Interaction at 3d - 5d Interfaces". *Physical Review Letters*, 117 24, 2016, p. 247202.

[32] A. Bogdanov and A. Hubert. "Thermodynamically stable magnetic vortex states in magnetic crystals". *Journal of Magnetism and Magnetic Materials*, 138 3, 1994, pp. 255–269.

[33] P. Bruno and C. Chappert. "Oscillatory coupling between ferromagnetic layers separated by a nonmagnetic metal spacer". *Physical Review Letters*, 67 12, 1991, pp. 1602–1605.

[34] P. Bruno and C. Chappert. "Ruderman-Kittel theory of oscillatory interlayer exchange coupling". *Physical Review B*, 46 1, 1992, pp. 261–270.

[35] M. A. Ruderman and C. Kittel. "Indirect Exchange Coupling of Nuclear Magnetic Moments by Conduction Electrons". *Physical Review*, 96 1, 1954, pp. 99–102.

[36] T. Kasuya. "A Theory of Metallic Ferro- and Antiferromagnetism on Zener's Model". *Progress of Theoretical Physics*, 16 1, 1956, pp. 45–57.

[37] S. S. P. Parkin and D. Mauri. "Spin engineering: Direct determination of the Ruderman-Kittel-Kasuya-Yosida far-field range function in ruthenium". *Physical Review B*, 44 13, 1991, pp. 7131–7134.

[38] P. Weiss. “L’hypothèse du champ moléculaire et la propriété ferromagnétique”. *Journal de Physique Théorique et Appliquée*, 6, 1907, pp. 661–690.

[39] M. Heide, G. Bihlmayer, and S. Blügel. “Dzyaloshinskii-Moriya interaction accounting for the orientation of magnetic domains in ultrathin films: Fe/W(110)”. *Physical Review B*, 78 14, 2008, p. 140403.

[40] A. Thiaville, S. Rohart, É. Jué, V. Cros, and A. Fert. “Dynamics of Dzyaloshinskii domain walls in ultrathin magnetic films”. *EPL (Europhysics Letters)*, 100 5, 2012, p. 57002.

[41] T. Gilbert. “Classics in Magnetics A Phenomenological Theory of Damping in Ferromagnetic Materials”. *IEEE Transactions on Magnetics*, 40 6, 2004, pp. 3443–3449.

[42] L. Landau and E. Lifshits. “ON THE THEORY OF THE DISPERSION OF MAGNETIC PERMEABILITY IN FERROMAGNETIC BODIES”. 53.

[43] A. Mougin, M. Cormier, J. P. Adam, P. J. Metaxas, and J. Ferre. “Domain wall mobility, stability and Walker breakdown in magnetic nanowires”. *Europhysics Letters (EPL)*, 78 5, 2007, p. 57007.

[44] N. L. Schryer and L. R. Walker. “The motion of 180° domain walls in uniform dc magnetic fields”. *Journal of Applied Physics*, 45 12, 1974, pp. 5406–5421.

[45] T. Ha Pham, J. Vogel, J. Sampaio, M. Vaňatka, J.-C. Rojas-Sánchez, M. Bonfim, D. S. Chaves, F. Choueikani, P. Ohresser, E. Otero, A. Thiaville, and S. Pizzini. “Very large domain wall velocities in Pt/Co/GdOx and Pt/Co/Gd trilayers with Dzyaloshinskii-Moriya interaction”. *EPL (Europhysics Letters)*, 113 6, 2016, p. 67001.

[46] A. Brataas, A. D. Kent, and H. Ohno. “Current-induced torques in magnetic materials”. *Nature Materials*, 11 5, 2012, pp. 372–381.

[47] A. Manchon, J. Zelezny, I. M. Miron, T. Jungwirth, J. Sinova, A. Thiaville, K. Garello, and P. Gambardella. “Current-induced spin-orbit torques in ferromagnetic and antiferromagnetic systems”. *Reviews of Modern Physics*, 91 3, 2019.

[48] O. Boulle, G. Malinowski, and M. Kläui. “Current-induced domain wall motion in nanoscale ferromagnetic elements”. *Materials Science and Engineering: R: Reports*, 72 9, 2011, pp. 159–187.

[49] J. Zhang, P. Levy, S. Zhang, and V. Antropov. “Identification of Transverse Spin Currents in Noncollinear Magnetic Structures”. *Physical Review Letters*, 93 25, 2004.

[50] A. Thiaville, Y. Nakatani, J. Miltat, and N. Vernier. “Domain wall motion by spin-polarized current: a micromagnetic study”. *Journal of Applied Physics*, 95 11, 2004, pp. 7049–7051.

[51] S. Zhang and Z. Li. “Roles of Nonequilibrium Conduction Electrons on the Magnetization Dynamics of Ferromagnets”. *Physical Review Letters*, 93 12, 2004.

[52] G. Tatara, T. Takayama, H. Kohno, J. Shibata, Y. Nakatani, and H. Fukuyama. “Threshold Current of Domain Wall Motion under Extrinsic Pinning, β-Term and Non-Adiabaticity”. *Journal of the Physical Society of Japan*, 75 6, 2006, p. 064708.

[53] G. Tatara, H. Kohno, and J. Shibata. “Microscopic approach to current-driven domain wall dynamics”. *Physics Reports*, 468 6, 2008, pp. 213–301.

[54] J. Xiao, A. Zangwill, and M. D. Stiles. “Spin-transfer torque for continuously variable magnetization”. *Physical Review B*, 73 5, 2006.

[55] J.-i. Ohe and B. Kramer. “Dynamics of a Domain Wall and Spin-Wave Excitations Driven by a Mesoscopic Current”. *Physical Review Letters*, 96 2, 2006.

[56] V. Edelstein. “Spin polarization of conduction electrons induced by electric current in two-dimensional asymmetric electron systems”. *Solid State Communications*, 73 3, 1990, pp. 233–235.

[57] P. Gambardella and I. M. Miron. “Current-induced spin–orbit torques”. *Philosophical Transactions of the Royal Society A: Mathematical, Physical and Engineering Sciences*, 369 1948, 2011, pp. 3175–3197.

[58] J. E. Hirsch. “Spin Hall effect”. *Physical Review Letters*, 83 9, 1999, pp. 1834–1837.

[59] J. Sinova, D. Culcer, Q. Niu, N. A. Sinitsyn, T. Jungwirth, and A. H. MacDonald. “Universal Intrinsic Spin Hall Effect”. *Physical Review Letters*, 92 12, 2004.

[60] M. Dyakonov and V. Perel. “Current-induced spin orientation of electrons in semiconductors”. *Physics Letters A*, 35 6, 1971, pp. 459–460.

[61] A. V. Khvalkovskiy, V. Cros, D. Apalkov, V. Nikitin, M. Krounbi, K. A. Zvezdin, A. Anane, J. Grollier, and A. Fert. “Matching domain-wall configuration and spin-orbit torques for efficient domain-wall motion”. *Physical Review B*, 87 2, 2013.

[62] H. L. Wang, C. H. Du, Y. Pu, R. Adur, P. C. Hammel, and F. Y. Yang. "Scaling of Spin Hall Angle in 3d, 4d, and 5d Metals fromY3Fe5O12/Metal Spin Pumping". *Physical Review Letters*, 112 19, 2014.

[63] L. Liu, O. J. Lee, T. J. Gudmundsen, D. C. Ralph, and R. A. Buhrman. "Current-Induced Switching of Perpendicularly Magnetized Magnetic Layers Using Spin Torque from the Spin Hall Effect". *Physical Review Letters*, 109 9, 2012.

[64] K. Garello, I. M. Miron, C. O. Avci, F. Freimuth, Y. Mokrousov, S. Blugel, S. Auffret, O. Boulle, G. Gaudin, and P. Gambardella. "Symmetry and magnitude of spin–orbit torques in ferromagnetic heterostructures". *Nature Nanotechnology*, 8 8, 2013, pp. 587–593.

[65] S. Emori, U. Bauer, S.-M. Ahn, E. Martinez, and G. S. D. Beach. "Current-driven dynamics of chiral ferromagnetic domain walls". *Nature Materials*, 12 7, 2013, pp. 611–616.

[66] L. Liu, C.-F. Pai, Y. Li, H. W. Tseng, D. C. Ralph, and R. A. Buhrman. "Spin-Torque Switching with the Giant Spin Hall Effect of Tantalum". *Science*, 336 6081, 2012, pp. 555–558.

[67] J. Kim, J. Sinha, M. Hayashi, M. Yamanouchi, S. Fukami, T. Suzuki, S. Mitani, and H. Ohno. "Layer thickness dependence of the current-induced effective field vector in Ta—CoFeB—MgO". *Nature Materials*, 12 3, 2013, pp. 240–245.

[68] C.-F. Pai, L. Liu, Y. Li, H. W. Tseng, D. C. Ralph, and R. A. Buhrman. "Spin transfer torque devices utilizing the giant spin Hall effect of tungsten". *Applied Physics Letters*, 101 12, 2012, p. 122404.

[69] A. Manchon and S. Zhang. "Theory of nonequilibrium intrinsic spin torque in a single nanomagnet". *Physical Review B*, 78 21, 2008.

[70] A. Manchon and S. Zhang. "Theory of spin torque due to spin-orbit coupling". *Physical Review B*, 79 9, 2009.

[71] T. Miyazaki and N. Tezuka. "Giant magnetic tunneling effect in Fe/AlzO3/Fejunction". *Journal of Magnetism and Magnetic Materials*, 1995.

[72] J. S. Moodera, L. R. Kinder, T. M. Wong, and R. Meservey. "Large Magnetoresistance at Room Temperature in Ferromagnetic Thin Film Tunnel Junctions". *Physical Review Letters*, 74 16, 1995, pp. 3273–3276.

[73] W. H. Butler, X.-G. Zhang, T. C. Schulthess, and J. M. MacLaren. "Spin-dependent tunneling conductance ofFe—MgO—Fesandwiches". *Physical Review B*, 63 5, 2001.

[74] J. Mathon and A. Umerski. "Theory of tunneling magnetoresistance of an epitaxial Fe/MgO/Fe(001) junction". *Physical Review B*, 63 22, 2001.

[75] S. S. P. Parkin, C. Kaiser, A. Panchula, P. M. Rice, B. Hughes, M. Samant, and S.-H. Yang. "Giant tunnelling magnetoresistance at room temperature with MgO (100) tunnel barriers". *Nature Materials*, 3 12, 2004, pp. 862–867.

[76] S. Yuasa, T. Nagahama, A. Fukushima, Y. Suzuki, and K. Ando. "Giant room-temperature magnetoresistance in single-crystal Fe/MgO/Fe magnetic tunnel junctions". *Nature Materials*, 3 12, 2004, pp. 868–871.

[77] S. Ikeda, J. Hayakawa, Y. Ashizawa, Y. M. Lee, K. Miura, H. Hasegawa, M. Tsunoda, F. Matsukura, and H. Ohno. "Tunnel magnetoresistance of 604% at 300K by suppression of Ta diffusion in CoFeB/MgO/CoFeB pseudo-spin-valves annealed at high temperature". *Applied Physics Letters*, 93 8, 2008.

[78] P. G. Mather, J. C. Read, and R. A. Buhrman. "Disorder, defects, and band gaps in ultrathin (001) MgO tunnel barrier layers". *Physical Review B*, 73 20, 2006.

[79] J. C. Slonczewski. "Conductance and exchange coupling of two ferromagnets separated by a tunneling barrier". *Physical Review B*, 39 10, 1989, pp. 6995–7002.

[80] N. Locatelli and V. Cros. "Basic Spintronic Transport Phenomena". In: *Introduction to Magnetic Random-Access Memory*. John Wiley & Sons, Ltd, 2017, pp. 1–28. ISBN: 978-1-119-07941-5. doi: https://doi.org/10.1002/9781119 URL: `https://onlinelibrary.wiley.com/doi/abs/10.1002/9781119079415.ch1` (cit. on p. 24).

[81] J. Z. Sun. "Spin-transfer torque switched magnetic tunnel junction for memory technologies". *Journal of Magnetism and Magnetic Materials*, 559, 2022, p. 169479.

[82] A. A. Timopheev, R. Sousa, M. Chshiev, L. D. Buda-Prejbeanu, and B. Dieny. "Respective influence of in-plane and out-of-plane spin-transfer torques in magnetization switching of perpendicular magnetic tunnel junctions". *Physical Review B*, 92 10, 2015.

[83] B. Dieny and M. Chshiev. "Perpendicular magnetic anisotropy at transition metal/oxide interfaces and applications". *Reviews of Modern Physics*, 89 2, 2017.

[84] C. Song, B. Cui, F. Li, X. Zhou, and F. Pan. "Recent progress in voltage control of magnetism: Materials, mechanisms, and performance". *Progress in Materials Science*, 87, 2017, pp. 33–82.

[85] T. Nozaki, T. Yamamoto, S. Miwa, M. Tsujikawa, M. Shirai, S. Yuasa, and Y. Suzuki. "Recent Progress in the Voltage-Controlled Magnetic Anisotropy Effect and the Challenges Faced in Developing Voltage-Torque MRAM". *Micromachines*, 10 5, 2019, p. 327.

[86] M. Weisheit, S. Fähler, A. Marty, Y. Souche, C. Poinsignon, and D. Givord. "Electric Field-Induced Modification of Magnetism in Thin-Film Ferromagnets". *Science*, 315 5810, 2007, pp. 349–351.

[87] C.-G. Duan, J. P. Velev, R. F. Sabirianov, Z. Zhu, J. Chu, S. S. Jaswal, and E. Y. Tsymbal. "Surface Magnetoelectric Effect in Ferromagnetic Metal Films". *Physical Review Letters*, 101 13, 2008.

[88] M. Tsujikawa and T. Oda. "Finite Electric Field Effects in the Large Perpendicular Magnetic Anisotropy SurfacePt/Fe/Pt(001): A First-Principles Study". *Physical Review Letters*, 102 24, 2009.

[89] Y. Shiota, T. Maruyama, T. Nozaki, T. Shinjo, M. Shiraishi, and Y. Suzuki. "Voltage-Assisted Magnetization Switching in Ultrathin $Fe_{80}Co_{20}$Alloy Layers". *Applied Physics Express*, 2, 2009, p. 063001.

[90] W.-G. Wang, M. Li, S. Hageman, and C. L. Chien. "Electric-field-assisted switching in magnetic tunnel junctions". *Nature Materials*, 11 1, 2012, pp. 64–68.

[91] K. Nakamura, T. Akiyama, T. Ito, M. Weinert, and A. J. Freeman. "Role of an interfacial FeO layer in the electric-field-driven switching of magnetocrystalline anisotropy at the Fe/MgO interface". *Physical Review B*, 81 22, 2010.

[92] M. Tsujikawa, S. Haraguchi, T. Oda, Y. Miura, and M. Shirai. "A comparative *ab initio* study on electric-field dependence of magnetic anisotropy in MgO/Fe/Pt and MgO/Fe/Au films". *Journal of Applied Physics*, 109 7, 2011.

[93] T. Maruyama, Y. Shiota, T. Nozaki, K. Ohta, N. Toda, M. Mizuguchi, A. A. Tulapurkar, T. Shinjo, M. Shiraishi, S. Mizukami, Y. Ando, and Y. Suzuki. "Large voltage-induced magnetic anisotropy change in a few atomic layers of iron". *Nature Nanotechnology*, 4 3, 2009, pp. 158–161.

[94] J. Zhang, P. V. Lukashev, S. S. Jaswal, and E. Y. Tsymbal. "Elucidating the Voltage Controlled Magnetic Anisotropy".

[95] P. K. Mishra, M. Sravani, A. Bose, and S. Bhuktare. "Voltage-controlled magnetic anisotropy-based spintronic devices for magnetic memory applications: Challenges and perspectives". *Journal of Applied Physics*, 135 22, 2024, p. 220701.

[96] B. Dai, M. Jackson, Y. Cheng, H. He, Q. Shu, H. Huang, L. Tai, and K. Wang. "Review of voltage-controlled magnetic anisotropy and magnetic insulator". *Journal of Magnetism and Magnetic Materials*, 563, 2022, p. 169924.

[97] Y. Shiota, T. Nozaki, F. Bonell, S. Murakami, T. Shinjo, and Y. Suzuki. "Induction of coherent magnetization switching in a few atomic layers of FeCo using voltage pulses". *Nature Materials*, 11 1, 2012, pp. 39–43.

[98] J. P. Liu, Z. Zhang, and G. Zhao, eds. *Skyrmions: Topological Structures, Properties, and Applications*. Series in Materials Science and Engineering. Foreword by Albert Fert. Boca Raton, FL: CRC Press – Taylor & Francis Group, 2017, pp. xix + 481. ISBN: 9781498753883 (cit. on p. 25).

[99] M. A. Armstrong. *Basic Topology*. Undergraduate Texts in Mathematics. ISSN: 0172-6056. New York, NY: Springer New York, 1983. ISBN: 978-1-4419-2819-1 978-1-4757-1793-8. doi: 10.1007/978-1-4757-1793-8. URL: `http://link.springer.com/10.1007/978-1-4757-1793-8` (visited on 07/18/2025) (cit. on p. 25).

[100] M. Mcintyre and G. Cairns. "A new formula for winding number". *Geometriae Dedicata*, 46 2, 1993, pp. 149–159.

[101] H.-B. Braun. "Topological effects in nanomagnetism: from superparamagnetism to chiral quantum solitons". *Advances in Physics*, 61 1, 2012, pp. 1–116.

[102] T. Skyrme. "A unified field theory of mesons and baryons". *Nuclear Physics*, 31, 1962, pp. 556–569.

[103] A. N. Bogdanov and D. A. Yablonskii. "Thermodynamicallystable "vortices" in magneticallyordered crystals.The mixed state of magnets".

[104] N. Nagaosa and Y. Tokura. "Topological properties and dynamics of magnetic skyrmions". *Nature Nanotechnology*, 8 12, 2013, pp. 899–911.

[105] A. Bernand-Mantel, L. Camosi, A. Wartelle, N. Rougemaille, M. Darques, and L. Ranno. "The skyrmion-bubble transition in a ferromagnetic thin film". *SciPost Physics*, 4 5, 2018.

[106] A. A. Thiele. "The Theory of Cylindrical Magnetic Domains". *Bell System Technical Journal*, 48 10, 1969, pp. 3287–3335.

[107] N. S. Kiselev, A. N. Bogdanov, R. Schäfer, and U. K. Rößler. "Chiral skyrmions in thin magnetic films: new objects for magnetic storage technologies?" *Journal of Physics D: Applied Physics*, 44 39, 2011, p. 392001.

[108] S. Rohart and A. Thiaville. "Skyrmion confinement in ultrathin film nanostructures in the presence of Dzyaloshinskii-Moriya interaction". *Physical Review B*, 88 18, 2013.

[109] A. Hubert and R. Schäfer. *Magnetic domains: the analysis of magnetic microstructures*. Corr. print., [Nachdr.] Berlin: Springer, 2011. 696 pp. ISBN: 978-3-540-64108-7 (cit. on p. 28).

[110] A. Bocdanov and A. Hubert. "The Properties of Isolated Magnetic Vortices". *physica status solidi (b)*, 186 2, 1994, pp. 527–543.

[111] X. Z. Yu, Y. Onose, N. Kanazawa, J. H. Park, J. H. Han, Y. Matsui, N. Nagaosa, and Y. Tokura. "Real-space observation of a two-dimensional skyrmion crystal". *Nature*, 465 7300, 2010, pp. 901–904.

[112] W. Münzer, A. Neubauer, T. Adams, S. Mühlbauer, C. Franz, F. Jonietz, R. Georgii, P. Böni, B. Pedersen, M. Schmidt, A. Rosch, and C. Pfleiderer. "Skyrmion lattice in the doped semiconductorFe1-xCoxSi". *Physical Review B*, 81 4, 2010.

[113] X. Z. Yu, N. Kanazawa, Y. Onose, K. Kimoto, W. Z. Zhang, S. Ishiwata, Y. Matsui, and Y. Tokura. "Near room-temperature formation of a skyrmion crystal in thin-films of the helimagnet FeGe". *Nature Materials*, 10 2, 2011, pp. 106–109.

[114] S. Heinze, K. von Bergmann, M. Menzel, J. Brede, A. Kubetzka, R. Wiesendanger, G. Bihlmayer, and S. Blügel. "Spontaneous atomic-scale magnetic skyrmion lattice in two dimensions". *Nature Physics*, 7 9, 2011, pp. 713–718.

[115] N. Romming, C. Hanneken, M. Menzel, J. E. Bickel, B. Wolter, K. von Bergmann, A. Kubetzka, and R. Wiesendanger. "Writing and Deleting Single Magnetic Skyrmions". *Science*, 341 6146, 2013, pp. 636–639.

[116] N. Romming, A. Kubetzka, C. Hanneken, K. von Bergmann, and R. Wiesendanger. "Field-Dependent Size and Shape of Single Magnetic Skyrmions". *Physical Review Letters*, 114 17, 2015.

[117] J. Sampaio, V. Cros, S. Rohart, A. Thiaville, and A. Fert. "Nucleation, stability and current-induced motion of isolated magnetic skyrmions in nanostructures". *Nature Nanotechnology*, 8 11, 2013, pp. 839–844.

[118] W. Jiang, P. Upadhyaya, W. Zhang, G. Yu, M. B. Jungfleisch, F. Y. Fradin, J. E. Pearson, Y. Tserkovnyak, K. L. Wang, O. Heinonen, S. G. E. te Velthuis, and A. Hoffmann. "Blowing magnetic skyrmion bubbles". *Science*, 349 6245, 2015, pp. 283–286.

[119] O. Boulle, J. Vogel, H. Yang, S. Pizzini, D. d. S. Chaves, A. Locatelli, T. O. M. A. Sala, L. D. Buda-Prejbeanu, O. Klein, M. Belmeguenai, Y. Roussigné, A. Stashkevich, S. M. Chérif, L. Aballe, M. Foerster, M. Chshiev, S. Auffret, I. M. Miron, and G. Gaudin. "Room temperature chiral magnetic skyrmion in ultrathin magnetic nanostructures". *Nature Nanotechnology*, 11 5, 2016, pp. 449–454.

[120] S. Woo, K. Litzius, B. Krüger, M.-Y. Im, L. Caretta, K. Richter, M. Mann, A. Krone, R. M. Reeve, M. Weigand, P. Agrawal, I. Lemesh, M.-A. Mawass, P. Fischer, M. Kläui, and G. S. D. Beach. "Observation of room-temperature magnetic skyrmions and their current-driven dynamics in ultrathin metallic ferromagnets". *Nature Materials*, 15 5, 2016, pp. 501–506.

[121] C. Moreau-Luchaire, C. Moutafis, N. Reyren, J. Sampaio, C. A. F. Vaz, N. Van Horne, K. Bouzehouane, K. Garcia, C. Deranlot, P. Warnicke, P. Wohlhüter, J.-M. George, M. Weigand, J. Raabe, V. Cros, and A. Fert. "Additive interfacial chiral interaction in multilayers for stabilization of small individual skyrmions at room temperature". *Nature Nanotechnology*, 11 5, 2016, pp. 444–448.

[122] A. Soumyanarayanan, M. Raju, A. L. Gonzalez Oyarce, A. K. C. Tan, M.-Y. Im, A. P. Petrović, P. Ho, K. H. Khoo, M. Tran, C. K. Gan, F. Ernult, and C. Panagopoulos. "Tunable room-temperature magnetic skyrmions in Ir/Fe/Co/Pt multilayers". *Nature Materials*, 16 9, 2017, pp. 898–904.

[123] S. Jaiswal, K. Litzius, I. Lemesh, F. Büttner, S. Finizio, J. Raabe, M. Weigand, K. Lee, J. Langer, B. Ocker, G. Jakob, G. S. D. Beach, and M. Kläui. "Investigation of the Dzyaloshinskii-Moriya interaction and room temperature skyrmions in W/CoFeB/MgO thin films and microwires". *Applied Physics Letters*, 111 2, 2017.

[124] W. Jiang, G. Chen, K. Liu, J. Zang, S. G. te Velthuis, and A. Hoffmann. "Skyrmions in magnetic multilayers". *Physics Reports*, 704, 2017, pp. 1–49.

[125] F. Jonietz, S. Mühlbauer, C. Pfleiderer, A. Neubauer, W. Münzer, A. Bauer, T. Adams, R. Georgii, P. Böni, R. A. Duine, K. Everschor, M. Garst, and A. Rosch. "Spin Transfer Torques in MnSi at Ultralow Current Densities". *Science*, 330 6011, 2010, pp. 1648–1651.

[126] T. Schulz, R. Ritz, A. Bauer, M. Halder, M. Wagner, C. Franz, C. Pfleiderer, K. Everschor, M. Garst, and A. Rosch. "Emergent electrodynamics of skyrmions in a chiral magnet". *Nature Physics*, 8 4, 2012, pp. 301–304.

[127] X. Yu, N. Kanazawa, W. Zhang, T. Nagai, T. Hara, K. Kimoto, Y. Matsui, Y. Onose, and Y. Tokura. "Skyrmion flow near room temperature in an ultralow current density". *Nature Communications*, 3 1, 2012.

[128] J. Iwasaki, M. Mochizuki, and N. Nagaosa. "Universal current-velocity relation of skyrmion motion in chiral magnets". *Nature Communications*, 4 1, 2013.

[129] R. Tomasello, E. Martinez, R. Zivieri, L. Torres, M. Carpentieri, and G. Finocchio. "A strategy for the design of skyrmion racetrack memories". *Scientific Reports*, 4 1, 2014.

[130] W. Legrand, D. Maccariello, N. Reyren, K. Garcia, C. Moutafis, C. Moreau-Luchaire, S. Collin, K. Bouzehouane, V. Cros, and A. Fert. "Room-Temperature Current-Induced Generation and Motion of sub-100 nm Skyrmions". *Nano Letters*, 17 4, 2017, pp. 2703–2712.

[131] A. A. Thiele. "Steady-State Motion of Magnetic Domains". *Physical Review Letters*, 30 6, 1973, pp. 230–233.

[132] X. Zhang, Y. Zhou, and M. Ezawa. "Magnetic bilayer-skyrmions without skyrmion Hall effect". *Nature Communications*, 7 1, 2016, p. 10293.

[133] J. Barker and O. A. Tretiakov. "Static and Dynamical Properties of Antiferromagnetic Skyrmions in the Presence of Applied Current and Temperature". *Physical Review Letters*, 116 14, 2016, p. 147203.

[134] S. Li, A. Du, Y. Wang, X. Wang, X. Zhang, H. Cheng, W. Cai, S. Lu, K. Cao, B. Pan, N. Lei, W. Kang, J. Liu, A. Fert, Z. Hou, and W. Zhao. "Experimental demonstration of skyrmionic magnetic tunnel junction at room temperature". *Science Bulletin*, 67 7, 2022, pp. 691–699.

[135] D. Culcer. "The Anomalous Hall Effect".

[136] N. Nagaosa, J. Sinova, S. Onoda, A. H. MacDonald, and N. P. Ong. "Anomalous Hall effect". *Reviews of Modern Physics*, 82 2, 2010, pp. 1539–1592.

[137] S. X. Huang and C. L. Chien. "Extended Skyrmion Phase in EpitaxialFeGe(111)Thin Films". *Physical Review Letters*, 108 26, 2012.

[138] M. Lee, W. Kang, Y. Onose, Y. Tokura, and N. P. Ong. "Unusual Hall Effect Anomaly in MnSi under Pressure". *Physical Review Letters*, 102 18, 2009.

[139] R. Ritz, M. Halder, C. Franz, A. Bauer, M. Wagner, R. Bamler, A. Rosch, and C. Pfleiderer. "Giant generic topological Hall resistivity of MnSi under pressure". *Physical Review B*, 87 13, 2013.

[140] Y. Li, N. Kanazawa, X. Z. Yu, A. Tsukazaki, M. Kawasaki, M. Ichikawa, X. F. Jin, F. Kagawa, and Y. Tokura. "Robust Formation of Skyrmions and Topological Hall Effect Anomaly in Epitaxial Thin Films of MnSi". *Physical Review Letters*, 110 11, 2013.

[141] D. Liang, J. P. DeGrave, M. J. Stolt, Y. Tokura, and S. Jin. "Current-driven dynamics of skyrmions stabilized in MnSi nanowires revealed by topological Hall effect". *Nature Communications*, 6 1, 2015.

[142] N. Kanazawa, Y. Onose, T. Arima, D. Okuyama, K. Ohoyama, S. Wakimoto, K. Kakurai, S. Ishiwata, and Y. Tokura. "Large Topological Hall Effect in a Short-Period Helimagnet MnGe". *Physical Review Letters*, 106 15, 2011.

[143] N. Kanazawa, M. Kubota, A. Tsukazaki, Y. Kozuka, K. S. Takahashi, M. Kawasaki, M. Ichikawa, F. Kagawa, and Y. Tokura. "Discretized topological Hall effect emerging from skyrmions in constricted geometry". *PHYSICAL REVIEW B*, 2015.

[144] N. A. Porter, J. C. Gartside, and C. H. Marrows. "Scattering mechanisms in textured FeGe thin films: Magnetoresistance and the anomalous Hall effect". *Physical Review B*, 90 2, 2014.

[145] H. Du, D. Liang, C. Jin, L. Kong, M. J. Stolt, W. Ning, J. Yang, Y. Xing, J. Wang, R. Che, J. Zang, S. Jin, Y. Zhang, and M. Tian. "Electrical probing of field-driven cascading quantized transitions of skyrmion cluster states in MnSi nanowires". *Nature Communications*, 6 1, 2015.

[146] C. Hanneken, F. Otte, A. Kubetzka, B. Dupé, N. Romming, K. von Bergmann, R. Wiesendanger, and S. Heinze. "Electrical detection of magnetic skyrmions by tunnelling non-collinear magnetoresistance". *Nature Nanotechnology*, 10 12, 2015, pp. 1039–1042.

[147] D. M. Crum, M. Bouhassoune, J. Bouaziz, B. Schweflinghaus, S. Blügel, and S. Lounis. "Perpendicular reading of single confined magnetic skyrmions". *Nature Communications*, 6 1, 2015.

[148] N. E. Penthorn, X. Hao, Z. Wang, Y. Huai, and H. W. Jiang. "Experimental Observation of Single Skyrmion Signatures in a Magnetic Tunnel Junction". *Physical Review Letters*, 122 25, 2019.

[149] B. He, Y. Hu, C. Zhao, J. Wei, J. Zhang, Y. Zhang, C. Cheng, J. Li, Z. Nie, Y. Luo, Y. Zhou, S. Zhang, Z. Zeng, Y. Peng, J. M. D. Coey, X. Han, and G. Yu. "Realization of Zero-Field Skyrmions in a Magnetic Tunnel Junction". *Advanced Electronic Materials*, 9 4, 2023, p. 2201240.

[150] S. Kasai, S. Sugimoto, Y. Nakatani, R. Ishikawa, and Y. K. Takahashi. "Voltage-controlled magnetic skyrmions in magnetic tunnel junctions". *Applied Physics Express*, 12 8, 2019, p. 083001.

[151] C. Schonenberger and S. F. Alvarado. "Understanding magnetic force microscopy". *Zeitschrift for Physik B Condensed Matter*, 80 3, 1990, pp. 373–383.

[152] D. Rugar, H. J. Mamin, P. Guethner, S. E. Lambert, J. E. Stern, I. McFadyen, and T. Yogi. "Magnetic force microscopy: General principles and application to longitudinal recording media". *Journal of Applied Physics*, 68 3, 1990, pp. 1169–1183.

[153] O. Kazakova, R. Puttock, C. Barton, H. Corte-León, M. Jaafar, V. Neu, and A. Asenjo. "Frontiers of magnetic force microscopy". *Journal of Applied Physics*, 125 6, 2019, p. 060901.

[154] *NanoMOKE3: an ultra-high sensitivity Kerr effect wafer mapping magnetometer*. Accessed on September 29, 2025. 2025. URL: `https://www.durhammagnetooptics.com/?product=nanomoke3-wafer-mapper` (visited on 09/29/2025) (cit. on p. 48).

[155] J. Stöhr, H. A. Padmore, S. Anders, T. Stammler, and M. R. Scheinfein. "Principles of X-Ray Magnetic Dichroism Spectromicroscopy". *Surface Review and Letters*, 05 6, 1998, pp. 1297–1308.

[156] C. T. Chen, Y. U. Idzerda, H.-J. Lin, N. V. Smith, G. Meigs, E. Chaban, G. H. Ho, E. Pellegrin, and F. Sette. "Experimental Confirmation of the X-Ray Magnetic Circular Dichroism Sum Rules for Iron and Cobalt". *Physical Review Letters*, 75 1, 1995, pp. 152–155.

[157] M. Weigand, S. Wintz, J. Gräfe, M. Noske, H. Stoll, B. Van Waeyenberge, and G. Schütz. "TimeMaxyne: A Shot-Noise Limited, Time-Resolved Pump-and-Probe Acquisition System Capable of 50 GHz Frequencies for Synchrotron-Based X-ray Microscopy". *Crystals*, 12 8, 2022, p. 1029.

[158] S. Wintz, V. Tiberkevich, M. Weigand, J. Raabe, J. Lindner, A. Erbe, A. Slavin, and J. Fassbender. "Magnetic vortex cores as tunable spin-wave emitters". *Nature Nanotechnology*, 11 11, 2016, pp. 948–953.

[159] M. Baumgartner, K. Garello, J. Mendil, C. O. Avci, E. Grimaldi, C. Murer, J. Feng, M. Gabureac, C. Stamm, Y. Acremann, S. Finizio, S. Wintz, J. Raabe, and P. Gambardella. "Spatially and time-resolved magnetization dynamics driven by spin–orbit torques". *Nature Nanotechnology*, 12 10, 2017, pp. 980–986.

[160] A. Locatelli and E. Bauer. "Recent advances in chemical and magnetic imaging of surfaces and interfaces by XPEEM". *Journal of Physics: Condensed Matter*, 20 9, 2008, p. 093002.

[161] Y. Yamaguchi, S. Takakusagi, Y. Sakai, M. Kato, K. Asakura, and Y. Iwasawa. "X-ray photoemission electron microscopy XPEEM/ as a new promising tool for the real-time chemical imaging of active surfaces". 1999.

[162] K. Litzius, J. Leliaert, P. Bassirian, D. Rodrigues, S. Kromin, I. Lemesh, J. Zazvorka, K.-J. Lee, J. Mulkers, N. Kerber, D. Heinze, N. Keil, R. M. Reeve, M. Weigand, B. Van Waeyenberge, G. Schütz, K. Everschor-Sitte, G. S. D. Beach, and M. Kläui. "The role of temperature and drive current in skyrmion dynamics". *Nature Electronics*, 3 1, 2020, pp. 30–36.

[163] K. Zeissler, S. Finizio, C. Barton, A. J. Huxtable, J. Massey, J. Raabe, A. V. Sadovnikov, S. A. Nikitov, R. Brearton, T. Hesjedal, G. van der Laan, M. C. Rosamond, E. H. Linfield, G. Burnell, and C. H. Marrows. "Diameter-independent skyrmion Hall angle observed in chiral magnetic multilayers". *Nature Communications*, 11 1, 2020.

[164] X. Zhang, Y. Zhou, and M. Ezawa. "Antiferromagnetic Skyrmion: Stability, Creation and Manipulation". *Scientific Reports*, 6 1, 2016.

[165] H. Velkov, O. Gomonay, M. Beens, G. Schwiete, A. Brataas, J. Sinova, and R. A. Duine. "Phenomenology of current-induced skyrmion motion in antiferromagnets". *New Journal of Physics*, 18 7, 2016, p. 075016.

[166] C. Jin, C. Song, J. Wang, and Q. Liu. "Dynamics of antiferromagnetic skyrmion driven by the spin Hall effect". *Applied Physics Letters*, 109 18, 2016.

[167] A. Salimath, F. Zhuo, R. Tomasello, G. Finocchio, and A. Manchon. "Controlling the deformation of antiferromagnetic skyrmions in the high-velocity regime". *Physical Review B*, 101 2, 2020.

[168] S. Komineas and N. Papanicolaou. "Traveling skyrmions in chiral antiferromagnets". *SciPost Physics*, 8 6, 2020.

[169] P. E. Roy. "Method to suppress antiferromagnetic skyrmion deformation in high speed racetrack devices". *Journal of Applied Physics*, 129 19, 2021.

[170] S. Gao, H. D. Rosales, F. A. Gómez Albarracín, V. Tsurkan, G. Kaur, T. Fennell, P. Steffens, M. Boehm, P. Čermák, A. Schneidewind, E. Ressouche, D. C. Cabra, C. Rüegg, and O. Zaharko. "Fractional antiferromagnetic skyrmion lattice induced by anisotropic couplings". *Nature*, 586 7827, 2020, pp. 37–41.

[171] H. Jani, J.-C. Lin, J. Chen, J. Harrison, F. Maccherozzi, J. Schad, S. Prakash, C.-B. Eom, A. Ariando, T. Venkatesan, and P. G. Radaelli. "Antiferromagnetic half-skyrmions and bimerons at room temperature". *Nature*, 590 7844, 2021, pp. 74–79.

[172] K. G. Rana, R. Lopes Seeger, S. Ruiz-Gómez, R. Juge, Q. Zhang, K. Bairagi, V. T. Pham, M. Belmeguenai, S. Auffret, M. Foerster, L. Aballe, G. Gaudin, V. Baltz, and O. Boulle. "Imprint from ferromagnetic skyrmions in an antiferromagnet via exchange bias". *Applied Physics Letters*, 119 19, 2021.

[173] R. Tomasello, V. Puliafito, E. Martinez, A. Manchon, M. Ricci, M. Carpentieri, and G. Finocchio. "Performance of synthetic antiferromagnetic racetrack memory: domain wall versus skyrmion". *Journal of Physics D: Applied Physics*, 50 32, 2017, p. 325302.

[174] J. Xia, X. Zhang, K.-Y. Mak, M. Ezawa, O. A. Tretiakov, Y. Zhou, G. Zhao, and X. Liu. "Current-induced dynamics of skyrmion tubes in synthetic antiferromagnetic multilayers". *Physical Review B*, 103 17, 2021.

[175] S. Panigrahy, S. Mallick, J. Sampaio, and S. Rohart. "Skyrmion inertia in synthetic antiferromagnets". *Physical Review B*, 106 14, 2022.

[176] Y. Hirata, D.-H. Kim, S. K. Kim, D.-K. Lee, S.-H. Oh, D.-Y. Kim, T. Nishimura, T. Okuno, Y. Futakawa, H. Yoshikawa, A. Tsukamoto, Y. Tserkovnyak, Y. Shiota, T. Moriyama, S.-B. Choe, K.-J. Lee, and T. Ono. "Vanishing skyrmion Hall effect at the angular momentum compensation temperature of a ferrimagnet". *Nature Nanotechnology*, 14 3, 2019, pp. 232–236.

[177] T. Dohi, S. DuttaGupta, S. Fukami, and H. Ohno. "Formation and current-induced motion of synthetic antiferromagnetic skyrmion bubbles". *Nature Communications*, 10 1, 2019.

[178] Y. Quessab, J.-W. Xu, E. Cogulu, S. Finizio, J. Raabe, and A. D. Kent. "Zero-Field Nucleation and Fast Motion of Skyrmions Induced by Nanosecond Current Pulses in a Ferrimagnetic Thin Film". *Nano Letters*, 22 15, 2022, pp. 6091–6097.

[179] S. Woo, K. M. Song, X. Zhang, Y. Zhou, M. Ezawa, X. Liu, S. Finizio, J. Raabe, N. J. Lee, S.-I. Kim, S.-Y. Park, Y. Kim, J.-Y. Kim, D. Lee, O. Lee, J. W. Choi, B.-C. Min, H. C. Koo, and J. Chang. "Current-driven dynamics and inhibition of the skyrmion Hall effect of ferrimagnetic skyrmions in GdFeCo films". *Nature Communications*, 9 1, 2018, p. 959.

[180] S. S. P. Parkin, N. More, and K. P. Roche. "Oscillations in exchange coupling and magnetoresistance in metallic superlattice structures: Co/Ru, Co/Cr, and Fe/Cr". *Physical Review Letters*, 64 19, 1990, pp. 2304–2307.

[181] S. Bandiera, R. C. Sousa, S. Auffret, B. Rodmacq, and B. Dieny. "Enhancement of perpendicular magnetic anisotropy thanks to Pt insertions in synthetic antiferromagnets". *Applied Physics Letters*, 101 7, 2012, p. 072410.

[182] J.-V. Kim and M.-W. Yoo. "Current-driven skyrmion dynamics in disordered films". *Applied Physics Letters*, 110 13, 2017, p. 132404.

[183] L. Ranno and M. A. Moro. *Design Rules for DMI-Stabilised Skyrmions*. July 1, 2021. doi: 10.48550/arXiv.2107.00767. arXiv: `2107.00767[cond-mat]`. URL: `http://arxiv.org/abs/2107.00767` (visited on 08/06/2025) (cit. on p. 60).

[184] D. W. Abraham and F. A. McDonald. "Theory of magnetic force microscope images". *Applied Physics Letters*, 56 12, 1990, pp. 1181–1183.

[185] L. Belliard, A. Thiaville, S. Lemerle, A. Lagrange, J. Ferré, and J. Miltat. "Investigation of the domain contrast in magnetic force microscopy". *Journal of Applied Physics*, 81 8, 1997, pp. 3849–3851.

[186] L. Berges, E. Haltz, S. Panigrahy, S. Mallick, R. Weil, S. Rohart, A. Mougin, and J. Sampaio. "Size-dependent mobility of skyrmions beyond pinning in ferrimagnetic GdCo thin films". *Physical Review B*, 106 14, 2022, p. 144408.

[187] A. Vansteenkiste, J. Leliaert, M. Dvornik, M. Helsen, F. Garcia-Sanchez, and B. Van Waeyenberge. "The design and verification of MuMax3". *AIP Advances*, 4 10, 2014, p. 107133.

[188] J. Masell, D. R. Rodrigues, B. F. McKeever, and K. Everschor-Sitte. "Spin-transfer torque driven motion, deformation, and instabilities of magnetic skyrmions at high currents". *Physical Review B*, 101 21, 2020, p. 214428.

[189] H. Vakili, J.-W. Xu, W. Zhou, M. N. Sakib, M. G. Morshed, T. Hartnett, Y. Quessab, K. Litzius, C. T. Ma, S. Ganguly, M. R. Stan, P. V. Balachandran, G. S. D. Beach, S. J. Poon, A. D. Kent, and A. W. Ghosh. "Skyrmionics—Computing and memory technologies based on topological excitations in magnets". *Journal of Applied Physics*, 130 7, 2021, p. 070908.

[190] K. Y. Guslienko, K.-S. Lee, and S.-K. Kim. "Dynamic Origin of Vortex Core Switching in Soft Magnetic Nanodots". *Physical Review Letters*, 100 2, 2008, p. 027203.

[191] R. E. Troncoso and Á. S. Núñez. "Brownian motion of massive skyrmions in magnetic thin films". *Annals of Physics*, 351, 2014, pp. 850–856.

[192] E. A. Tremsina and G. S. D. Beach. "Atomistic simulations of distortion-limited high-speed dynamics of antiferromagnetic skyrmions". *Physical Review B*, 106 22, 2022, p. L220402.

[193] P. J. Metaxas, J. P. Jamet, A. Mougin, M. Cormier, J. Ferré, V. Baltz, B. Rodmacq, B. Dieny, and R. L. Stamps. "Creep and Flow Regimes of Magnetic Domain-Wall Motion in Ultrathin Pt / Co / Pt Films with Perpendicular Anisotropy". *Physical Review Letters*, 99 21, 2007, p. 217208.

[194] S.-G. Je, D.-H. Kim, S.-C. Yoo, B.-C. Min, K.-J. Lee, and S.-B. Choe. "Asymmetric magnetic domain-wall motion by the Dzyaloshinskii-Moriya interaction". *Physical Review B*, 88 21, 2013, p. 214401.

[195] C. O. Avci, K. Garello, C. Nistor, S. Godey, B. Ballesteros, A. Mugarza, A. Barla, M. Valvidares, E. Pellegrin, A. Ghosh, I. M. Miron, O. Boulle, S. Auffret, G. Gaudin, and P. Gambardella. "Fieldlike and antidamping spin-orbit torques in as-grown and annealed Ta/CoFeB/MgO layers". *Physical Review B*, 89 21, 2014, p. 214419.

[196] C. Reichhardt, C. J. O. Reichhardt, and M. V. Milošević. "Statics and dynamics of skyrmions interacting with disorder and nanostructures". *Reviews of Modern Physics*, 94 3, 2022, p. 035005.

[197] Y. Wu, K. Meng, J. Miao, X. Xu, and Y. Jiang. "Enhanced spin-orbit torque in Pt/Co/Pt multilayers with inserting Ru layers". *Journal of Magnetism and Magnetic Materials*, 472, 2019, pp. 14–19.

[198] J. Kim and Y. Otani. "Orbital angular momentum for spintronics". *Journal of Magnetism and Magnetic Materials*, 563, 2022, p. 169974.

[199] R. Gupta, C. Bouard, F. Kammerbauer, J. O. Ledesma-Martin, I. Kononenko, S. Martin, G. Jakob, M. Drouard, and M. Kläui. *Harnessing Orbital Hall Effect in Spin-Orbit Torque MRAM*. Apr. 3, 2024. doi: 10.48550/arXiv.2404.02821. arXiv: `2404.02821[physics]`. URL: `http://arxiv.org/abs/2404.02821` (visited on 08/05/2025) (cit. on p. 67).

[200] K.-F. Huang, D.-S. Wang, H.-H. Lin, and C.-H. Lai. "Engineering spin-orbit torque in Co/Pt multilayers with perpendicular magnetic anisotropy". *Applied Physics Letters*, 107 23, 2015, p. 232407.

[201] B. Jinnai, C. Zhang, A. Kurenkov, M. Bersweiler, H. Sato, S. Fukami, and H. Ohno. "Spin-orbit torque induced magnetization switching in Co/Pt multilayers". *Applied Physics Letters*, 111 10, 2017, p. 102402.

[202] T. Devolder, O. Bultynck, P. Bouquin, V. D. Nguyen, S. Rao, D. Wan, B. Sorée, I. P. Radu, G. S. Kar, and S. Couet. "Back hopping in spin transfer torque switching of perpendicularly magnetized tunnel junctions". *Physical Review B*, 102 18, 2020, p. 184406.

[203] J. Von Neumann. *The Computer and the Brain*. New Haven: Yale University Press, 1958 (cit. on p. 84).

[204] P. Hess. *Why a decades old architecture decision is impeding the power of AI computing*. Accessed 2025-08-21. IBM Research. Feb. 10, 2025. URL: `https://research.ibm.com/blog/why-von-neumann-architecture-is-impeding-the-power-of-ai-computing` (cit. on p. 84).

[205] Z. Qi, L. Mi, H. Qian, W. Zheng, Y. Guo, and Y. Chai. "Physical Reservoir Computing Based on Nanoscale Materials and Devices". *Advanced Functional Materials*, 33 43, 2023, p. 2306149.

[206] M. Ramon, S. Caharel, and B. Rossion. "The Speed of Recognition of Personally Familiar Faces". *Perception*, 40 4, 2011, pp. 437–449.

[207] K. M. Stiefel and J. S. Coggan. "The energy challenges of artificial superintelligence". *Frontiers in Artificial Intelligence*, 6, 2023, p. 1240653.

[208] C. Golgi. "Sulla struttura della sostanza grigia del cervello". *Gazzetta Medica Italiana - Lombardia*, 33, 1873, pp. 244–246.

[209] S. Ramón y Cajal. *Textura del sistema nervioso del hombre y de los vertebrados: Estudios sobre el plan estructural y composición histológica de los centros nerviosos adicionados de consideraciones fisiológicas fundadas en los nuevos descubrimientos*. Accessed 2025-08-21. Madrid: Moya, 1899. URL: `https://digibug.ugr.es/handle/10481/69715` (cit. on p. 85).

[210] A. S. Pivovarov, F. Calahorro, and R. J. Walker. "Na+/K+-pump and neurotransmitter membrane receptors". *Invertebrate Neuroscience*, 19 1, 2019, p. 1.

[211] L. Abbott. "Lapicque's introduction of the integrate-and-fire model neuron (1907)". *Brain Research Bulletin*, 50 5, 1999, pp. 303–304.

[212] F. Ponulak 2 and A. Kasinski. "Introduction to spiking neural networks: Information processing, learning and applications". *Acta Neurobiologiae Experimentalis*, 71 4, 2011, pp. 409–433.

[213] W. Mcculloch and W. Pitts. "A Logical Calculus of Ideas Immanent in Nervous Activity". *Bulletin of Mathematical Biophysics*, 5, 1943, pp. 127–147.

[214] F. Rosenblatt. "The perceptron: A probabilistic model for information storage and organization in the brain." *Psychological Review*, 65 6, 1958, pp. 386–408.

[215] D. Svozil, V. Kvasnicka, and J. Pospichal. "Introduction to multi-layer feed-forward neural networks". *Chemometrics and Intelligent Laboratory Systems*, 39 1, 1997, pp. 43–62.

[216] G. Bebis and M. Georgiopoulos. "Feed-forward neural networks". *IEEE Potentials*, 13 4, 1994, pp. 27–31.

[217] L. C. Jain and L. R. Medsker. *Recurrent Neural Networks: Design and Applications*. 1st. USA: CRC Press, Inc., 1999. ISBN: 0849371813 (cit. on p. 88).

[218] D. P. Mandic and J. A. Chambers. *Recurrent Neural Networks for Prediction: Learning Algorithms, Architectures and Stability*. 1st ed. Wiley, Aug. 6, 2001. ISBN: 978-0-471-49517-8 978-0-470-84535-6. doi: 10.1002/047084535X. URL: https://onlinelibrary.wiley.com/doi/book/10.1002/047084535X (visited on 08/08/2025) (cit. on p. 88).

[219] W. Zaremba, I. Sutskever, and O. Vinyals. *Recurrent Neural Network Regularization*. arXiv:1409.2329. arXiv, Feb. 19, 2015. doi: 10.48550/arXiv.1409.2329. arXiv: 1409.2329[cs]. URL: http://arxiv.org/abs/1409.2329 (visited on 08/08/2025) (cit. on p. 88).

[220] R. M. Schmidt. *Recurrent Neural Networks (RNNs): A gentle Introduction and Overview*. Nov. 23, 2019. doi: 10.48550/arXiv.1912.05911. arXiv: 1912.05911[cs]. URL: http://arxiv.org/abs/1912.05911 (visited on 08/08/2025) (cit. on p. 88).

[221] A. Graves. *Supervised Sequence Labelling with Recurrent Neural Networks*. Vol. 385. Studies in Computational Intelligence. Berlin, Heidelberg: Springer Berlin Heidelberg, 2012. ISBN: 978-3-642-24796-5 978-3-642-24797-2. doi: 10.1007/978-3-642-24797-2. URL: https://link.springer.com/10.1007/978-3-642-24797-2 (visited on 08/08/2025) (cit. on p. 89).

[222] K. Cho, B. v. Merrienboer, D. Bahdanau, and Y. Bengio. *On the Properties of Neural Machine Translation: Encoder-Decoder Approaches*. Oct. 7, 2014. doi: 10.48550/arXiv.1409.1259. arXiv: 1409.1259[cs]. URL: http://arxiv.org/abs/1409.1259 (visited on 08/08/2025) (cit. on p. 89).

[223] W. Maass. "Liquid State Machines: Motivation, Theory, and Applications". In: S. B. Cooper and A. Sorbi. *Computability in Context*. IMPERIAL COLLEGE PRESS, Feb. 2011, pp. 275–296. ISBN: 978-1-84816-245-7 978-1-84816-277-8. doi: 10.1142/9781848162778˙0008. URL: http://www.worldscientific.com/doi/abs/10.1142/9781848162778_0008 (visited on 08/08/2025) (cit. on pp. 89, 90).

[224] W. Maass and H. Markram. "On the computational power of circuits of spiking neurons". *Journal of Computer and System Sciences*, 69 4, 2004, pp. 593–616.

[225] H. Jaeger. "The"echo state"approach to analysing and training recurrent neural networks". 2001.

[226] H. Jaeger. "The "echo state" approach to analysing and training recurrent neural networks – with an Erratum note".

[227] U. D. Schiller and J. J. Steil. "Analyzing the weight dynamics of recurrent learning algorithms". *Neurocomputing*, 63, 2005, pp. 5–23.

[228] F. Grezes. *Reservoir Computing: A New Paradigm for Neural Networks*. Apr. 3, 2025. doi: 10.48550/arXiv.2504.02639. arXiv: 2504.02639[cs]. URL: http://arxiv.org/abs/2504.02639 (visited on 09/17/2025) (cit. on p. 89).

[229] H. Jaeger. "A tutorial on training recurrent neural networks, covering BPTT, RTRL, EKF and the "echo state network" approach".

[230] I. B. Yildiz, H. Jaeger, and S. J. Kiebel. "Re-visiting the echo state property". *Neural Networks*, 35, 2012, pp. 1–9.

[231] M. Lukoševičius. "A Practical Guide to Applying Echo State Networks". In: *Neural Networks: Tricks of the Trade*. Ed. by G. Montavon, G. B. Orr, and K.-R. Müller. Vol. 7700. Series Title: Lecture Notes in Computer Science. Berlin, Heidelberg: Springer Berlin Heidelberg, 2012, pp. 659–686. ISBN: 978-3-642-35288-1 978-3-642-35289-8. doi: 10.1007/978-3-642-35289-8˙36. URL: http://link.springer.com/10.1007/978-3-642-35289-8_36 (visited on 01/06/2025) (cit. on p. 90).

[232] D. Verstraeten, B. Schrauwen, M. D'Haene, and D. Stroobandt. "An experimental unification of reservoir computing methods". *Neural Networks*, 20 3, 2007, pp. 391–403.

[233] M. Cucchi, S. Abreu, G. Ciccone, D. Brunner, and H. Kleemann. "Hands-on reservoir computing: a tutorial for practical implementation". *Neuromorphic Computing and Engineering*, 2 3, 2022, p. 032002.

[234] P. J. Werbos. "Backpropagation Through Time: What It Does and How to Do It". *Proceedings of the IEEE*, 78 10, 1990, pp. 1550–1560.

[235] L. Appeltant, M. Soriano, G. Van der Sande, J. Danckaert, S. Massar, J. Dambre, B. Schrauwen, C. Mirasso, and I. Fischer. "Information processing using a single dynamical node as complex system". *Nature Communications*, 2 1, 2011, p. 468.

[236] G. Tanaka, T. Yamane, J. B. Héroux, R. Nakane, N. Kanazawa, S. Takeda, H. Numata, D. Nakano, and A. Hirose. "Recent advances in physical reservoir computing: A review". *Neural Networks*, 115, 2019, pp. 100–123.

[237] R. Penrose. "A Generalized Inverse for Matrices". In: *Proceedings of the Cambridge Philosophy Society*. Vol. 51. 1955, pp. 406–413 (cit. on p. 92).

[238] J. Torrejon, M. Riou, F. A. Araujo, S. Tsunegi, G. Khalsa, D. Querlioz, P. Bortolotti, V. Cros, K. Yakushiji, A. Fukushima, H. Kubota, S. Yuasa, M. D. Stiles, and J. Grollier. "Neuromorphic computing with nanoscale spintronic oscillators". *Nature*, 547 7664, 2017, pp. 428–431.

[239] M. Riou, F. A. Araujo, J. Torrejon, S. Tsunegi, G. Khalsa, D. Querlioz, P. Bortolotti, V. Cros, K. Yakushiji, A. Fukushima, H. Kubota, S. Yuasa, M. D. Stiles, and J. Grollier. "Neuromorphic computing through time-multiplexing with a spin-torque nano-oscillator". In: *2017 IEEE International Electron Devices Meeting (IEDM)*. 2017 IEEE International Electron Devices Meeting (IEDM). San Francisco, CA: IEEE, Dec. 2017, pp. 36.3.1–36.3.4. ISBN: 978-1-5386-3559-9. doi: 10.1109/IEDM.2017.8268505. URL: https://ieeexplore.ieee.org/document/8268505/ (visited on 03/04/2024) (cit. on p. 94).

[240] M. Riou, J. Torrejon, B. Garitaine, F. Abreu Araujo, P. Bortolotti, V. Cros, S. Tsunegi, K. Yakushiji, A. Fukushima, H. Kubota, S. Yuasa, D. Querlioz, M. Stiles, and J. Grollier. "Temporal Pattern Recognition with Delayed-Feedback Spin-Torque Nano-Oscillators". *Physical Review Applied*, 12 2, 2019, p. 024049.

[241] D. Marković, N. Leroux, M. Riou, F. Abreu Araujo, J. Torrejon, D. Querlioz, A. Fukushima, S. Yuasa, J. Trastoy, P. Bortolotti, and J. Grollier. "Reservoir computing with the frequency, phase, and amplitude of spin-torque nano-oscillators". *Applied Physics Letters*, 114 1, 2019, p. 012409.

[242] J. Williame, A. D. Accioly, D. Rontani, M. Sciamanna, and J.-V. Kim. *Chaotic dynamics in a macrospin spin-torque nano-oscillator with delayed feedback*. Mar. 11, 2019. doi: 10.48550/arXiv.1709.04310. arXiv: 1709.04310[cond-mat]. URL: http://arxiv.org/abs/1709.04310 (visited on 08/12/2025) (cit. on p. 94).

[243] T. Furuta, K. Fujii, K. Nakajima, S. Tsunegi, H. Kubota, Y. Suzuki, and S. Miwa. "Macromagnetic Simulation for Reservoir Computing Utilizing Spin Dynamics in Magnetic Tunnel Junctions". *Physical Review Applied*, 10 3, 2018, p. 034063.

[244] T. Kanao, H. Suto, K. Mizushima, H. Goto, T. Tanamoto, and T. Nagasawa. "Reservoir Computing on Spin-Torque Oscillator Array". *Physical Review Applied*, 12 2, 2019, p. 024052.

[245] K. Raab, M. A. Brems, G. Beneke, T. Dohi, J. Rothörl, F. Kammerbauer, J. H. Mentink, and M. Kläui. "Brownian reservoir computing realized using geometrically confined skyrmion dynamics". *Nature Communications*, 13 1, 2022, p. 6982.

[246] M.-K. Lee and M. Mochizuki. "Handwritten digit recognition by spin waves in a Skyrmion reservoir". *Scientific Reports*, 13 1, 2023, p. 19423.

[247] T. Yokouchi, S. Sugimoto, B. Rana, S. Seki, N. Ogawa, Y. Shiomi, S. Kasai, and Y. Otani. "Pattern recognition with neuromorphic computing using magnetic field–induced dynamics of skyrmions". *Science Advances*, 8 39, 2022, eabq5652.

[248] R. Msiska, J. Love, J. Mulkers, J. Leliaert, and K. Everschor-Sitte. *Audio Classification with Skyrmion Reservoirs*. arXiv:2209.13946. arXiv, Sept. 28, 2022. arXiv: 2209.13946[cond-mat]. URL: http://arxiv.org/abs/2209.13946 (visited on 08/22/2023) (cit. on pp. 94, 95, 100).

[249] D. Prychynenko, M. Sitte, K. Litzius, B. Krüger, G. Bourianoff, M. Kläui, J. Sinova, and K. Everschor-Sitte. "Magnetic Skyrmion as a Nonlinear Resistive Element: A Potential Building Block for Reservoir Computing". *Physical Review Applied*, 9 1, 2018, p. 014034.

[250] G. Bourianoff, D. Pinna, M. Sitte, and K. Everschor-Sitte. "Potential implementation of reservoir computing models based on magnetic skyrmions". *AIP Advances*, 8 5, 2018, p. 055602.

[251] D. Pinna, G. Bourianoff, and K. Everschor-Sitte. “Reservoir Computing with Random Skyrmion Textures”. *Physical Review Applied*, 14 5, 2020, p. 054020.

[252] G. Beneke, T. B. Winkler, K. Raab, M. A. Brems, F. Kammerbauer, P. Gerhards, K. Knobloch, S. Krishnia, J. H. Mentink, and M. Kläui. “Gesture recognition with Brownian reservoir computing using geometrically confined skyrmion dynamics”. *Nature Communications*, 15 1, 2024, p. 8103.

[253] Y. Lecun, L. Bottou, Y. Bengio, and P. Haffner. “Gradient-based learning applied to document recognition”. *Proceedings of the IEEE*, 86 11, 1998, pp. 2278–2324.

[254] M. C. Mackey and L. Glass. “Oscillation and Chaos in Physiological Control Systems”. *Science*, 197 4300, 1977, pp. 287–289.

[255] R. Nakane, G. Tanaka, and A. Hirose. “Reservoir Computing With Spin Waves Excited in a Garnet Film”. *IEEE Access*, 6, 2018, pp. 4462–4469.

[256] R. Nakane, A. Hirose, and G. Tanaka. “Spin waves propagating through a stripe magnetic domain structure and their applications to reservoir computing”. *Physical Review Research*, 3 3, 2021, p. 033243.

[257] C. Fernando and S. Sojakka. “Pattern Recognition in a Bucket”. In: *Advances in Artificial Life: 7th European Conference, ECAL 2003, Dortmund, Germany, September 14–17, 2003, Proceedings*. Vol. 2801. Lecture Notes in Computer Science. Springer Berlin Heidelberg, 2003, pp. 588–597. doi: 10.1007/978-3-540-39432-7“‘63 (cit. on p. 96).

[258] M.-K. Lee and M. Mochizuki. “Reservoir Computing with Spin Waves in a Skyrmion Crystal”. *Physical Review Applied*, 18 1, 2022, p. 014074.

[259] W. Namiki, D. Nishioka, Y. Yamaguchi, T. Tsuchiya, T. Higuchi, and K. Terabe. *Experimental Demonstration of High-Performance Physical Reservoir Computing with Nonlinear Interfered Spin Wave Multi-Detection*. 2022. arXiv: 2207.03216 [cs.ET]. URL: https://arxiv.org/abs/2207.03216 (cit. on p. 96).

[260] C. Wringe, M. Trefzer, and S. Stepney. “Reservoir Computing Benchmarks: a tutorial review and critique”. *International Journal of Parallel, Emergent and Distributed Systems*, 40 4, 2025, pp. 313–351.

[261] W. Namiki, D. Nishioka, T. Tsuchiya, and K. Terabe. “Fast physical reservoir computing, achieved with nonlinear interfered spin waves”. *Neuromorphic Computing and Engineering*, 4 2, 2024, p. 024015.

[262] H. Liu, R. Wang, P. Guo, Z. Wen, J. Feng, H. Wei, X. Han, Y. Ji, and S. Zhang. “Manipulation of magnetization switching and tunnel magnetoresistance via temperature and voltage control”. *Scientific Reports*, 5 1, 2015, p. 18269.

[263] M. Riou, T. Chauveau, T. de Keijzer, J.-G. Caputo, J. Torrejon, and J. Grollier. “Reservoir computing leveraging the transient non-linear dynamics of spin-torque nano-oscillators”. In: *Neuromorphic Computing with Nanoscale Devices*. Ed. by J. Grollier, J. Carrey, and D. Mailly. ISTE Ltd and John Wiley & Sons Inc, 2021, pp. 223–246. URL: https://dev.flavio.be/bibtex/lib/Riou2021_book.pdf (cit. on p. 108).

[264] J. Shlens. “A Tutorial on Principal Component Analysis”. *arXiv preprint arXiv:1404.1100*, 2014.

[265] J. Love, J. Mulkers, R. Msiska, G. Bourianoff, J. Leliaert, and K. Everschor-Sitte. *Spatial Analysis of Physical Reservoir Computers*. arXiv:2108.01512. arXiv, Nov. 14, 2022. arXiv: 2108.01512[cond-mat]. URL: http://arxiv.org/abs/2108.01512 (visited on 08/22/2023) (cit. on p. 111).

[266] O. Lee, T. Wei, K. D. Stenning, J. C. Gartside, D. Prestwood, S. Seki, A. Aqeel, K. Karube, N. Kanazawa, Y. Taguchi, C. Back, Y. Tokura, W. R. Branford, and H. Kurebayashi. “Task-adaptive physical reservoir computing”. *Nature Materials*, 2023.

[267] S. Das, R. Mansell, L. Flajšman, M.-A. Syskaki, J. Langer, and S. van Dijken. “Magneto-ionic synapse for reservoir computing”. *Physical Review Applied*, 23, 2025, p. 054043.

[268] M. Dale. “Reservoir Computing in Materio”. Unpublished. 2018. URL: https://etheses.whiterose.ac.uk/id/eprint/22306/ (cit. on p. 112).

[269] A. Atiya and A. Parlos. “New results on recurrent network training: unifying the algorithms and accelerating convergence”. *IEEE Transactions on Neural Networks*, 11 3, 2000, pp. 697–709.

[270] B. Schrauwen, L. Buesing, and R. Legenstein. “On Computational Power and the Order-Chaos Phase Transition in Reservoir Computing”. In: *Advances in Neural Information Processing Systems 21 (NIPS 2008)*. See section 3 for details on NARMA benchmarks. 2008, pp. 1425–1432. URL: https://papers.nips.cc/paper/3535-on-computational-power-and-the-order-chaos-phase-transition-in-reservoir-computing (cit. on p. 112).

[271] K. Nakae and K. Nakajima. “Natural quantum reservoir computing for temporal information processing”. *Scientific Reports*, 12, 2022, p. 1353.

[272] J. Lou, Z. Ashtiani, Y. Wu, X. Li, Y. Wan, Z. Yang, X. Wang, B. Hu, C. Liu, R. Zhang, G. Xiao, and Q. Xia. "Reservoir Computing with Thin-film Ferromagnetic Devices". *Advanced Intelligent Systems*, 2023.

[273] M. Dale, J. F. Miller, S. Stepney, and M. A. Trefzer. "A substrate-independent framework to characterize reservoir computers". *Proceedings of the Royal Society A: Mathematical, Physical and Engineering Sciences*, 475 2226, 2019, p. 20180723.

[274] M. C. Mackey and L. Glass. "Oscillation and Chaos in Physiological Control Systems". *Science*, 197 4300, 1977, pp. 287–289.

[275] L. Glass and M. Mackey. "From Clocks to Chaos: The Rhythms of Life". *Princeton University Press*, 2010.

[276] L. Giovannini, D. Raiteri, E. Arecchi, S. Donati, and F. Prati. "Efficient optimisation of physical reservoir computers using delayed input". *Communications Physics*, 8, 2025.

[277] TU Chemnitz Magnetism Group. *Amorphous Magnetic Phases and Spin Glasses*. Describes that in amorphous metals, the absence of crystalline order, grain boundaries, and dislocations eliminates typical pinning sites, producing low-coercivity materials. 2025. URL: `https://www.tu-chemnitz.de/physik/OFGF/research/spinglasses.php` (cit. on p. 119).

[278] C. Cirillo. "Magnetotransport and Magnetic Properties of Amorphous $NdNi_5$ Thin Films". *Scientific Reports*, 10, 2020, p. 70646.

[279] M. Yamaguchi, Y. Uraoka, and K. Sugiyama. "Compositional Effect on Crystallization of (Fe, Ni, Co)-Si-B Amorphous Alloys". *Journal of the Japan Institute of Metals*, 42 3, 2008, pp. 294–303.

[280] Z. Hu, J. Besbas, K. Siewierska, R. Smith, P. Stamenov, and J. M. D. Coey. "Magnetism, transport, and atomic structure of amorphous binary Y_xCo_{1-x} alloys". *arXiv preprint arXiv:2309.16996*, 2023.

[281] R. Guedas, I. D. Manici, F. Disdier, S. Wintz, M. Weigand, R. Belkhou, G. Gaudin, B. Fernandez, and O. Boulle. "Manipulation of magnetic skyrmions in a three terminal magnetic tunnel junction observed via operando magnetic microscopy". In: *Spintronics XVIII*. Ed. by J.-E. Wegrowe, J. S. Friedman, M. Razeghi, and H. Jaffrès. Vol. 13586. International Society for Optics and Photonics. SPIE, 2025, p. 135860D. doi: 10.1117/12.3083070. URL: `https://doi.org/10.1117/12.3083070` (cit. on p. 119).

[282] L. Šmejkal, J. Sinova, and T. Jungwirth. "Emerging Research Landscape of Altermagnetism". *Phys. Rev. X*, 12, 2022, p. 040501.

[283] C. et al. "Altermagnetism: An unconventional spin-ordered phase of matter". *Science Advances*, 2024.

[284] L. Kong, Z. Sheng, L. Pan, and et al. "History-dependent domain and skyrmion formation in 2D van der Waals magnet Fe3GeTe2". *Nature Communications*, 13, 2022, p. 2585.

[285] J. Zhang, Y. Liu, S. Nie, K. Shen, and Z. Li. "Generation of magnetic skyrmions in two-dimensional magnets via interfacial proximity". *Physical Review B*, 107, 2023, p. 024402.